

**ULTRASOUND AND PHOTOACOUSTIC TECHNIQUES
FOR SURGICAL GUIDANCE INSIDE AND AROUND
THE SPINE**

by
Eduardo. A. Gonzalez

A dissertation submitted to The Johns Hopkins University in conformity with the
requirements for the degree of Doctor of Philosophy

Baltimore, Maryland
September 2022

© 2022 E. A. Gonzalez
All rights reserved

Abstract

Technological advances in image-guidance have made a significant impact in surgical standards, allowing for safer and less invasive procedures. Ultrasound and photoacoustic imaging are promising options for surgical guidance given their real-time capabilities without the use of ionizing radiation. However, challenges to improve the feasibility of ultrasound- and photoacoustic-based surgical guidance persist in the presence of bone.

In this thesis, we address four challenges surrounding the implementation of ultrasound- and photoacoustic-based surgical guidance in clinical scenarios inside and around the spine. First, we introduce a novel regularized implementation of short-lag spatial coherence (SLSC) beamforming, named locally-weighted short-lag spatial coherence (LW-SLSC). LW-SLSC improves the segmentation of bony structures in ultrasound images, thus reducing the hardware and software cost of registering pre- and intra-operative volumes. Second, we describe a contour analysis framework to characterize and differentiate photoacoustic signals originating from cancellous and cortical bone, which is critical for a safety navigation of surgical tools through small bony cavities such as the pedicle. This analysis is also useful for localizing tool tips within the pedicle. Third, we developed a GPU approach to SLSC beamforming to improve the signal-to-noise ratio of photoacoustic targets using low laser energies, thus improving the performance of robotic visual servoing of tool tips and enabling miniaturization of laser systems in the operating room. Finally, we developed a novel acoustic-based atlas method to identify photoacoustic contrast agents and discriminate

them from tissue using only two laser wavelength. This approach significantly reduces acquisition times in comparison to conventional spectral unmixing techniques.

These four contributions are beneficial for the transition of a combined ultrasound- and photoacoustic-based image-guidance system towards more challenging scenarios of surgical navigation. Focusing on bone structures inside and surrounding the spine, the newly combined systems and techniques demonstrated herein feature robust, accurate, and real-time capabilities to register to preoperative images, localize surgical tool tips, and characterize biomarkers. These contributions strengthen the range of possibilities for spinous and transthoracic ultrasound and photoacoustic navigation, broaden the scope of this field, and shorten the road to clinical implementation in the operating room.

PhD Committee Members

Muyinatu A. Lediju Bell, Ph.D. (Primary Reader & Advisor)

John C. Malone Assistant Professor
Department of Electrical and Computer Engineering
Johns Hopkins University

J. Webster Stayman, Ph.D. (Secondary Reader)

Associate Professor
Department of Biomedical Engineering
Johns Hopkins University

Israel Gannot, Ph.D.

Associate Research Professor
Department of Electrical and Computer Engineering
Johns Hopkins University

Amit Jain, M.D.

Associate Professor
Department of Orthopaedic Surgery
Johns Hopkins University

A mis padres, porque nunca fui, soy, o seré sin su incondicionable apoyo
A mi abuelo, por mostrarme el otro significado de la palabra "perseverancia"

Dedicated to my parents, for I never was, am, nor will be
without your unconditional support
Dedicated to Grandfather, for showing me the other meaning of perseverance

Acknowledgements

Throughout the writing of this dissertation I have received a great deal of support and assistance.

I would first like to thank my advisor, Professor Muyinatu A. Lediju Bell, whose expertise in ultrasound, photoacoustic, and signal processing was invaluable not only for formulating my research questions and methodology, but also in helping me to hone my rhetoric and oratory speech skills to the scientific community. Your insightful feedback pushed me to improve my critical thinking and brought my work to a higher level.

Similarly, I would like to thank Professors Vishal Patel, Trac D. Tran, Adam Sylvester, and Wojciech Zbijewski, who were members of my DBO committee and vouched my academic knowledge required for this PhD program. I would also like to thank Professors J. Webster Stayman and Israel Gannot for being part of my dissertation committee and Professor Amit Jain, for his contributions and guidance during the pedicle cannulation experiment.

Finally, I would like to acknowledge my colleagues at the PULSE Lab: Alycen Wiacek, Michelle Graham, Mardava Gubbi, and Arun Nair, for all the effort and patience in debugging each other codes. Those long hours spent past working time scratching our heads for the beamforming repository became extremely useful for each of our projects, so I am proud of what we accomplished for the future generations to come. The journal club session was also a nice addition that, although it was

interrupted during this pandemic, helped us to level up our understanding of state-of-art technologies in our field. I would also like to thank you all for the leisure time we share together, including drink nights, trips (huzzah for the international conferences!), movies, and board game weekends. There is no better work environment than when surrounded by true friends. I would gladly continue to be the DM of our DnD sessions, where I hope you one day follow the MAIN adventure I intended...

Contents

Abstract	ii
Acknowledgements	v
List of Tables	xiii
List of Figures	xiv
List of Symbols	xxvii
List of Abbreviations	xxix
Chapter 1 Introduction	1
1.1 Image-Guided Surgery	1
1.1.1 Overview	1
1.1.2 Challenges for Current Image-Guided Approaches	2
1.1.3 Ultrasound- and Photoacoustic-Based Image Guidance	2
1.2 Challenges for Photoacoustic and Ultrasound Image-Guided Surgery in the Presence of Bone	3
1.2.1 Spinal Fusion Surgery	3
1.2.2 Spinal Needle and Catheter Insertions	4
1.2.3 Cardiac Catheter Interventions	5
1.3 Image-Guided Tasks Inside and Surrounding the Spine	6
1.3.1 Overview	6

1.3.2	Ultrasound-to-CT Registration	6
1.3.3	Differentiation of Cortical from Cancellous Bone	7
1.3.4	Surgical Tool Tip Tracking	8
1.3.5	Contrast Agent Administration	8
1.4	Dissertation Outline	9
	References	11

Chapter 2 Segmentation of Bone Boundaries and Assessment of Bone

	Content	16
2.1	Introduction	16
2.2	Methods	19
2.2.1	Coherence-Based Beamforming Methods	19
2.2.1.1	Short-Lag Spatial Coherence	19
2.2.1.2	Locally Weighted Short-Lag Spatial Coherence	20
2.2.2	Segmentation of an <i>Ex Vivo</i> Caprine Vertebra	22
2.2.3	Vertebral Imaging of a Human Cadaver	23
2.2.3.1	Specimen and Surgery Details	23
2.2.3.2	Data Acquisition	24
2.2.3.3	Ultrasound and Photoacoustic Imaging	24
2.2.3.4	Ultrasound and Photoacoustic Segmentation	25
2.2.3.5	Landmark Registration	26
2.2.3.6	Cancellous vs. Cortical Bone Differentiation	26
2.2.4	Image Quality Assessments and Data Representation	28
2.3	Results	28
2.3.1	Bony Segmentation of an <i>Ex Vivo</i> Caprine Vertebra	28
2.3.2	Vertebral Imaging of a Human Cadaver	32
2.4	Discussion	39
2.5	Conclusions	42

2.6	Acknowledgments	43
2.7	Appendix: Out-of-plane Photoacoustic Signals Originated Inside Human Vertebrae	43
2.8	Appendix: Image Quality Assessment of Reconstructed Ultrasound Images of Human Vertebrae	44
	References	46
 Chapter 3 Countour Analysis of Photoacoustic Signals from Cortical Bone, Cancellous Bone, and a Fiber Tip		
		51
3.1	Introduction	51
3.2	Method	53
3.3	Results	55
3.4	Discussion	58
3.5	Conclusion	59
3.6	Acknowledgements	60
	References	61
 Chapter 4 GPU Implementation of Photoacoustic SLSC Imaging for Segmentation and Robotic Surgical Guidance		
		63
4.1	Introduction	63
4.2	Method	67
4.2.1	GPU Implementation of Photoacoustic SLSC Imaging	67
4.2.2	Processing Time Assessments	70
4.2.3	Image Quality Assessments	71
4.2.4	Application to Visual Servoing	74
4.2.5	<i>In vivo</i> Segmentation Assessment	75
4.3	Results	77
4.3.1	Selection of Beamforming Parameters	77

4.3.2	Speedup of GPU-SLSC Compared to CPU-SLSC	78
4.3.3	Performance in <i>Ex Vivo</i> Tissue	80
4.3.4	In Vivo Performance	84
4.4	Discussion	86
4.5	Conclusion	90
4.6	Acknowledgements	91
	References	92

Chapter 5 Acoustic Frequency-Based Identification of Photoacoustic

	Surgical Biomarkers	98
5.1	Introduction	98
5.2	Method	101
5.2.1	Experimental setup	101
5.2.2	Ground-truth Labelling	103
5.2.3	Atlas of Photoacoustic-Sensitive Materials	104
5.2.4	Comparison with Previous Methods	106
5.2.4.1	Spectral Unmixing Techniques	106
5.2.4.2	F-mode Imaging	107
5.2.4.3	Acoustic-Based Clustering with Calibrated Spectra	108
5.2.5	Evaluation of Laser Wavelength and Hyperparameters	108
5.2.6	Classification Performance Metrics	108
5.3	Results	110
5.3.1	Image and Segmentation Examples	110
5.3.2	Comparison of Sensitivity, Specificity, and Accuracy	112
5.3.3	Spectra Examples & Multiple Possible Dual-Wavelength Com- binations	115
5.3.4	Dataset Sensitivity	117
5.3.5	Sensitivity Against Fluence Changes	120

5.3.6	Performance with Aberrating Media	120
5.4	Discussion	122
5.5	Conclusions	126
5.6	Acknowledgments	127
5.7	Appendix: Parameter Optimization for Photoacoustic Spectral Analysis	127
5.8	Appendix: Selection of Reference Spectra for K-means Clustering . .	131
	References	133
 Chapter 6 Estimating Fractional Chromophore Contents during Sur-		
	gical Interventions	138
6.1	Introduction	138
6.2	Method	140
6.2.1	Experimental setup	140
6.2.2	Dual-wavelength atlas method for mixture estimation	142
6.2.3	Quantitative metrics	145
6.3	Results	147
6.3.1	Concentration Estimations from MB and Human Hb	147
6.3.2	Concentration Estimations from MB and Porcine Hb	151
6.3.3	Effect of mask size on concentration estimation performance .	155
6.4	Discussion	157
6.5	Conclusion	159
6.6	Acknowledgments	159
	References	160
 Chapter 7 Conclusions and Future Directions		167
7.1	Summary	167
7.2	Future Directions	169
7.2.1	Real-Time Coherence-Based Bone Segmentation	169

7.2.2	Complementary Bone Characterization	169
7.2.3	Visual Servoing with Pulsed Laser Diodes	170
7.2.4	<i>In Vivo</i> Estimation of Mixture Concentrations	170
7.3	Outlook	171
	References	172
	Biographical sketch	175
	Vita	176

List of Tables

Table 2-1 Discrimination of bone structures in ultrasound images of vertebrae in a human cadaver (determined using the ROIs shown in the Appendix)	33
Table 2-2 Euclidean distances between the fiducial marker segmented from the LW-SLSC photoacoustic image and each of the manual markers of the pedicle hole obtained from the registered CT images in Fig. 2-7	34
Table 5-1 Wavelengths and hyperparameters evaluated	109
Table 5-2 Best classification result achieved with each method. Bold font indicates the maximum value in each column	113
Table 5-3 Mean \pm standard deviation of the sensitivity, specificity, and accuracy measured across the wavelengths investigated for each method. Bold font indicates the maximum value in each column.	115
Table 5-4 Average among best 5 cases for each method. ^a Bold font indicates the maximum value in each column.	116
Table 6-1 Processing times (in seconds) for each training and testing stage of the dual-wavelength atlas method	155

List of Figures

Figure 1-1	Example of a spinal fusion technique, adapted from [29].	3
Figure 1-2	(a) Example of an epidural administration with a needle followed by catheter insertion, adapted from [46]. (b) Location of heart at the thoracic level of the spine and cardiac catheter placement within the abdominal aorta, adapted from [47]. (c) Illustration of a cardiac catheter within a heart, which is the final destination for cardiac catheter interventions, adapted from [48]	5
Figure 1-3	Challenges of photoacoustic and ultrasound imaging for surgical guidance, tasks, and major contributions of this thesis.	7
Figure 2-1	Acquisition setup for evaluating bony structure enhancement with an <i>ex vivo</i> caprine vertebra.	23
Figure 2-2	Setup to acquire ultrasound and photoacoustic data from the lumbar region of an <i>ex vivo</i> human cadaver. (a) Insertion of the optical fiber into the pedicle hole while the ultrasound transducer is placed across several lumbar laminae. (b) Posterior view of the lumbar vertebrae when the optical fiber is inserted into the pre-drilled pedicle hole.	25

Figure 2-3	Examples of reconstructed CT, DAS, SLSC ($M = 9$) and LW-SLSC ($N_L = 28$, $\alpha=0.1$) images of the caprine sample (not registered). Regions selected for gCNR measurements are denoted by the dashed boxes.	29
Figure 2-4	Examples of photoacoustic images overlaid on ultrasound images from an oblique view of L3-L5 vertebrae reconstructed with (a) DAS, (b) SLSC and (c) LW-SLSC ultrasound and photoacoustic beamforming. Top row: beamformed images. Bottom row: segmented masks. The triangles and circles represent the center of mass of isolated components from ultrasound and photoacoustic images, respectively, which are later combined and used as landmarks for CT registration. The insets show magnified views of the photoacoustic signal originating from the fiber tip.	30
Figure 2-5	(a) Registered US-CT bone boundaries after applying threshold segmentation to images of the <i>ex vivo</i> caprine vertebra. The ultrasound images were beamformed using DAS (left) SLSC (middle) and LW-SLSC (right). (b) Differences in the integrated thickness of the segmented bone boundary in lateral and axial dimensions, when comparing CT results to DAS, SLSC, and LW-SLSC results. Each boxplot shows the median (horizontal black line), interquartile range, maximum and minimum values of the differences in the integrated thickness.	31
Figure 2-6	Co-registered ultrasound (color) and CT (grayscale) images using ultrasound and photoacoustic landmarks (magenta) from segmented LW-SLSC images.	34

Figure 2-7	(a) X-Z and (b) Y-Z planes of the CT volume registered to the ultrasound and photoacoustic images. The yellow marker represents the centroid of the photoacoustic signal reconstructed with the LW-SLSC image, which was used as a fiducial marker for landmark registration. The blue markers show the outline of the pedicle hole.	35
Figure 2-8	Examples of photoacoustic signals generated when the tip of the optical fiber is touching a (a) medial breach, (b) lateral breach, and (c) cancellous core. Left column: CT axial slice. Right column: LW-SLSC ultrasound image co-registered with DAS photoacoustic image.	36
Figure 2-9	Areas of -6dB-contours around the center of photoacoustic targets from cortical and cancellous core using DAS beamforming. Each boxplot shows the median, interquartile range, maximum and minimum values of the estimated areas over 10 frames for cancellous (left) and cortical (right) bone.	37
Figure 2-10	Comparison of -6dB-contours from photoacoustic targets inside cortical and cancellous bone in a human cadaver vertebrae using DAS, SLSC and LW-SLSC beamforming. Each boxplot shows the median, interquartile range, maximum and minimum values of the estimated areas over 60 frames for cancellous and 50 frames for cortical bone.	38

Figure 2-11	Qualitative and quantitative assessment of photoacoustic images originating from out-of-plane signals. (a) Examples of cancellous, cortical, and out-of-plane DAS photoacoustic images. (b) SNR assessment measured from photoacoustic signals associated with the cancellous core, cortical bone, and characteristic out-of-plane signals. The shaded area represents signals that did not achieve the $\text{SNR} > 3$ threshold and were therefore not included in the area results of Figs. 2-9 and 2-10.	44
Figure 2-12	Examples of ultrasound and co-registered photoacoustic images from an oblique view of L3-L5 vertebrae reconstructed with DAS, SLSC and LW-SLSC. S_1 , S_2 , S_3 , and B denote the selected regions for quantitative assessments.	45
Figure 3-1	Examples of accurate and inaccurate pedicle screw placement [8].	52
Figure 3-2	CT axial slice (top) and corresponding LW-SLSC ultrasound images co-registered with DAS photoacoustic image (bottom). The photoacoustic images represent example signals obtained when the tip of the optical fiber touches the bottom of the cancellous core, the cortical bone of a lateral breach, and the cortical bone of a medial breach, from left to right, respectively. The yellow boxes indicate regions of interest for Fig. 3-3.	55
Figure 3-3	Contour plots of photoacoustic DAS, SLSC, and LW-SLSC images, taken from the region highlighted with the yellow box in Fig. 3-2, when the tip of the optical fiber was touching cancellous (top) or cortical (bottom) bone.	56

Figure 3-4	Difference of areas from DAS, SLSC, and LW-SLSC images of photoacoustic targets inside cortical and cancellous bone using contours of (a) -6dB, (b) -10dB, (c) -15dB, and (d) -20 dB. Each boxplot shows the median, interquartile range, maximum and minimum values of the estimated areas over 60 frames for cancellous bone and 50 frames for cortical bone. *** $p < 0.001$. .	56
Figure 4-1	Overview of photoacoustic-based visual servoing.	64
Figure 4-2	Workflow for acquiring a real-time photoacoustic SLSC image with the Alpinion ultrasound system. The diagrams on the right shows graphical displays of GPU kernel distributions for the “Remove DC”, “Receive delay”, and “Norm. log compress” (Normalize and Log compress) steps of real-time photoacoustic SLSC imaging. The x , y , D , and d shown in the CUDA kernels denote the input memory, output memory, high pass filter coefficients, and receive delays, respectively. Variables t , q , and l are indices for axial sample, channel, and scanline, respectively.	68
Figure 4-3	Photoacoustic acquisition setup. An optical fiber was attached to translation stage and inserted into <i>ex vivo</i> bovine tissue. As the optical fiber was translated, an ultrasound probe connected to a robot arm performed visual servoing.	72
Figure 4-4	GPU-SLSC processing times for a single image frame, acquired with $d=5$ cm and $d=15$ cm imaging depths, while varying the cumulative lag M and axial kernel size k	78
Figure 4-5	Image quality comparisons of gCNR (top) and lateral resolution (bottom) as functions of cumulative lag and axial kernel size for imaging depths of $d = 5$ cm (left) and $d = 10$ cm (right). . . .	79

Figure 4-6	Processing times for each stage of SLSC beamforming using GPU and CPU implementations.	80
Figure 4-7	(a) Photoacoustic images of the optical fiber inserted into <i>ex vivo</i> bovine muscle at 25 mm axial depth, operating at 268 μ J laser energy. Images were reconstructed with DAS, CPU-SLSC and GPU-SLSC beamformers. (b) SNR results from the optical fiber inserted into <i>ex vivo</i> bovine muscle as a function of the laser energy.	80
Figure 4-8	(a) Example of probe centering results for high and low laser energies with DAS and GPU-SLSC photoacoustic images. The first and second columns for each energy show the initial and final position of the fiber before and after probe centering, respectively. The dashed blue line represents the center of the image. The blue circle denotes the target detected by the segmentation algorithm. Video 1 contains a real-time display of these results, including additional photoacoustic images acquired between the before and after still frames (Video 1, MP4, 8.34 MB) (b) Probe centering experiment errors.	81
Figure 4-9	Fiber tracking results. (a) Example of robot positions with fiber tracking at 248 μ J. The circles represent time stamps when the visual servoing algorithm failed to segment the photoacoustic signal. (b) Fiber tracking errors at mid-range energies.	82

Figure 4-10	(a) Examples of <i>in vivo</i> DAS, CPU-SLSC, and GPU-SLSC photoacoustic images, created from the same raw data after adding Gaussian-distributed noise to achieve -30 dB channel SNR. The segmentation algorithm failed on the DAS image and succeeded with the CPU-SLSC and GPU-SLSC images. (b) For each channel SNR, the percentage of failed segmentations is represented as the mean \pm one standard deviation of 10 measurements obtained after varying the amplitude threshold in the segmentation algorithm from 35% to 66% of the maximum amplitude within each photoacoustic image.	85
Figure 5-1	Acquisition setup to test the differentiation of methylene blue (MB) from blood (Hb). These photoacoustic-sensitive materials fill the hollow chambers of a custom polyvinyl chloride plastisol phantom.	102
Figure 5-2	Overview of proposed method to differentiate photoacoustic signal sources using acoustic frequency information. The blue and red coherence masks show regions of interest for methylene blue (MB) and blood (Hb), respectively. These regions are known for the training set and need to be correctly classified through atlas comparisons during testing. Spectra are asymmetric with respect to frequency because baseband signals were analyzed after IQ demodulation.	104
Figure 5-3	Two proposed spectral analyses for characterization based on single (top) and dual (bottom) wavelength emissions.	106

Figure 5-4	Locally-weighted short-lag spatial coherence (LW-SLSC) photoacoustic images overlaid on DAS ultrasound images of MB and Hb, obtained with a laser wavelength emission of (a) 710 nm (c), 800 nm (e) 890 nm, and (g) 920 nm. Segmented masks for MB and Hb after a -10 dB threshold was applied to the LW-SLSC photoacoustic images with single-wavelength masks shown for wavelengths of (b) 710 nm and (f) 890 nm, (d) the compound mask from "OR" logical operation on masks generated from 690 nm to 800 nm, and (h) the resulting mask from the "OR" logical operation of the 690 nm and 920 nm masks.	111
Figure 5-5	Example of segmented regions of MB and Hb using different classification approaches. The blue and red regions represent correctly classified pixels of MB and Hb, respectively, while the yellow regions represent misclassified pixels. Each image shows the frame of the dataset generated with the wavelength emission that achieved the highest accuracy.	112

Figure 5-6	Overall classification results with dual-wavelength atlas, single-wavelength atlas, spectral unmixing methods, F-mode, and k-means clustering using Dataset 1, 2, and 3. Top, middle and bottom rows show the sensitivity, specificity and accuracy of classification, respectively. The left and right columns show the mean and standard deviation over 10 frames, respectively. For each image, the first 2 vertical stripes counting from the left represents the results for spectral unmixing and spectral unmixing + NNMF, respectively, which have a single value from 690 to 800 nm wavelengths. The next 3 stripes represent the results for single-wavelength atlas, F-mode, and k-means clustering, respectively, as a function of wavelength emission. Finally, the upper triangle represents the results of the dual-wavelength atlas for each pair of wavelength combination.	114
Figure 5-7	(a) Examples of stacked spectra of in-phase quadrature data from MB and Hb using (top) single-wavelength atlas method and (bottom) dual-wavelength atlas method. The spectra show combined results obtained with 710 nm and 870 nm laser wavelength. (b) Comparison of sensitivity and 1-specificity from single- and dual-wavelengths atlas method using a one frame per wavelength and wavelength pair, respectively. The threshold regions delimits cases with both sensitivity and specificity greater than 0.8, which represents a good classification performance.	117
Figure 5-8	Classification accuracy of the spectral unmixing techniques for three testing datasets while varying the additive coefficient γ . .	118

Figure 5-9	Classification accuracy of each method when tested on Datasets 1-3, evaluated with (a) the full range of wavelengths and additive coefficient γ (with each distribution obtained from 270-3510 samples, i.e., 10 acquired frames \times 27-351 wavelengths, wavelength pairs, or γ) and (b) the best 5 cases of wavelengths and γ among the datasets (with each distribution obtained from 50 samples, i.e., 10 frames \times 5 cases). SU = Spectral Unmixing, NNMF = Non-negative Matrix Factorization.	119
Figure 5-10	Classification accuracy of each method when tested with four fluence pairs, evaluated using the best 5 cases of wavelengths and additive coefficient γ among the datasets. Each distribution was obtained from 150 samples (10 frames \times 5 cases \times 3 datasets). SU = Spectral Unmixing, NNMF = Non-negative Matrix Factorization.	121
Figure 5-11	Classification accuracy of the dual-wavelength atlas method when varying the thickness of the aberrating tissue layers, evaluated with 5 different wavelength pairs. Each distribution was obtained from 10 samples (10 frames \times one wavelength pair)	122
Figure 5-12	Criteria for determining the optimal number of principal components for the dual-wavelength atlas method using the (left) Kaiser rule [53] and (right) a 80% variance threshold.	128
Figure 5-13	Mean accuracy classification results of the dual-wavelength atlas method per wavelength pair with a dataset of 10 frames per wavelength using the initial parameters of Gonzalez <i>et al.</i> [23] and the updated parameters.	129
Figure 5-14	Summary of sensitivity, specificity, and accuracy results of the dual-wavelength atlas method before and after parameter optimization.	129

Figure 5-15	Setup for reference spectra acquisition. A and B represent the imaging depths of 5 and 9 cm for aluminum, respectively. C and D represent the imaging depths of 5 and 9 cm for steel, respectively.	130
Figure 5-16	Mean classification accuracy of k-means clustering with different reference spectra. The box plots represent the group of frames evaluated with laser wavelength that achieved the overall best accuracy among reference spectra (i.e., 840 nm). The three letter codes on the abscissa represent the material of the reference (i.e., A = Aluminum or S = Steel), followed by the orientation of the material relative to the ultrasound transducer (i.e., O = Orthogonal or T= Tilted), followed by the imaging depth of 5 cm or 9 cm (i.e., T = Top or B = Bottom, respectively).	130
Figure 6-1	(a) Experimental setup and (b) framework of the dual-wavelength atlas method for mixture estimation of methylene blue (MB) and Hb (Hb)	142
Figure 6-2	Evaluation of monotonicity and linearity of photoacoustic spectra obtained from mixtures of MB and Hb. (a) Stacked photoacoustic spectra of several mixture concentration (y axis) when using 710 nm and 870 nm laser wavelength (x axis). Each spectrum is normalized and log compressed to a 60 dB dynamic range. (b) Spearman's ρ coefficient and R^2 values of linear regression of concentration levels vs. acoustic frequency while varying the log compression dynamic range of the acoustic spectra. (c) Example of an acoustic frequency whose spectral amplitude of concentration levels follow a monotonic trend ($\rho = -0.88$) and a linear trend ($R^2 = 0.76$).	148

Figure 6-3	Performance optimization of the dual-wavelength atlas algorithm using the human Hb dataset. (a) R^2 values as a function of axial kernel size (z axis), threshold for spectra log compression (x axis), and number of principal components used (y axis). (b) Examples of mixture estimations (y axis) vs ground truth concentrations (x axis) when using the parameter set that yielded the highest R^2 value (i.e., 0.80), represented by dotted square in (a)	150
Figure 6-4	Estimated concentrations from porcine Hb. (a) R^2 value of a 1:1 linear fit between estimated and true concentration levels while varying the threshold for spectra log compression (y axis) and number of principal components used (x axis). (b) Mixture estimation (y axis) vs ground truth concentration (x axis) when using a 40 dB threshold and 1 principal component.	151
Figure 6-5	Example of photoacoustic DAS images, coherence masks used for segmentation, and estimated concentration map for a ground-truth concentration of 60% (i.e., 60% MB and 40% experimental porcine Hb). The purple contours represent the masks obtained by thresholding the coherence images at -3 dB and merging the results from 710 nm and 870 nm.	153
Figure 6-6	Examples of concentration maps of MB and porcine Hb generated by the dual-wavelength atlas method in a phantom experiment. The concentration maps (colored) are overlaid on ultrasound images generated with LW-SLSC.	154
Figure 6-7	Mean absolute error of the estimated chromophore concentration obtained with the dual-wavelength atlas method as a function of M-weighted SLSC coherence thresholds.	155

Figure 6-8	Example concentration maps generated with different coherence threshold values.	156
Figure 7-1	Timeline of publications towards the implementation of an ultrasound- and photoacoustic-based surgical guidance system. The publications are grouped by novel solutions to the primary challenges tackled in this thesis: (1) image segmentation for registration [1–3], (2) bone tissue characterization [3, 4], (3) visual servoing [5–8], and (4) photoacoustic contrast agents [9–12]	168

List of Symbols

A	matrix of ones
B	2D TV operator
C	coherence factor
\mathcal{C}	source component reconstruction
\tilde{C}	estimated concentration
d	imaging depth
D	1D TV operator
f	optimization expression combining sensitivity, specificity, and accuracy
F_{Hb}	number of false Hb pixels
F_{MB}	number of false MB pixels
H	Hessian matrix for LW-SLSC computation
k	length of the SLSC correlation kernel in number samples
\mathbf{k}	number of chromophores
\tilde{k}	ground-truth concentration
k_x	number of lateral samples of the LW-SLSC kernel
k_z	number of axial samples of the LW-SLSC kernel
m	spacing between two transducer elements or lag
\mathbf{m}	number of laser wavelength acquisitions
M	short-lag value
\mathcal{M}	measurement matrix
\mathbf{n}	number of pixels in the image for spectral unmixing
N	number of samples of the spectrum for dual-wavelength atlas
N_i	number of elements for the GPU-SLSC image
N_L	number of short-lag values evaluated for LW-SLSC
N_x	number of lateral samples for the GPU-SLSC image
N_z	number of axial samples for the GPU-SLSC image
p	p-value
\mathbf{p}	iteration index
p_i	probability density function of signal amplitudes of a target region

p_o	probability density function of signal amplitudes of a background region
\vec{p}_0	lateral center line of the image
\vec{p}	lateral position of centroid
$\Delta\vec{p}$	lateral difference between \vec{p} and \vec{p}_0 for visual servoing
P	number of samples of the concatenated spectra for dual-wavelength atlas
r_Δ	lateral width of the photoacoustic target
R^2	coefficient of determination
R	rank variable
\hat{R}	coherence function
s	time-delayed, zero-mean signal
\mathcal{S}	absorption coefficient matrix
\mathcal{S}'	adjusted absorption coefficient matrix
T_{Hb}	number of true Hb pixels
T_{MB}	number of true MB pixels
α	regularization factor for LW-SLSC
γ	additive coefficient for spectral unmixing
η	improvement tolerance for stopping criteria
Θ	hyperparameter for chromophore classifier
$\hat{\Theta}$	optimal hyperparameter for chromophore classifier
λ	optical wavelength
Λ	acoustic wavelength (i.e., inverse of the center frequency of an ultrasound transmission)
μ_C	mean estimated concentration
μ_t	mean value of the target region
ρ	Spearman's rank correlation coefficient
σ_o	standard deviation of the background region
∇	gradient operator
$\ \cdot\ _1$	L_1 norm, Manhattan norm

List of Abbreviations

ACC	Accuracy
ANN	Artificial neural network
CF	Coherence factor
CNR	Contrast-to-noise ratio
CPU	Central processing Unit
CT	Computed tomography
CUDA	Compute unified device architecture
DAS	Delay-and-sum
DMAS	Delay-multiply-and-sum
FDA	Food and drug administration
FFT	Fast Fourier transform
FN	False negative
FP	False positive
FWHM	Full width half maximum
gCNR	Generalized contrast-to-noise ratio
GPU	Graphical processing unit
Hb	Hemoglobin
IQ	In-phase quadrature
IQR	Interquartile range
LDA	Linear discriminant analysis
LW-SLSC	Locally-weighted short-lag spatial coherence
MAE	Mean absolute error
MB	Methylene blue
MPE	Maximum permissible exposure
MRI	Magnetic resonance imaging
MV	Minimum variance
NN	Nearest neighbour
NNMF	Non-negative matrix factorization
OR	Operating room
PCA	Principal component analysis
PRP	Pulse repetition frequency
PVCP	Polyvinyl chloride-plastisol
RAM	Random-Access Memory
RF	Radio-frequency
ROI	Region of interest

SAF	Synthetic aperture focusing
SLSC	Short-lag spatial coherence
SNR	Signal-to-noise ratio
SRC	Sparse representation-based classifier
TN	True negative
TNR	True negative rate
TP	True positive
TPR	True positive rate
TV	Total variation
VRAM	Video random-access memory

Chapter 1

Introduction

1.1 Image-Guided Surgery

1.1.1 Overview

For several centuries, at the patient's table, surgeons have asked themselves the same four questions: (1) Where am I anatomically? or more precisely, where is my surgical tool? (2) where is my organ, tissue, or mass of interest? (3) how do I reach it without compromising other nearby structures in my path? and (4) how is my patient doing as I am operating? [1]. Over the past three decades, recent discoveries in physics and advances in technology and computing have achieved significant milestones in addressing these four questions, which has transformed surgical standards, allowing for safer and less invasive procedures [2]. From the first non-invasive visualization of the human bone in 1895 with the invention of X-rays [3], to the advent of stereotactic system for surgical guidance in the mid-70s [4], to the introduction of robotic-surgery by the end of last century [5], safe and sophisticated approaches have been proposed and developed to tackle challenging scenarios of surgical navigation in the operating room (OR).

1.1.2 Challenges for Current Image-Guided Approaches

Surgical image-guidance is the field of medical imaging where the surgeon relies on feedback from images representing the physical properties of an interrogating region to assess the outcome of a specific pathway during a procedure [6]. Computed tomography (CT), fluoroscopy, and magnetic resonance imaging (MRI), are some of the most commonly used imaging technologies for computer-assisted intervention, as they provide preoperative information that can be later used as a map for navigating a surgical tool with the aid of tracking and registration devices. However, CT-based imaging techniques use ionizing radiation which can be harmful for the patient, operators, and children in misused dose and exposure times, while MRI imaging techniques require long processing times and considerable space in the OR, often making both CT and MRI imaging infeasible for providing real-time information of the targets of interest during surgery.

1.1.3 Ultrasound- and Photoacoustic-Based Image Guidance

Overcoming many of the limitations noted in Section 1.1.2, ultrasound imaging provides real-time capabilities at low cost and portability which are suitable for intraoperative use [7, 8]. With the use of pressure waves instead of ionizing radiation, radiologists can visualize a map representing the acoustic impedance of the interrogated tissue at a higher resolution than CT or MRI.

Complementary to ultrasound, photoacoustic imaging is an emerging imaging modality that has shown promise to exceed penetration depths in comparison purely optical imaging methods, provide similar spatial resolution to ultrasound imaging, and determine functional information based on changes in optical properties in tissue [9]. This technique utilizes a light source, instead of an ultrasound pressure wave, to excite tissue [10]. When the optically absorbing targets of interest are illuminated, they undergo thermal expansion, which results in an initial pressure distribution that

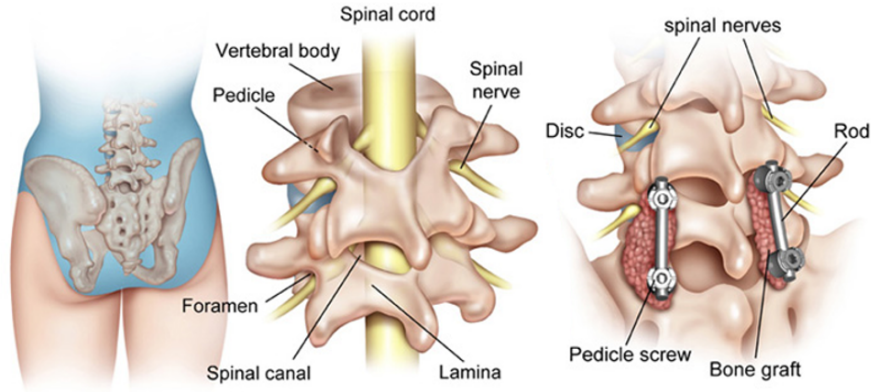


Figure 1-1. Example of a spinal fusion technique, adapted from [29].

relaxes to form a pressure wave. This pressure wave propagates through a localized region of the body and is received by an ultrasound transducer [11].

In the last decade, a wide range of applications of photoacoustic imaging for surgical guidance has been proposed [12, 13], including visualization of tool tips and blood vessels during fetal surgeries [14], endonasal surgeries [15–18], hysterectomy procedures [19, 20], core needle biopsies [21], abdominal surgeries [22], cardiac catheter interventions [23–25], brachytherapy procedures [26], as well as incorporation of robotics with teleoperated surgery [19] and robotic visual servoing [27, 28].

1.2 Challenges for Photoacoustic and Ultrasound Image-Guided Surgery in the Presence of Bone

1.2.1 Spinal Fusion Surgery

Spinal fusion surgeries are invasive procedures conducted to treat spine instability caused by degenerative disorders, trauma, and primary or metastatic cancer. These procedures involve drilling holes into the pedicles of vertebrae, inserting pedicle screws, and attaching each screw to a metal rod with the goal of stabilizing the spine to allow for bony fusion to occur, as illustrated in Fig. 1-1. When cannulating pedicles, it is critical to ensure the correct trajectory during drilling in order to avoid accidental bone breaches and screw misplacement. In particular, pedicle screw misplacement

occurs in approximately 14–39.8% of procedures [30–33], which compromises neighboring structures such as nerves (and in some cases, spinal cord), erodes long-term biomechanical stability, [34, 35], and causes adjacent degeneration [36, 37].

The presence of bone in spinal fusion procedures hinders the application of ultrasound and photoacoustic-based image guidance in relation to other environments due to the increased speed-of-sound, attenuation coefficient, and scattering present in the medium [38, 39]. However, the application of image guidance in the spine is not only a challenge but an opportunity to develop novel ultrasound- and photoacoustic-based solutions that register to preoperative images, characterize tissue contents, autonomously track surgical tool tips, and contribute to the feasibility of surgical guidance when navigating through bone. In addition, acoustic solutions designed for bone structure (i.e., in the spine) may be similarly applied to enhance the performance of image-guided tasks in soft tissue and vascularity (i.e., surrounding the spine).

1.2.2 Spinal Needle and Catheter Insertions

Regional anesthesia techniques such as epidural injections are perioperative procedures applied in regions surrounding the spine for managing chronic pain [40]. While traditional protocols resort to palpation for identifying key anatomical landmarks in order to provide an accurate needle trajectory, followed by catheter insertion, challenges arise for obese patients with high body mass index [41]. As a complementary tool for surgical guidance, ultrasound imaging has shown promise to enhance the accuracy of epidural injections by providing non-invasive, safe, and real-time feedback of the bone surface without exposing the patient to ionizing-radiation [40]. However, while some studies of ultrasound-guided epidural catheter placement report reduced placement times and number of needle passes when compared to landmark palpation [42, 43], other randomized controlled trials showed no benefit of procedural ultrasound imaging to epidural guidance [44].

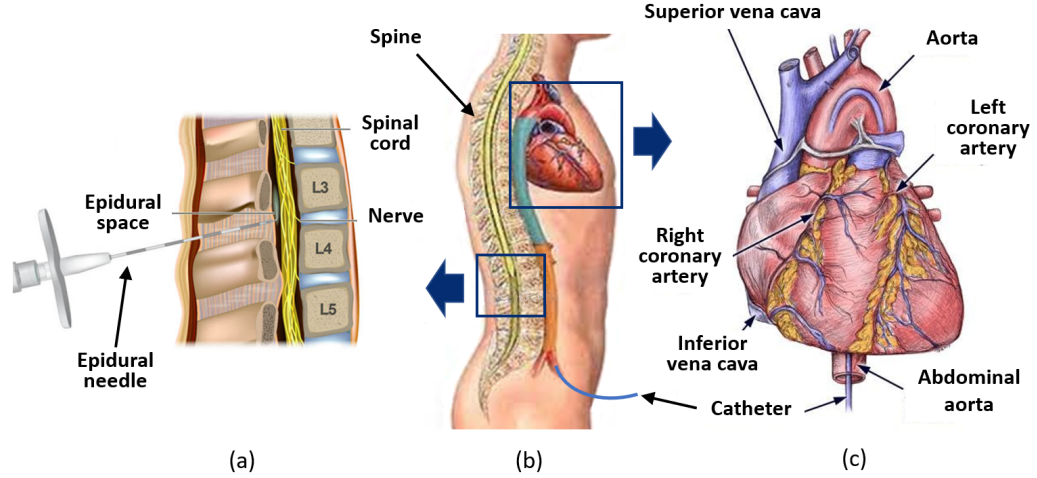


Figure 1-2. (a) Example of an epidural administration with a needle followed by catheter insertion, adapted from [46]. (b) Location of heart at the thoracic level of the spine and cardiac catheter placement within the abdominal aorta, adapted from [47]. (c) Illustration of a cardiac catheter within a heart, which is the final destination for cardiac catheter interventions, adapted from [48]

To enhance the benefits of ultrasound-guidance for spinal needle and catheter drug delivery interventions, fluoroscopy-based contrast agents have been used to determine epidural spreading and characterize the success of spinal injections [45]. However, as fluoroscopy uses ionizing radiation, a more suitable alternative to contrast enhancement can possibly be achieved with photoacoustic-based contrast agents. To demonstrate initial feasibility, we turn our attention to a related catheter intervention that suffers from similar challenges (i.e., cardiac catheter interventions), yet does not require operation in narrow interspinous spaces with limited intraoperative flexibility (which are considered secondary challenges to integrating photoacoustic-based contrast agents with interventional spinal procedures).

1.2.3 Cardiac Catheter Interventions

Cardiac catheter-based procedures (e.g., percutaneous coronary interventions, percutaneous transluminal angioplasty, catheter angiography, cardiac radiofrequency ablation) occur at the thoracic level of the spine, as illustrated in Fig. 1-2. Advances

in ultrasound- and photoacoustic-based techniques for image-guidance of these procedures consist of either placing an ultrasound transducer externally on the intercostal space or utilizing an internal catheter transducer that fits within the intravascular region. In particular, photoacoustic imaging provides additional benefits to identify pathological structures in the vessel wall with the insertion of light-sensitive contrast agents or exogenous chromophores. However, depending on the dose, exposure time, and number of target cells, adverse effects due to misuse of contrast agents include acute inflammation [49], apoptosis [49, 50], necrosis [51], cellular toxicity [52], allergies [53], reduction in cellular viability [54], nephropathy [55], hemolysis [56], and photo-damage [57]. Therefore, it is critical to monitor the concentration levels of exogenous chromophores mixed with endogenous chromophores (e.g., blood and lipids) when deploying photoacoustic-based contrast agents.

1.3 Image-Guided Tasks Inside and Surrounding the Spine

1.3.1 Overview

Fig. 1-3 summarizes key challenges presented in Section 1.2 for ultrasound- and photoacoustic-based image-guidance inside and surrounding the spine and four associated tasks to consider when navigating to the spine, through the pedicle, and administering photoacoustic contrast agents: (1) enable 2D ultrasound-to-CT registration, (2) differentiate cortical from cancellous bone, (3) track the tip of a surgical tool (e.g., drill, pedicle probe) with low laser energies, and (4) monitor and control administered contrast agent doses.

1.3.2 Ultrasound-to-CT Registration

The first step to implementing an ultrasound- and photoacoustic-based guidance system requires identification of anatomical landmarks for registration to pre-operative

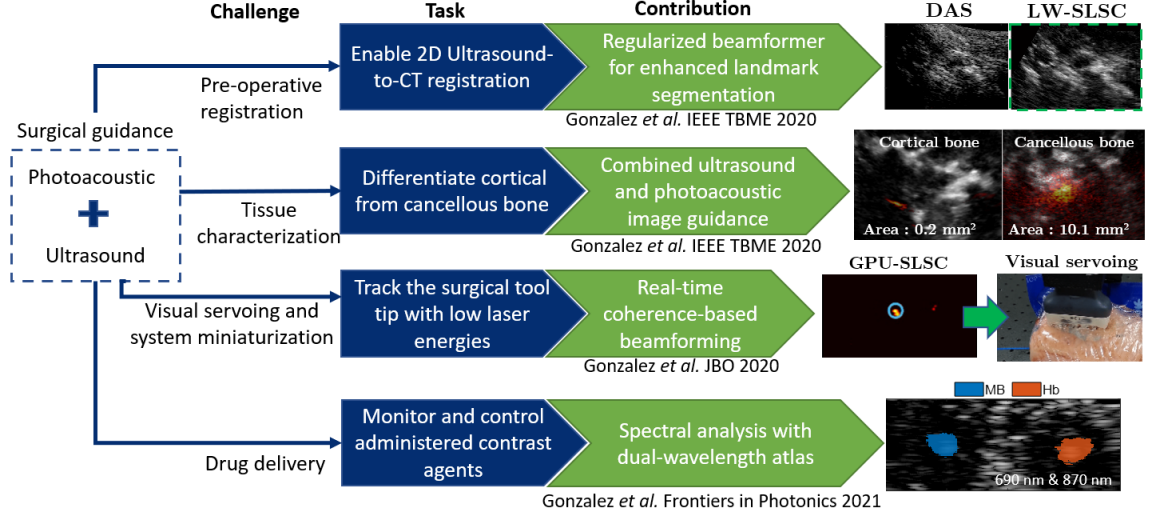


Figure 1-3. Challenges of photoacoustic and ultrasound imaging for surgical guidance, tasks, and major contributions of this thesis.

volumes. Current methods for this first step include measuring the bone contours obtained from ultrasound volumes and registering the ultrasound-based measurement to pre-operative CT volumes [58–61]. However, these techniques rely on the accuracy of the bone contours and require significant computational resources for fast registration. To avoid the use of ultrasound volumes, this dissertation presents a novel regularized beamformer for enhanced landmark segmentations that enable two-dimensional (2D) ultrasound-to-CT registration. The same beamformer is then applied to localize a surgical tool tip in photoacoustic images when navigating through the spine.

1.3.3 Differentiation of Cortical from Cancellous Bone

The differentiation of cortical (hard) from cancellous (spongy) bone plays a critical role in avoiding accidental pedicle breaches. As the cancellous core of the pedicle is rich with blood in comparison to surrounding cortical bone, photoacoustic imaging is an ideal for identifying, validating, and course-correcting regions targeted for pedicle screw insertion. Building on the novel landmark segmentation method noted in Section 1.3.2, this dissertation presents the first known combined ultrasound and photoacoustic image guidance system optimized for pedicle cannulation in posterior spinal fusion

surgery. This contribution demonstrates that both amplitude- and coherence based beamforming methods are mutually beneficial for localization of surgical tool tips and differentiation of cortical from cancellous bone.

1.3.4 Surgical Tool Tip Tracking

The surgical guidance system noted in Section 1.3.3 can be augmented with robotic assistance to autonomously track the surgical tool tip (i.e., visual servoing) by segmenting photoacoustic targets. To provide accurate segmentation, previous photoacoustic-based visual servoing implementations were implemented with laser energies ranging 300 μJ to 3.4 mJ [23, 62]. Although this approach maximizes the amplitude of photoacoustic signals, it introduces side lobes and other photoacoustic image artifacts. In contrast, coherence-based beamforming improves the quality of photoacoustic signals acquired with lower laser energies (e.g., 2.4 μJ to 8 μJ) [63], which is advantageous to ensure laser safety. Miniaturized low-energy light delivery systems are additionally beneficial for portability in the operating room. This dissertation presents the first known implementation of a real-time coherence-based beamformer for photoacoustic imaging, which was enabled by a graphical processing unit (GPU) and parallel processing techniques. This contribution allows tracking of the surgical tool tip with low laser energies (e.g., 118 μJ to 364 μJ), which is beneficial for visual servoing and system miniaturization.

1.3.5 Contrast Agent Administration

Monitoring and controlling administered photoacoustic-based contrast agents is critical during drug delivery in order to avoid adverse effects. Spectral unmixing is a photoacoustic-based technique typically implemented to measure the concentration of endogenous and exogenous chromophores. However, this technique requires long acquisition times due to the responses required from multiple (e.g., 45 [64]) laser wavelengths, which is prohibitive to real-time surgical guidance. This dissertation

presents a novel acoustic-based photoacoustic estimator that relies on training sets to estimate concentration levels from mixtures of photoacoustic-sensitive materials. In particular, the method is evaluated with mixtures of methylene blue (an exogenous chromophore) and hemoglobin (an endogenous chromophore). By using the normalized photoacoustic response from only two laser wavelengths, this estimator is beneficial for real-time monitoring the concentration of contrast agents in the operating room or interventional suite.

1.4 Dissertation Outline

The primary content of this thesis relies on peer-reviewed publications presented in their original, unaltered form. These contributions address initial barriers to implementing ultrasound- and photoacoustic-based image guidance systems inside and surrounding the spine according to the following outline:

- Starting with pre-operative registration, Chapter 2 presents a novel regularized coherence-based beamformer for segmentation of bone boundaries and assessment of bone content, which are necessary tasks for spinal fusion surgeries.
- Moving on to tissue characterization, Chapter 3 describes a photoacoustic-based contour analysis for differentiation of cortical from cancellous bone in order to avoid accidental bone breaches. Similarly, complementary information regarding the fiber tip location is achieved with the coherence-based beamformer described in Chapter 2.
- Coherence-based beamformers are computationally intensive. Therefore, Chapter 4 introduces a GPU-based coherence beamformer for photoacoustic segmentation and robotic surgical guidance.
- Transitioning to catheter interventions, Chapter 5 summarizes a novel acoustic-frequency analysis for the identification of endogenous and exogenous chro-

mophores requiring photoacoustic acquisitions from only two laser wavelength emissions. The GPU-based beamformer described in Chapter 4 is utilized to identify catheter tip positions.

- To monitor concentration levels of mixed chromophores, Chapter 6 expands the framework of Chapter 5 to estimate fractional methylene blue and hemoglobin contents, which is beneficial to avoid adverse effect due to misused dose during enhanced catheter interventions.
- Finally, Chapter 7 summarizes the major contributions of this dissertation and presents future directions for surgical guidance based on combined ultrasound and photoacoustic imaging.

References

- [1] U. Mezger, C. Jendrewski, and M. Bartels, “Navigation in surgery,” *Langenbeck’s Archives of Surgery*, vol. 398, no. 4, pp. 501–514, 2013.
- [2] Y. Enchev, “Neuronavigation: Geneology, reality, and prospects,” *Neurosurgical Focus*, vol. 27, no. 3, E11, 2009.
- [3] R. F. Mould, “The early history of x-ray diagnosis with emphasis on the contributions of physics 1895-1915,” *Physics in Medicine & Biology*, vol. 40, no. 11, p. 1741, 1995.
- [4] B. A. Kall, “The impact of computer and imaging technology on stereotactic surgery,” *Stereotactic and Functional Neurosurgery*, vol. 50, no. 1-6, pp. 9–22, 1987.
- [5] D. Ranev and J. Teixeira, “History of computer-assisted surgery,” *Surgical Clinics*, vol. 100, no. 2, pp. 209–218, 2020.
- [6] R. L. Galloway Jr, “Introduction and historical perspectives on image-guided surgery,” in *Image-Guided Neurosurgery*, Elsevier, 2015, pp. 1–22.
- [7] M. Ahmed and M. Douek, “Intra-operative ultrasound versus wire-guided localization in the surgical management of non-palpable breast cancers: Systematic review and meta-analysis,” *Breast Cancer Research and Treatment*, vol. 140, no. 3, pp. 435–446, 2013.
- [8] I. J. Gerard, M. Kersten-Oertel, J. A. Hall, D. Sirhan, and D. L. Collins, “Brain shift in neuronavigation of brain tumors: An updated review of intra-operative ultrasound applications,” *Frontiers in Oncology*, vol. 10, p. 3390, 2021.
- [9] L. V. Wang, *Photoacoustic imaging and spectroscopy*. CRC press, 2017.
- [10] P. Beard, “Biomedical photoacoustic imaging,” *Interface focus*, vol. 1, no. 4, pp. 602–631, 2011.
- [11] I. Steinberg, D. M. Huland, O. Vermesh, H. E. Frostig, W. S. Tummers, and S. S. Gambhir, “Photoacoustic clinical imaging,” *Photoacoustics*, vol. 14, pp. 77–98, 2019.
- [12] A. Wiacek and M. A. L. Bell, “Photoacoustic-guided surgery from head to toe,” *Biomedical Optics Express*, vol. 12, no. 4, pp. 2079–2117, 2021.
- [13] M. A. Lediju Bell, “Photoacoustic imaging for surgical guidance: Principles, applications, and outlook,” *Journal of Applied Physics*, vol. 128, no. 6, p. 060 904, 2020.
- [14] W. Xia, E. Maneas, D. I. Nikitichev, C. A. Mosse, G. S. Dos Santos, T. Vercauteren, A. L. David, J. Deprest, S. Ourselin, P. C. Beard, and A. E. Desjardins, “Interventional photoacoustic imaging of the human placenta with ultrasonic tracking for minimally invasive fetal surgeries,” in *International Conference on Medical Image Computing and Computer-Assisted Intervention*, Springer, 2015, pp. 371–378.
- [15] M. A. L. Bell, A. K. Ostrowski, P. Kazanzides, and E. Boctor, “Feasibility of transcranial photoacoustic imaging for interventional guidance of endonasal surgeries,” in *Photons Plus Ultrasound: Imaging and Sensing 2014*, International Society for Optics and Photonics, vol. 8943, 2014, p. 894 307.
- [16] M. A. L. Bell, A. K. Ostrowski, K. Li, P. Kazanzides, and E. M. Boctor, “Localization of transcranial targets for photoacoustic-guided endonasal surgeries,” *Photoacoustics*, vol. 3, no. 2, pp. 78–87, 2015.

- [17] M. T. Graham, J. Huang, F. Creighton, and M. A. L. Bell, "Simulations and human cadaver head studies to identify optimal acoustic receiver locations for minimally invasive photoacoustic-guided neurosurgery," *Photoacoustics*, p. 100183, 2020.
- [18] B. Eddins and M. A. L. Bell, "Design of a multifiber light delivery system for photoacoustic-guided surgery," *Journal of Biomedical Optics*, vol. 22, no. 4, p. 041011, 2017.
- [19] M. Allard, J. Shubert, and M. A. L. Bell, "Feasibility of photoacoustic-guided teleoperated hysterectomies," *Journal of Medical Imaging*, vol. 5, no. 2, p. 021213, 2018.
- [20] A. Wiacek, K. C. Wang, H. Wu, and M. A. L. Bell, "Dual-wavelength photoacoustic imaging for guidance of hysterectomy procedures," in *Advanced Biomedical and Clinical Diagnostic and Surgical Guidance Systems XVIII*, International Society for Optics and Photonics, vol. 11229, 2020, p. 112291D.
- [21] D. Piras, C. Grijsen, P. Schutte, W. Steenbergen, and S. Manohar, "Photoacoustic needle: Minimally invasive guidance to biopsy," *Journal of Biomedical Optics*, vol. 18, no. 7, p. 070502, 2013.
- [22] K. M. Kempinski, A. Wiacek, M. Graham, E. González, B. Goodson, D. Allman, J. Palmer, H. Hou, S. Beck, J. He, and M. A. L. Bell, "In vivo photoacoustic imaging of major blood vessels in the pancreas and liver during surgery," *Journal of Biomedical Optics*, vol. 24, no. 12, p. 121905, 2019.
- [23] M. Graham, F. Assis, D. Allman, A. Wiacek, E. Gonzalez, M. Gubbi, J. Dong, H. Hou, S. Beck, J. Chrispin, and M. A. L. Bell, "In vivo demonstration of photoacoustic image guidance and robotic visual servoing for cardiac catheter-based interventions," *IEEE Transactions on Medical Imaging*, vol. 39, no. 4, pp. 1015–1029, 2020.
- [24] Y. Zhang, Y. Cao, and J.-X. Cheng, "High-resolution photoacoustic endoscope through beam self-cleaning in a graded index fiber," *Optics Letters*, vol. 44, no. 15, pp. 3841–3844, 2019.
- [25] A. B. Karpouk, B. Wang, and S. Y. Emelianov, "Development of a catheter for combined intravascular ultrasound and photoacoustic imaging," *Review of Scientific Instruments*, vol. 81, no. 1, p. 014901, 2010.
- [26] M. K. A. Singh, V. Parameshwarappa, E. Hendriksen, W. Steenbergen, and S. Manohar, "Photoacoustic-guided focused ultrasound for accurate visualization of brachytherapy seeds with the photoacoustic needle," *Journal of Biomedical Optics*, vol. 21, no. 12, p. 120501, 2016.
- [27] M. A. L. Bell and J. Shubert, "Photoacoustic-based visual servoing of a needle tip," *Scientific Reports*, vol. 8, no. 1, p. 15519, 2018.
- [28] E. A. Gonzalez and M. A. L. Bell, "GPU implementation of photoacoustic short-lag spatial coherence imaging for improved image-guided interventions," *Journal of Biomedical Optics*, vol. 25, no. 7, pp. 1–19, 2020.
- [29] Bones and Spine Surgery Inc., *Transforaminal Lumbar Interbody Fusion (TLIF)*, <https://www.waynecheng.com/transforaminal-lumbar-interbody-fusion-tlif/w>, Accessed: 2022-04-23, 2022.
- [30] K. Abul-Kasim and A. Ohlin, "The rate of screw misplacement in segmental pedicle screw fixation in adolescent idiopathic scoliosis: The effect of learning and cumulative experience," *Acta Orthopaedica*, vol. 82, no. 1, pp. 50–55, 2011.

- [31] S. D. Gertzbein and S. E. Robbins, “Accuracy of pedicular screw placement in vivo.,” *Spine*, vol. 15, no. 1, pp. 11–14, 1990.
- [32] W. H. Castro, H. Halm, J. Jerosch, J. Malms, J. Steinbeck, and S. Blasius, “Accuracy of pedicle screw placement in lumbar vertebrae,” *Spine*, vol. 21, no. 11, pp. 1320–1324, 1996.
- [33] T. Laine, K. Mäkitalo, D. Schlenzka, K. Tallroth, M. Poussa, and A. Alho, “Accuracy of pedicle screw insertion: a prospective CT study in 30 low back patients,” *European Spine Journal*, vol. 6, no. 6, pp. 402–405, 1997.
- [34] N. Hecht, H. Yassin, M. Czabanka, B. Föhre, K. Arden, T. Liebig, and P. Vajkoczy, “Intraoperative computed tomography versus 3d c-arm imaging for navigated spinal instrumentation,” *Spine*, vol. 43, no. 5, pp. 370–377, 2018.
- [35] S. Açıkbaş, F. Arslan, and M. Tuncer, “The effect of transpedicular screw misplacement on late spinal stability,” *Acta Neurochirurgica*, vol. 145, no. 11, pp. 949–955, 2003.
- [36] P. Park, H. J. Garton, V. C. Gala, J. T. Hoff, and J. E. McGillicuddy, “Adjacent segment disease after lumbar or lumbosacral fusion: Review of the literature,” *Spine*, vol. 29, no. 17, pp. 1938–1944, 2004.
- [37] Y. Aota, K. Kumano, and S. Hirabayashi, “Postfusion instability at the adjacent segments after rigid pedicle screw fixation for degenerative lumbar spinal disorders.,” *Journal of Spinal Disorders*, vol. 8, no. 6, pp. 464–473, 1995.
- [38] P. Nicholson, R. Strelitzki, R. Cleveland, and M. Buxsein, “Scattering of ultrasound in cancellous bone: Predictions from a theoretical model,” *Journal of Biomechanics*, vol. 33, no. 4, pp. 503–506, 2000.
- [39] J. Töyräs, M. Nieminen, H. Kröger, and J. Jurvelin, “Bone mineral density, ultrasound velocity, and broadband attenuation predict mechanical properties of trabecular bone differently,” *Bone*, vol. 31, no. 4, pp. 503–507, 2002.
- [40] M. K. Karmakar and K. J. Chin, *Spinal sonography and applications of ultrasound for central neuraxial blocks*, 2017.
- [41] C. Edwards, E. C. Leira, and P. Gonzalez-Alegre, “Residency training: A failed lumbar puncture is more about obesity than lack of ability,” *Neurology*, vol. 84, no. 10, e69–e72, 2015.
- [42] J.-H. Lee, D.-H. Kim, and W. U. Koh, “Real-time ultrasound guided thoracic epidural catheterization: A technical review,” *Anesthesia and Pain Medicine*, 2021.
- [43] T. Ungi, P. Abolmaesumi, R. Jalal, M. Welch, I. Ayukawa, S. Nagpal, A. Lasso, M. Jaeger, D. P. Borschneck, G. Fichtinger, and P. Mousavi, “Spinal needle navigation by tracked ultrasound snapshots,” *IEEE Transactions on Biomedical Engineering*, vol. 59, no. 10, pp. 2766–2772, 2012.
- [44] C. Arzola, R. Mikhael, C. Margarido, and J. C. Carvalho, “Spinal ultrasound versus palpation for epidural catheter insertion in labour: A randomised controlled trial,” *European Journal of Anaesthesiology (EJA)*, vol. 32, no. 7, pp. 499–505, 2015.
- [45] D.-H. Kim, J.-H. Lee, J. H. Sim, W. Jeong, D. Lee, H.-M. Kwon, S.-S. Choi, and S.-M. Jeong, “Real-time ultrasound-guided low thoracic epidural catheter placement: Technical consideration and fluoroscopic evaluation,” *Regional Anesthesia & Pain Medicine*, vol. 46, no. 6, pp. 512–517, 2021.

- [46] Cleveland Clinic, *Epidural: What is it, Procedure, Risks, and Side Effects*, <https://my.clevelandclinic.org/health/treatments/21896-epidural>, Accessed: 2022-04-23, 2021.
- [47] Goodman, Jess, *Secrets of the spine*, <https://jessgoodman.medium.com/secrets-of-the-spine-fb3767c5c135>, Accessed: 2022-04-23, 2017.
- [48] Olade, Roger B., *Cardiac catheterization of left heart*, <https://emedicine.medscape.com/article/1819224-overview>, Accessed: 2022-04-23, 2016.
- [49] W.-S. Cho, M. Cho, J. Jeong, M. Choi, H.-Y. Cho, B. S. Han, S. H. Kim, H. O. Kim, Y. T. Lim, B. H. Chung, and J. Jeong, "Acute toxicity and pharmacokinetics of 13 nm-sized PEG-coated gold nanoparticles," *Toxicology and Applied pharmacology*, vol. 236, no. 1, pp. 16–24, 2009.
- [50] M. Tsoli, H. Kuhn, W. Brandau, H. Esche, and G. Schmid, "Cellular uptake and toxicity of Au55 clusters," *Small*, vol. 1, no. 8-9, pp. 841–844, 2005.
- [51] Y.-J. Gu, J. Cheng, C.-C. Lin, Y. W. Lam, S. H. Cheng, and W.-T. Wong, "Nuclear penetration of surface functionalized gold nanoparticles," *Toxicology and Applied Pharmacology*, vol. 237, no. 2, pp. 196–204, 2009.
- [52] A. M. Alkilany and C. J. Murphy, "Toxicity and cellular uptake of gold nanoparticles: What we have learned so far?" *Journal of Nanoparticle Research*, vol. 12, no. 7, pp. 2313–2333, 2010.
- [53] M. Hope-Ross, L. A. Yannuzzi, E. S. Gragoudas, D. R. Guyer, J. S. Slakter, J. A. Sorenson, S. Krupsky, D. A. Orlock, and C. A. Puliafito, "Adverse reactions due to indocyanine green," *Ophthalmology*, vol. 101, no. 3, pp. 529–533, 1994.
- [54] N. Salahuddin, A. Akelah, M. Elnagar, and M. A. Abdelwahab, "Antibacterial and cytotoxicity of methylene blue loaded-cellulose nanocarrier on breast cancer cell line," *Carbohydrate Polymer Technologies and Applications*, vol. 2, p. 100 138, 2021.
- [55] T. H. Au, A. Bruckner, S. M. Mohiuddin, and D. E. Hilleman, "The prevention of contrast-induced nephropathy," *Annals of Pharmacotherapy*, vol. 48, no. 10, pp. 1332–1342, 2014.
- [56] C. Kim, K. H. Song, F. Gao, and L. V. Wang, "Sentinel lymph nodes and lymphatic vessels: Noninvasive dual-modality in vivo mapping by using indocyanine green in rats—volumetric spectroscopic photoacoustic imaging and planar fluorescence imaging," *Radiology*, vol. 255, no. 2, pp. 442–450, 2010.
- [57] J. J. Nogueira, M. Meixner, M. Bittermann, and L. González, "Impact of lipid environment on photodamage activation of methylene blue," *ChemPhotoChem*, vol. 1, no. 5, pp. 178–182, 2017.
- [58] B. Brendel, S. W. A. Rick, M. Stockheim, and H. Ermert, "Registration of 3D CT and ultrasound datasets of the spine using bone structures," *Computer Aided Surgery*, vol. 7, no. 3, pp. 146–155, 2002.
- [59] S. Winter, B. Brendel, I. Pechlivanis, K. Schmieder, and C. Igel, "Registration of CT and intraoperative 3-D ultrasound images of the spine using evolutionary and gradient-based methods," *IEEE Transactions on Evolutionary Computation*, vol. 12, no. 3, pp. 284–296, 2008.

- [60] W. Wein, B. Roper, and N. Navab, “Integrating diagnostic B-mode ultrasonography into CT-based radiation treatment planning,” *IEEE Transactions on Medical Imaging*, vol. 26, no. 6, pp. 866–879, 2007.
- [61] K. Xu, B. Jiang, A. Moghekar, P. Kazanzides, and E. Boctor, “Autoinfocus, a new paradigm for ultrasound-guided spine intervention: A multi-platform validation study,” *International Journal of Computer Assisted Radiology and Surgery*, pp. 1–10, 2022.
- [62] M. A. Lediju Bell and J. Shubert, “Photoacoustic-based visual servoing of a needle tip,” *Scientific Reports*, vol. 8, no. 1, pp. 1–12, 2018.
- [63] M. A. L. Bell, X. Guo, H. J. Kang, and E. Boctor, “Improved contrast in laser-diode-based photoacoustic images with short-lag spatial coherence beamforming,” in *2014 IEEE International Ultrasonics Symposium*, IEEE, 2014, pp. 37–40.
- [64] V. Grasso, J. Holthof, and J. Jose, “An automatic unmixing approach to detect tissue chromophores from multispectral photoacoustic imaging,” *Sensors*, vol. 20, no. 11, p. 3235, 2020.

Chapter 2

Segmentation of Bone Boundaries and Assessment of Bone Content

The work presented in this chapter was published in the following manuscript:
E. A. Gonzalez, A. Jain, and M. A. L. Bell, “Combined ultrasound and photoacoustic image guidance of spinal pedicle cannulation demonstrated with intact ex vivo specimens,” *IEEE Transactions on Biomedical Engineering*, vol. 68, no. 8, pp. 2479–2489, 2020. This publication is licensed under a Creative Commons Attribution 4.0 International License.

2.1 Introduction

Spinal instability can be caused by degenerative disorders, trauma, and primary or metastatic cancer [2]. These abnormalities are commonly treated with spinal fusion surgeries, which help to alleviate pain and recover neurological functionality. Contemporary posterior spinal fusion surgeries involve drilling holes into the pedicles of vertebrae, inserting pedicle screws, and attaching each screw to a metal rod with the goal of stabilizing the spine to allow for bony fusion to occur. When cannulating pedicles, it is critical to ensure the correct trajectory during drilling in order to avoid accidental bone breaches and screw misplacement. In particular, pedicle screw misplacement occurs in approximately 14–39.8% of procedures [3–6], which

compromises neighboring structures such as nerves (and in some cases, spinal cord), erodes long-term biomechanical stability, [7, 8], and causes adjacent degeneration [9, 10].

Computer assisted spinal surgery methods are becoming increasingly prevalent, as they improve the accuracy of pedicle screw placement and patient outcomes in comparison to the conventional free-hand screw fixation [11]. Currently, these methods utilize computed tomography (CT) [12], 2D or 3D fluoroscopy navigation [13, 14], and robotic assistance [15] to provide intraoperative information, which can be registered to preoperative CT images. The surgical tool and anatomical landmarks are then identified in the registered images to help surgeons localize the pedicle anatomic corridor location. However, limitations of these methods include exposure to ionizing radiation, the requirement to insert reference and intraoperative markers, and relatively prolonged surgery times.

Ultrasound imaging is a safer alternative to potentially provide real-time intraoperative information for pre-operative CT image registration [16]. However, limitations with ultrasound imaging for pedicle screw guidance include sound attenuation in the presence of bone, poor signal-to-noise ratios (SNRs), and the presence of clutter and speckle noise. Conventional ultrasound imaging has limited ability to detect deep-lying features beneath bone tissue due to sound attenuation and sound speed differences, requiring the use of several ultrasound slices as redundant information for registration (i.e., 3D ultrasound imaging) [17–19]. The feasibility of multiple slice registration is accomplished with additional tracking devices and custom hardware [20].

To overcome limitations with ultrasound imaging, photoacoustic imaging [21] has been proposed as a guidance method for pedicle screw insertion [22]. The proposed technique consists of delivering laser light to generate an acoustic pressure response. The acoustic pressure is then received by an ultrasound probe, and beamforming is applied to create a photoacoustic image. Applications of photoacoustic imaging to

surgical guidance include visualization of tool tips such as a neurosurgical drill tip [23], a needle tip [24–27], or a cardiac catheter tip [28], visualization of underlying structures such as blood vessels [29], and photoacoustic-based guidance during a range of surgeries, such as fetal surgeries [30], endonasal surgeries, [31–33], hysterectomy procedures [34, 35], and prostate surgeries [36]. The incorporation of robotics with teleoperated surgery [34] and robotic visual servoing [37, 38] has also been demonstrated. Applications related to the spine include stem cell injection guidance [39] and discrimination of cortical bone from cancellous bone to identify optimal insertion points prior to initiating pedicle screw placement [22]. Despite these remarkable advances, no previous studies investigate the accuracy of photoacoustic signal visualization and localization within the pedicle of a vertebra.

This paper investigates two hypotheses. First, based on previous studies to visualize photoacoustic signals from the surface of human vertebrae [22], we hypothesize that similar visibility can be achieved beneath the bony structure in a more realistic setup and closer to the surgical environment of a spinal fusion surgery. Second, we hypothesize that improvements to 2D ultrasound imaging would reduce the computational burden associated with requiring 3D ultrasound images to complete the segmentation task for ultrasound-to-CT registration. To address the poor 2D ultrasound segmentation that otherwise compromises the performance of ultrasound-to-CT registration, we propose a novel coherence-based beamforming technique named locally weighted short-lag spatial coherence (LW-SLSC) beamforming. LW-SLSC beamforming is a regularized version of short-lag spatial coherence (SLSC) beamforming [40], designed to minimize the trade off between contrast and spatial resolution. Therefore, LW-SLSC has the potential to enhance the vertebral boundaries adjacent to soft tissue when compared to conventional delay-and-sum (DAS) beamforming, as previously demonstrated in an *ex vivo* caprine vertebra [41].

Our hypotheses were tested with *ex vivo* caprine and human vertebrae. First, the

segmentation enhancement achieved with LW-SLSC beamforming was compared to that obtained from SLSC beamforming and conventional DAS beamforming in an *ex vivo* caprine vertebra. Then, we demonstrated the visualization of photoacoustic signals originating from inside the lumbar vertebrae located inside a human cadaver during pedicle hole creation, using the same methods implemented during spinal fusion surgeries. Validation of the photoacoustic signal locations was based on manual registration of post-operative CT volumes to co-registered ultrasound and photoacoustic images. This registration relied on identified landmarks within segmented ultrasound images that were enhanced with LW-SLSC beamforming. Finally, we successfully differentiated photoacoustic signals originating from cancellous and cortical bone inside the human cadaver by measuring the areas of -6dB contours of DAS photoacoustic images.

This chapter is organized as follows. Section 2.2 details our acquisition, beamforming, segmentation, and registration methods. Section 2.3 presents our experimental results. Section 2.4 discusses insights from the experimental results. Section 2.5 summarizes our conclusions.

2.2 Methods

2.2.1 Coherence-Based Beamforming Methods

2.2.1.1 Short-Lag Spatial Coherence

Unlike the conventional amplitude-based DAS beamformer, SLSC beamforming [40] displays the similarity of received signals in the aperture domain, as a function of element separation m . A received time-delayed sample is represented as $s_i(n)$, where i is the channel index and n is the depth index in a zero-mean radio frequency signal s_i . First, the coherence function $\hat{R}(m)$ is calculated using an axial kernel as follows:

$$\hat{R}(m) = \frac{1}{N-m} \sum_{i=1}^{N-m} \frac{\sum_{n=n_1}^{n_2} s_i(n) s_{i+m}(n)}{\sqrt{\sum_{n=n_1}^{n_2} s_i^2(n) \sum_{n=n_1}^{n_2} s_{i+m}^2(n)}}, \quad (2.1)$$

where N is the the number of elements in the aperture, and n_1 and n_2 are the limits of the axial kernel k in units of sample number. Then, an SLSC image is generated as the integral of the spatial coherence function over the first M lags:

$$\text{SLSC}(M) = \int_1^M \hat{R}(m) dm \approx \sum_{m=1}^M \hat{R}(m). \quad (2.2)$$

2.2.1.2 Locally Weighted Short-Lag Spatial Coherence

Enhancement of bone boundaries can be achieved by implementing a regularized version of the SLSC beamformer [41]. Instead of averaging the cumulative sum up to a lag value M (out of a preselected total of N_L lags, where $M < N_L$), LW-SLSC beamforming computes the weighted coefficients for N_L lags by minimizing the total variation (TV) of the weighted sum within a moving kernel $\hat{R}_i \in \mathbb{R}^{k_z \times k_x \times N_L}$ obtained from the correlation matrix $\hat{R} \in \mathbb{R}^{N_z \times N_x \times N_L}$. In order to preserve the high resolution information available at higher lags (i.e., $M > 15$), this adaptive solution was regularized using the L2-norm with a gradient operator. Then, the TV minimization was defined as:

$$\hat{w}_i = \underset{w_i}{\text{argmin}} \{ \text{TV}(f(w_i, \hat{R}_i)) + \alpha^2 \|\nabla w_i\|_2^2 \} \quad (2.3)$$

$$f(w_i, \hat{R}_i) = \sum_{m=1}^{N_L} \hat{R}_i[m] \cdot w_i[m]$$

$$\text{Subject to : } \|w_i\|_1 = 1$$

$$0 \leq w_i \leq 1$$

where TV is the 2D total variation with the L2-norm applied to the cost function f , \hat{R}_i is the kernel i of the correlation matrix \hat{R} , and $w_i \in \mathbb{R}^{1 \times N_L}$ is the optimized weight vector for the calculated summed lags of \hat{R}_i . The weighted sum kernels $\hat{w}_i \hat{R}_i$ were stacked into multiple layers and positioned relative to the center of each \hat{R}_i . The

LW-SLSC image was the median of the stacked kernels $\hat{w}_i \hat{R}_i$. The main advantage of LW-SLSC relies on the adaptive selection of lower lags in kernels surrounding isoechoic regions, which enhances contrast, and higher lags otherwise, which enhances resolution. The selective combination of higher and lower lags is known to reduce the noise commonly observed in SLSC images created with higher lags [42].

The original formulation in (2.3) can be simplified using the framework of Barbero *et al.* [43] for Total Variance alternatives. However, these simplifications only hold when computing TV with the L2-norm. The gradient operator ∇ (i.e., 1D TV operator) used in the penalty term is simplified to:

$$D = \begin{pmatrix} -1 & 1 & & & \\ & -1 & 1 & & \\ & & \ddots & \ddots & \\ & & & \ddots & \ddots & \\ & & & & -1 & 1 \end{pmatrix}$$

$$\text{TV}_{1D}(w_i) = \|Dw_i\|_p \quad D \in \mathbb{R}^{(N_L-1) \times N_L} \quad (2.4)$$

Similarly, the two dimensional TV operator used in the fidelity term is reduced to:

$$B = \begin{pmatrix} -1 & 1 & & & & \\ & \ddots & \ddots & & & \\ & & -1 & 1 & & \\ & & & \ddots & \ddots & \\ & & & & -1 & 1 \\ & & & & & \ddots & \ddots \\ -1 & & & & & & -1 & 1 \\ & & & & & & & \ddots & \ddots \\ & & & & & & & & -1 & 1 \\ & & & & & & & & & 1 \end{pmatrix}$$

$$\text{TV}_{2D}(X) \approx \|BX\|_p, \quad B \in \mathbb{R}^{(2k_z k_x - k_z - k_x) \times (k_z k_x)} \quad (2.5)$$

Reshaping \hat{R} into the form $\hat{R}_i \in \mathbb{R}^{k_z k_x \times N_L}$ and using (2.4) and (2.5) in (2.3), results in the following expression:

$$\hat{w} = \underset{w}{\operatorname{argmin}} \{ \|B\hat{R}_i w\|_2^2 + \alpha^2 \|Dw\|_2^2 \} \quad (2.6)$$

$$= \underset{w}{\operatorname{argmin}} \{ w^T H w \}, \quad H = (B\hat{R}_i)^T B\hat{R}_i + \alpha^2 D^T D \quad (2.7)$$

The reduction presented in (2.7) has several advantages over (2.3). First, by assuming the kernel size is constant during the LW-SLSC computation, the term $\alpha^2 D^T D$ is independent from the kernel R_i and thus can be computed only once. Second, matrix operations in $(B\hat{R}_i)^T B\hat{R}_i$ can be parallelized using built-in libraries for computational speed up, where the matrix B is pre-computed. Finally, the Hessian H allows quadratic programming using Newton step optimizers instead of the conventional gradient descent, featuring faster convergence rates. In this study, the primal-dual interior point method [44] is used for estimating the solution of (2.7).

2.2.2 Segmentation of an *Ex Vivo* Caprine Vertebra

The segmentation accuracy of bony structures achieved with DAS, SLSC and LW-SLSC were tested on an *ex vivo* caprine thoracic vertebra (with surrounding tissue intact). This vertebra was imaged with a L3-8 linear array ultrasound probe connected to an Alpinion E-CUBE 12R ultrasound system (Alpinion, Seoul, South Korea), as shown in Fig. 2-1. The linear array had 128 elements, 0.3 mm pitch and 0.06 mm kerf. Raw ultrasound data were acquired with a center frequency of 4 MHz, an image depth of 40 mm, and a focus located at 30 mm depth. To compare with conventional techniques used for image guidance during spinal fusion surgeries, CT acquisitions were performed using a Siemens ARCADIS Orbic 3D C-Arm with 190 raw projections, generating a 6 cm³ volume of 0.12 mm³ voxel resolution.

SLSC images were computed with a M value of 9 and an axial kernel of 2Λ , where Λ is the wavelength of the transmit frequency. LW-SLSC images were computed with a 1.20 mm (lateral) x 1.92 mm (axial) kernel, 50% overlap, $N_L = 28$, and a regularization factor $\alpha = 0.12$.

Bone boundaries from DAS, SLSC, and LW-SLSC images were computed by applying a binary threshold of 50% of the maximum pixel amplitude and selecting the closest contour to the vertebral foramen. These boundaries were registered with

manually selected horizontal slices from volumetric 3D CT data. The registration used Mattes Mutual Information as the similarity metric [45], with One Plus One step evolutionary as the heuristic optimizer [46].

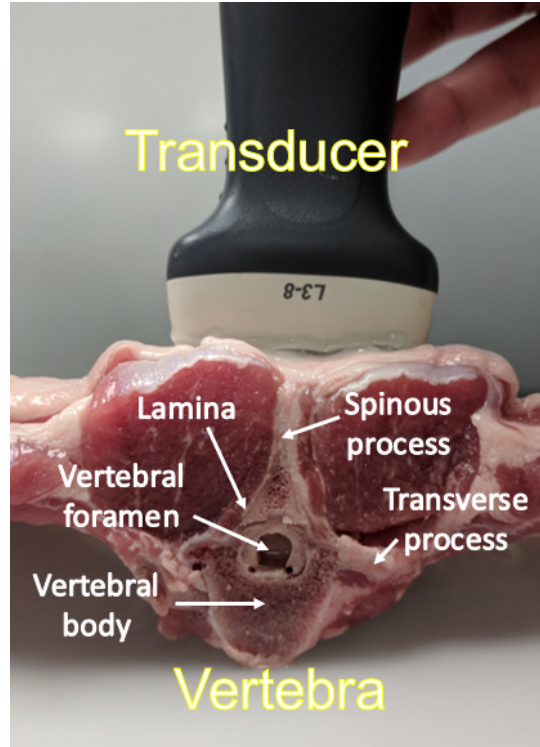


Figure 2-1. Acquisition setup for evaluating bony structure enhancement with an *ex vivo* caprine vertebra.

2.2.3 Vertebral Imaging of a Human Cadaver

2.2.3.1 Specimen and Surgery Details

An adult male human cadaver was placed in prone position and dissection was carried along the cranio-caudal axis with the aid of a Cobb elevator to reveal the spinous process, lamina, and facet joints at each level from L1 to S1. The specimen had no reports of spine pathologies, malformations, or previous spinal surgeries, which was also confirmed with pre-operative CT imaging. The pedicles were cannulated bilaterally from L2 through L4 along anatomic trajectories using a standard free hand technique with a pedicle probe. Intentional medial and lateral breaches were made in

some of the pedicle cannulation attempts. The total depth of the pedicle tracts from the bone surface ranged from 14 mm to 25 mm, as measured with the ruler on pedicle probe.

2.2.3.2 Data Acquisition

Fig. 2-2 shows the acquisition setup for ultrasound and photoacoustic data from the human lumbar vertebrae. A 1-mm diameter optical fiber was inserted to touch the bottom of the pedicle hole. The optical fiber was used to transmit 750 nm wavelength laser light from a Phocus Mobile laser (Opotek Inc., Carlsbad, CA, USA) with an energy of 13.4 mJ at the fiber tip. Photoacoustic signals were received by a SC1-6 convex array ultrasound probe connected to an Alpinion E-CUBE 12R ultrasound system. The probe was positioned in an oblique axis across several lumbar laminae. Enhanced real-time visualization of photoacoustic signals was achieved with GPU implementation of SLSC [38, 47, 48] for a convex array. This photoacoustic beamforming method was chosen because it was the best real-time imaging option available to assist the surgeon with fiber tip localization during the surgery.

2.2.3.3 Ultrasound and Photoacoustic Imaging

Ultrasound and photoacoustic radiofrequency data were acquired up to a depth of 70 mm, with a focal depth of 25 mm for the ultrasound data. No frame averaging was applied in order to avoid the blurring artifacts that would hinder the performance of ultrasound-to-CT registration. SLSC ultrasound images were computed with $M = 5$ and 1λ axial kernel length, whereas LW-SLSC ultrasound images were computed with $N_L = 15$, a 2.0 mm (lateral) \times 3.1 mm (axial) kernel, 60% overlap, and $\alpha = 1$. Similarly, SLSC photoacoustic images were computed with $M = 15$ and 1λ axial kernel length, whereas LW-SLSC photoacoustic images were computed with $N_L = 25$, a 2.0 mm (lateral) \times 3.1 (axial) kernel, 60% overlap, and $\alpha = 1$.

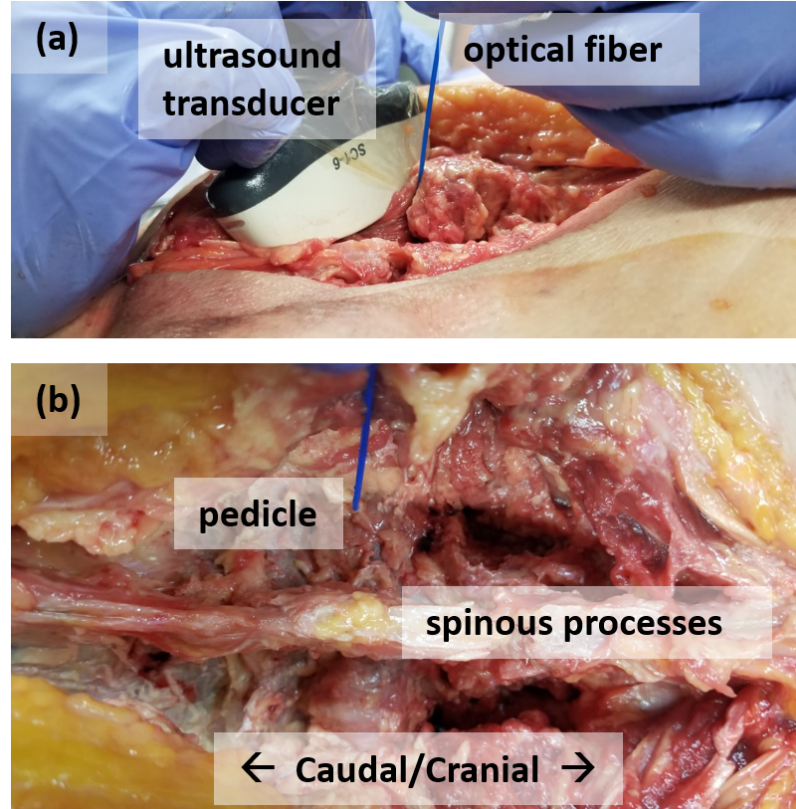


Figure 2-2. Setup to acquire ultrasound and photoacoustic data from the lumbar region of an ex vivo human cadaver. (a) Insertion of the optical fiber into the pedicle hole while the ultrasound transducer is placed across several lumbar laminae. (b) Posterior view of the lumbar vertebrae when the optical fiber is inserted into the pre-drilled pedicle hole.

2.2.3.4 Ultrasound and Photoacoustic Segmentation

The segmentation of bony structures and their respective centers of mass were measured from DAS, SLSC, and LW-SLSC ultrasound images, whereas the segmentation of the tip of the optical fiber and its respective center of mass was measured from DAS, SLSC, and LW-SLSC photoacoustic images. Note that the fiber tip was in contact with bone during each image acquisition, thus the fiber tip segmentation was considered to be representative of a bony landmark within the created hole. To achieve the ultrasound and photoacoustic segmentations, binary masks were computed with 30% maximum pixel amplitude threshold. Then, the removal of isolated pixels was achieved with morphological opening with a structuring element size of $0.38 \text{ mm} \times$

0.38 mm, whereas small holes in the bony masks were filled with morphological closing with a structuring element size of $0.63 \text{ mm} \times 0.63 \text{ mm}$. Ultrasound and photoacoustic images were filtered with the computed mask and further segmented into separated bony structures through a connected component routine. For each component, the center of mass was calculated based on the position of pixels and the amplitude of the ultrasound or photoacoustic image, which was normalized over the maximum amplitude of each component.

2.2.3.5 Landmark Registration

Pre-operative and post-operative CT volumes ($512 \times 512 \times 192$ samples) of the human cadaver were acquired with an O-arm O2 (Medtronic, Minnesota, USA) using 140 kV-peak and $0.78 \times 0.78 \times 0.83 \text{ mm}^3$ voxel resolution. The CT volumes were optimized for bone visualization by adjusting the window level to 2000 Hounsfield units (HU) and the window width to 2000 HU. Centers of mass calculated from both ultrasound and photoacoustic images were used as fiducial markers for landmark registration, which was conducted with 3D Slicer [49]. The corresponding fiducial markers in the CT volume were manually placed to match bony contours in the registered CT slices to those in the ultrasound images. The registered CT volume was displayed in X-Z and Y-Z views, where X, Y, and Z represent the lateral, elevation, and axial dimensions of the ultrasound probe.

2.2.3.6 Cancellous vs. Cortical Bone Differentiation

Photoacoustic imaging was used to differentiate signals originating from cortical and cancellous bone. Photoacoustic signals from cancellous bone were acquired when the tip of the optical fiber was either touching cancellous bone after being placed within a correctly created pedicle hole or touching the cortical bone surrounding walls of the pedicle after creating an intentional medial or lateral breach. Medial and lateral breaches in the cortical bone were confirmed with the CT volume described in

Section 2.2.3.5.

SNR was calculated to determine which signals would be included in the analysis of bone differentiation, using the equation:

$$\text{SNR} = \frac{\mu_i}{\sigma_o}, \quad (2.8)$$

where μ_t and σ_b are the mean and standard deviation of signals within photoacoustic target and background regions of interest (ROIs), respectively, prior to log-compression. To identify appropriate target ROIs, LW-SLSC images were used to estimate the center of the photoacoustic targets (which was challenging with DAS photoacoustic images because of the diffuse patterns observed in some cases [22]). Then, a 10 mm \times 10 mm ROI was centered on the photoacoustic target and a background ROI was placed 25 mm above the center of the target.

As demonstrated in the Appendix, photoacoustic acquisitions that yielded a SNR value of 3 or less were considered as out-of-plane signals to be discarded from additional analysis. We reasoned that signals with $\text{SNR} > 3$ were more likely to be associated with a photoacoustic signal from the fiber tip, while SNR values below this threshold produced images that mostly contained noise. These noisy images were suspected to result from signal sources located outside of the imaging plane.

After removing the out-of-plane signal cases, 6 cases of cancellous bone and 5 cases of cortical bone were analyzed. For each case, DAS, SLSC, and LW-SLSC photoacoustic images were processed with the same parameters as described in Section 2.2.3.3. Then, contours of -6dB were computed around a 10 mm \times 10 mm ROI that was centered on the photoacoustic target. This process was repeated for 10 acquired frames from each cortical and cancellous bone case. Finally, a t-test was used to evaluate the statistical significance ($p < 0.01$) of the difference in areas generated from the contours measured when the optical fiber was touching either cancellous or cortical bone. This statistical analysis was repeated for each beamformer.

2.2.4 Image Quality Assessments and Data Representation

The generalized contrast-to-noise ratio (gCNR) [50, 51] was used to assess the separability of bone structures and surrounding soft tissue in ultrasound images, defined as:

$$\text{gCNR} = 1 - \sum_{x=0}^1 \min\{p_i(x), p_o(x)\}, \quad (2.9)$$

where p_i and p_o are the probability density functions of signal amplitudes within regions of interest (ROIs) inside and outside of the lamina, respectively. The probability density functions were calculated from histograms computed with 256 bins. Similarly, the contrast-to-noise ratio (CNR) was measured and compared, defined as:

$$\text{CNR} = \frac{|\mu_i - \mu_o|}{\sqrt{\sigma_i^2 + \sigma_o^2}}, \quad (2.10)$$

where μ_i and σ_i are the mean and standard deviation, respectively, within a ROI inside of the target prior to log-compression and μ_o and σ_o are the mean and standard deviation, respectively, of a ROI outside of the target prior to log-compression.

Results from measurements of the thickness of segmented lines (Section 2.2.2) and from areas of photoacoustic signal originating from cancellous and cortical bone (Section 2.2.3.6) are both presented as box-and-whiskers plots in Section 2.3. In these plots, the horizontal lines represent the median, the upper and lower edges of each box represents the upper and lower quartiles of each data set, the top and bottom lines extending from the boxes indicate the maximum and minimum of each data set, and the crosses indicate outliers (defined as any value larger than 1.5 times the interquartile range).

2.3 Results

2.3.1 Bony Segmentation of an *Ex Vivo* Caprine Vertebra

Fig. 2-3 shows examples of CT, DAS, SLSC and LW-SLSC images of the *ex vivo* caprine thoracic section. The SLSC and LW-SLSC images were computed with

parameters that maximized gCNR, yielding values of 0.98 and 0.99, respectively, for the selected regions of interest. The gCNR of the DAS image was 0.67. In addition to improving gCNR, SLSC and LW-SLSC imaging improved the boundary between soft tissue and the spinous, lamina, and transverse processes of the vertebra, when compared to DAS imaging. CNR was also enhanced in the SLSC and LW-SLSC images (2.13 and 4.59, respectively), when compared to that of the DAS image, which was 0.55.

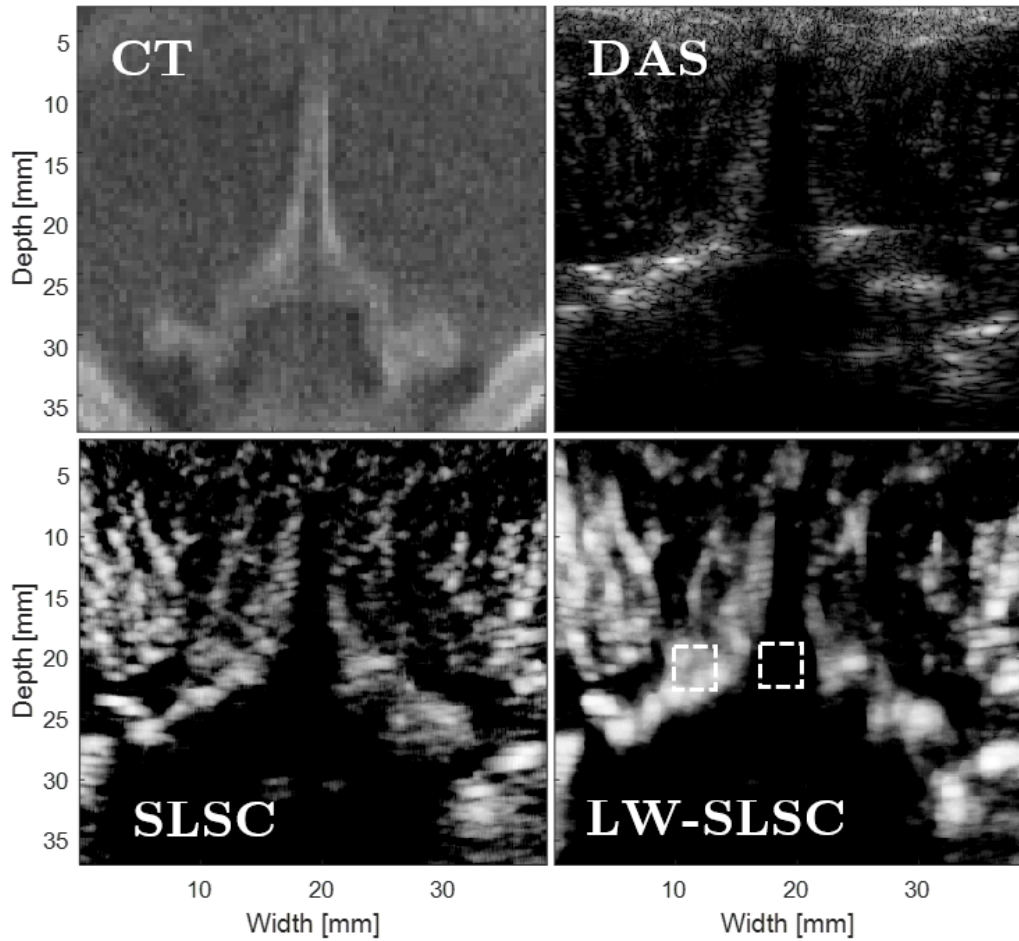


Figure 2-3. Examples of reconstructed CT, DAS, SLSC ($M = 9$) and LW-SLSC ($N_L = 28$, $\alpha=0.1$) images of the caprine sample (not registered). Regions selected for gCNR measurements are denoted by the dashed boxes.

Fig. 2-5(a) shows the registration of vertebral boundaries segmented from CT and ultrasound images. While the segmented boundaries successfully converged in the

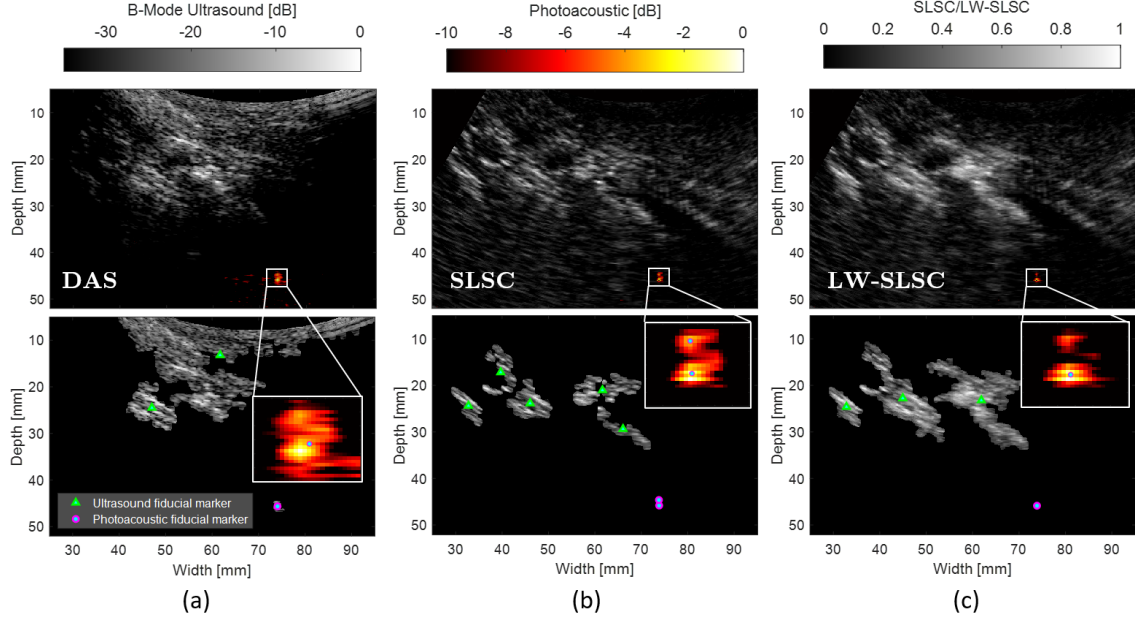


Figure 2-4. Examples of photoacoustic images overlaid on ultrasound images from an oblique view of L3-L5 vertebrae reconstructed with (a) DAS, (b) SLSC and (c) LW-SLSC ultrasound and photoacoustic beamforming. Top row: beamformed images. Bottom row: segmented masks. The triangles and circles represent the center of mass of isolated components from ultrasound and photoacoustic images, respectively, which are later combined and used as landmarks for CT registration. The insets show magnified views of the photoacoustic signal originating from the fiber tip.

final ultrasound-to-CT registration, a notable difference was observed with DAS when compared to SLSC and LW-SLSC boundaries. Specifically, a fuzzier segmentation was produced from the DAS image, while the coherence-based methods reduced outliers and produced finer contours. An additional reduction of pixel outliers is observed for the LW-SLSC image result which more closely follows the CT contour when compared to SLSC image result.

Fig. 2-5(b) shows the corresponding thickness difference for the lateral and axial dimension of the segmented boundaries. To quantitatively compare the thickness of the segmented boundaries, the integration of the segmented regions was calculated in the axial and lateral dimensions for each boundary. The differences between these integrated segmentation thicknesses at each lateral or axial position was computed to compare the obtained CT boundary with each of the ultrasound boundaries. The

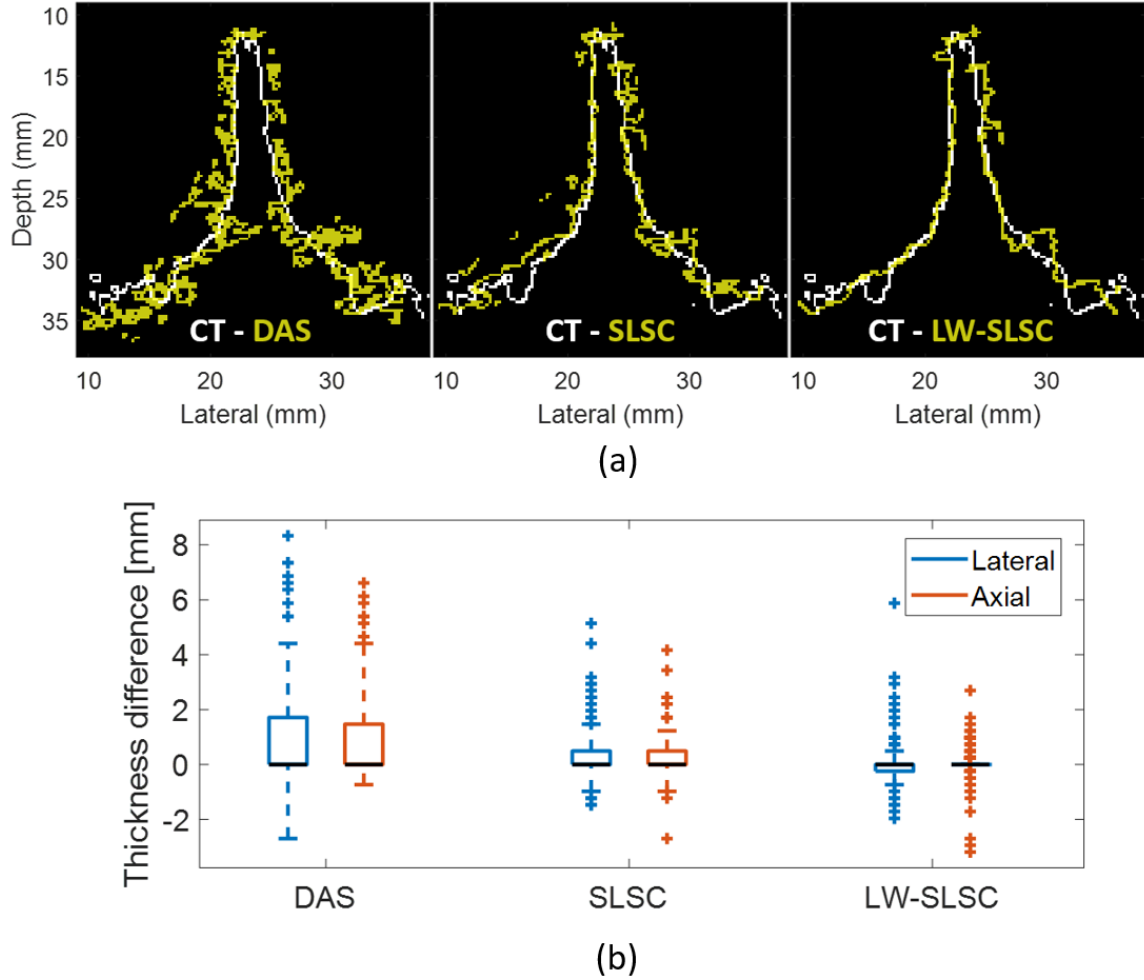


Figure 2-5. (a) Registered US-CT bone boundaries after applying threshold segmentation to images of the *ex vivo* caprine vertebra. The ultrasound images were beamformed using DAS (left) SLSC (middle) and LW-SLSC (right). (b) Differences in the integrated thickness of the segmented bone boundary in lateral and axial dimensions, when comparing CT results to DAS, SLSC, and LW-SLSC results. Each boxplot shows the median (horizontal black line), interquartile range, maximum and minimum values of the differences in the integrated thickness.

overall thickness of the CT contour in each dimension (axial: 1.84 mm, lateral: 1.79 mm) was closer to that obtained from the LW-SLSC image (axial: 2.09 mm, lateral: 2.03 mm) than that obtained from the SLSC image (axial: 2.98 mm, lateral: 2.89 mm) or DAS image (axial: 5.86 mm, lateral: 5.67 mm).

2.3.2 Vertebral Imaging of a Human Cadaver

Fig. 2-4 shows examples of ultrasound and photoacoustic images from a lumbar vertebra inside an intact human cadaver. The top row shows the photoacoustic images overlaid on ultrasound images created with DAS, SLSC, and LW-SLSC beamforming. The discrimination of bone structures in the ultrasound images was determined using the ROIs shown in the Appendix (not shown in Fig. 2-4 to facilitate the comparison between matched images). SLSC and LW-SLSC beamforming produced average gCNR values of 0.98 and 0.88, respectively, which were both higher than the average 0.77 gCNR calculated from corresponding DAS images. The enhancement of bone visualization is additionally confirmed with the average CNR values, which measured 1.17, 1.75, and 2.68 in DAS, SLSC, and LW-SLSC images, respectively. A summary of the individual gCNR and CNR measurements is presented in Table 2-1.

The photoacoustic signals in Fig. 2-4 are shown registered to the ultrasound images, with a magnified view shown as a figure inset. These photoacoustic signals arise from the tip of the optical fiber that was inserted into the prepared pedicle hole. Coherence-based images were qualitatively observed to produce more focused photoacoustic signals when compared to DAS photoacoustic images, which is expected to enhance the estimation accuracy of the fiber tip location. Quantitatively, the distance between the center of mass and the brightest pixel of each photoacoustic image created with DAS, SLSC, and LW-SLSC beamforming was 0.26 mm, 0.21 mm, and 0.18 mm, respectively, where a shorter distance represents a more compact and less diffuse photoacoustic signal.

The bottom row of Fig. 2-4 shows the segmented ultrasound and photoacoustic masks for the three beamformers. The green triangles and magenta circles represent the center of mass of the isolated components from ultrasound and photoacoustic masks, respectively. The segmented masks from the DAS ultrasound image include undesirable soft tissue and a single bony structure, while coherence methods identify at

least 3 bony structures. Similarly, SLSC images created with greater M values have an increased number of outliers (i.e., pixels with coherence values that differ significantly from their surroundings and from their values at other lags [42]) and decreased SNR and CNR [40], which caused some otherwise continuous bony structures to appear disconnected, affecting the estimation of center of mass and resulting in redundant landmarks. This effect is mitigated with LW-SLSC.

Table 2-1. Discrimination of bone structures in ultrasound images of vertebrae in a human cadaver (determined using the ROIs shown in the Appendix)

Method	Beamformer	S_1	S_2	S_3	Mean
gCNR	DAS	0.34	0.98	0.99	0.77
	SLSC	0.84	0.87	0.93	0.88
	LW-SLSC	0.98	0.99	1.00	0.98
CNR	DAS	0.54	2.09	2.10	1.17
	SLSC	1.61	1.64	2.21	1.75
	LW-SLSC	2.49	2.66	4.50	2.68

Fig. 2-6 shows the registration of the post operative CT volume with the landmarks obtained from the segmented ultrasound and photoacoustic LW-SLSC images. The shape of the segmented LW-SLSC ultrasound image closely resembles that of the lamina of the L3, L4 and L5 vertebrae in the CT image. Similarly, the fiducial markers for the photoacoustic signals originating from the optical fiber is visualized near the end of the pedicle hole.

Fig. 2-7 shows the X-Z and Y-Z views of the registered CT volume and the fiber tip fiducial marker segmented from the LW-SLSC photoacoustic image. To assess the proximity of the registered fiducial marker to the bottom of the pedicle hole, five manual markers were selected around the border of the pedicle hole for each X-Z (Fig. 2-7(a)) and Y-Z view (Fig. 2-7(b)). The position of the manual markers represents the potential positions of the optical fiber tip when it was inserted in the pedicle hole. Euclidean distances between the fiducial marker and each of the

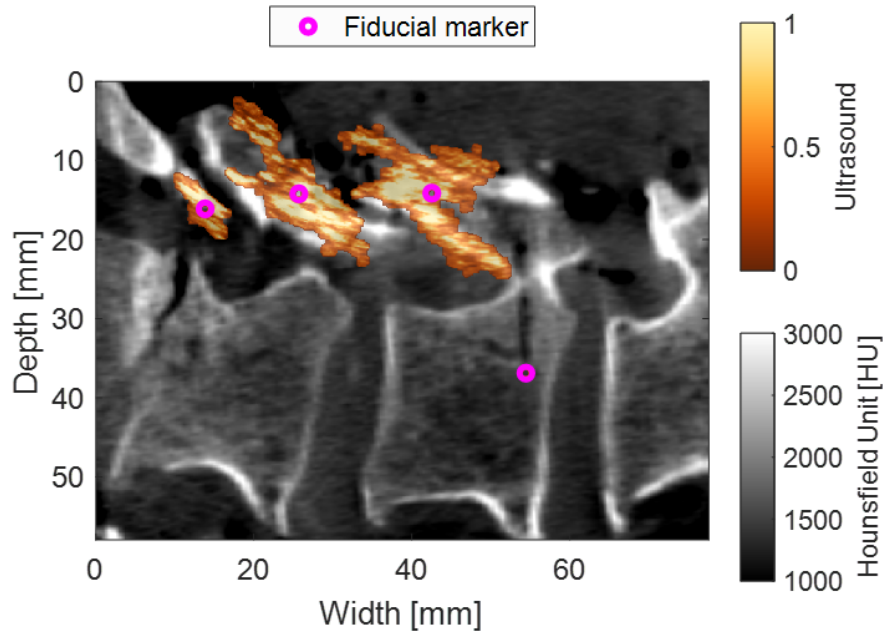


Figure 2-6. Co-registered ultrasound (color) and CT (grayscale) images using ultrasound and photoacoustic landmarks (magenta) from segmented LW-SLSC images.

manual markers are reported in Table 2-2. The minimum distances are shown in bold, indicating the marker associated with the location of the bone surface that the tip of the optical fiber was most likely touching when inserted in the pedicle hole.

Table 2-2. Euclidean distances between the fiducial marker segmented from the LW-SLSC photoacoustic image and each of the manual markers of the pedicle hole obtained from the registered CT images in Fig. 2-7

	X-Z view	Y-Z view
Marker 1	2.02 mm	1.16 mm
Marker 2	1.49 mm	0.72 mm
Marker 3	1.91 mm	1.06 mm
Marker 4	1.28 mm	1.69 mm
Marker 5	0.98 mm	2.48 mm
Average	1.53 ± 0.39 mm	1.42 ± 0.61 mm

Fig. 2-8 shows examples of co-registered LW-SLSC ultrasound images and DAS photoacoustic images when the tip of the optical fiber was placed in holes corresponding

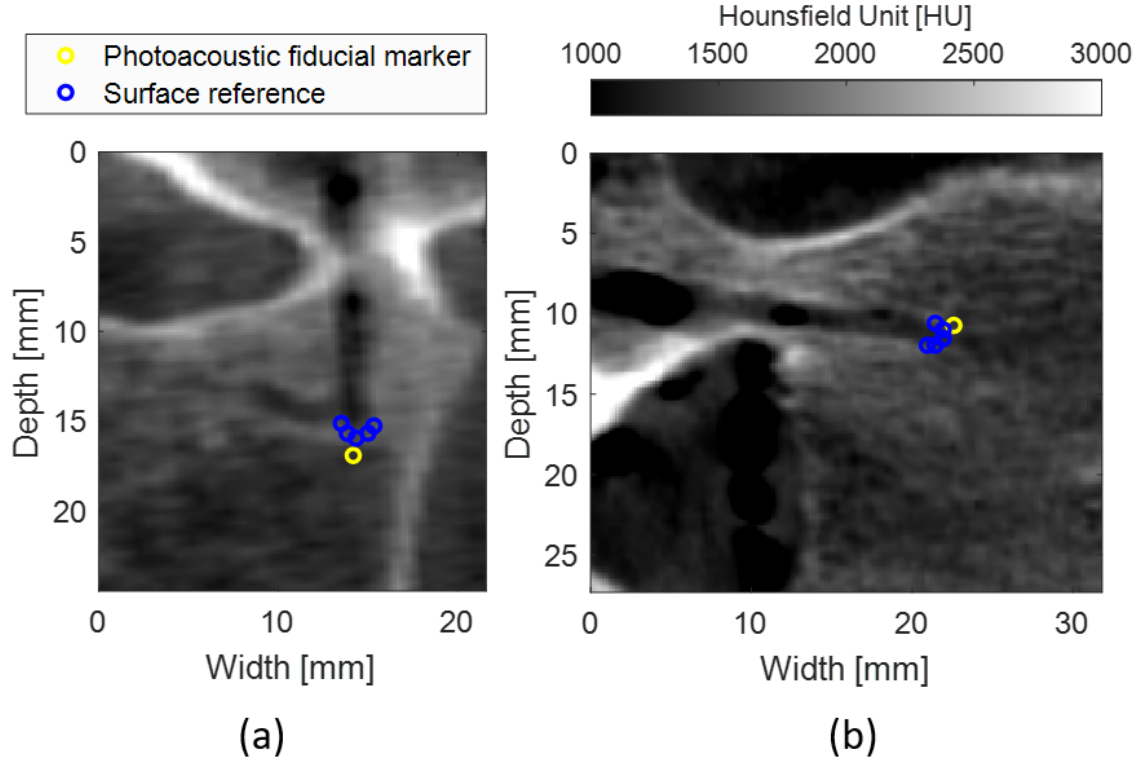


Figure 2-7. (a) X-Z and (b) Y-Z planes of the CT volume registered to the ultrasound and photoacoustic images. The yellow marker represents the centroid of the photoacoustic signal reconstructed with the LW-SLSC image, which was used as a fiducial marker for landmark registration. The blue markers show the outline of the pedicle hole.

to a medial breach (Fig. 2-8(a)), a lateral breach (Fig. 2-8(b)), and the cancellous core of the pedicle (Fig. 2-8(c)). The corresponding CT slices were chosen to optimize visual confirmation of the fiber placement description, and therefore they are not registered to the photoacoustic and ultrasound images. It was not possible to perform ultrasound-to-CT registration for these figures, because of the absence of clear anatomical landmarks in the ultrasound image of the lumbar vertebrae. Our primary goal was instead to obtain ground truth images while touching the tip of the hole identified by post-operative CT images, without regard to the presence of suitable bony landmarks in the ultrasound images. Axial slices of the CT volume are shown in Fig. 2-8 in order to clearly visualize the pedicle hole and intentional lateral and medial breaches.

In particular, the medial breach in the CT image of Fig. 2-8(a) shows the tip of

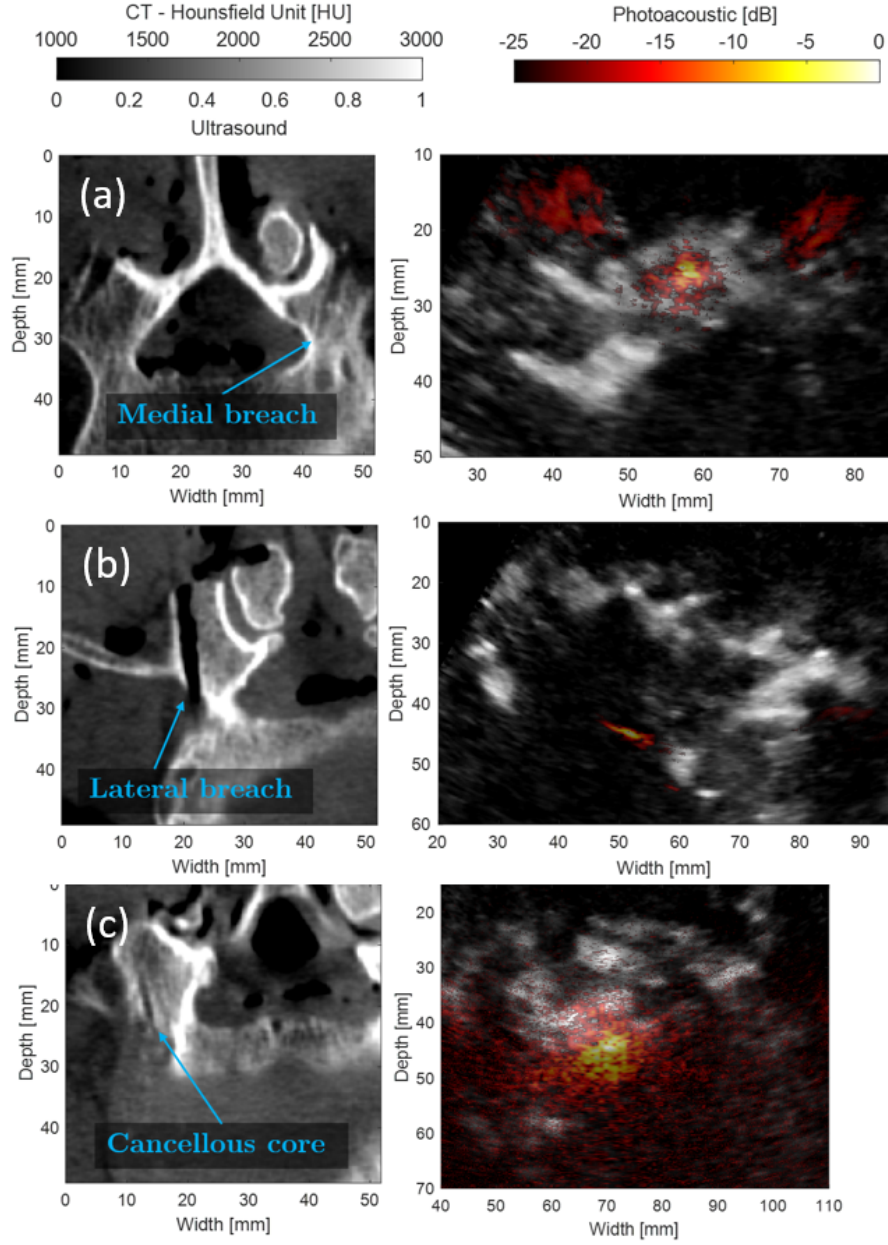


Figure 2-8. Examples of photoacoustic signals generated when the tip of the optical fiber is touching a (a) medial breach, (b) lateral breach, and (c) cancellous core. Left column: CT axial slice. Right column: LW-SLSC ultrasound image co-registered with DAS photoacoustic image.

the hole coinciding with high density bone (i.e., the cortical bone) where the tip of the optical fiber was placed. Similarly, the tip of the fiber is in close proximity to the outer cortical wall of the pedicle in Fig. 2-8(b). In contrast, the tip of the hole in Fig. 2-8(c) is surrounded by low density bone (i.e., cancellous bone). Qualitatively,

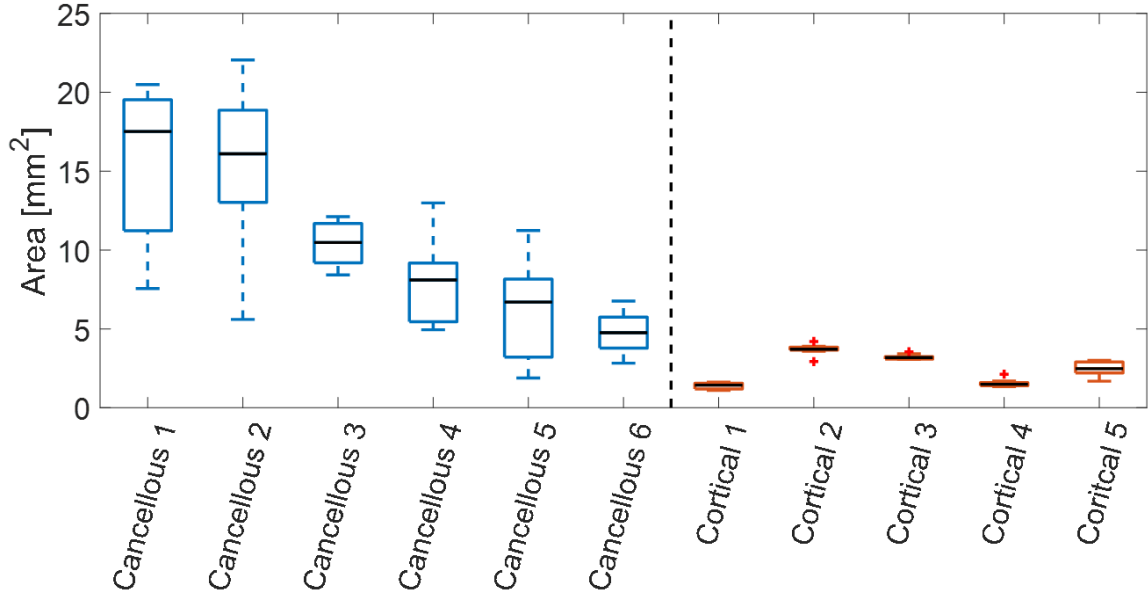


Figure 2-9. Areas of -6dB-contours around the center of photoacoustic targets from cortical and cancellous core using DAS beamforming. Each boxplot shows the median, interquartile range, maximum and minimum values of the estimated areas over 10 frames for cancellous (left) and cortical (right) bone.

DAS photoacoustic images show distinct pattern differences when the optical fiber was touching either cancellous or cortical bone. Specifically, DAS photoacoustic signals from the cancellous core produced signals with greater area coverage than that present with lateral and medial breaches (i.e., fiber touching cortical bone) when images were displayed with the same dynamic range of 25 dB. Because coherence-based methods reduced the appearance of incoherent signals, the area of photoacoustic signals originating from cancellous bone (see Fig. 2-4) was reduced when compared to the same signals in DAS photoacoustic images, resulting in reduced differentiation between these signal origins with the coherence-based images.

Fig. 2-9 shows quantitative comparisons of the differences observed in Fig. 2-8, as measured by the enclosed area of the -6dB contours generated from DAS photoacoustic images. These results are grouped by the expected location of the optical fiber tip, touching either cortical or cancellous bone, based on the corresponding CT images. The total mean area measured within the -6dB-contours was 7.59 mm² greater when

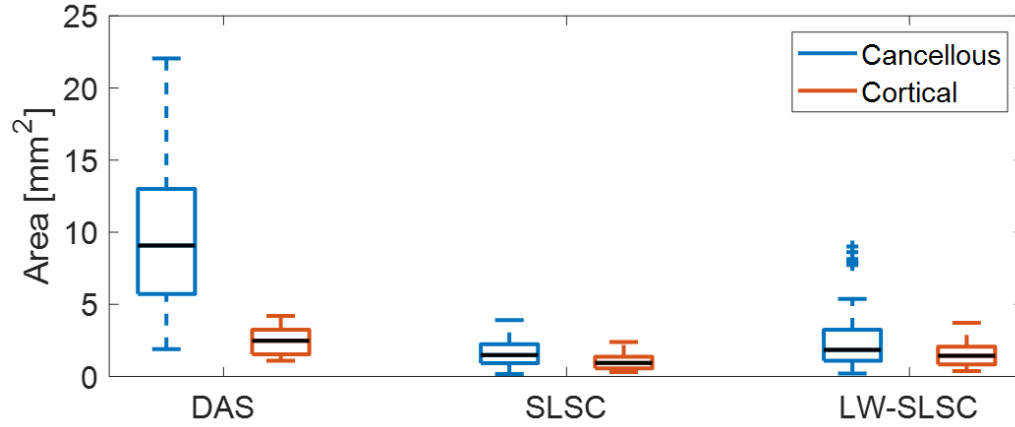


Figure 2-10. Comparison of -6dB-contours from photoacoustic targets inside cortical and cancellous bone in a human cadaver vertebrae using DAS, SLSC and LW-SLSC beamforming. Each boxplot shows the median, interquartile range, maximum and minimum values of the estimated areas over 60 frames for cancellous and 50 frames for cortical bone.

touching cancellous bone compared to cortical bone ($p < 0.01$). In addition, greater standard deviations in these measurements were observed for cancellous bone (5.22 mm^2) when compared to cortical bone (0.96 mm^2).

Fig. 2-10 compares areas of the -6dB contours obtained from DAS, SLSC, and LW-SLSC images of the optical fiber touching either cortical or cancellous bone. The mean \pm one standard deviation of measurements from DAS images was $10.06 \pm 5.22 \text{ mm}^2$ for cancellous bone and $2.47 \pm 0.96 \text{ mm}^2$ for cortical bone. In comparison, the mean \pm one standard deviation of measurements from SLSC images was 1.64 ± 0.88 and $1.06 \pm 0.59 \text{ mm}^2$ for cancellous and cortical bone, respectively. The mean \pm one standard deviation of measurements from LW-SLSC images was 2.60 ± 2.25 and $1.51 \pm 0.77 \text{ mm}^2$, for cancellous and cortical bone, respectively. While the three beamformers showed statistically significant differences between the mean of measured areas from cortical and cancellous bone ($p < 0.01$), DAS images offered the greatest distinction.

2.4 Discussion

We successfully demonstrated that combined ultrasound and photoacoustic imaging has the potential to improve pedicle screw placement during posterior spinal fusion surgeries. Coherence-based beamforming plays an important role in both ultrasound and photoacoustic image formation for this task. Specifically, coherence-based ultrasound imaging improves the visualization of bone structures (Figs. 2-3 and 2-4), which enables individual landmarks for each independent bone structure during the registration of ultrasound to CT images (Figs. 2-4 and 2-6). As a complement to this information, coherence-based photoacoustic imaging enables localization of fiber tips (Fig. 2-4).

On the other hand, amplitude-based methods such as DAS photoacoustic imaging of signals inside the lumbar vertebrae allowed differentiation between cortical and cancellous bone. As observed in Fig. 2-8, DAS photoacoustic images show a diffuse pattern when the optical fiber was inside the pedicle, where its core is composed of cancellous bone. This pattern is understandable, as reflections within the porous, blood-rich structure of the cancellous bone are expected to compromise the alignment of the delayed signals during the beamforming process. In contrast, a well-defined, compact signal was observed for the medial and lateral breaches, which can be explained by the wall surrounding the pedicle being composed by cortical bone, which is more dense than cancellous bone [52] and is expected to produce less signal reflections. Similar signal appearance differences were previously obtained prior to the removal of any bone, presenting photoacoustic imaging as a potential option to find the ideal starting points for pedicle screw insertion [22]. The new contributions of this work demonstrate that these same differences in bone appearance can be used to determine if the pedicle hole is being created with the correct trajectory to avoid impending bone breaches. As out-of-plane signals need to be identified and excluded for successful

implementation of this concept, the use of a 2D ultrasound array to identify the out-of-plane photoacoustic signals is a promising alternative to our empirical $\text{SNR} > 3$ threshold.

We additionally note that coherence-based beamforming was not sufficient to visualize nor quantify differentiation between cortical and cancellous bone (Fig 2-4). These coherence-based beamformers reduced the incoherent signals associated with the cancellous bone, which is a necessary feature of bone differentiation that is emphasized with amplitude-based beamforming methods. However, the added value of coherence-based beamforming is its ability to localize the coherent signal source with more clarity for photoacoustic signal tracking during pedicle hole creation. Thus, we conclude that amplitude- and coherence-based photoacoustic beamformers are synergistically and mutually beneficial for the clinical task of guiding spinal fusion surgeries. Specifically, SLSC and LW-SLSC beamformers have the potential to improve target localization that is otherwise difficult in the presence of noise [38] or diffuse patterns from the cancellous core of the pedicle [22], while DAS beamforming can assist with determining proximity to cortical bone based on the shape of the amplitude-based signal.

In a previous study, a single vertebra with tissue attachments removed was submerged in a water tank [53], and the presence of reverberations required the introduction of some assumptions about fiber tip positions in order to estimate true locations within pre-drilled pedicle holes. However, the human cadaver study presented in this chapter did not require these additional assumptions. As observed in Figs. 2-4 and 2-8, photoacoustic signals from the optical fiber tip did not produce additional artifacts that would otherwise negatively impact tip position estimates (compared with Fig. 2 in [53]). While the previous study differed from the cadaver study by using a custom drill bit that surrounded the optical fiber, we hypothesize that reverberations in [53] were primarily generated by the absence of muscle, nerves, fat, and blood vessels. These additional artifacts were substantially reduced in the human cadaver experiments

because of sound attenuation in the surrounding soft tissue, which emphasizes the importance of conducting cadaver studies on the path to clinical translation of this photoacoustic-guided surgery concept, as noted in [54].

Regarding real-time capabilities, DAS and SLSC or LW-SLSC photoacoustic images can be interleaved during surgeries. Previous work describing a real-time GPU implementation of the SLSC beamformer on a research ultrasound system indicates that this is a viable possibility [38]. We demonstrated that photoacoustic SLSC images can be displayed in high-noise-level environments generated with $< 200 \mu\text{J}$ laser energies at 41 frames per second [38]. Given that LW-SLSC operates on independent kernels \hat{R}_i as described in Section 2.2.1.2, real-time imaging can be similarly achieved by concurrent execution of each \hat{R}_i in a separate thread inside the GPU. The complexity of the operations per thread is further reduced by pre-computing matrix B and $\alpha^2 D^T D$, which are defined in Section 2.2.1.2. With a GeForce GTX Titan X graphic card, we estimated a computation time of 60 ms based on the number of cores of the GPU (i.e., 3072 cores) and the computation time when executed in MATLAB (i.e., approximately 3 minutes). This estimation does not consider memory transfer and pre-computation times. In addition, we previously developed a deep neural network architecture (i.e., CohereNet) to estimate spatial coherence functions [55], which are foundational to LW-SLSC imaging. This deep learning approach achieved real-time computational processing times and can potentially be adapted to include the additional regularization steps needed for LW-SLSC imaging.

We envision several implementation possibilities to achieve the stated benefits of combined amplitude- and coherence-based ultrasound and photoacoustic images. First, as the fiber tips are ultimately envisioned to be inserted into the hollow core of custom drill bits [22, 37, 53, 56], the observed benefits of coherence-based photoacoustic images can potentially be extended to benefits for tracking the tips of common surgical tools used during spinal fusions surgeries (e.g., drill tips, pedicle probe tips). The feasibility

of this concept was demonstrated for drill bits in a previous publication from our group [56]. As observed in Fig. 2 of [56], a stationary optical fiber was connected to the laser source, and the opposite end of the fiber was inserted into a stationary interface. The other end of this stationary interface accommodated a rotating drill bit, which was custom-fabricated with holes on both ends to house a rigidly attached optical fiber that rotated with the drill bit. Both the stationary and rotating optical fibers were air coupled to each other to permit light transmission from the stationary laser to the tip of the rotating drill bit. If attachment to tool tips are not possible, a surgeon may periodically check trajectories by removing the pedicle probe (or any other surgical instrument used to create pedicle holes) and replacing the instrument with an optical fiber, as implemented for the human cadaver study described in this chapter.

2.5 Conclusions

This chapter presents the first known combined ultrasound and photoacoustic image guidance system with software capabilities that are optimized for pedicle cannulation in posterior spinal fusion surgery, demonstrating that both amplitude- and coherence-based beamforming methods are mutually beneficial for this task. Specifically, coherence-based beamforming of ultrasound images improved the visualization of bone for ultrasound-to-CT registration, while coherence-based beamforming of photoacoustic images has the potential to improve target localization and tracking during pedicle hole creation. Amplitude-based photoacoustic beamforming has the potential to provide complementary quantitative information regarding proximity to the cortical bone surrounding the desired pedicle hole trajectory. Overall, this proposed combination of imaging modalities and beamforming methods is promising to assist surgeons with identifying and avoiding impeding bone breaches during spinal fusion surgeries. These new findings are complementary to previous work demonstrating that

photoacoustic imaging is useful to determine optimal entry points into the pedicle [22]. Together with these previous findings, we have successfully demonstrated a complete system that has the potential to significantly impact the standard of image guidance methods for spinal fusion surgery.

2.6 Acknowledgments

This work was supported by NSF CAREER Award ECCS-1751522 and NIH R00-EB018994. The authors acknowledge the support of NVIDIA Corporation with the donation of the Titan Xp GPU used for this research. In addition, the authors thank Gerhard Kleinzig and Sebastian Vogt from Siemens Healthineers for making a Siemens ARCADIS Orbic 3D available.

2.7 Appendix: Out-of-plane Photoacoustic Signals Originated Inside Human Vertebrae

To provide additional justification and rationale for omitted acquisitions, Fig. 2-11(a) shows examples of DAS photoacoustic images chosen from the lowest SNR cases for the cancellous core, the cortical bone, and signals originating from outside of the imaging plane. The corresponding mean \pm one standard deviation SNR were 3.45 ± 0.06 , 3.88 ± 0.07 , and 2.09 ± 0.03 , respectively. In contrast to signals originating from the cancellous or the cortical bone, our observation and experience indicate that of out-of-plane signals are characterized by a high noise level throughout the entire DAS image and a relatively small area coverage around the target identified with LW-SLSC beamforming. SNR measurements were calculated as described in Section 2.2.3.6. Fig. 2-11(b) quantifies the SNR within DAS images from photoacoustic targets originating from cancellous core, cortical bone, and out-of-plane signals. By empirically defining a threshold SNR of 3, out-of-plane signals were discarded from the area analysis.

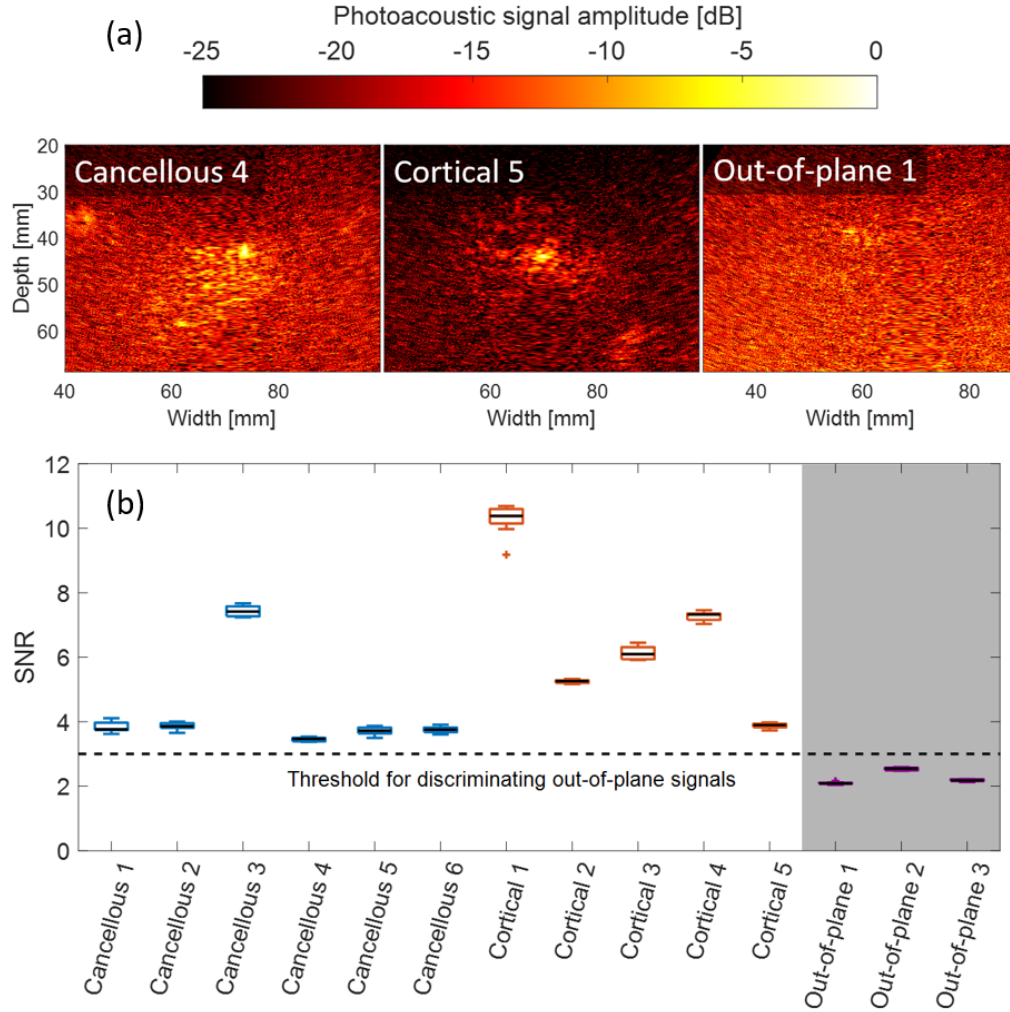


Figure 2-11. Qualitative and quantitative assessment of photoacoustic images originating from out-of-plane signals. (a) Examples of cancellous, cortical, and out-of-plane DAS photoacoustic images. (b) SNR assessment measured from photoacoustic signals associated with the cancellous core, cortical bone, and characteristic out-of-plane signals. The shaded area represents signals that did not achieve the $\text{SNR} > 3$ threshold and were therefore not included in the area results of Figs. 2-9 and 2-10.

2.8 Appendix: Image Quality Assessment of Reconstructed Ultrasound Images of Human Vertebrae

To facilitate comparisons between the DAS images and each SLSC and LW-SLSC image, ROIs are not shown in Fig. 2-4. However, to provide a reference point, Fig. 2-12 shows the ROIs used for quantitative assessment of ultrasound image quality reported

in Table 2-1.

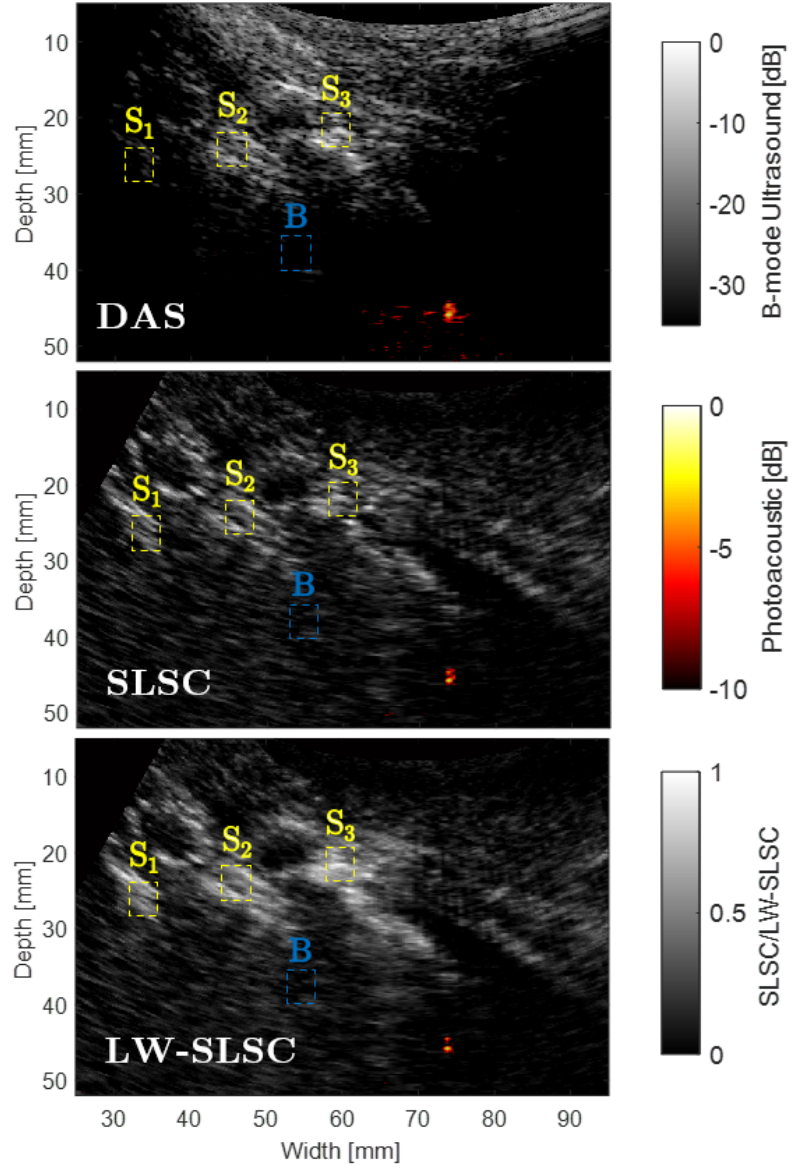


Figure 2-12. Examples of ultrasound and co-registered photoacoustic images from an oblique view of L3-L5 vertebrae reconstructed with DAS, SLSC and LW-SLSC. S_1 , S_2 , S_3 , and B denote the selected regions for quantitative assessments.

References

- [1] E. A. Gonzalez, A. Jain, and M. A. L. Bell, “Combined ultrasound and photoacoustic image guidance of spinal pedicle cannulation demonstrated with intact ex vivo specimens,” *IEEE Transactions on Biomedical Engineering*, vol. 68, no. 8, pp. 2479–2489, 2020.
- [2] A. Manbachi, R. S. Cobbold, and H. J. Ginsberg, “Guided pedicle screw insertion: Techniques and training,” *The Spine Journal*, vol. 14, no. 1, pp. 165–179, 2014.
- [3] K. Abul-Kasim and A. Ohlin, “The rate of screw misplacement in segmental pedicle screw fixation in adolescent idiopathic scoliosis: The effect of learning and cumulative experience,” *Acta Orthopaedica*, vol. 82, no. 1, pp. 50–55, 2011.
- [4] S. D. Gertzbein and S. E. Robbins, “Accuracy of pedicular screw placement in vivo.,” *Spine*, vol. 15, no. 1, pp. 11–14, 1990.
- [5] W. H. Castro, H. Halm, J. Jerosch, J. Malms, J. Steinbeck, and S. Blasius, “Accuracy of pedicle screw placement in lumbar vertebrae,” *Spine*, vol. 21, no. 11, pp. 1320–1324, 1996.
- [6] T. Laine, K. Mäkitalo, D. Schlenzka, K. Tallroth, M. Poussa, and A. Alho, “Accuracy of pedicle screw insertion: a prospective CT study in 30 low back patients,” *European Spine Journal*, vol. 6, no. 6, pp. 402–405, 1997.
- [7] N. Hecht, H. Yassin, M. Czabanka, B. Föhre, K. Arden, T. Liebig, and P. Vajkoczy, “Intraoperative computed tomography versus 3d c-arm imaging for navigated spinal instrumentation,” *Spine*, vol. 43, no. 5, pp. 370–377, 2018.
- [8] S. Açıkbaş, F. Arslan, and M. Tuncer, “The effect of transpedicular screw misplacement on late spinal stability,” *Acta Neurochirurgica*, vol. 145, no. 11, pp. 949–955, 2003.
- [9] P. Park, H. J. Garton, V. C. Gala, J. T. Hoff, and J. E. McGillicuddy, “Adjacent segment disease after lumbar or lumbosacral fusion: Review of the literature,” *Spine*, vol. 29, no. 17, pp. 1938–1944, 2004.
- [10] Y. Aota, K. Kumano, and S. Hirabayashi, “Postfusion instability at the adjacent segments after rigid pedicle screw fixation for degenerative lumbar spinal disorders.,” *Journal of Spinal Disorders*, vol. 8, no. 6, pp. 464–473, 1995.
- [11] L.-P. Amiot, K. Lang, M. Putzier, H. Zippel, and H. Labelle, “Comparative results between conventional and computer-assisted pedicle screw installation in the thoracic, lumbar, and sacral spine,” *Spine*, vol. 25, no. 5, pp. 606–614, 2000.
- [12] B. Ishak, A. Younsi, C. Wieckhusen, P. Slonczewski, A. W. Unterberg, and K. L. Kiening, “Accuracy and revision rate of intraoperative computed tomography point-to-point navigation for lateral mass and pedicle screw placement: 11-year single-center experience in 1054 patients,” *Neurosurgical Review*, pp. 1–11, 2018.
- [13] B. N. Upendra, D. Meena, B. Chowdhury, A. Ahmad, and A. Jayaswal, “Outcome-based classification for assessment of thoracic pedicular screw placement,” *Spine*, vol. 33, no. 4, pp. 384–390, 2008.

- [14] J. Fichtner, N. Hofmann, A. Rienmüller, N. Buchmann, J. Gempt, J. S. Kirschke, F. Ringel, B. Meyer, and Y.-M. Ryang, “Revision rate of misplaced pedicle screws of the thoracolumbar spine—comparison of three-dimensional fluoroscopy navigation with freehand placement: A systematic analysis and review of the literature,” *World Neurosurgery*, vol. 109, e24–e32, 2018.
- [15] P. A. Laudato, K. Pierzchala, and C. Schizas, “Pedicle screw insertion accuracy using o-arm, robotic guidance, or freehand technique,” *Spine*, vol. 43, no. 6, E373–E378, 2018.
- [16] W. Wein, A. Khamene, D.-A. Clevert, O. Kutter, and N. Navab, “Simulation and fully automatic multimodal registration of medical ultrasound,” in *International Conference on Medical Image Computing and Computer-Assisted Intervention*, Springer, 2007, pp. 136–143.
- [17] B. Brendel, S. W. A. Rick, M. Stockheim, and H. Ermert, “Registration of 3D CT and ultrasound datasets of the spine using bone structures,” *Computer Aided Surgery*, vol. 7, no. 3, pp. 146–155, 2002.
- [18] S. Winter, B. Brendel, I. Pechlivanis, K. Schmieder, and C. Igel, “Registration of CT and intraoperative 3-D ultrasound images of the spine using evolutionary and gradient-based methods,” *IEEE Transactions on Evolutionary Computation*, vol. 12, no. 3, pp. 284–296, 2008.
- [19] W. Wein, B. Roper, and N. Navab, “Integrating diagnostic B-mode ultrasonography into CT-based radiation treatment planning,” *IEEE Transactions on Medical Imaging*, vol. 26, no. 6, pp. 866–879, 2007.
- [20] W. Wein, S. Brunke, A. Khamene, M. R. Callstrom, and N. Navab, “Automatic CT-ultrasound registration for diagnostic imaging and image-guided intervention,” *Medical Image Analysis*, vol. 12, no. 5, pp. 577–585, 2008.
- [21] P. Beard, “Biomedical photoacoustic imaging,” *Interface Focus*, vol. 1, no. 4, pp. 602–631, 2011.
- [22] J. Shubert and M. A. L. Bell, “Photoacoustic imaging of a human vertebra: Implications for guiding spinal fusion surgeries,” *Physics in Medicine and Biology*, 2018.
- [23] B. Eddins and M. A. L. Bell, “Design of a multifiber light delivery system for photoacoustic-guided surgery,” *Journal of Biomedical Optics*, vol. 22, no. 4, p. 041 011, 2017.
- [24] D. Piras, C. Grijsen, P. Schutte, W. Steenbergen, and S. Manohar, “Photoacoustic needle: Minimally invasive guidance to biopsy,” *Journal of Biomedical Optics*, vol. 18, no. 7, p. 070 502, 2013.
- [25] M. K. A. Singh, V. Parameshwarappa, E. Hendriksen, W. Steenbergen, and S. Manohar, “Photoacoustic-guided focused ultrasound for accurate visualization of brachytherapy seeds with the photoacoustic needle,” *Journal of Biomedical Optics*, vol. 21, no. 12, p. 120 501, 2016.
- [26] A. B. Karpouk, B. Wang, and S. Y. Emelianov, “Development of a catheter for combined intravascular ultrasound and photoacoustic imaging,” *Review of Scientific Instruments*, vol. 81, no. 1, p. 014 901, 2010.

- [27] Y. Zhang, Y. Cao, and J.-X. Cheng, “High-resolution photoacoustic endoscope through beam self-cleaning in a graded index fiber,” *Optics Letters*, vol. 44, no. 15, pp. 3841–3844, 2019.
- [28] M. Graham, F. Assis, D. Allman, A. Wiacek, E. Gonzalez, M. Gubbi, J. Dong, H. Hou, S. Beck, J. Chrispin, and M. A. L. Bell, “In vivo demonstration of photoacoustic image guidance and robotic visual servoing for cardiac catheter-based interventions,” *IEEE Transactions on Medical Imaging*, vol. 39, no. 4, pp. 1015–1029, 2020.
- [29] R. G. Kolkman, W. Steenbergen, and T. G. van Leeuwen, “In vivo photoacoustic imaging of blood vessels with a pulsed laser diode,” *Lasers in Medical Science*, vol. 21, no. 3, pp. 134–139, 2006.
- [30] W. Xia, E. Maneas, D. I. Nikitichev, C. A. Mosse, G. S. Dos Santos, T. Vercauteren, A. L. David, J. Deprest, S. Ourselin, P. C. Beard, and A. E. Desjardins, “Interventional photoacoustic imaging of the human placenta with ultrasonic tracking for minimally invasive fetal surgeries,” in *International Conference on Medical Image Computing and Computer-Assisted Intervention*, Springer, 2015, pp. 371–378.
- [31] M. A. L. Bell, A. K. Ostrowski, P. Kazanzides, and E. Boctor, “Feasibility of transcranial photoacoustic imaging for interventional guidance of endonasal surgeries,” in *Photons Plus Ultrasound: Imaging and Sensing 2014*, International Society for Optics and Photonics, vol. 8943, 2014, p. 894307.
- [32] M. A. L. Bell, A. K. Ostrowski, K. Li, P. Kazanzides, and E. M. Boctor, “Localization of transcranial targets for photoacoustic-guided endonasal surgeries,” *Photoacoustics*, vol. 3, no. 2, pp. 78–87, 2015.
- [33] M. T. Graham, J. Huang, F. Creighton, and M. A. L. Bell, “Simulations and human cadaver head studies to identify optimal acoustic receiver locations for minimally invasive photoacoustic-guided neurosurgery,” *Photoacoustics*, p. 100183, 2020.
- [34] M. Allard, J. Shubert, and M. A. L. Bell, “Feasibility of photoacoustic-guided teleoperated hysterectomies,” *Journal of Medical Imaging*, vol. 5, no. 2, p. 021213, 2018.
- [35] A. Wiacek, K. C. Wang, H. Wu, and M. A. L. Bell, “Dual-wavelength photoacoustic imaging for guidance of hysterectomy procedures,” in *Advanced Biomedical and Clinical Diagnostic and Surgical Guidance Systems XVIII*, International Society for Optics and Photonics, vol. 11229, 2020, p. 112291D.
- [36] A. Horiguchi, K. Tsujita, K. Irisawa, T. Kasamatsu, K. Hirota, M. Kawaguchi, M. Shinchu, K. Ito, T. Asano, H. Shinmoto, H. Tsuda, and M. Ishihara, “A pilot study of photoacoustic imaging system for improved real-time visualization of neurovascular bundle during radical prostatectomy,” *The Prostate*, vol. 76, no. 3, pp. 307–315, 2016.
- [37] M. A. L. Bell and J. Shubert, “Photoacoustic-based visual servoing of a needle tip,” *Scientific Reports*, vol. 8, no. 1, p. 15519, 2018.
- [38] E. A. Gonzalez and M. A. L. Bell, “GPU implementation of photoacoustic short-lag spatial coherence imaging for improved image-guided interventions,” *Journal of Biomedical Optics*, vol. 25, no. 7, pp. 1–19, 2020.
- [39] K. P. Kubelick and S. Y. Emelianov, “In vivo photoacoustic guidance of stem cell injection and delivery for regenerative spinal cord therapies,” *Neurophotonics*, vol. 7, no. 3, p. 030501, 2020.

- [40] M. A. Lediju, G. E. Trahey, B. C. Byram, and J. J. Dahl, “Short-lag spatial coherence of backscattered echoes: Imaging characteristics,” *IEEE Transactions on Ultrasonics, Ferroelectrics, and Frequency Control*, vol. 58, no. 7, pp. 1377–1388, 2011.
- [41] E. Gonzalez and M. A. L. Bell, “Segmenting bone structures in ultrasound images with Locally Weighted SLSC (LW-SLSC) beamforming,” in *2018 IEEE International Ultrasonics Symposium (IUS)*, IEEE, 2018, pp. 1–9.
- [42] A. A. Nair, T. D. Tran, and M. A. L. Bell, “Robust short-lag spatial coherence imaging,” *IEEE Transactions on Ultrasonics, Ferroelectrics, and Frequency Control*, vol. 65, no. 3, pp. 366–377, 2017.
- [43] A. Barbero Jimenez and S. Sra, “Fast algorithms for total-variation based optimization,” 2010.
- [44] S. Mehrotra, “On the implementation of a primal-dual interior point method,” *SIAM Journal on Optimization*, vol. 2, no. 4, pp. 575–601, 1992.
- [45] D. Mattes, D. R. Haynor, H. Vesselle, T. K. Lewellyn, and W. Eubank, “Nonrigid multi-modality image registration,” in *Medical imaging 2001: image processing*, International Society for Optics and Photonics, vol. 4322, 2001, pp. 1609–1620.
- [46] M. Styner, C. Brechbuhler, G. Szckely, and G. Gerig, “Parametric estimate of intensity inhomogeneities applied to MRI,” *IEEE Transactions on Medical Imaging*, vol. 19, no. 3, pp. 153–165, 2000.
- [47] E. Gonzalez and M. A. L. Bell, “A GPU approach to real-time coherence-based photoacoustic imaging and its application to photoacoustic visual servoing,” in *Photons Plus Ultrasound: Imaging and Sensing 2020*, International Society for Optics and Photonics, vol. 11240, 2020, p. 1124054.
- [48] E. Gonzalez, M. R. Gubbi, and M. A. L. Bell, “GPU implementation of coherence-based photoacoustic beamforming for autonomous visual servoing,” in *2019 IEEE International Ultrasonics Symposium (IUS)*, IEEE, 2019, pp. 24–27.
- [49] A. Fedorov, R. Beichel, J. Kalpathy-Cramer, J. Finet, J.-C. Fillion-Robin, S. Pujol, C. Bauer, D. Jennings, F. Fennessy, M. Sonka, J. Buatti, S. Aylward, J. V. Miller, S. Pieper, and R. Kikinis, “3D Slicer as an image computing platform for the Quantitative Imaging Network,” *Magnetic Resonance Imaging*, vol. 30, no. 9, pp. 1323–1341, 2012.
- [50] A. Rodriguez-Molares, O. M. H. Rindal, J. D’hooge, S.-E. Måsøy, A. Austeng, M. A. L. Bell, and H. Torp, “The generalized contrast-to-noise ratio: A formal definition for lesion detectability,” *IEEE Transactions on Ultrasonics, Ferroelectrics, and Frequency Control*, vol. 67, no. 4, pp. 745–759, 2019.
- [51] K. M. Kempinski, M. T. Graham, M. R. Gubbi, T. Palmer, and M. A. L. Bell, “Application of the generalized contrast-to-noise ratio to assess photoacoustic image quality,” *Biomedical Optics Express*, vol. 11, no. 7, pp. 3684–3698, 2020.
- [52] P. Zioupos, R. B. Cook, and J. R. Hutchinson, “Some basic relationships between density values in cancellous and cortical bone,” *Journal of Biomechanics*, vol. 41, no. 9, pp. 1961–1968, 2008.
- [53] E. Gonzalez, A. Wiacek, and M. A. L. Bell, “Visualization of custom drill bit tips in a human vertebra for photoacoustic-guided spinal fusion surgeries,” in *Photons Plus Ultrasound: Imaging and Sensing 2019*, International Society for Optics and Photonics, vol. 10878, 2019, p. 108785M.

- [54] M. A. Lediju Bell, “Photoacoustic imaging for surgical guidance: Principles, applications, and outlook,” *Journal of Applied Physics*, vol. 128, no. 6, p. 060 904, 2020.
- [55] A. Wiacek, E. González, and M. A. L. Bell, “Coherenet: A deep learning architecture for ultrasound spatial correlation estimation and coherence-based beamforming,” *IEEE Transactions on Ultrasonics, Ferroelectrics, and Frequency Control*, 2020.
- [56] J. Shubert and M. A. L. Bell, “A novel drill design for photoacoustic guided surgeries,” in *Photons Plus Ultrasound: Imaging and Sensing 2018*, International Society for Optics and Photonics, vol. 10494, 2018, 104940J.

Chapter 3

Countour Analysis of Photoacoustic Signals from Cortical Bone, Cancellous Bone, and a Fiber Tip

The work presented in this chapter was published in the following manuscript:

E. Gonzalez, A. Jain, and M. A. L. Bell, “Photoacoustic differentiation of cortical from cancellous bone in the lumbar vertebrae of an intact human cadaver to prevent bone breaches during spinal fusion surgeries,” in *Photons Plus Ultrasound: Imaging and Sensing 2021*, International Society for Optics and Photonics, vol. 11642, 2021, p. 1164210

3.1 Introduction

When cannulating pedicles, it is critical to ensure the correct trajectory during the hole creation process in order to avoid accidental bone breaches and screw misplacement [2], which compromises neighboring structures of the peripheral and central nervous system, erodes long-term biomechanical stability [2, 3], and causes adjacent degeneration [4, 5]. These breaches occur in 14% to 38.5% of procedures, characterized by misplaced screws within the surrounding cortical bone rather than the cancellous core of the pedicle [6], as shown in Fig. 3-1.

Based on previous studies to visualize photoacoustic signals from the surface of

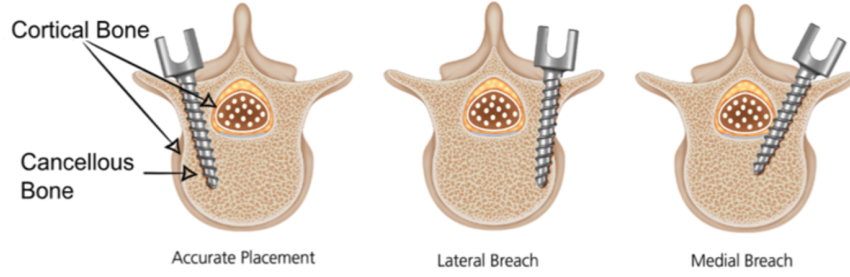


Figure 3-1. Examples of accurate and inaccurate pedicle screw placement [8].

human vertebrae [7], we hypothesize that similar visibility can be achieved beneath the bony structure in a more realistic setup and closer to the surgical environment of a spinal fusion surgery.

One key difference between cancellous and cortical bone is the greater porosity of the cancellous bone when compared to the more dense, more compact cortical bone [9]. This difference can be visualized in conventional computer-assisted methods such as computed tomography (CT) [10], 2D- [11], and 3D-fluoroscopy navigation [12], where the brightest pixels are indications of high attenuation values originating from cortical bone. However, limitations of these methods include exposure to ionizing radiation, the requirement to insert reference and intraoperative markers, and relatively prolonged surgery times.

To overcome the limitations listed above, our group recently proposed photoacoustic imaging as a guidance method for pedicle screw insertion [7, 13]. The proposed technique consists of delivering laser light at the tip of a device (e.g., pedicle probe, drill) while it is being inserted into the pedicle to create a hole for the screw. The emission of laser pulses generate an acoustic pressure response from the surrounding bone. The acoustic pressure is then received by an externally placed ultrasound probe, and beamforming is applied to create a photoacoustic image. As cancellous bone is more blood-rich in comparison to cortical bone, a distinctive photoacoustic response is expected between these two types of bone. This distinction was demonstrated when

visualizing photoacoustic signals from the surface of a human vertebra [7] and when visualizing photoacoustic signals from beneath the bony surface in a more realistic setup and closer to the surgical environment of a spinal fusion surgery [14].

The work in this chapter expands our previous work [14] by providing a more detailed analysis of the ability to distinguish cortical from cancellous bone when photoacoustic signals originate from beneath the bone surface. This more detailed analysis is performed in the lumbar vertebrae of an intact human cadaver, with the ultimate goal of developing a novel photoacoustic surgical system to prevent breaches. Coherence-based beamforming techniques such as short-lag spatial coherence (SLSC) [15] and locally weighted short-lag spatial coherence (LW-SLSC) [16] were investigated in addition to conventional delay-and-sum (DAS) beamforming to characterize signal morphology as well as to determine the location of the fiber tip that initiates the photoacoustic effect.

3.2 Method

An adult male human cadaver was placed in the prone position and dissection was carried along the cranio-caudal axis with the aid of a Cobb elevator to reveal the spinous process, lamina, and facet joints at each level from L1 to S1. The specimen had no reports of spine pathologies, malformations, or previous spinal surgeries, which was also confirmed with pre-operative CT imaging. The pedicles were cannulated bilaterally from L2 through L4 along anatomic trajectories using a standard free hand technique with a pedicle probe.

Six pre-bored holes were created in the cancellous core of the pedicle, and five pre-bored holes either created an intentional breach of the lateral wall or an obvious path toward an intentional breach (leaving the surrounding cortical bone intact). The total depth of the pedicle tracts from the bone surface ranged from 14 mm to 25 mm, as measured with the ruler on pedicle probe. A 1-mm diameter optical fiber was

inserted into the bottom of the pre-bored pedicle holes. The optical fiber was used to transmit 750 nm wavelength laser light from a Phocus Mobile laser (Opotek Inc., Carlsbad, CA, USA) with an energy of 13.4 mJ at the fiber tip. An Alpinion SC1-6 convex array ultrasound transducer, which was connected to an Alpinion E-CUBE 12R ultrasound system (Alpinion, Seoul, South Korea), was placed on the exposed tissue surface to receive the photoacoustic signals originating from the tip of the fiber. To assist the surgeon with fiber tip localization, a GPU implementation of SLSC for photoacoustic imaging [17–19] was used during the surgery.

For each fiber tip location, 10 photoacoustic image frames were acquired. SLSC and LW-SLSC beamforming were used to determine the position of the optical fiber tip, which was difficult to determine from DAS photoacoustic images due to the presence of incoherent signals that were removed with the coherence-based beamforming [14, 18]. Photoacoustic images were overlaid on co-registered ultrasound image acquisitions that were interleaved with photoacoustic image acquisitions. For each photoacoustic acquisition, contour maps were created from the DAS, SLSC, and LW-SLSC photoacoustic images within a 15 mm \times 15 mm region surrounding the center of the target identified by LW-SLSC images. The -6, -10, -15, and -20 dB contour lines were displayed in each contour map.

The total area encompassed by each contour line was calculated for each of the four contour levels. A Mann-Whitney test was used to evaluate the statistical significance ($p < 0.001$) of the difference in areas measured when the optical fiber was touching either cancellous or cortical bone. The bone type was based on ground truth information available in post-operative CT images. This statistical analysis was repeated for each contour level and for each beamforming method.

3.3 Results

Fig. 3-2 shows CT, ultrasound, and overlaid photoacoustic images of an accurately created hole, a lateral breach, and a medial breach, from left to right respectively. The CT slices (top row) were chosen to optimize visual confirmation of the fiber placement description and are not registered to the ultrasound and photoacoustic images. The left CT image shows the tip of the hole surrounded by low density bone (i.e., cancellous bone), where the tip of the optical fiber was placed to generate the corresponding photoacoustic image. The middle and right CT images show the tip of the hole in close proximity to high density bone (i.e., cortical bone). Corresponding photoacoustic signals from the cancellous core and the cortical bone are shown in the bottom row. Qualitatively, the DAS photoacoustic images show a more spatially

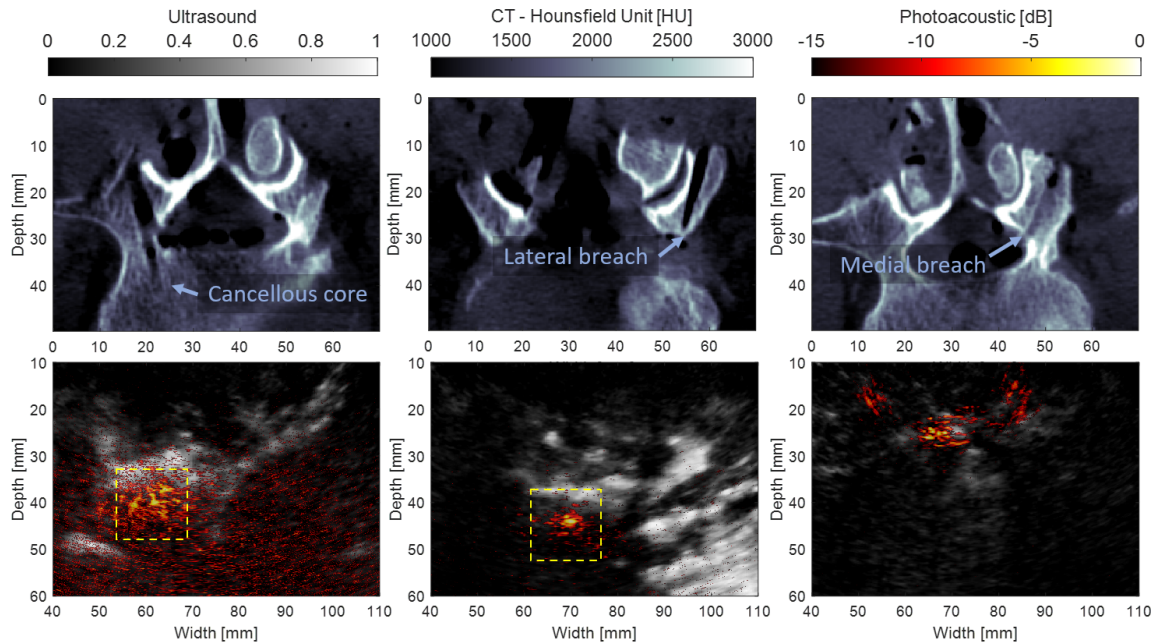


Figure 3-2. CT axial slice (top) and corresponding LW-SLSC ultrasound images co-registered with DAS photoacoustic image (bottom). The photoacoustic images represent example signals obtained when the tip of the optical fiber touches the bottom of the cancellous core, the cortical bone of a lateral breach, and the cortical bone of a medial breach, from left to right, respectively. The yellow boxes indicate regions of interest for Fig. 3-3.

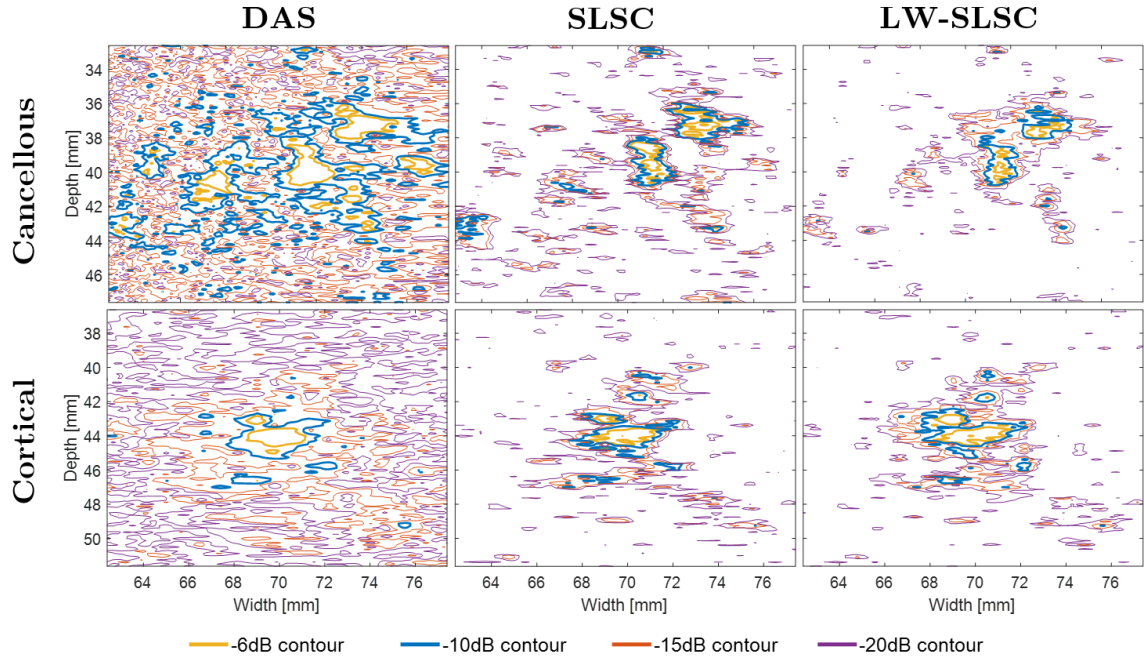


Figure 3-3. Contour plots of photoacoustic DAS, SLSC, and LW-SLSC images, taken from the region highlighted with the yellow box in Fig. 3-2, when the tip of the optical fiber was touching cancellous (top) or cortical (bottom) bone.

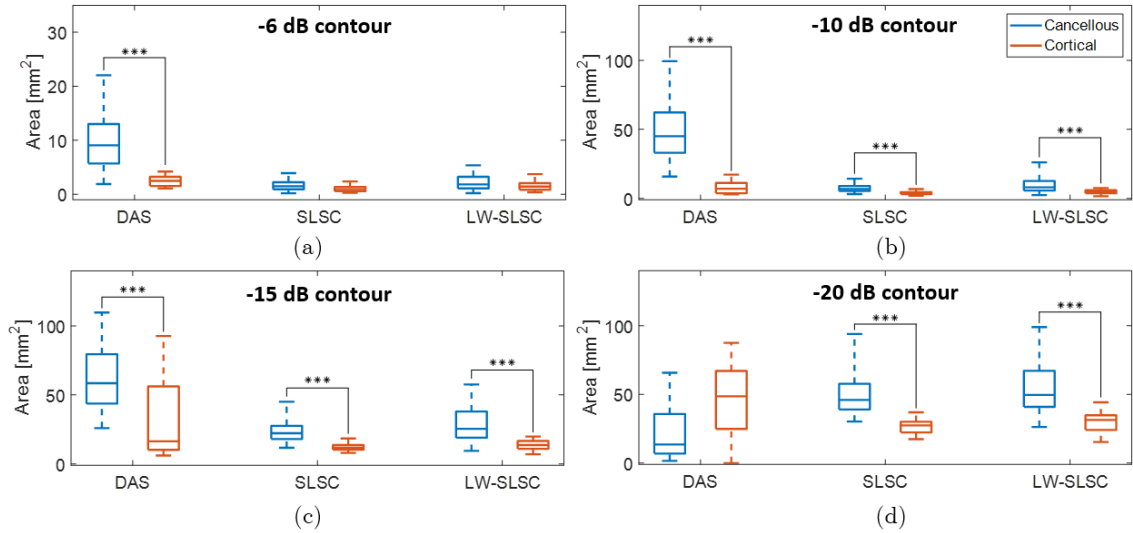


Figure 3-4. Difference of areas from DAS, SLSC, and LW-SLSC images of photoacoustic targets inside cortical and cancellous bone using contours of (a) -6dB, (b) -10dB, (c) -15dB, and (d) -20 dB. Each boxplot shows the median, interquartile range, maximum and minimum values of the estimated areas over 60 frames for cancellous bone and 50 frames for cortical bone. *** $p < 0.001$.

diffuse pattern when the optical fiber was touching cancellous bone compared to the pattern generated when the fiber was touching cortical bone.

Fig. 3-3 shows contour plots of the photoacoustic signals originating from cancellous bone (top) and cortical bone (bottom), when zooming in on the regions highlighted by the yellow boxes in Fig. 3-2. Contour lines are shown after beamforming the associated signals with DAS (left), SLSC (middle), and LW-SLSC (right) beamformers. The diffuse pattern of signals originating from cancellous bone, as observed with DAS beamforming in Fig. 3-2, complicates localization of the fiber tip. Localization was improved with the use of coherence-based beamforming methods. In particular, the -6 dB and -10 dB contours occupy less total area and are closer together in the corresponding SLSC and LW-SLSC photoacoustic, which enables more accurate localization of the fiber tip. The total areas of the -6 dB contours for the cortical bone were 3.41, 0.40, and 1.06 mm² for DAS, SLSC, and LW-SLSC, respectively. In contrast, the total areas of the -6 dB contours for the cancellous bone were 17.55, 0.42, and 0.47 mm² for DAS, SLSC, and LW-SLSC, respectively.

Fig. 3-4 compares the total areas enclosed by the -6, -10, -15, and -20 dB contour levels in DAS, SLSC, and LW-SLSC images, for the cancellous and cortical bone cases shown in Fig. 3-3, combined with 5 additional cases from an optical fiber in contact with cancellous bone within a prepared pedicle hole and 4 additional cases from an optical fiber in contact with cortical bone after an intentional breach.

Each box plot shows the median, interquartile range, maximum, and minimum values of the estimated areas over 60 frames for cancellous and 50 frames for cortical bone (i.e., from 10 repeated acquisitions per case). Overall, DAS, SLSC, and LW-SLSC images showed statistically significant differences between the medians of measured areas from cortical and cancellous bone ($p < 0.001$) for contours of -10 dB and -15 dB. In addition, DAS sufficiently differentiated between these two types of bone structures with statistical significance ($p < 0.001$) at -6 dB contours. SLSC and LW-SLSC achieved

differentiation with statistical significance ($p < 0.001$) at -20 dB contour levels, while DAS did not.

3.4 Discussion

The work presented in this chapter is the first to investigate the morphology of photoacoustic signals originating from cancellous and cortical bone within an *ex vivo* human cadaver at multiple contour levels. Previously, we analyzed the feasibility of differentiating photoacoustic signals from cortical and cancellous bone at a contour level of -6 dB, using DAS, SLSC, and LW-SLSC beamforming [14]. This chapter presents results for three additional contour levels (i.e., -10, -15, and -20 dB), with the goal of summarizing the relative differentiation capabilities.

While results show that photoacoustic differentiation is possible with either of the three beamformers at contour levels of -10 and -15 dB, using the amplitude-based beamformer (i.e., DAS) and a contour level of -6 dB is considered the most robust solution. The rationale for this robustness is that a contour level of -6 dB allows more localized visualization of the photoacoustic response from the fiber tip (either independently or possibly attached to a surgical tool) without confusing this response from that of surrounding tissue. In addition, differentiation based on the -6 dB contour level is recommended for clinical translation, as out-of-plane signals and photoacoustic reverberations contribute to additive noise that affects higher contour levels, making these higher levels less reliable for differentiation. In contrast, coherence-based photoacoustic imaging enables the localization of fiber tips, which is advantageous in conjunction with anatomical landmarks obtained from ultrasound acquisitions [14], because surgeons can track the tool tip as the hole is being created in order to ensure a correct trajectory. Accurately created pedicle holes reduce the risk of complications surrounding bone breaches during spinal fusion surgeries.

The improved localization of the tool tip can be appreciated by estimating the

centroid of the -6 dB contour levels for the SLSC and LW-SLSC images represented in Fig. 3-3 (in comparison that of the DAS image). Therefore, amplitude- and coherence-based photoacoustic images can be synergistically employed to differentiate between signals originating from cortical and cancellous bone at -6 dB contour levels and to detect the tip of surgical tools, respectively.

In a clinical scenario, the optical fiber can be inserted in the core of the tool used to bore the hole, providing simultaneous DAS-based and SLSC-based photoacoustic images in real-time [18]. A computer vision algorithm could be incorporated into the framework to display in real-time the areas of the -6 dB DAS photoacoustic signals surrounding the fiber tip. When creating the pedicle hole, the area of this contour level would then be expected to decrease if the fiber tip approaches the cortical walls. Therefore, the displayed areas would serve as additional information to the surgeon regarding undesirable proximity to cortical bone, which has the potential to prevent a lateral or medial breach during spinal fusion surgery. In addition to correcting trajectories during the hole creation process, previous work demonstrates that photoacoustic imaging can also be used to determine the appropriate starting point for pedicle cannulation [7]. The combination of these findings with the contributions of this chapter constitute a complete photoacoustic-based solution to avoid accidental bone breaches [14].

3.5 Conclusion

In this chapter, we analyzed the morphology of photoacoustic signals originating from cancellous and cortical bone in the pedicles of an *ex vivo* human cadaver, using amplitude-based and coherence-based beamforming techniques. By measuring the area at different contour levels, DAS beamforming provided better photoacoustic differentiation between cancellous and cortical bone in comparison to coherence-based SLSC and LW-SLSC beamforming at the -6 dB contour level. This contour level

also enabled both fiber tip localization with the coherence-based beamformers. These results are promising for surgical guidance within the desired cancellous core of the pedicle and away from the surrounding cortical bone, in order to avoid costly and painful bone breaches during spinal fusion surgery.

3.6 Acknowledgements

The authors acknowledge the support of NVIDIA Corporation with the donation of the Titan Xp GPU used for this research. In addition, the authors thank Gerhard Kleinzigand Sebastian Vogt from Siemens Healthineers for making a Siemens ARCADIS Orbic 3D available.

References

- [1] E. Gonzalez, A. Jain, and M. A. L. Bell, “Photoacoustic differentiation of cortical from cancellous bone in the lumbar vertebrae of an intact human cadaver to prevent bone breaches during spinal fusion surgeries,” in *Photons Plus Ultrasound: Imaging and Sensing 2021*, International Society for Optics and Photonics, vol. 11642, 2021, p. 1 164 210.
- [2] N. Hecht, H. Yassin, M. Czabanka, B. Föhre, K. Arden, T. Liebig, and P. Vajkoczy, “Intraoperative computed tomography versus 3D C-arm imaging for navigated spinal instrumentation,” *Spine*, vol. 43, no. 5, pp. 370–377, 2018.
- [3] S. Açıkbaş, F. Arslan, and M. Tuncer, “The effect of transpedicular screw misplacement on late spinal stability,” *Acta Neurochirurgica*, vol. 145, no. 11, pp. 949–955, 2003.
- [4] P. Park, H. J. Garton, V. C. Gala, J. T. Hoff, and J. E. McGillicuddy, “Adjacent segment disease after lumbar or lumbosacral fusion: Review of the literature,” *Spine*, vol. 29, no. 17, pp. 1938–1944, 2004.
- [5] Y. Aota, K. Kumano, and S. Hirabayashi, “Postfusion instability at the adjacent segments after rigid pedicle screw fixation for degenerative lumbar spinal disorders.,” *Journal of Spinal Disorders*, vol. 8, no. 6, pp. 464–473, 1995.
- [6] K. Abul-Kasim and A. Ohlin, “The rate of screw misplacement in segmental pedicle screw fixation in adolescent idiopathic scoliosis: The effect of learning and cumulative experience,” *Acta Orthopaedica*, vol. 82, no. 1, pp. 50–55, 2011.
- [7] J. Shubert and M. A. L. Bell, “Photoacoustic imaging of a human vertebra: Implications for guiding spinal fusion surgeries,” *Physics in Medicine and Biology*, 2018.
- [8] N. Fedrigo, “Improving spinal fusions: Redesigning the pedicle probe to prevent vertebral breaches,” *Canadian Science Fair Journal*, vol. 1, no. 2, 2019.
- [9] P. Roschger, S. Rinnerthaler, J. Yates, G. Rodan, P. Fratzl, and K. Klaushofer, “Alendronate increases degree and uniformity of mineralization in cancellous bone and decreases the porosity in cortical bone of osteoporotic women,” *Bone*, vol. 29, no. 2, pp. 185–191, 2001.
- [10] B. Ishak, A. Younsi, C. Wieckhusen, P. Slonczewski, A. W. Unterberg, and K. L. Kiening, “Accuracy and revision rate of intraoperative computed tomography point-to-point navigation for lateral mass and pedicle screw placement: 11-year single-center experience in 1054 patients,” *Neurosurgical Review*, pp. 1–11, 2018.
- [11] B. N. Upendra, D. Meena, B. Chowdhury, A. Ahmad, and A. Jayaswal, “Outcome-based classification for assessment of thoracic pedicular screw placement,” *Spine*, vol. 33, no. 4, pp. 384–390, 2008.
- [12] J. Fichtner, N. Hofmann, A. Rienmüller, N. Buchmann, J. Gempt, J. S. Kirschke, F. Ringel, B. Meyer, and Y.-M. Ryang, “Revision rate of misplaced pedicle screws of the thoracolumbar spine—comparison of three-dimensional fluoroscopy navigation with freehand placement: A systematic analysis and review of the literature,” *World Neurosurgery*, vol. 109, e24–e32, 2018.
- [13] M. A. Lediju Bell, “Photoacoustic imaging for surgical guidance: Principles, applications, and outlook,” *Journal of Applied Physics*, vol. 128, no. 6, p. 060 904, 2020.

- [14] E. A. Gonzalez, A. Jain, and M. A. L. Bell, “Combined ultrasound and photoacoustic image guidance of spinal pedicle cannulation demonstrated with intact ex vivo specimens,” *IEEE Transactions on Biomedical Engineering*, vol. 68, no. 8, pp. 2479–2489, 2020.
- [15] M. A. Lediju, G. E. Trahey, B. C. Byram, and J. J. Dahl, “Short-lag spatial coherence of backscattered echoes: Imaging characteristics,” *IEEE Transactions on Ultrasonics, Ferroelectrics, and Frequency Control*, vol. 58, no. 7, pp. 1377–1388, 2011.
- [16] E. Gonzalez and M. A. L. Bell, “Segmenting bone structures in ultrasound images with Locally Weighted SLSC (LW-SLSC) beamforming,” in *2018 IEEE International Ultrasonics Symposium (IUS)*, IEEE, 2018, pp. 1–9.
- [17] —, “A GPU approach to real-time coherence-based photoacoustic imaging and its application to photoacoustic visual servoing,” in *Photons Plus Ultrasound: Imaging and Sensing 2020*, International Society for Optics and Photonics, vol. 11240, 2020, p. 1 124 054.
- [18] E. A. Gonzalez and M. A. L. Bell, “GPU implementation of photoacoustic short-lag spatial coherence imaging for improved image-guided interventions,” *Journal of Biomedical Optics*, vol. 25, no. 7, pp. 1–19, 2020.
- [19] E. Gonzalez, M. R. Gubbi, and M. A. L. Bell, “GPU implementation of coherence-based photoacoustic beamforming for autonomous visual servoing,” in *2019 IEEE International Ultrasonics Symposium (IUS)*, IEEE, 2019, pp. 24–27.

Chapter 4

GPU Implementation of Photoacoustic SLSC Imaging for Segmentation and Robotic Surgical Guidance

The work presented in this chapter was published in the following manuscript:

E. A. Gonzalez and M. A. L. Bell, “GPU implementation of photoacoustic short-lag spatial coherence imaging for improved image-guided interventions,” *Journal of Biomedical Optics*, vol. 25, no. 7, pp. 1–19, 2020

4.1 Introduction

Visual servoing [2–4] is a promising approach to maintain visualization of surgical tools during minimally invasive procedures and to keep track of the location of nearby anatomical targets within the body. This approach broadly refers to vision-based robot control, and the robot “vision” that we focus on in this chapter is provided through photoacoustic images [5, 6]. Photoacoustic imaging is achieved by transmitting pulsed light to a structure of interest, which absorbs the light, undergoes thermal expansion, and generates an acoustic response that is received by a conventional ultrasound probe [7–9]. This photoacoustic imaging technique was previously demonstrated for multiple applications that require surgery or interventions, such as visualization of

brachytherapy seeds [10, 11], intravascular imaging [12], cardiac catheter visualization [6], fetal surgeries [13], prostate surgeries [14], and endonasal surgeries [15–17]. In these applications, structures of interest include blood vessels, nerves, drill tips, and catheter or needle tips [6, 18, 19]. One or more optical fibers may be coupled to the tool, catheter, or needle tips in order to transmit the light pulses [12, 20–22]. Alternatively, a fiber or fiber bundle may be operated independently to provide a photoacoustic-based anatomical guidance in the absence of surgical tools [23–25].

With the rise of robotic surgery [26–29], we can reasonably envision photoacoustic system components that are robotically controlled to enable more successful surgeries and interventions [30]. A summary of the procedures required to achieve photoacoustic-based visual servoing in particular is summarized in Fig. 4-1, starting with a robot-held ultrasound probe that receives photoacoustic signals. Receive beamforming techniques are then applied to create a photoacoustic image, and an image segmentation algorithm locates features of interest within the image. Beamforming techniques are implemented rather than photoacoustic reconstruction techniques like backprojection due to two considerations. First, beamforming is sufficient to accurately quantify the position and size of photoacoustic sources [31], which are two parameters of primary interest for photoacoustic-based visual servoing. Second, conventional linear or phased array ultrasound probes would be placed externally for the proposed visual

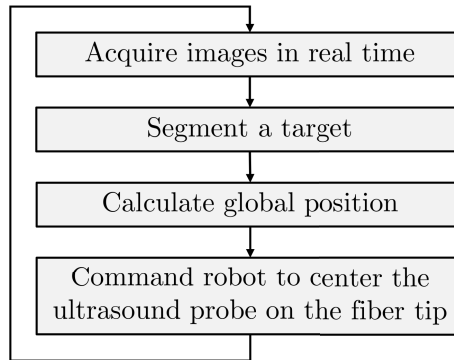


Figure 4-1. Overview of photoacoustic-based visual servoing.

servoing application, rather than the ring arrays (i.e., spherical or cylindrical detection surfaces) that are more favorable for backprojection algorithms and quantitative photoacoustic applications [31]. After beamforming and image segmentation, the ultrasound probe motion is controlled by the robot to ensure that targets of interest remain at the center of the image.

Previous photoacoustic-based visual servoing studies implemented conventional delay-and-sum (DAS) receive beamforming [5, 6]. However, DAS photoacoustic images contain poor SNR when using low laser energies, which compromises the performance of the segmentation step shown in Fig. 4-1. This limitation may be overcome by increasing the incident laser energy or otherwise enhancing the amplitude of photoacoustic signals. Although stable segmentation is often achieved with high laser energies, these energies tend to introduce side lobes and other artifacts. Therefore, alternative options for signal amplitude enhancement would be more suitable. For example, frame averaging enables the use of lower energies and simultaneously reduces incoherent noise and artifacts [32, 33], but this option introduces motion artifacts [34, 35], which negatively impact the overall accuracy of visual servoing.

Alternatives to DAS beamforming have demonstrated potential to overcome the limitations of poor target visibility without assistance from frame averaging. For example, minimum variance (MV) beamforming has been shown to suppress off-axis signals and improve spatial resolution by decreasing main lobe widths [36]. However, MV beamforming is sensitive to sound speed changes and requires sub-array averaging [37], more than one stage of MV calculations, or the combination of weighting factors [36, 38]. These additional steps increase the computational burden of this beamforming alternative. Similarly, a synthetic aperture focusing approach is beneficial with regard to enhancing lateral resolution along the depth (or axial) dimension [39, 40], as well as reducing reverberation artifacts [41]. However, these techniques require a combination of delay sequences for each pixel in the reconstructed image [42], which increases

computational burden. Additional beamforming alternatives include coherence factor (CF) weighting [43] or a combination of beamforming methods (e.g., DAS+CF [44], SAF+CF [45], and MV+CF [38]), and these options suffer from similar challenges stated above.

Short-lag spatial coherence (SLSC) beamforming [46–49] is another option that has shown substantial promise in multiple interventional tasks [10, 16, 30, 50]. Therefore, SLSC is considered to be one of the more suitable beamforming options available to improve photoacoustic-based visual servoing. SLSC beamforming requires multiple normalized cross-correlations of delayed data in order to directly display measurements of aperture-domain spatial coherence rather than amplitude. Although SLSC beamforming is known to be insensitive to signal amplitude [49, 51], the proposed application of visual servoing and surgical tool tracking does not require this sensitivity. The benefits of using SLSC beamforming for the proposed application are that it enhances the contrast of single-frame photoacoustic images (i.e., no frame averaging required) [16, 47, 52] and triples effective penetration depths when compared to DAS beamforming [10]. In addition, SLSC beamforming improves the quality of photoacoustic signals acquired with low laser energies [53], which is advantageous because the use of low laser energies can help to ensure laser safety. Miniaturized low-energy light delivery systems (such as pulsed laser diodes [53–55] or light emitting diodes [56]) are additionally beneficial for portability in the operating room and to increase frame rates when compared to Q-switched lasers. Therefore, we are interested in exploring capabilities and limitations of SLSC beamforming with regard to low energy light sources.

Drawing on this history of promise and success, this chapter extends our two previous conference publications [57, 58], which describe elements of the first known real-time implementation of the SLSC beamformer for photoacoustic imaging, utilizing the graphical processing unit (GPU) of an FDA-approved joint clinical and

research Alpinion E-CUBE 12R ultrasound system. The new contributions of this chapter include a detailed assessment of the relationships among SLSC beamforming parameters, processing time, and image quality, as well as reports of photoacoustic signal-to-noise ratios (SNRs) obtained with a range of laser energies, target depths, and SLSC beamforming parameters. This information is then used to evaluate the two essential visual servoing tasks of fiber tip tracking and probe centering and to compare these tasks with both the real-time SLSC beamformer and the DAS beamformer. Finally, our presented GPU-SLSC approach is evaluated with *in vivo* data.

This chapter is organized as follows. Section 4.2 details the framework of our GPU-SLSC photoacoustic implementation and describes the methods used to assess performance. Section 4.3 demonstrates GPU-SLSC feasibility for real-time applications, as well as the improved SNR and increased tracking accuracy achieved with GPU-SLSC during visual servoing with low laser energies. Section 4.4 discusses these findings and their implications. Finally, Section 4.5 concludes the chapter with a summary of the major technical contributions and achievements of this work.

4.2 Method

4.2.1 GPU Implementation of Photoacoustic SLSC Imaging

The steps to implement real-time SLSC imaging with photoacoustic data acquired with an Alpinion E-CUBE 12R system, are presented in Fig. 4-2. First, raw channel data were acquired by the ultrasound system, which was triggered by a signal from the laser system. Depending on the ultrasound system memory allocation and the number of available channels, a regrouping process (i.e., “Regroup channels” in Fig. 4-2) was performed and transferred to the device texture memory as a $N_i \times N_z$ matrix, where N_i is the number of elements and N_z is the number of axial samples. The total number of acquisitions needed before processing the data is an integer computed as $N_A = N_i/N_c$,

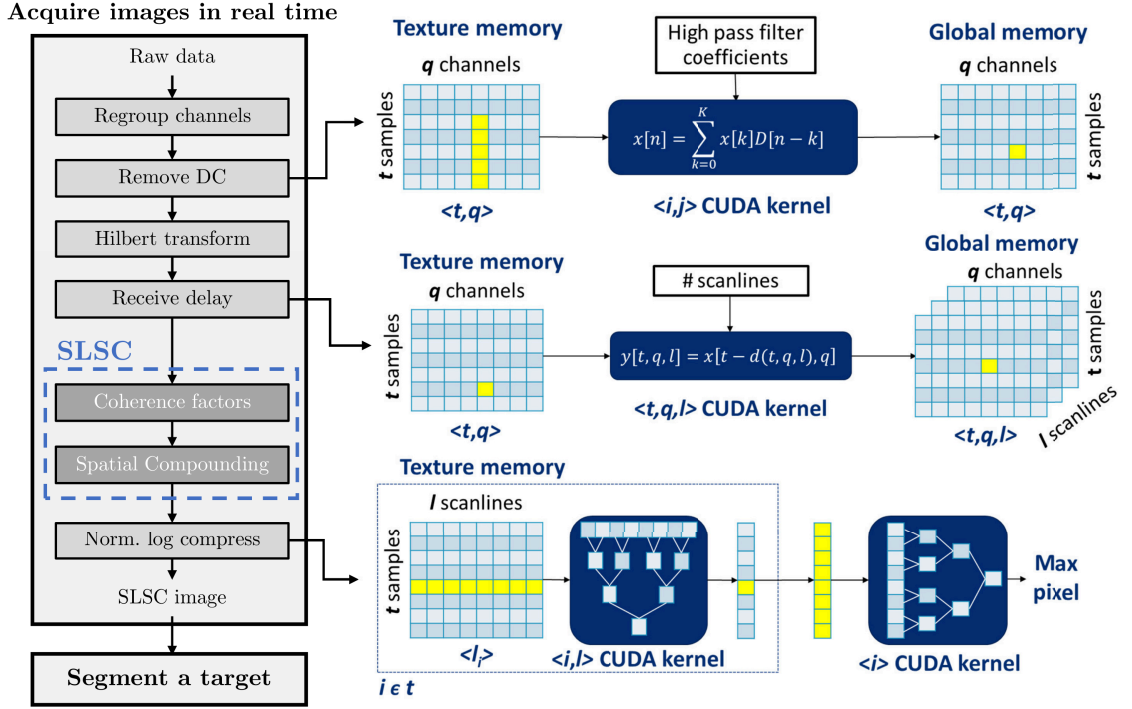


Figure 4-2. Workflow for acquiring a real-time photoacoustic SLSC image with the Alpinion ultrasound system. The diagrams on the right shows graphical displays of GPU kernel distributions for the “Remove DC”, “Receive delay”, and “Norm. log compress” (Normalize and Log compress) steps of real-time photoacoustic SLSC imaging. The x , y , D , and d shown in the CUDA kernels denote the input memory, output memory, high pass filter coefficients, and receive delays, respectively. Variables t , q , and l are indices for axial sample, channel, and scanline, respectively.

where N_c is the number of channels.

The ordered raw data was stored in texture memory (i.e., read-only cached memory that optimizes physically adjacent 2D operations). DC removal was then computed by applying 1D convolutions of time-domain kernels, executed independently along the axial dimension. This operation is graphically displayed to the right of the “Remove DC” block in Fig. 4-2, showing operations at the compute unified device architecture (CUDA) kernel level when transitioning from texture memory to global memory (i.e., the general memory of the GPU device that lasts for the duration of the process). The Hilbert transform was then computed along the axial dimension using the fast Fourier transform (FFT) libraries embedded in CUDA (NVIDIA, Santa Clara, CA,

USA). Here, FFT kernels ran independently across the element dimension N_i .

Next, synthetic receive aperture imaging was performed to generate a specific number of scanlines, N_x , determined by the user as an input parameter, obtaining a $N_i \times N_x \times N_z$ matrix. This operation is graphically displayed to the right of the “Receive delay” block in Fig. 4-2, showing operations at the CUDA kernel level when transitioning from texture memory to global memory. The computation of receive delays was performed in the device texture memory, optimized for 2D linear interpolation, and kernels were distributed with a ratio of one thread per axial sample, executed independently across elements.

The SLSC computations were the same as those described for a comparative Verasonics ultrasound system implementation [59] developed by Hyun *et al.* [60]. These processes are denoted as the dark gray boxes in Fig. 4-2. In contrast to the original SLSC implementation [46], the GPU approach computes a single ensemble correlation coefficient from an ensemble sum of coherence factors C_{ij} , C_{ii} , and C_{jj} rather than an average over each coherence value from element pairs separated by a lag m , as described by the following equations:

$$C_{ij}(z, x, m) = \sum_{i=1}^{N_i-m} s_i(z, x) s_{i+m}(z, x)^* \quad (4.1)$$

$$C_{ii}(z, x, m) = \sum_{i=1}^{N_i-m} |s_i(z, x)|^2 \quad (4.2)$$

$$C_{jj}(z, x, m) = \sum_{i=1}^{N_i-m} |s_{i+m}(z, x)|^2 \quad (4.3)$$

where $s_i(z, x)$ is a complex signal at element i , scanline x , and axial sample z , and $*$ denotes the complex conjugate. The coherence factors (C_{ij} , C_{ii} , and C_{jj}) were stored in the device global memory, then compounded across an axial kernel size, k , and a cumulative lag, M , which is defined as the cumulative sum up to the first M lags, as follows:

$$\text{SLSC}(z, x) = \sum_{m=1}^M \frac{\sum_{\hat{z} \in k} C_{ij}(\hat{z}, x, m)}{\sqrt{\sum_{\hat{z} \in k} C_{ii}(\hat{z}, x, m) \sum_{\hat{z} \in k} C_{jj}(\hat{z}, x, m)}} \quad (4.4)$$

Finally, the negative SLSC values were set to zero [61], and the SLSC image was then normalized and log-compressed. The maximum term for normalization was computed using logarithmic reduction strategies [62]. A graphical representation of the logarithmic reduction is shown to the right of the “Norm. log compress” block in Fig. 4-2 for two consecutive CUDA kernels. The first CUDA kernel computed the maximum value across the lateral dimension given a specific depth. This computation was performed by calculating a vector of maximum values from a layer of element pairs. The vector of maximum values was then distributed to a smaller layer of element pairs until a single maximum remains. The maximum value across the lateral dimension was stored in an axial vector, where a second CUDA kernel calculated the maximum value of the image with the same steps as the first CUDA kernel.

The entire GPU-SLSC photoacoustic implementation represented in Fig. 4-2 was executed on a GeForce GTX 1080 GPU (NVIDIA Corporation, Santa Clara, CA, USA), with 8GB of VRAM and a core clock speed of 1733 MHz. This GPU was installed on the Alpinion E-CUBE 12R ultrasound research system.

4.2.2 Processing Time Assessments

Processing times of the GPU-SLSC photoacoustic implementation were assessed as functions of beamforming parameters M and k , and as a function of the overall image depth, d . M was varied from 5 to 35 in increments of 5, k was evaluated as 3, 11, 19 and 31 axial samples, and d was evaluated as 5 cm and 15 cm axial depths. An axial depth of 15 cm was evaluated as a worst-case scenario in which memory transfer between CPU and GPU would limit real-time imaging capabilities.

In order to provide computation time measurements that are not limited by the laser pulse repetition frequency (i.e., 10 Hz), the external trigger from the laser (needed for synchronization of the laser and ultrasound systems to perform photoacoustic imaging) was disabled. While no synchronization between the laser system and ultrasound

system results in meaningless photoacoustic data, this absence of synchronization does not affect algorithm processing times nor the speed of the GPU-SLSC algorithm. In the absence of wait times for synchronization, each acquisition and beamforming process was performed immediately after the previous frame was displayed on the ultrasound software of the Alpinion E-CUBE 12R. The inverse of the frame rate displayed with the laser trigger disabled was reported as the processing time estimate of the real-time GPU-SLSC algorithm. Robustness in the estimation of computation times was achieved by averaging 10 readings of frame rate obtained over a time span of 10 seconds.

In addition to measuring overall processing times, the processing time for each stage of the flow diagram shown in Fig. 4-2 was measured for the GPU and CPU versions of SLSC beamforming (with the selected optimal values of M , k , and d defined in more detail in Section 4.2.3). CPU-SLSC computations were conducted in a MATLAB environment using the host CPU of the Alpinion E-CUBE 12R system, which is an Intel Xeon E5-1620 with 3.5 GHz clock speed and 32 GB RAM. The processing times from 10 CPU-SLSC executions were averaged to achieve robust estimates.

4.2.3 Image Quality Assessments

The experimental setup to assess image quality consisted of photoacoustic signals originating from an optical fiber tip inserted in *ex vivo* bovine muscle. The optical fiber was used to transmit 900 nm wavelength laser light from a Phocus Mobile laser (Opotek Inc., Carlsbad, CA, USA) with an energy of 726 μJ at the fiber tip. Photoacoustic signals were received by a L3-8 linear array ultrasound probe that was attached to a Sawyer robot arm (Rethink Robotics, Boston, MA), as shown in Fig. 4-3. To incorporate the effects of acoustic scattering and the expected depth-dependent image degradation, the optical fiber tip was located at depths of $s = 4$ cm and $s = 7$ cm. Considering that the primary source of photoacoustic signals is expected to

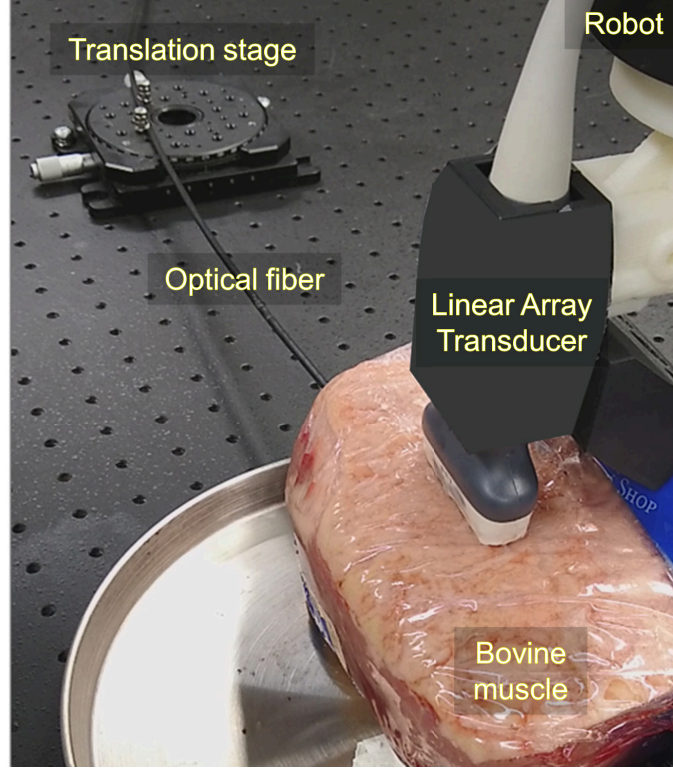


Figure 4-3. Photoacoustic acquisition setup. An optical fiber was attached to translation stage and inserted into *ex vivo* bovine tissue. As the optical fiber was translated, an ultrasound probe connected to a robot arm performed visual servoing.

originate from the tip of the fiber in interventional applications [6], we did not attach the fiber to any surgical tools in this study.

The overall image depth, d , was adjusted based on the target depth (i.e., $d = 5$ cm when $s = 4$ cm and $d = 10$ cm when $s = 7$ cm). M and k were additionally varied for each target depth using the same ranges and increment sizes reported in Section 4.2.2 (i.e., M was varied from 5 to 35 in increments of 5 and k was evaluated as 3, 11, 19 and 31 axial samples). The selection of optimal M and k values for these experiments were obtained by implementing three optimization criteria: (1) maximizing the differentiation between photoacoustic signals and background noise, (2) minimizing side lobes, and (3) minimizing temporal resolution (i.e., processing times).

The generalized contrast-to-noise ratio (gCNR) [63–65] was used to assess the

likelihood of discrimination between regions of interest (ROIs) of beamformed photoacoustic data and after normalization but before log compression stage (i.e., the first optimization criterion for parameter selection):

$$\text{gCNR} = 1 - \sum_{x=0}^1 \min_x \{p_i(x), p_o(x)\} \quad (4.5)$$

where p_i and p_o are the probability density functions of signal amplitudes within ROIs inside and outside of the target, respectively. The probability density functions were calculated from histograms computed with 256 bins. The inside ROI was a 3 mm \times 3 mm rectangle centered on the target center, which was defined as the brightest pixel within the photoacoustic image. The outside ROI was the same size and shifted 5 mm to the right of the lateral center of the target.

The lateral width of the photoacoustic target, r_Δ , was assessed to quantify the extent and minimize the presence of side lobes (i.e., the second optimization criterion for parameter selection). This assessment was obtained by measuring the full width at half maximum (FWHM) of line plots passing through the center of the photoacoustic target, defined as :

$$r_\Delta = \text{FWHM} \quad (4.6)$$

To determine the minimum possible energy limits for SLSC and DAS beamforming, the same experimental setup shown in Fig. 4-3 and described above was implemented with a shallower target depth of $s = 2.5$ cm. Although the real-time parameters were optimized for deeper depths, it is reasonable to assume that similar or better image quality will be achieved at shallower depths. Given the 1 mm-core-diameter optical fiber geometry and the current standards for skin [66], the maximum permissible exposure (MPE) was 50 mJ/cm². This MPE translates to a maximum energy safety limit of 394.6 μ J. The laser energy was varied relative to this MPE (i.e., laser energies of 118, 184, 268, 364, 463, 570, and 645 μ J) for multiple photoacoustic image acquisitions.

The resulting SNR for each laser energy was evaluated with real-time SLSC and

off-line DAS beamforming as follows:

$$\text{SNR} = \frac{\mu_i}{\sigma_o}, \quad (4.7)$$

where μ_i is the mean value within a ROI of beamformed photoacoustic data inside of the target (after normalization but before log compression stage) and σ_o is the standard deviation within a ROI of beamformed photoacoustic data outside of the target (after normalization but before log compression stage). The ROI for the signal was manually defined as a rectangle of approximately 2.5 mm x 2.5 mm, centered on the target. Five independent background ROIs of the same size were placed 10-15 mm to the left of the lateral center of the target to obtain 5 SNR measurements that were used to report the mean \pm standard deviation of SNR measurements. For each laser energy, SNR differences between DAS and either CPU-SLSC or GPU-SLSC, as well as SNR differences between CPU-SLSC and GPU-SLSC, were each evaluated using a repeated-measure analysis of variance to determine statistical significance ($p < 0.05$).

4.2.4 Application to Visual Servoing

The visual servoing process (outlined in Fig. 4-1 and detailed as the velocity-based visual servoing procedure reported in our previous publication[6]) initiated with the acquisition of a real-time photoacoustic image that was then sent to a post-processing algorithm for target detection. Fast computation and transferring of the photoacoustic image is a critical component of the visual servoing algorithm in order to avoid bottlenecks, as well as to enable smooth ultrasound probe motions. Morphological operations such as dilation and erosion were then performed on the beamformed photoacoustic image in order to detect a single connected component and calculate its centroid. The lateral position of the centroid \vec{p} was then saved and compared with the lateral center line of the image \vec{p}_0 . The lateral difference was similarly computed ($\Delta\vec{p} = \vec{p} - \vec{p}_0$). Finally, the ultrasound probe was positioned with the goal

of minimizing $\Delta\vec{p}$, effectively centering the ultrasound probe on the fiber tip.

Two visual servoing experiments were conducted in the *ex vivo* bovine muscle to assess the performance of visual servoing with real-time SLSC (i.e., GPU-SLSC) and real-time DAS beamforming. The first visual servoing experiment consisted of a probe centering test [5]. During the initialization of this experiment, the probe was placed on the surface of the bovine tissue, and the length of the optical fiber was aligned with the imaging plane (i.e., $\Delta\vec{p} = 0$). Then, the tip of the optical fiber was laterally displaced 6 mm from the center of the image. Visual servoing was deployed with the goal of ensuring that the final position of the lateral center of the ultrasound probe coincided with the segmented location of the fiber tip.

The second visual servoing experiment was performed after the ultrasound probe was centered. This experiment tested the ability of the visual servoing system to follow the fiber tip over a total distance of 10 mm, using a translation stage to achieve fiber advancement in tissue and to obtain ground truth displacement measurements. We refer to this second experiment as the fiber tracking experiment. The two visual servoing experiments (i.e., probe centering and fiber tracking) were performed with laser energies of 169, 248, and 322 μJ , which were lower than the maximum energy required to achieve laser safety with our system configuration (i.e., 394.6 μJ at the fiber tip, as reported in Section 4.2.3). The statistical significance of performance differences between real-time SLSC and real-time DAS was evaluated with a Mann-Whitney U test [67].

4.2.5 *In vivo* Segmentation Assessment

Ideally, the experiments described in Section 4.2.4 would be repeated in an *in vivo* setting. However, the use of low laser energies were difficult to detect with DAS beamforming and repeated fiber tracking and probe centering experiments were anticipated to unnecessarily extend the duration of an *in vivo* study, potentially

causing unnecessary animal discomfort.

Therefore, we implemented an alternative plan. The segmentation performance with DAS, CPU-SLSC, and GPU-SLSC imaging was tested with *in vivo* data obtained from a previously completed experiment consisting of an optical fiber inserted in a porcine heart, as described in more detail in our previous publication[6]. To summarize the data acquisition procedure, the optical fiber was first inserted into a cardiac catheter, then the fiber-catheter pair was guided to the right atrium of the heart. The fiber emitted a laser wavelength of 750 nm with a pulse energy of 2.98 mJ. A total of 10 frames of resulting photoacoustic data were acquired with an Alpinion SP1-5 phased array ultrasound probe. This study was approved by the Johns Hopkins University Animal Care and Use Committee.

Considering the relatively high laser energy that was utilized in this previous experiment [6], Gaussian-distributed noise was added to the raw *in vivo* channel data as a surrogate for decreasing the laser energy. The resulting channel SNR of the raw *in vivo* data was evaluated as follows:

$$\text{SNR}_c = 20 \log_{10} \left(\frac{\text{signal}_{rms}}{\text{noise}_{rms}} \right), \quad (4.8)$$

where the *rms* subscript refers to the root mean square of either the signal or the noise. The signal was defined as the entire channel data recording, and the noise was defined as the Gaussian random matrix added to the channel data. The channel data with added noise were then beamformed using DAS, CPU-SLSC, and GPU-SLSC, and photoacoustic signals were segmented using the algorithm described in our previous publication[6]. The locations of the segmented signals were compared with ground truth segmentations derived from corresponding *in vivo* channel data with no noise added. A failed segmentation was defined as either no segmentation result or no overlap of the segmented signal with the ground truth segmentation.

4.3 Results

4.3.1 Selection of Beamforming Parameters

Fig. 4-4 shows GPU-SLSC processing time results for several pairs of M and k at two imaging depths. These processing times are limited by the maximum pulse repetition period (PRP) of any laser, which equals 100 ms for our laser which has a 10 Hz pulse repetition frequency (PRF). Ideally, the processing times would be maintained below this limit (indicated by the dashed line) in order to avoid bottlenecks due to signal processing.

At 5 cm image depth, GPU-SLSC imaging reconstructs frames below this limit. At 15 cm image depth (which represents a worst-case scenario for internal light delivery with external ultrasound probe placement [10, 16, 47, 50, 68]), the majority of possible M and k parameters also fell below this limit. Specifically, pairs of $[M > 20, k \geq 31]$ and $[M > 25, k \geq 19]$ resulted in processing times above the laser PRP indicated by the dashed line. In addition, the observed increase in standard deviation as M increased is proportional to the increased number of loops in the CUDA kernels.

Fig. 4-5 shows image quality metrics as functions of M , k , and d . The discrimination between the source and the background provided by the gCNR metric (top of Fig. 4-5) is the worst for both depth values when $k = 3$, although the gCNR is generally good in most of these cases. The mean \pm one standard deviation of gCNR values shown in Fig. 4-5 is 0.97 ± 0.02 and 0.89 ± 0.70 when $d = 5$ cm and $d = 10$ cm, respectively. When $d = 10$ cm, the lowest M and k values in Fig. 4-5 show decreased gCNR, and gCNR is otherwise constant as M increases. The bottom of Fig. 4-5 shows that lateral resolution improves as M increases, which is expected [10, 46, 49].

The optimal M and k values were selected based on our observations of Figs. 4-4 and 4-5. Specifically, lateral resolution improvement was minimal when $M > 25$ (see Fig. 4-5) and temporal resolution generally remained below the 100 ms PRP limit at M

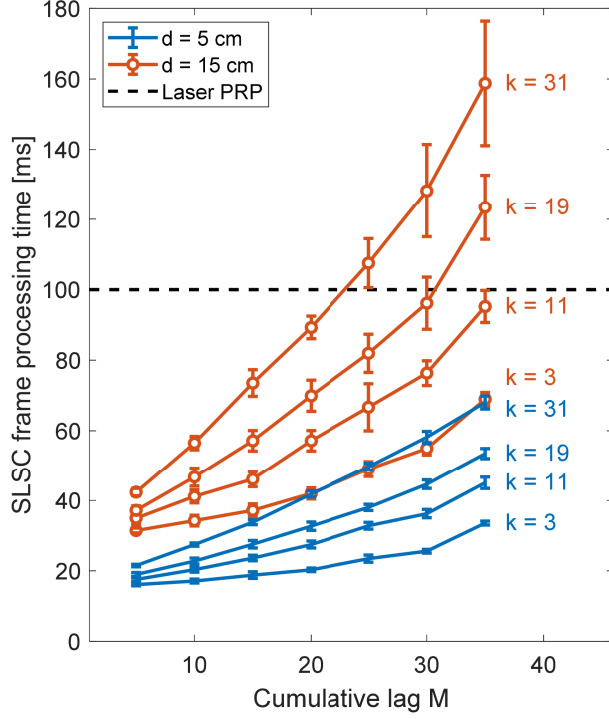


Figure 4-4. GPU-SLSC processing times for a single image frame, acquired with $d=5$ cm and $d=15$ cm imaging depths, while varying the cumulative lag M and axial kernel size k .

$= 25$ (see Fig. 4-4). Therefore, $M = 25$ was selected as optimal. The optimal k value was selected by maximizing gCNR, considering that successful discrimination between target and background is critical for the visual servoing segmentation algorithm. A value of $k = 11$ was chosen because this value results in a gCNR of approximately 1 and increasing k beyond this value is expected to decrease temporal resolution and axial resolution, as previously reported for ultrasound SLSC implementations [60, 69].

4.3.2 Speedup of GPU-SLSC Compared to CPU-SLSC

A depth of $d = 5$ cm and the optimal values determined in Section 4.3.1 (i.e., $M = 25$ and $k = 11$) were implemented to compare computation times. The size of the raw data was a 3328×128 matrix of 16-bit resolution for this evaluation. Fig. 4-6

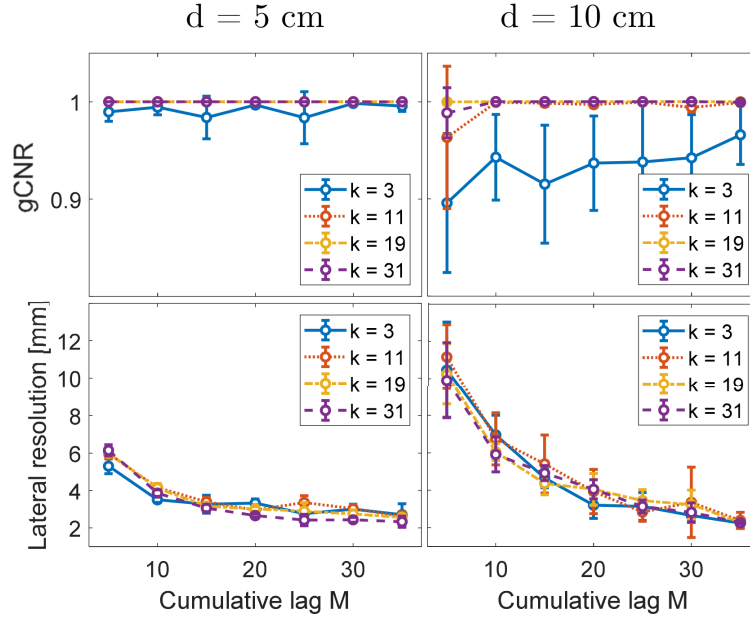


Figure 4-5. Image quality comparisons of gCNR (top) and lateral resolution (bottom) as functions of cumulative lag and axial kernel size for imaging depths of $d = 5$ cm (left) and $d = 10$ cm (right).

shows the average processing times for each stage of the SLSC beamforming flow diagram with GPU-SLSC and CPU-SLSC implementations. GPU-SLSC imaging reduced computation times for each of the processing stages in comparison to CPU-SLSC imaging, with speedups of 13.5x, 49.7x, 12.1x, 711.2x, 550.9x, and 16.9x for the “Reorder”, “No DC”, “Hilbert”, “Delays”, “SLSC”, and “Normalize” stages, respectively.

Comparing the sum of the processing times (i.e., 15.91 ms) with the computation time between frames (i.e., 24.3 ms) resulted in a measured overhead of 8.39 ms. This overhead, likely due to memory transfer and intrinsic subroutines of the ultrasound software of the Alpinion E-CUBE 12R, was included when assessing the overall performance of our real-time implementation. With this inclusion, GPU-SLSC provided an overall speedup of 348.7x when compared to CPU-SLSC. Translating the computation time to real-time imaging scenarios, GPU-SLSC enabled a frame rate up to 41.2

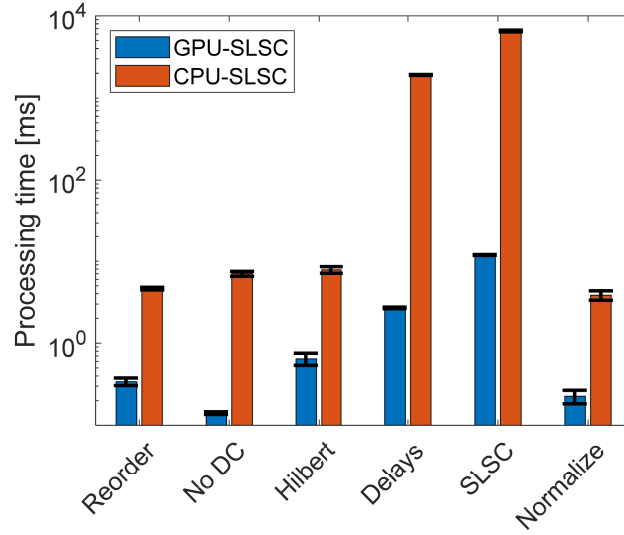


Figure 4-6. Processing times for each stage of SLSC beamforming using GPU and CPU implementations.

Hz.

4.3.3 Performance in *Ex Vivo* Tissue

Fig. 4-7 shows examples of beamformed photoacoustic images of the fiber tip acquired with a laser energy of 268 μJ (Fig. 4-7(a)) along with SNR measurements as a function of laser energy (Fig. 4-7(b)). The SLSC and DAS images in Fig. 4-7(a)

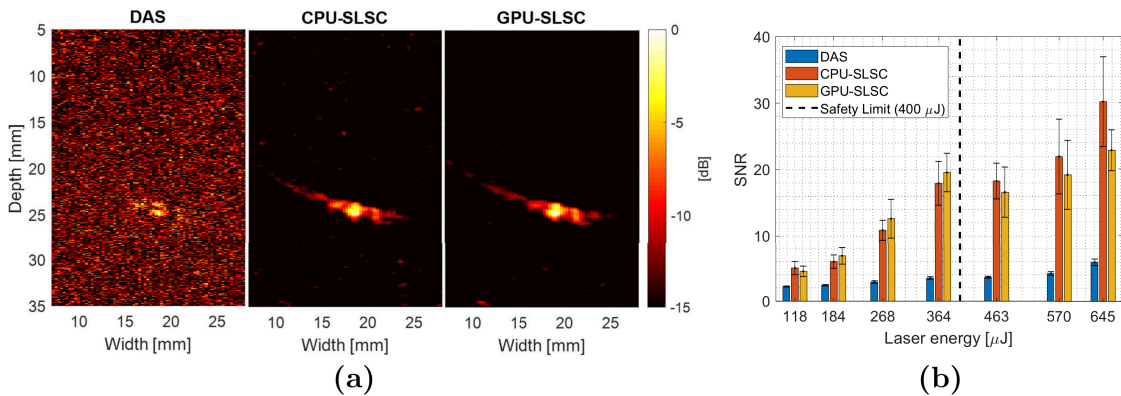


Figure 4-7. (a) Photoacoustic images of the optical fiber inserted into *ex vivo* bovine muscle at 25 mm axial depth, operating at 268 μJ laser energy. Images were reconstructed with DAS, CPU-SLSC and GPU-SLSC beamformers. (b) SNR results from the optical fiber inserted into *ex vivo* bovine muscle as a function of the laser energy.

were normalized, log-compressed and displayed with a dynamic range of 15 dB. The mean \pm one standard deviation of the SNR measured in the DAS, CPU-SLSC, and GPU-SLSC images of Fig. 4-7(a) were 3.5 ± 0.9 dB, 11.4 ± 2.9 dB, and 12.1 ± 4.2 dB, respectively. In Fig. 4-7(a), SLSC imaging consistently outperforms DAS imaging and visualizes low-energy signals ($\leq 268 \mu\text{J}$) with a mean SNR of 11.2 ± 2.4 ($p < 0.05$) The corresponding DAS SNR was 3.5 ± 0.8 . The mean SNR difference between the CPU-based and GPU-based SLSC implementations was 1.14. This difference was not statistically significant ($p > 0.05$).

Fig. 4-8 shows results from the probe centering experiment. Photoacoustic images acquired with one low laser energy (i.e., $110 \mu\text{J}$) and one higher laser energy (i.e., $645 \mu\text{J}$)

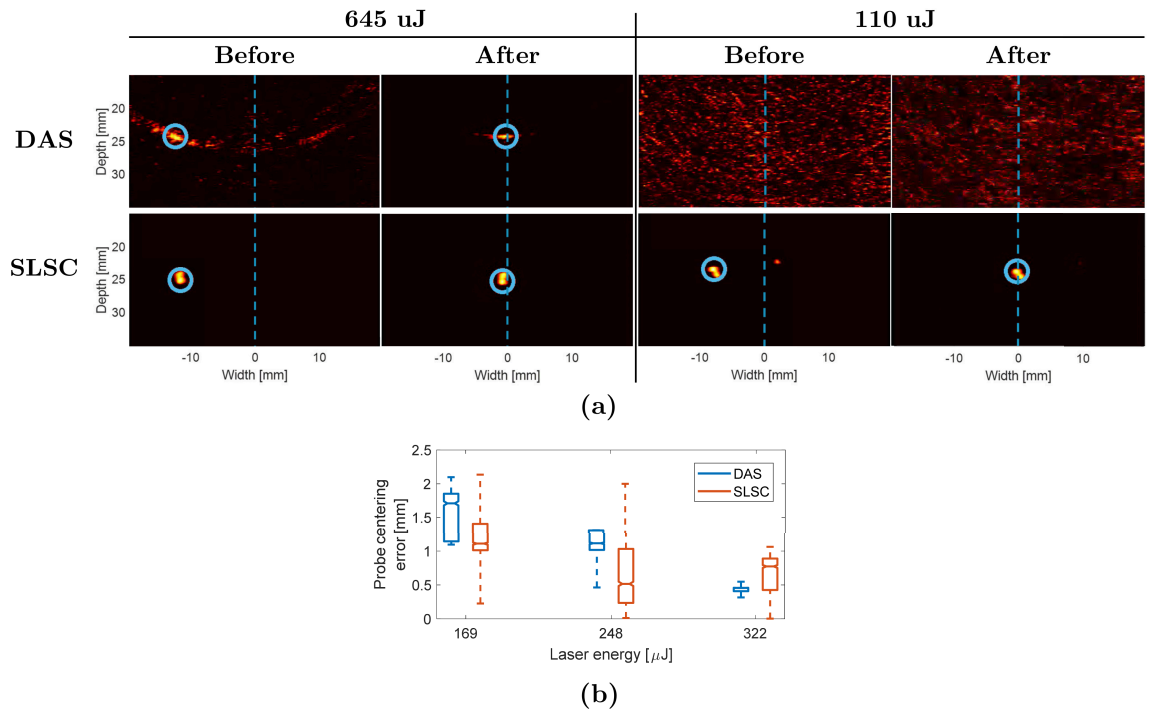


Figure 4-8. (a) Example of probe centering results for high and low laser energies with DAS and GPU-SLSC photoacoustic images. The first and second columns for each energy show the initial and final position of the fiber before and after probe centering, respectively. The dashed blue line represents the center of the image. The blue circle denotes the target detected by the segmentation algorithm. Video 1 contains a real-time display of these results, including additional photoacoustic images acquired between the before and after still frames (Video 1, MP4, 8.34 MB) (b) Probe centering experiment errors.

μJ) are displayed in Fig. 4-8(a). For the higher laser energy (which is higher than the safety limit of $394.6 \mu\text{J}$), visual servoing with either DAS or GPU-SLSC beamforming successfully accomplished the probe centering task. The left side of Fig. 4-8(a) shows the position of the fiber tip before and after the execution of visual servoing. The segmented target (denoted by the blue circle) is present and constant in both DAS and SLSC images at $645 \mu\text{J}$. The right side of Fig. 4-8(a) shows a corresponding result for the lower laser energy. While visual servoing with DAS generally failed to segment the target due to the low SNR, visual servoing with SLSC beamforming successfully performed the probe centering task.

Probe centering errors measured between desired centering locations and the actual robot positions are displayed in Fig. 4-8(b) for three energies below the safety energy limit and within the range of energies shown in Fig. 4-8(a). These probe centering errors were obtained over a time period of 12 to 15 s after the first intersection of segmented target position with the center of the image. Five error measurements were computed for each energy. The horizontal line inside each box displays median error. The upper and lower edges of each box represent the first and third quartiles of the data set. The vertical lines connected to the boxes show the minimum and maximum values in each data set.

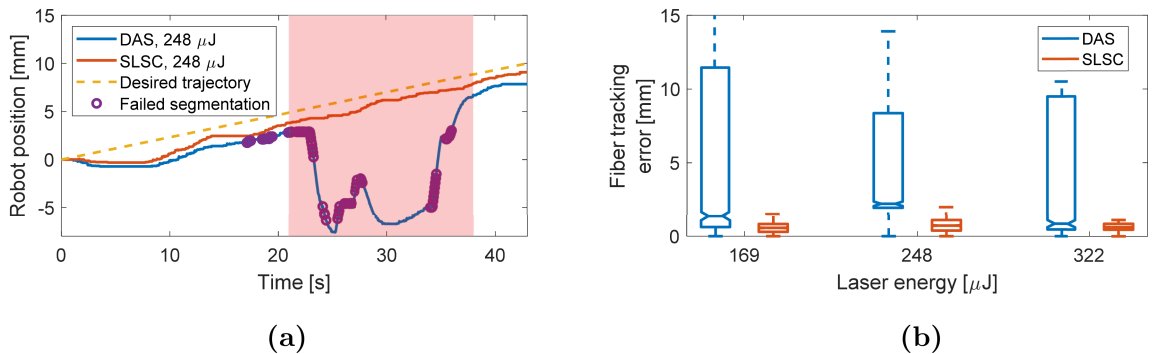


Figure 4-9. Fiber tracking results. (a) Example of robot positions with fiber tracking at $248 \mu\text{J}$. The circles represent time stamps when the visual servoing algorithm failed to segment the photoacoustic signal. (b) Fiber tracking errors at mid-range energies.

With 169 μJ laser energy, the median and interquartile range (IQR) of tracking errors were 1.71 mm and 0.71 mm, respectively, with DAS-based visual servoing and 1.11 mm and 0.39 mm, respectively, with SLSC-based visual servoing. Similarly, with 248 μJ laser energy, there was a higher median tracking error with DAS beamforming (i.e., 1.11 mm) than that obtained with SLSC beamforming (i.e., 0.52 mm). However, SLSC beamforming had a higher IQR of tracking errors (i.e., 0.79 mm) when compared to DAS beamforming (i.e., 0.29 mm) at the same laser energy. With 322 μJ laser energy, the median and IQR of tracking errors were 0.46 mm and 0.05 mm, respectively, with DAS-based visual servoing. These errors were lower than the median and IQR of tracking errors obtained with SLSC beamforming, which were 0.77 mm and 0.47 mm, respectively. Overall, for the three laser energies (i.e., 169 μJ , 248 μJ , and 322 μJ), the median and IQR of tracking errors were 1.10 mm and 0.85 mm, respectively, with DAS and 0.81 mm and 0.68 mm, respectively, with SLSC. For each laser energy in Fig. 4-8(b), the differences between the median probe centering error results with SLSC- and DAS-based visual servoing were statistically significant ($p < 0.01$).

Fig. 4-9 shows results from the fiber tracking experiment. The trajectories of the robot-held ultrasound probe obtained during DAS- and SLSC-based visual servoing are compared to the desired trajectory in Fig. 4-9(a). Ideally, the trajectories generated with visual servoing would be closely related to the desired trajectory performed manually with the translation stage and indicated with the dashed line. Both DAS- and SLSC-based visual servoing followed the fiber displacement during the 0 s to 18 s time interval. After 18 seconds, the noise present in the DAS image contributed to failed segmentations, resulting in a visual servoing failure, which is shown as the circles in Fig. 4-9(a).

When consecutive instances of failed segmentation were recorded over a 1 s time period, the robot performed a search around the current region in the lateral and elevation ultrasound probe directions. This searching algorithm was responsible for

the increased deviation of the segmented target locations from desired locations with DAS-based visual servoing, as observed in the red shaded region of Fig. 4-9(a) (i.e., within the 21 s to 38 s time interval). During this time interval, the median and IQR of tracking errors were 10.64 mm and 7.68 mm, respectively, with DAS-based visual servoing. When excluding this interval, the median and IQR of the difference between actual and desired trajectories were 2.02 mm and 0.41 mm, respectively, with DAS beamforming and 1.17 mm and 0.68 mm, respectively, with SLSC beamforming. Therefore, the real-time SLSC approach produced less deviations from the desired trajectory overall.

Tracking errors measured between the desired locations and the measured robot positions are summarized in Fig. 4-9(b). These errors were computed from visual servoing data obtained between two timestamps. The first timestamp was acquired when both the robot position and the desired location were initialized (i.e., $\vec{p} = \vec{p}_0, t = 0$). The second timestamp was acquired after the fiber was displaced by 10 mm with the translation stage. Generally, tracking errors were larger with DAS compared to SLSC beamforming for each laser energy shown in Fig. 4-9(b). Overall, for the three laser energies (i.e., 169 μJ , 248 μJ , and 322 μJ), the median and IQR of tracking errors were 2.01 mm and 8.97 mm, respectively, with DAS beamforming and 0.64 mm and 0.52 mm, respectively, with SLSC beamforming. For each laser energy, the differences between the median tracking error results with SLSC- and DAS-based visual servoing were statistically significant ($p < 0.01$).

4.3.4 In Vivo Performance

Fig. 4-10(a) shows *in vivo* images created with DAS, CPU-SLSC, and GPU-SLSC beamformers after adding noise resulting in -30 dB channel SNR (i.e., SNR_c in Eq. 4.8). The percentage of failed segmentations measured from 10 frames of photoacoustic data is shown as a function of channel SNR in Fig. 4-10(b), represented

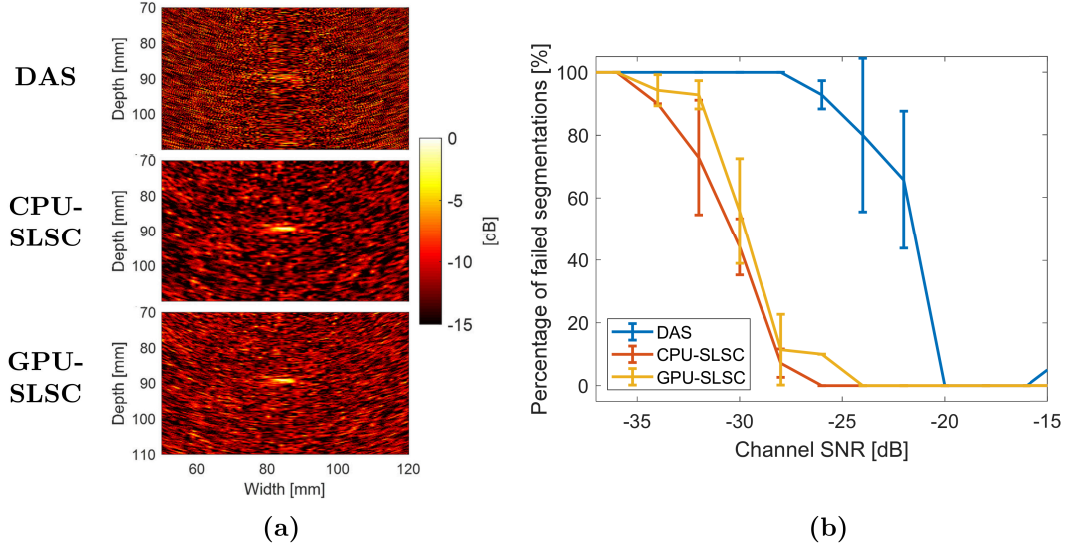


Figure 4-10. (a) Examples of *in vivo* DAS, CPU-SLSC, and GPU-SLSC photoacoustic images, created from the same raw data after adding Gaussian-distributed noise to achieve -30 dB channel SNR. The segmentation algorithm failed on the DAS image and succeeded with the CPU-SLSC and GPU-SLSC images. (b) For each channel SNR, the percentage of failed segmentations is represented as the mean \pm one standard deviation of 10 measurements obtained after varying the amplitude threshold in the segmentation algorithm from 35% to 66% of the maximum amplitude within each photoacoustic image.

as the mean \pm one standard deviation of measurements obtained after varying the amplitude threshold in the segmentation algorithm from 35% to 66% of the maximum amplitude within each photoacoustic image. At -36 dB channel SNR, each beamforming method completely fails to segment the photoacoustic target (i.e., 100% failure). As channel SNR improved, the percentage of failed segmentations was reduced with CPU-SLSC and GPU-SLSC beamforming, measuring an average of 2.5% from -28 dB to -20 dB channel SNR. On the other hand, DAS beamforming resulted in a higher percentage of failed segmentations for the same range of channel SNRs. For channel SNRs greater than -20 dB, the noise levels were not sufficient to affect the segmentation performance of each beamformer, which is consistent with our observations at higher laser energies.

4.4 Discussion

Image-guided interventions often require visualization and tracking of important targets and structures. This requirement is well-suited to photoacoustic-based visual servoing of surgical tool tips. GPU-SLSC beamforming in particular provides three advantages to photoacoustic-based visual servoing in comparison to DAS and offline SLSC implementations. The first advantage is the reduction in computation times when compared with CPU-SLSC with minimal alterations to the precision of the coherence value estimations, as qualitatively observed in Fig. 4-7(a). The SNR difference between CPU-SLSC imaging and GPU-SLSC imaging is 1.14 ± 3.99 . Although minimal and not statistically significant, this difference is likely due to the single-precision libraries and linear interpolation in the GPU texture memory. Specifically, the GPU-SLSC algorithm utilizes CUDA embedded functions such as the inverse square root, power, and cosine functions. These single precision functions have a unit-in-the-last-place error of 9, 2, and 2, respectively [70], which decreases the precision of the coherence factors and the overall SLSC value. In addition, a GPU-SLSC imaging frame rate of 41.2 Hz, as reported in Section 4.3.2, allows visual servoing without overlapping subsequent acquisitions controlled by the laser trigger, which had a pulse repetition frequency of 10 Hz. After the SLSC image generation, a wait time of approximately 75 ms was required until the next trigger event, because raw data were acquired every 100 ms and GPU-SLSC generated an image every 24.3 ms.

The second advantage of GPU-SLSC beamforming is the improvement of photoacoustic signals at low energy levels, as demonstrated in Fig. 4-7(b). We focus on low-energy lasers for two reasons. First, low laser energies enable miniaturization of the light delivery system. Second, low laser energies ensure minimal risk of damage to tissues in cases where no safety limits currently exist (which is true for most tissues with the exception of skin and eyes [66]). Although we can increase the laser energy,

the presence of artifacts may be misinterpreted by the visual servoing algorithm if the energy is too high, and in other cases within the safety limit, a smaller increase in laser energy does not affect the GPU-SLSC visual servoing performance, as shown in Figs. 4-8(b) and 4-9(b). From this perspective, the focus of our work is targeted toward clinical applications that will require miniaturized systems with reduced risk of exposure to patients. With the experimental setup shown in Fig. 4-3, the laser safety limit for skin is 394.6 μJ , as determined by the diameter of the optical fiber and wavelength of excitation. An optical fiber with a smaller diameter would produce a lower safety limit at this same excitation wavelength (e.g., 142 μJ for a 0.6 mm-diameter optical fiber). Because GPU-SLSC can successfully recover signals obtained with energies as low as 118 μJ (particularly in cases where DAS beamforming failed), our results indicate that GPU-SLSC will be beneficial in smaller and more portable light delivery systems [53], which is a necessary design requirement for effective visual servoing in the operating room.

The third advantage of GPU-SLSC beamforming is the robustness of SLSC-based visual servoing to segmenting and tracking signals at low (e.g., 110 μJ) and mid-range (e.g., 169 to 322 μJ) laser energies, when compared to photoacoustic-based visual servoing with DAS images. This robustness is particularly advantageous when considering that the visual servoing algorithm initiates a search process after a series of unsuccessful segmentation events are recorded [6]. The probe centering and fiber tracking results (Figs. 4-8(a) and 4-9, respectively) indicate that the search process would be triggered more often with DAS than SLSC (see example provided in Video 1). This search motion would hinder effective tool tracking during surgery and add delays to the overall surgical or interventional procedure. GPU-SLSC beamforming has the potential to avoid these interruptions, which is additionally supported by the *in vivo* results presented in Fig. 4-10.

One detail that does not support these three advantages of SLSC is the similar probe

centering errors obtained at the mid-range energies shown in Fig. 4-8(b). However, DAS beamforming produced considerably higher fiber tracking errors than SLSC beamforming (i.e., the difference between the IQR of tracking errors reported in Fig. 4-9(b) was 8.45 mm). Based on the combined outcome of these two experiments and the minimal overall percentage of failed segmentations with GPU-SLSC, GPU-SLSC is preferred over DAS when considering clinical photoacoustic-based visual servoing applications utilizing energies within existing laser safety limits.

The computation times reported in Fig. 4-4 suggest that real-time GPU-SLSC imaging is achievable for most clinical scenarios where the photoacoustic source is located as deep as 10 cm, with a laser PRP of 100 ms or higher. Fig. 4-4 indicates that image depth d has the largest effect on the processing time (of the three parameters varied), as frame rate decreases by a factor of approximately 2 when increasing d from 5 cm to 15 cm. While the feasibility of real-time imaging modalities depends on the amount of data to process, an imaging depth of 15 cm is uncommon for most interventional applications of photoacoustic imaging, including cardiac [6], abdominal [71], intravascular [72], hysterectomy [73], and spinal fusion surgery [52, 74] applications, suggesting that image depths as large as 15 cm is an unlikely concern for the real-time feasibility of GPU-SLSC in a majority of these cases. Nonetheless, the presented results at this 15 cm depth provide us with a worst-case scenario for system speed with internal light delivery and external ultrasound probe placement in these interventional applications.

The frame rate of 41.2 Hz (i.e., processing time of 24.3 ms) obtained with GPU-SLSC is either similar to or better than that obtained with GPU implementations of other advanced beamforming techniques. For example, real-time, 4 cm-deep DAS, delay-multiply-and-sum (DMAS), DAS+CF, or DMAS+CF imaging was achieved with processing times of 7.5, 7.6, 11.1, or 11.3 ms, respectively (with the exclusion of memory transfer times between the GPU and CPU)[44]. A variation of DMAS,

namely the multiple delay and sum with enveloping beamformer, was implemented on a Quadro P5000 GPU to reconstruct 512×512 images in 41.62 ms [75]. Another version of DMAS, proposed by Miri *et al.* [76], reported a 12 ms processing time for images of size 256×256 pixels. In addition to these beamformers, the reported GPU-SLSC frame rate is better than that achieved with a parallel backprojection algorithm reporting 17 Hz frame rates when reconstructing 1024×512 duplex images [77]. A more detailed comparison of processing speeds requires standardization of factors such as input data size, output image size, memory transfer evaluation, GPU hardware, and overhead.

An additional observation is that photoacoustic targets reconstructed with SLSC beamforming produced signals with different shapes when compared to targets reconstructed with DAS beamforming, as seen in Fig. 4-8(a). This change in signal morphology is caused by the degradation in axial resolution with the chosen axial kernel size of $k = 11$ and the improved lateral resolution with the chosen $M = 25$. Although an axial kernel size of $k = 11$ was chosen to maximize the gCNR value between signal and background regions, the associated axial resolution degradation does not significantly affect the performance of our visual servoing algorithm, which tracks the displacement of the optical fiber in the lateral dimension.

One study limitation is that the the number of scanlines and high pass filter coefficients were not varied nor evaluated. However, we determined that a line density of 1 (i.e., 128 scanlines) was sufficient to visualize an optical fiber fiber with a core diameter of 1 mm, considering that the resolution in the lateral dimension is approximately half the element pitch (i.e., 0.15 mm). Although an increased number of high pass filter coefficient ensures the removal of DC components without compromising the frequency spectrum of the radiofrequency signals of interest, in practice, the radiofrequency signals are band-pass filtered to the operation range of the ultrasound probe before being stored in memory. Therefore, increasing the high pass

filter coefficient is not expected to affect the overall quality of the SLSC images.

Future work will advance implementation of GPU-SLSC beamforming for clinical visual servoing applications with the primary goal of reducing the risk of ionizing radiation exposure by substituting fluoroscopy usage with the proposed approach [6, 78]. For example, the *in vivo* setup described in our previous publication[6] implemented visual servoing with DAS beamforming to guide a cardiac catheter tip using a fluence of 365.5 mJ/cm², which is higher than the 25.2 mJ/cm² safety limit for skin at the same 750 nm wavelength [66]. SLSC-based visual servoing has the potential to provide similar visual servoing performance to higher energy DAS results when using energies below existing safety limits, as indicated by the results in Fig. 4-10. In addition, the SNR enhancement provided with GPU-SLSC is expected to be beneficial in other applications with high noise and high acoustic scattering or attenuation, such as navigating inside bony anatomy during spinal fusion surgeries [52] or endonasal transphenoidal surgeries [17], as well as navigating within liver tissue during surgeries, biopsies, or radiofrequency ablations [71, 79].

4.5 Conclusion

This paper presents the first known implementation of real-time SLSC beamforming for photoacoustic imaging, which was enabled by GPUs and parallel processing techniques. When selecting optimal beamforming parameters for visual servoing tasks, a factor of 348 speedup was achieved when compared to CPU-SLSC implementations. This speedup allows real-time visualization of photoacoustic images for any laser with pulse repetition frequencies up to 41.2 Hz. *Ex vivo* results with bovine tissue and *in vivo* results from cardiac data demonstrate that GPU-SLSC imaging has the potential to enable visualization of photoacoustic signals obtained with low laser energies during photoacoustic-guided interventions, which is promising for the miniaturization of lasers to perform photoacoustic-based visual servoing in the operating room or

interventional suite. In addition, GPU-SLSC imaging outperformed DAS imaging when jointly comparing probe centering, image segmentation, and fiber tracking tasks in the presence of low channel SNRs and when using laser energies that meet existing laser safety requirements.

4.6 Acknowledgements

This work was supported by the National Science Foundation CAREER Award ECCS-1751522 and NIH R00-EB018994. The authors acknowledge Dongwoon Hyun for sharing SLSC GPU example code specific to the Verasonics ultrasound imaging system and NVIDIA Corporation for the donation of the Titan Xp GPU used for this research.

References

- [1] E. A. Gonzalez and M. A. L. Bell, “GPU implementation of photoacoustic short-lag spatial coherence imaging for improved image-guided interventions,” *Journal of Biomedical Optics*, vol. 25, no. 7, pp. 1–19, 2020.
- [2] B. Espiau, F. Chaumette, and P. Rives, “A new approach to visual servoing in robotics,” *IEEE Transactions on Robotics and Automation*, vol. 8, no. 3, pp. 313–326, 1992.
- [3] G.-Q. Wei, K. Arbter, and G. Hirzinger, “Real-time visual servoing for laparoscopic surgery. controlling robot motion with color image segmentation,” *IEEE Engineering in Medicine and Biology Magazine*, vol. 16, no. 1, pp. 40–45, 1997.
- [4] P. Abolmaesumi, S. E. Salcudean, W.-H. Zhu, M. R. Sirouspour, and S. P. DiMaio, “Image-guided control of a robot for medical ultrasound,” *IEEE Transactions on Robotics and Automation*, vol. 18, no. 1, pp. 11–23, 2002.
- [5] M. A. L. Bell and J. Shubert, “Photoacoustic-based visual servoing of a needle tip,” *Scientific Reports*, vol. 8, no. 1, p. 15 519, 2018.
- [6] M. Graham, F. Assis, D. Allman, A. Wiacek, E. Gonzalez, M. Gubbi, J. Dong, H. Hou, S. Beck, J. Chrispin, and M. A. L. Bell, “In vivo demonstration of photoacoustic image guidance and robotic visual servoing for cardiac catheter-based interventions,” *IEEE Transactions on Medical Imaging*, vol. 39, no. 4, pp. 1015–1029, 2020.
- [7] P. Beard, “Biomedical photoacoustic imaging,” *Interface Focus*, vol. 1, no. 4, pp. 602–631, 2011.
- [8] M. Xu and L. V. Wang, “Photoacoustic imaging in biomedicine,” *Review of Scientific Instruments*, vol. 77, no. 4, p. 041 101, 2006.
- [9] R. Bouchard, O. Sahin, and S. Emelianov, “Ultrasound-guided photoacoustic imaging: Current state and future development,” *IEEE Transactions on Ultrasonics, Ferroelectrics, and Frequency Control*, vol. 61, no. 3, pp. 450–466, 2014.
- [10] M. A. L. Bell, N. P. Kuo, D. Y. Song, J. U. Kang, and E. M. Boctor, “In vivo visualization of prostate brachytherapy seeds with photoacoustic imaging,” *Journal of Biomedical Optics*, vol. 19, no. 12, p. 126 011, 2014.
- [11] K. L. Bell, T. Harrison, N. Usmani, and R. J. Zemp, “Integrated transrectal probe for translational ultrasound-photoacoustic imaging,” in *Photons Plus Ultrasound: Imaging and Sensing 2016*, International Society for Optics and Photonics, vol. 9708, 2016, 97080A.
- [12] A. B. Karpouk, B. Wang, and S. Y. Emelianov, “Development of a catheter for combined intravascular ultrasound and photoacoustic imaging,” *Review of Scientific Instruments*, vol. 81, no. 1, p. 014 901, 2010.
- [13] W. Xia, E. Maneas, D. I. Nikitichev, C. A. Mosse, G. S. Dos Santos, T. Vercauteren, A. L. David, J. Deprest, S. Ourselin, P. C. Beard, and A. E. Desjardins, “Interventional photoacoustic imaging of the human placenta with ultrasonic tracking for minimally invasive fetal surgeries,” in *International Conference on Medical Image Computing and Computer-Assisted Intervention*, Springer, 2015, pp. 371–378.

- [14] A. Horiguchi, K. Tsujita, K. Irisawa, T. Kasamatsu, K. Hirota, M. Kawaguchi, M. Shinchu, K. Ito, T. Asano, H. Shinmoto, H. Tsuda, and M. Ishihara, "A pilot study of photoacoustic imaging system for improved real-time visualization of neurovascular bundle during radical prostatectomy," *The Prostate*, vol. 76, no. 3, pp. 307–315, 2016.
- [15] M. A. L. Bell, A. K. Ostrowski, P. Kazanzides, and E. Boctor, "Feasibility of transcranial photoacoustic imaging for interventional guidance of endonasal surgeries," in *Photons Plus Ultrasound: Imaging and Sensing 2014*, International Society for Optics and Photonics, vol. 8943, 2014, p. 894307.
- [16] M. A. L. Bell, A. K. Ostrowski, K. Li, P. Kazanzides, and E. M. Boctor, "Localization of transcranial targets for photoacoustic-guided endonasal surgeries," *Photoacoustics*, vol. 3, no. 2, pp. 78–87, 2015.
- [17] M. T. Graham, J. Huang, F. Creighton, and M. A. L. Bell, "Simulations and human cadaver head studies to identify optimal acoustic receiver locations for minimally invasive photoacoustic-guided neurosurgery," *Photoacoustics*, p. 100183, 2020.
- [18] B. Eddins and M. A. L. Bell, "Design of a multifiber light delivery system for photoacoustic-guided surgery," *Journal of Biomedical Optics*, vol. 22, no. 4, p. 041011, 2017.
- [19] J. Su, A. Karpouk, B. Wang, and S. Emelianov, "Photoacoustic imaging of clinical metal needles in tissue," *Journal of Biomedical Optics*, vol. 15, no. 2, pp. 021309–021309, 2010.
- [20] D. Piras, C. Grijsen, P. Schutte, W. Steenbergen, and S. Manohar, "Photoacoustic needle: Minimally invasive guidance to biopsy," *Journal of Biomedical Optics*, vol. 18, no. 7, p. 070502, 2013.
- [21] M. K. A. Singh, V. Parameshwarappa, E. Hendriksen, W. Steenbergen, and S. Manohar, "Photoacoustic-guided focused ultrasound for accurate visualization of brachytherapy seeds with the photoacoustic needle," *Journal of Biomedical Optics*, vol. 21, no. 12, p. 120501, 2016.
- [22] Y. Zhang, Y. Cao, and J.-X. Cheng, "High-resolution photoacoustic endoscope through beam self-cleaning in a graded index fiber," *Optics Letters*, vol. 44, no. 15, pp. 3841–3844, 2019.
- [23] Y. Liang, L. Jin, L. Wang, X. Bai, L. Cheng, and B.-O. Guan, "Fiber-laser-based ultrasound sensor for photoacoustic imaging," *Scientific Reports*, vol. 7, p. 40849, 2017.
- [24] J. Kim, E.-Y. Park, B. Park, W. Choi, K. J. Lee, and C. Kim, "Towards clinical photoacoustic and ultrasound imaging: Probe improvement and real-time graphical user interface," *Experimental Biology and Medicine*, p. 1535370219889968, 2020.
- [25] H. Luo, G. Yang, and Q. Zhu, "Fiber endface illumination diffuser for endo-cavity photoacoustic imaging," *Optics Letters*, vol. 45, no. 3, pp. 632–635, 2020.
- [26] J. A. Smith, J. Jivraj, R. Wong, and V. Yang, "30 years of neurosurgical robots: Review and trends for manipulators and associated navigational systems," *Annals of Biomedical Engineering*, vol. 44, no. 4, pp. 836–846, 2016.

- [27] M. Azizian, M. Khoshnam, N. Najmaei, and R. V. Patel, “Visual servoing in medical robotics: A survey. part i: Endoscopic and direct vision imaging—techniques and applications,” *The International Journal of Medical Robotics and Computer Assisted Surgery*, vol. 10, no. 3, pp. 263–274, 2014.
- [28] M. Azizian, N. Najmaei, M. Khoshnam, and R. Patel, “Visual servoing in medical robotics: A survey. part ii: Tomographic imaging modalities—techniques and applications,” *The International Journal of Medical Robotics and Computer Assisted Surgery*, vol. 11, no. 1, pp. 67–79, 2015.
- [29] O. Zettinig, B. Frisch, S. Virga, M. Esposito, A. Rienmüller, B. Meyer, C. Hennersperger, Y.-M. Ryang, and N. Navab, “3d ultrasound registration-based visual servoing for neurosurgical navigation,” *International Journal of Computer Assisted Radiology and Surgery*, vol. 12, no. 9, pp. 1607–1619, 2017.
- [30] N. Gandhi, M. Allard, S. Kim, P. Kazanzides, and M. A. L. Bell, “Photoacoustic-based approach to surgical guidance performed with and without a da vinci robot,” *Journal of Biomedical Optics*, vol. 22, no. 12, p. 121606, 2017.
- [31] A. Rosenthal, V. Ntziachristos, and D. Razansky, “Acoustic inversion in optoacoustic tomography: A review,” *Current Medical Imaging*, vol. 9, no. 4, pp. 318–336, 2013.
- [32] J. Kang, H. K. Zhang, A. Rahmim, D. F. Wong, J. U. Kang, and E. M. Boctor, “Toward high-speed transcranial photoacoustic imaging using compact near-infrared pulsed LED illumination system,” in *Photons Plus Ultrasound: Imaging and Sensing 2017*, International Society for Optics and Photonics, vol. 10064, 2017, 100643B.
- [33] K. Daoudi, P. Van Den Berg, O. Rabot, A. Kohl, S. Tisserand, P. Brands, and W. Steenbergen, “Handheld probe integrating laser diode and ultrasound transducer array for ultrasound/photoacoustic dual modality imaging,” *Optics Express*, vol. 22, no. 21, pp. 26365–26374, 2014.
- [34] S. Huber, M. Wagner, M. Medl, and H. Czembirek, “Real-time spatial compound imaging in breast ultrasound,” *Ultrasound in Medicine & Biology*, vol. 28, no. 2, pp. 155–163, 2002.
- [35] A. Taruttis, E. Herzog, D. Razansky, and V. Ntziachristos, “Real-time imaging of cardiovascular dynamics and circulating gold nanorods with multispectral optoacoustic tomography,” *Optics Express*, vol. 18, no. 19, pp. 19592–19602, 2010.
- [36] M. Mozaffarzadeh, A. Mahloojifar, M. Orooji, K. Kratkiewicz, S. Adabi, and M. Nasiriavanaki, “Linear-array photoacoustic imaging using minimum variance-based delay multiply and sum adaptive beamforming algorithm,” *Journal of Biomedical Optics*, vol. 23, no. 2, p. 026002, 2018.
- [37] J.-F. Synnevag, A. Austeng, and S. Holm, “Benefits of minimum-variance beamforming in medical ultrasound imaging,” *IEEE Transactions on Ultrasonics, Ferroelectrics, and Frequency Control*, vol. 56, no. 9, pp. 1868–1879, 2009.
- [38] S. Park, A. B. Karpouk, S. R. Aglyamov, and S. Y. Emelianov, “Adaptive beamforming for photoacoustic imaging,” *Optics Letters*, vol. 33, no. 12, pp. 1291–1293, 2008.
- [39] J. Kortbek, J. A. Jensen, and K. L. Gammelmark, “Synthetic aperture sequential beamforming,” in *2008 IEEE Ultrasonics Symposium*, IEEE, 2008, pp. 966–969.

- [40] Z. Deng, X. Yang, H. Gong, and Q. Luo, "Adaptive synthetic-aperture focusing technique for microvasculature imaging using photoacoustic microscopy," *Optics Express*, vol. 20, no. 7, pp. 7555–7563, 2012.
- [41] J. Park, S. Jeon, J. Meng, L. Song, J. S. Lee, and C. Kim, "Delay-multiply-and-sum-based synthetic aperture focusing in photoacoustic microscopy," *Journal of Biomedical Optics*, vol. 21, no. 3, p. 036 010, 2016.
- [42] H. K. Zhang, M. A. L. Bell, X. Guo, H. J. Kang, and E. M. Boctor, "Synthetic-aperture based photoacoustic re-beamforming (SPARE) approach using beamformed ultrasound data," *Biomedical Optics Express*, vol. 7, no. 8, pp. 3056–3068, 2016.
- [43] M. Mozaffarzadeh, Y. Yan, M. Mehrmohammadi, and B. Makkiabadi, "Enhanced linear-array photoacoustic beamforming using modified coherence factor," *Journal of Biomedical Optics*, vol. 23, no. 2, p. 026 005, 2018.
- [44] S. Jeon, E.-Y. Park, W. Choi, R. Managuli, K. jong Lee, and C. Kim, "Real-time delay-multiply-and-sum beamforming with coherence factor for in vivo clinical photoacoustic imaging of humans," *Photoacoustics*, vol. 15, p. 100 136, 2019.
- [45] C.-K. Liao, M.-L. Li, and P.-C. Li, "Optoacoustic imaging with synthetic aperture focusing and coherence weighting," *Optics Letters*, vol. 29, no. 21, pp. 2506–2508, 2004.
- [46] M. A. Lediju, G. E. Trahey, B. C. Byram, and J. J. Dahl, "Short-lag spatial coherence of backscattered echoes: Imaging characteristics," *IEEE Transactions on Ultrasonics, Ferroelectrics, and Frequency Control*, vol. 58, no. 7, 2011.
- [47] M. A. L. Bell, N. Kuo, D. Y. Song, and E. M. Boctor, "Short-lag spatial coherence beamforming of photoacoustic images for enhanced visualization of prostate brachytherapy seeds," *Biomedical Optics Express*, vol. 4, no. 10, pp. 1964–1977, 2013.
- [48] B. Pourebrahimi, S. Yoon, D. Dopsa, and M. C. Kolios, "Improving the quality of photoacoustic images using the short-lag spatial coherence imaging technique," in *Photons Plus Ultrasound: Imaging and Sensing 2013*, International Society for Optics and Photonics, vol. 8581, 2013, 85813Y.
- [49] M. T. Graham and M. A. L. Bell, "Photoacoustic spatial coherence theory and applications to coherence-based image contrast and resolution," *IEEE Transactions on Ultrasonics, Ferroelectrics, and Frequency Control*, 2020.
- [50] M. A. L. Bell, X. Guo, D. Y. Song, and E. M. Boctor, "Transurethral light delivery for prostate photoacoustic imaging," *Journal of Biomedical Optics*, vol. 20, no. 3, p. 036 002, 2015.
- [51] J. J. Dahl, D. Hyun, Y. Li, M. Jakovljevic, M. A. Bell, W. J. Long, N. Bottenus, V. Kakkad, and G. E. Trahey, "Coherence beamforming and its applications to the difficult-to-image patient," in *2017 IEEE International Ultrasonics Symposium (IUS)*, IEEE, 2017, pp. 1–10.
- [52] E. Gonzalez, A. Wiacek, and M. A. L. Bell, "Visualization of custom drill bit tips in a human vertebra for photoacoustic-guided spinal fusion surgeries," in *Photons Plus Ultrasound: Imaging and Sensing 2019*, International Society for Optics and Photonics, vol. 10878, 2019, p. 108785M.
- [53] M. A. L. Bell, X. Guo, H. J. Kang, and E. Boctor, "Improved contrast in laser-diode-based photoacoustic images with short-lag spatial coherence beamforming," in *2014 IEEE International Ultrasonics Symposium*, IEEE, 2014, pp. 37–40.

- [54] T. J. Allen and P. C. Beard, “Pulsed near-infrared laser diode excitation system for biomedical photoacoustic imaging,” *Optics Letters*, vol. 31, no. 23, pp. 3462–3464, 2006.
- [55] R. G. Kolkman, W. Steenbergen, and T. G. van Leeuwen, “In vivo photoacoustic imaging of blood vessels with a pulsed laser diode,” *Lasers in Medical Science*, vol. 21, no. 3, pp. 134–139, 2006.
- [56] E. Mackle, E. Maneas, W. Xia, S. West, and A. Desjardins, “LED-Based Photoacoustic Imaging for Guiding Peripheral Minimally Invasive Procedures,” in *LED-Based Photoacoustic Imaging*, Springer, 2020, pp. 321–334.
- [57] E. Gonzalez, M. R. Gubbi, and M. A. L. Bell, “GPU implementation of coherence-based photoacoustic beamforming for autonomous visual servoing,” in *2019 IEEE International Ultrasonics Symposium (IUS)*, IEEE, 2019, pp. 24–27.
- [58] E. Gonzalez and M. A. L. Bell, “A GPU approach to real-time coherence-based photoacoustic imaging and its application to photoacoustic visual servoing,” in *Photons Plus Ultrasound: Imaging and Sensing 2020*, International Society for Optics and Photonics, vol. 11240, 2020, p. 1 124 054.
- [59] D. Hyun, A. L. C. Crowley, M. LeFevre, J. Cleve, J. Rosenberg, and J. J. Dahl, “Improved visualization in difficult-to-image stress echocardiography patients using real-time harmonic spatial coherence imaging,” *IEEE Transactions on Ultrasonics, Ferroelectrics, and Frequency Control*, vol. 66, no. 3, pp. 433–441, 2018.
- [60] D. Hyun, A. L. C. Crowley, and J. J. Dahl, “Efficient strategies for estimating the spatial coherence of backscatter,” *IEEE Transactions on Ultrasonics, Ferroelectrics, and Frequency Control*, vol. 64, no. 3, pp. 500–513, 2016.
- [61] A. A. Nair, T. D. Tran, and M. A. L. Bell, “Robust short-lag spatial coherence imaging,” *IEEE Transactions on Ultrasonics, Ferroelectrics, and Frequency Control*, vol. 65, no. 3, pp. 366–377, 2017.
- [62] S. Cook, *CUDA programming: a developer’s guide to parallel computing with GPUs*. Newnes, 2012.
- [63] A. Rodriguez-Molares, O. M. Hoel Rindal, J. D’hooge, S. Måsøy, A. Austeng, and H. Torp, “The generalized contrast-to-noise ratio,” in *2018 IEEE International Ultrasonics Symposium*, Oct. 2018, pp. 1–4.
- [64] A. Rodriguez-Molares, O. M. H. Rindal, J. D’hooge, S.-E. Måsøy, A. Austeng, M. A. L. Bell, and H. Torp, “The generalized contrast-to-noise ratio: A formal definition for lesion detectability,” *IEEE Transactions on Ultrasonics, Ferroelectrics, and Frequency Control*, vol. 67, no. 4, pp. 745–759, 2019.
- [65] K. M. Kempinski, M. T. Graham, M. R. Gubbi, T. Palmer, and M. A. L. Bell, “Application of the generalized contrast-to-noise ratio to assess photoacoustic image quality,” *Biomedical Optics Express*, vol. 11, no. 7, pp. 3684–3698, 2020.
- [66] American National Standards Institute (ANSI), *American national standard for safe use of lasers, ANSI Z136.1-2014*. Laser Institute of America, 2014.
- [67] M. Kraska-Miller, *Nonparametric statistics for social and behavioral sciences*. CRC Press, 2013.

- [68] M. A. L. Bell, D. Y. Song, and E. M. Boctor, “Coherence-based photoacoustic imaging of brachytherapy seeds implanted in a canine prostate,” in *Medical Imaging 2014: Ultrasonic Imaging and Tomography*, International Society for Optics and Photonics, vol. 9040, 2014, 90400Q.
- [69] M. A. L. Bell, J. J. Dahl, and G. E. Trahey, “Resolution and brightness characteristics of short-lag spatial coherence (SLSC) images,” *IEEE Transactions on Ultrasonics, Ferroelectrics, and Frequency Control*, vol. 62, no. 7, pp. 1265–1276, 2015.
- [70] NVIDIA, *CUDA C Programming Guide v8. 0*, <https://docs.nvidia.com/cuda/cuda-c-programming-guide/index.html#mathematical-functions-appendix>, 2017.
- [71] K. M. Kempinski, A. Wiacek, M. Graham, E. González, B. Goodson, D. Allman, J. Palmer, H. Hou, S. Beck, J. He, and M. A. L. Bell, “In vivo photoacoustic imaging of major blood vessels in the pancreas and liver during surgery,” *Journal of Biomedical Optics*, vol. 24, no. 12, p. 121 905, 2019.
- [72] K. Jansen, M. Wu, A. F. van der Steen, and G. van Soest, “Photoacoustic imaging of human coronary atherosclerosis in two spectral bands,” *Photoacoustics*, vol. 2, no. 1, pp. 12–20, 2014.
- [73] A. Wiacek, K. C. Wang, and M. A. L. Bell, “Techniques to distinguish the ureter from the uterine artery in photoacoustic-guided hysterectomies,” in *Photons Plus Ultrasound: Imaging and Sensing 2019*, International Society for Optics and Photonics, vol. 10878, 2019, 108785K.
- [74] J. Shubert and M. A. L. Bell, “Photoacoustic imaging of a human vertebra: Implications for guiding spinal fusion surgeries,” *Physics in Medicine & Biology*, vol. 63, no. 14, p. 144 001, 2018.
- [75] X. Ma, C. Peng, J. Yuan, Q. Cheng, G. Xu, X. Wang, and P. L. Carson, “Multiple delay and sum with enveloping beamforming algorithm for photoacoustic imaging,” *IEEE Transactions on Medical Imaging*, 2019.
- [76] S. R. Miri Rostami, M. Mozaffarzadeh, M. Ghaffari-Miab, A. Hariri, and J. Jokerst, “GPU-accelerated double-stage delay-multiply-and-sum algorithm for fast photoacoustic tomography using LED excitation and linear arrays,” *Ultrasonic Imaging*, vol. 41, no. 5, pp. 301–316, 2019.
- [77] J. Yuan, G. Xu, Y. Yu, Y. Zhou, P. L. Carson, X. Wang, and X. Liu, “Real-time photoacoustic and ultrasound dual-modality imaging system facilitated with graphics processing unit and code parallel optimization,” *Journal of Biomedical Optics*, vol. 18, no. 8, p. 086 001, 2013.
- [78] M. T. Graham, F. Assis, D. Allman, A. Wiacek, E. Gonzalez, M. R. Gubbi, J. Dong, H. Hou, S. Beck, J. Chrispin, and M. Bell, “Photoacoustic image guidance and robotic visual servoing to mitigate fluoroscopy during cardiac catheter interventions,” in *Advanced Biomedical and Clinical Diagnostic and Surgical Guidance Systems XVIII*, International Society for Optics and Photonics, vol. 11229, 2020, 112291E.
- [79] K. J. Francis and S. Manohar, “Photoacoustic imaging in percutaneous radiofrequency ablation: Device guidance and ablation visualization,” *Physics in Medicine & Biology*, vol. 64, no. 18, p. 184 001, 2019.

Chapter 5

Acoustic Frequency-Based Identification of Photoacoustic Surgical Biomarkers

The work presented in this chapter was published in the following manuscript:
E. A. Gonzalez, C. A. Graham, and M. A. Lediju Bell, “Acoustic frequency-based approach for identification of photoacoustic surgical biomarkers,” *Frontiers in Photonics*, vol. 2, 2021. DOI: [10.3389/fphot.2021.716656](https://doi.org/10.3389/fphot.2021.716656)

5.1 Introduction

In photoacoustic imaging, spectral unmixing techniques [2] are often used to isolate signal origins in the fields of oxymetry [3–5], reporter genes [6, 7], and molecular details [8]. Clinical applications include detection of tumors [9] and discriminating among critical chromophores (e.g., blood, contrast agents, lipids) during surgical interventions [10].

Existing spectral unmixing techniques generally consist of generating an overdetermined system of equations (i.e., more equations than variables) from the signal response of each chromophore at different laser wavelengths, which can then be solved with an optimization technique based on the known optical absorption coefficient for each chromophore at each wavelength. For example, Xia *et al.* [11] used a pseudo

inverse approach to differentiate photoacoustic responses originating from water, blood, and lipids. Ding *et al.* [12] investigated the effect of alternative versions with non-negativity constraints to determine the concentration levels of contrast agent injected in *in vivo* mice. More recently, Grasso *et al.* [13] proposed an iterative approach to discriminate blood oxygenation levels by solving the system of equations with a non-negative matrix factorization, which compensates for the ill-conditioned invertibility of the absorption coefficient matrix.

Despite their effectiveness, these spectral unmixing techniques are typically not feasible for most real-time applications because of the lengthy acquisition times associated with transmitting multiple laser wavelengths to achieve a single estimate. Traditional spectral unmixing techniques also do not typically consider differences in acoustic spectra, which has the potential to provide additional information for differentiation between biomarkers or different soft tissues.

An alternative to optimization techniques is to consider an analysis of the acoustic spectra using spectral parameters. Initially, spectral parameters obtained from photoacoustic signals were used for characterization of tissues. For example, Kumon *et al.* [14] conducted an *in vivo* study to detect prostate adenocarcinomas using the intercept, slope, and mid-band fit of the frequency response of photoacoustic RF signals, where the use of mid-band fit resulted in statistically significant differentiation between pathological and healthy tissue ($p < 0.01$). Similarly, Strohm *et al.* [15] used both the slope of a linear fit and the spectral peak to discriminate between concentrations of red blood cells. Later, Wang *et al.* [16] used the slope parameter to accurately differentiate ($p < 0.01$) the photoacoustic signals from particles of different diameters in phantom experiments. However, by reducing the dimensionality of the feature space, spectral parameter methods provide a limited snapshot of frequency characteristics. In addition, these methods use a calibration stage from a reference spectra whose source varies among studies (e.g., hair fibers [14], stainless steel blocks

[17], gold-films [15], and black-dyed polymer micro-spheres [16]), which limits the repeatability of classification performance for *in vivo* applications.

In contrast to spectral unmixing methods, two distinct approaches (i.e., F-mode imaging [18] and a method proposed by Cao *et al.* [17]) utilize the complete acoustic spectra for differentiation of photoacoustic targets. F-mode imaging [18] consists of dividing the spectra with filter banks and displaying a series of images of a specific frequency content, which are later combined with a label-free photoacoustic microscopy (PAM) map to selectively enhance the visualization of organelles. The method proposed by Cao *et al.* [17] uses the acoustic spectra filtered with the frequency response of the ultrasound transducer to perform k-means clustering of photoacoustic signals originating from two different photoacoustic-sensitive materials. These two approaches share two limitations. First, in contrast to spectral unmixing techniques, labelled regions for each desired chromophore are required. Second, these labelled regions rely on *a priori* information about the location of materials to be differentiated. These limitations are not ideal for image guidance during surgical interventions and reduce overall classification performance.

To overcome these challenges with traditional spectral unmixing [11, 13], F-mode [18], and k-means clustering [17], we propose a novel, more general acoustic frequency-based analysis method to discriminate photoacoustic responses from different materials. The proposed method does not depend on a reference spectrum (as opposed to k-means clustering [17]). In addition, the proposed method applies a classification framework using training and testing sets containing known photoacoustic-sensitive materials (i.e., no *a priori* signal location information is required, unlike F-mode [18] and traditional spectral unmixing techniques [11, 13]). We hypothesize that our proposed method, which relies on an analysis of the acoustic frequency response from a single- or dual-wavelength emission, is sufficient to differentiate biomarkers and has the potential to increase possible frame rates for real-time implementation in the

operating room.

To test our hypothesis, a frequency analysis was applied to the received photoacoustic signals from two chromophores – blood and methylene blue. The necessity to differentiate these two chromophores is motivated by recently proposed photoacoustic-guided hysterectomy techniques that require differentiation of uterine arteries from ureters containing methylene blue [19]. Although the focus of this chapter is the distinction of these two chromophores, the proposed photoacoustic differentiation is applicable to other chromophores of interest during a surgical procedure.

The remainder of this chapter is organized as follows. Section 5.2 details acquisition, segmentation, and classification methods to identify photoacoustic signals originating from either methylene blue or blood, followed by summaries of existing methods used to benchmark the performance of our approach on the same datasets. Section 5.3 presents the quantitative and qualitative comparison of the classification performance between the proposed and the existing methods. Section 5.4 discusses insights from these results and Section 5.5 summarizes our conclusions.

5.2 Method

5.2.1 Experimental setup

We designed a phantom that mimics the clinical setup of photoacoustic catheter-based interventions, where an optical fiber is attached to a cardiac catheter as it is being inserted through a major vein [20]. Another possibility is that a contrast agent may be injected into this vein through the same catheter. Based on these details, Fig. 5-1 shows the experimental setup used to differentiate the two photoacoustic-sensitive materials of hemoglobin and methylene blue discussed throughout this chapter. A 29 cm \times 18 cm \times 10 cm (length \times width \times height) polyvinyl chloride-plastisol (PVCP) phantom was fabricated to contain ten cylindrical, hollow chambers. Each chamber had a diameter of 15 mm and a depth of 55 mm. Two of the chambers were filled

with either a 100 μM aqueous solution of methylene blue (MB, ID: S25431A, Fisher Scientific, Waltham, MA) or human blood (Hb), and a 1-mm-diameter optical fiber was inserted in each of the filled chambers. These fibers originated from a bifurcated fiber bundle that was connected to a Phocus Mobile laser (Opotek Inc., Carlsbad, CA, USA), transmitting laser light with wavelengths ranging from 690 nm to 950 nm in 10 nm increments.

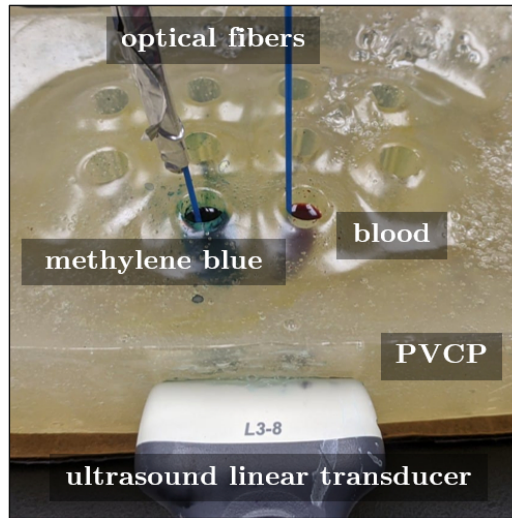


Figure 5-1. Acquisition setup to test the differentiation of methylene blue (MB) from blood (Hb). These photoacoustic-sensitive materials fill the hollow chambers of a custom polyvinyl chloride plastisol phantom.

The tip of each optical fiber was positioned approximately 15 mm below the top surface of the chambers, and light was emitted from each fiber tip. By transmitting light locally into each chamber and not globally illuminating multiple chambers simultaneously, we minimized (or systematically controlled) fluence differences and the related amplitude of responses to the optical excitation. The generated photoacoustic signals were received by an Alpinion L3-8 linear array ultrasound probe (center frequency of 5.5 MHz and pitch of 0.3 mm) that was positioned on the lateral wall of the phantom, approximately 40 mm away from the hollow chamber cross section, as shown in Fig. 5-1.

To evaluate the reproducibility of our proposed method, three datasets were acquired

(i.e., Datasets 1, 2, and 3). Dataset 1 was acquired first followed by Dataset 2 (acquired 10 hours later), followed by Dataset 3 (acquired 13 hours after Dataset 2). The Hb samples were stored with interim refrigeration at a temperature of 4° C. The fluence emitted from each fiber tip measured 1.0 mJ.

To characterize the effects of unequal fluence emitted from each fiber tip, three additional datasets were acquired with fluence pairs in the MB and Hb chambers recorded as 0.4 and 1.8 mJ, 1.0 and 1.8 mJ, and 0.4 and 1.0 mJ, respectively. These three datasets were labeled as “Fluence Pair 1”, “Fluence Pair 2”, and “Fluence Pair 3”, respectively. Each fluence pair dataset comprised three subsets, acquired with the same time intervals described in the preceding paragraph for Datasets 1-3.

To evaluate the performance of our proposed method in more challenging environments, particularly in the presence of an aberrating media composed of mostly fatty tissue, three additional datasets were acquired with 2-, 5-, and 7-mm-thick layers of turkey bacon placed between the phantom and the ultrasound probe. This dataset was acquired immediately prior to Dataset 2, thus it is expected to contain similar Hb degradation to that of Dataset 2. The added tissue layers can be considered to represent the fat that is commonly located within skin and within the subcutaneous region of healthy human tissue [21]. The fluence emitted from each fiber tip measured 1.0 mJ.

5.2.2 Ground-truth Labelling

Fig. 5-2 presents an overview of the proposed framework for differentiating photoacoustic signals sources. For each laser wavelength emission, 10 acquisitions of raw radiofrequency data were acquired. Photoacoustic images were then generated using conventional delay-and-sum (DAS) beamforming. Two regions of interest (ROIs) were automatically defined to separate photoacoustic signals generated from MB and Hb, located on the right and the left sides of the photoacoustic images, respectively. These

ground-truth labels were automatically segmented using binary-thresholding of locally weighted short-lag spatial coherence (LW-SLSC) images [22], with a regularization factor of $\alpha = 1$ and an axial correlation kernel of 0.56 mm. Binary segmentation was performed using a -10 dB threshold mask applied to the LW-SLSC images. A single binary mask was computed per laser wavelength emission, which was the result of the logical inclusive “OR” operation of the 10 masks obtained from the 10 frames. This segmentation resulted in two distinct signals on the left and right sides of the mask, which were assigned the ground-truth labels of MB and Hb, respectively. For each image, only those pixels included in the coherence masks were used for feature extraction, training, and classification.

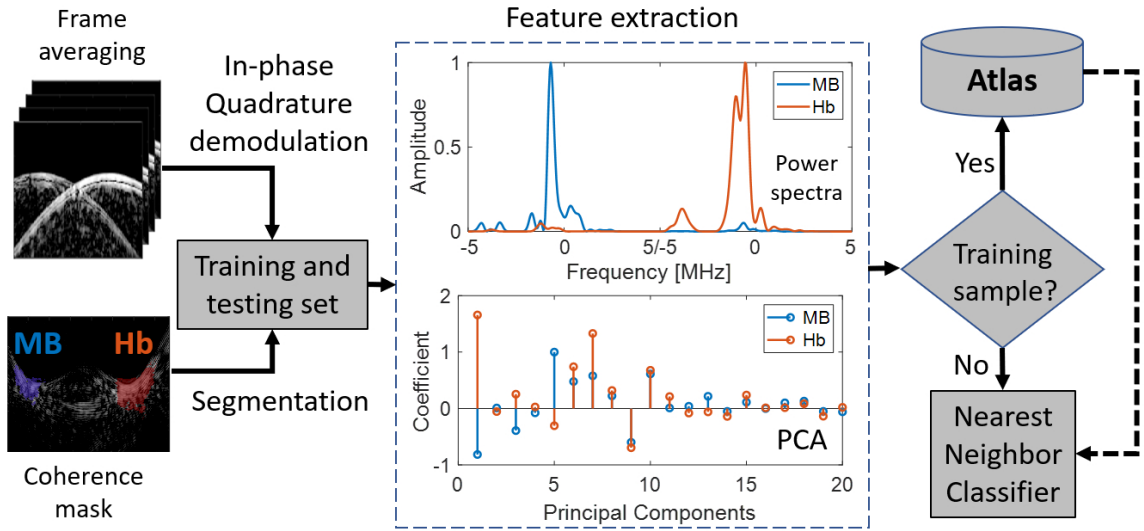


Figure 5-2. Overview of proposed method to differentiate photoacoustic signal sources using acoustic frequency information. The blue and red coherence masks show regions of interest for methylene blue (MB) and blood (Hb), respectively. These regions are known for the training set and need to be correctly classified through atlas comparisons during testing. Spectra are asymmetric with respect to frequency because baseband signals were analyzed after IQ demodulation.

5.2.3 Atlas of Photoacoustic-Sensitive Materials

A frequency analysis of the photoacoustic pressure waves was performed. For each material (i.e., MB and Hb), the normalized power spectra were calculated from

a sliding window of axial kernels of in-phase and quadrature (IQ) data. Principal component analysis (PCA) was applied to the power spectra of photoacoustic signals acquired at each laser wavelength in order to reduce the complexity of the feature space. When using a training set, the principal components were stored in an “atlas” describing each material. Finally, when evaluating the spectra of a test signal, nearest neighbor (k-NN) classification was applied with the L2-norm as the measure of distance between the PCA of the test spectra and the PCA of the spectra within the atlas.

Datasets 1-3 (described in Section 5.2.1) were utilized to compare the performance of the proposed atlas-based method with the performance of the existing classification methods described in Section 5.2.4. Because these atlas methods require a training set in addition to a test set, Dataset 1 was used for training the atlas methods when testing with Datasets 2 and 3. In addition, to include performance when testing with Dataset 1, Dataset 2 was arbitrarily chosen for training in this scenario.

Fig. 5-3 shows two proposed spectral analyses using either one or two wavelengths. In the dual-wavelength analysis, the magnitude of the IQ spectra of the photoacoustic response from a region of interest using two different wavelengths were concatenated, resulting in a region of interest producing a spectrum of size $[1 \times N]$ from one wavelength, where N is the number of samples of the spectrum, producing a concatenated spectra P of size $[1 \times 2N]$. This concatenated spectrum was then normalized to its maximum value. No concatenation was required for the single-wavelength analysis.

The initial parameters of the single- and dual-wavelength atlas method used in our previous publication [23] were modified to maximize the sensitivity, specificity, and accuracy of our approach (see Section 5.2.6 for metric definitions). In particular, the parameters for in-phase quadrature demodulation, PCA, and k-NN were optimized through an iterative search using laser wavelengths ranging from 690 nm to 950 nm (see Section 5.7 for more details). The optimized parameters were utilized for the proposed spectral analyses throughout the chapter.

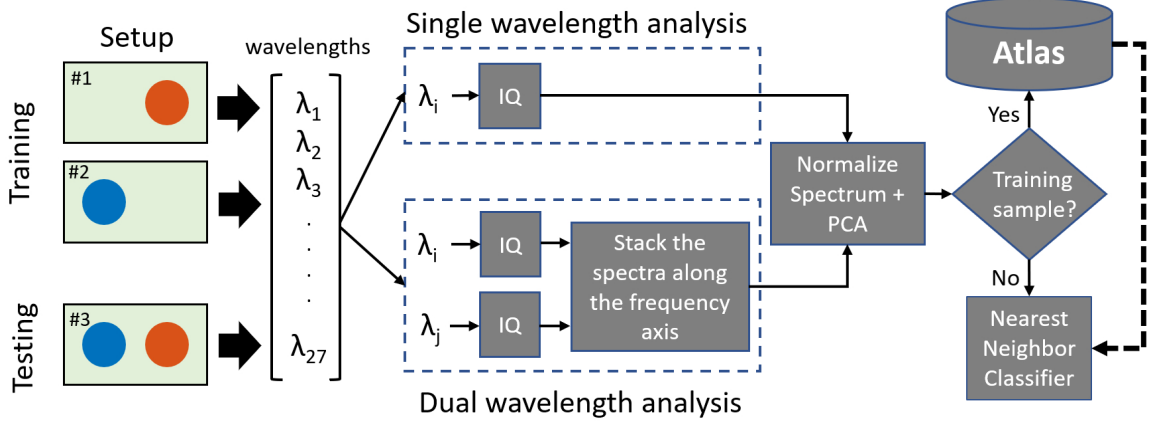


Figure 5-3. Two proposed spectral analyses for characterization based on single (top) and dual (bottom) wavelength emissions.

5.2.4 Comparison with Previous Methods

5.2.4.1 Spectral Unmixing Techniques

Spectral unmixing techniques solve the source component reconstruction \mathcal{C} of a scanned region by using the multispectral measurement matrix \mathcal{M} and an *a priori* absorption coefficient matrix \mathcal{S} of the number of chromophores present in the image. A conventional spectral unmixing solution is the least square method presented below [2, 11, 24]:

$$\mathcal{C} = \mathcal{M}\mathcal{S}^{\dagger}, \quad \mathcal{C} \in \mathbb{R}^{n \times k}, \mathcal{M} \in \mathbb{R}^{n \times m}, \mathcal{S}^{\dagger} \in \mathbb{R}^{m \times k}, \quad (5.1)$$

where \mathcal{C} segments k number of chromophores over a grid of n pixels, m is the number of laser wavelength acquisitions, and \mathcal{S}^{\dagger} is the Moore-Penrose pseudoinverse of the absorption coefficient matrix \mathcal{S} (i.e., $\mathcal{S}^{\dagger} = \mathcal{S}^T(\mathcal{S}\mathcal{S}^T)^{-1}$). A more robust approach proposed by Grasso *et al.* [13] used an iterative non-negative matrix factorization (NNMF) to adjust the initial \mathcal{S} and further reduce residual errors:

$$[\mathcal{C}, \hat{\mathcal{S}}] = \min_{\mathcal{C}, \mathcal{S}} \frac{1}{2} \|\mathbf{m} - \mathcal{C}\mathcal{S}\|_2^2, \quad \mathcal{S} \in \mathbb{R}^{k \times m}, \quad \mathcal{C}_{ij} \geq 0, \quad \mathcal{S}_{ij} \geq 0 \quad (5.2)$$

$$\mathcal{S}(\mathbf{p} + 1) = \mathcal{S}(\mathbf{p}) \otimes \frac{(W^T \mathcal{M})}{(\mathcal{C}^T \mathcal{C} \mathcal{S})}, \quad \mathcal{C}(\mathbf{p} + 1) = \mathcal{C}(\mathbf{p}) \otimes \frac{(\mathcal{M} \mathcal{S}^T)}{(\mathcal{C} \mathcal{S} \mathcal{S}^T)}$$

where \otimes denotes multiplication. The multiplication and division steps are considered

element-wise operations and the stopping criteria is defined by an improvement tolerance η . Eqs. 5.1 and 5.2 are considered overdetermined systems (i.e., $\mathbf{m} > \mathbf{k}$). Both methods were applied to DAS images of the testing data described in Section 5.2.2 and Fig. 5-3 for two chromophores (i.e., $\mathbf{k} = 2$). However, because there is no report of absorption coefficients for methylene blue at optical wavelengths greater than 800 nm, only 12 of the 27 wavelength acquisitions were used for the construction of the matrix \mathbf{m} (i.e., $\mathbf{m} = 12$). In addition, each equation was regularized by modifying the initial \mathcal{S} to:

$$\mathcal{S}' = \mathcal{S} + \gamma A, \quad (5.3)$$

where A is a matrix of ones, and γ is an additive coefficient that was varied from 10^{-1} to 10^3 cm^{-1} in multiplicative increments of $10^{0.188}$ (i.e., $\gamma[n] = 10^{-1} \times 10^{0.188n}$).

5.2.4.2 F-mode Imaging

Using the testing data, non-normalized DAS images were generated without log-compression and segmented with the coherence mask described in Section 5.2.2. Log-compressed power spectra were calculated from a sliding window of axial kernels of radiofrequency signals, each 3.85 mm in length. For each spectrum, the integrated frequency content was estimated from 4 sectors of the frequency domain of 0.2 MHz width and center frequencies of 1, 2, 3, and 4 MHz. Then, for each segmented DAS image, k-means clustering was applied to separate MB and Hb axial kernels. This process was repeated for each single-wavelength acquisition and each frame. Given that the labelling provided by k-mean clustering is arbitrary for each instance of classification, the f value (see Eq. (5.7)) was computed for both original labels (i.e., “1” = Hb and “2” = MB) and inverted labels (i.e., “1” = MB and “2” = Hb) for each testing frame. Then, the labelling convention that provided the highest f value was chosen as the final clustering result.

5.2.4.3 Acoustic-Based Clustering with Calibrated Spectra

To perform the acoustic-based clustering method reported by Cao *et al.* [17], the spectra of each radio-frequency axial kernel were first calibrated to a reference spectrum that models the characteristic frequency response of the ultrasound system. The experiment for determining the optimal reference spectra is detailed in Section 5.8. The generation of the log spectra was similar to that of F-mode imaging. However, each spectrum was then calibrated over the reference spectrum and then further normalized at 0 dB, as specified in [17]. Finally, k-means clustering was conducted using the same labelling criteria as described in Section 5.2.4.2, and the process was repeated for each single-wavelength acquisition and each frame. For the remainder of this chapter, we refer to this acoustic-based clustering method as the k-means clustering method.

5.2.5 Evaluation of Laser Wavelength and Hyperparameters

Table 5-1 summarizes the range of light-emission wavelengths used for each method as well as the corresponding hyperparameter to further improve the robustness of the classification performance. The additive coefficient γ represents a trade off between classification performance and reproducibility for the spectral unmixing methods, as the condition number of matrix \mathcal{S}' increases when γ increases, and the system becomes more ill-posed. The variation of the reference spectra evaluates the consistency of the classifications results for the k-means clustering method when considering different materials and acquisition setups.

5.2.6 Classification Performance Metrics

MB and Hb were considered to be the positive and negative samples, respectively, when calculating sensitivity, specificity, and accuracy metrics of classification performance. Sensitivity or true positive rate (TPR) measures the fraction of pixels that

Table 5-1. Wavelengths and hyperparameters evaluated

Method	Wavelengths evaluated	Hyperparameter
Spectral unmixing	690 - 800 nm	γ
Spectral unmixing + NNMF	690 - 800 nm	γ
F-mode imaging	690 - 950 nm	-
k-means clustering	690 - 950 nm	reference spectra
Single-wavelength atlas	690 - 950 nm	-
Dual-wavelength atlas	690 - 950 nm	-

were correctly classified as methylene blue:

$$\text{Sensitivity} = \text{TPR} = \frac{T_{MB}}{T_{MB} + F_{Hb}}, \quad (5.4)$$

where T_{MB} and F_{Hb} are the number of true MB and false Hb pixels, respectively. Similarly, specificity or true negative rate (TNR) measures the fraction of pixels that are correctly classified as deoxygenated blood:

$$\text{Specificity} = \text{TNR} = \frac{T_{Hb}}{T_{Hb} + F_{MB}}, \quad (5.5)$$

where T_{Hb} and F_{MB} are the number of true Hb and false MB pixels, respectively. The combination of sensitivity and specificity is described by the accuracy metric, defined as:

$$\text{Accuracy} = \text{ACC} = \frac{T_{MB} + T_{Hb}}{T_{MB} + T_{Hb} + F_{MB} + F_{Hb}} \quad (5.6)$$

To determine the optimal parameter for each method, the three quantitative metrics were considered simultaneously, using the optimization expression:

$$\hat{\Theta} = \max_{\Theta} f(\Theta), f(\Theta) = \frac{1}{2} \left(\frac{\text{TPR}(\Theta) + \text{TNR}(\Theta)}{2} + \text{ACC}(\Theta) \right), \quad (5.7)$$

where Θ is either: (1) a single wavelength for the single-wavelength atlas method, k-means clustering or F-mode imaging method; (2) a pair of wavelengths for the dual-wavelength atlas method; or (3) equivalent to the additive coefficient γ for the spectral unmixing methods, while $\hat{\Theta}$ is the optimal Θ .

Given that a large number of Θ values would result in non-optimal or poor classification performance for each method, a subset of 5 best cases for each classification method was defined for a fair comparison, with the term "case" referring to either a wavelength, wavelength pair, or γ . For the experiment of assessing reproducibility, we first averaged the f values among the 10 frames for each wavelength, wavelength pair, or γ . Then, the first 5 cases with the highest average f were selected, and the distribution was obtained from the accuracy values of each of these cases \times 10 frames per case. For the experiment of characterizing the effects of unequal fluence emitted from each fiber tip, we first averaged the f values among the 10 frames and among the datasets for each wavelength, wavelength pair, or γ . Then, the first 5 cases with the highest average f were selected, and the distribution was obtained from the accuracy values of each of these cases \times 10 frames \times 3 datasets per case.

Finally, a pair-wise t-test was used to evaluate the statistical significance ($p < 0.001$) of the difference between MB and Hb spectra obtained from either the single-wavelength atlas or dual-wavelength atlas method. This statistical analysis used 56,800 spectral samples of MB and 43,060 spectral samples of Hb for the wavelength pair of 710-870 nm (i.e., one of the wavelength pairs that yielded a classification accuracy of 1.00).

5.3 Results

5.3.1 Image and Segmentation Examples

The left column of Fig. 5-4 shows example LW-SLSC photoacoustic images co-registered to a DAS ultrasound image obtained with the laser wavelength indicated on each image. The right column of Fig. 5-4 shows the corresponding segmentation mask, where the blue and red regions represent the ground truth labeled pixels for MB and Hb, respectively. Fig. 5-4(d) shows example compound masks generated by the "OR" logical operation of a range of masks obtained from 690 nm to 800 nm

wavelengths. Fig. 5-4(h) shows example compound masks generated by the “OR” logical operation from a mask pair obtained with 690 nm and 920 nm wavelengths. Note that the varying areas of the LW-SLSC signals and corresponding mask sizes for the MB and Hb regions obtained with different laser wavelength emissions are responsible for different proportions of MB-to-Hb kernel sizes when calculating the quantitative metrics.

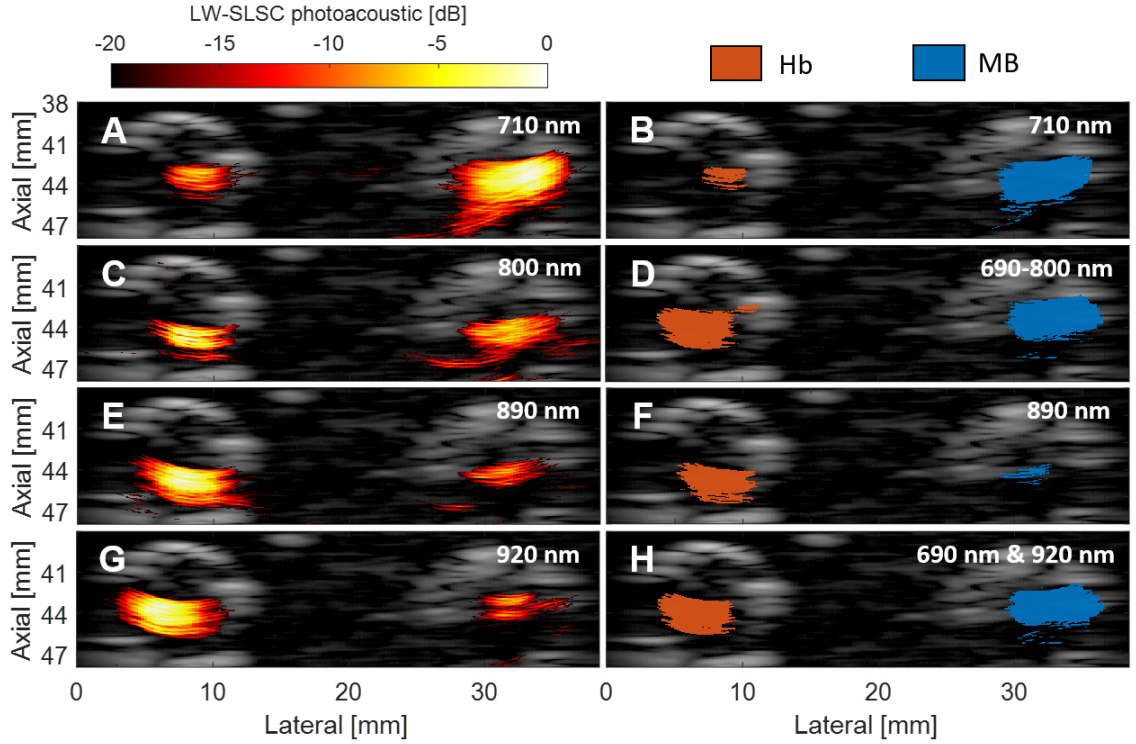


Figure 5-4. Locally-weighted short-lag spatial coherence (LW-SLSC) photoacoustic images overlaid on DAS ultrasound images of MB and Hb, obtained with a laser wavelength emission of (a) 710 nm (c), 800 nm (e) 890 nm, and (g) 920 nm. Segmented masks for MB and Hb after a -10 dB threshold was applied to the LW-SLSC photoacoustic images with single-wavelength masks shown for wavelengths of (b) 710 nm and (f) 890 nm, (d) the compound mask from “OR” logical operation on masks generated from 690 nm to 800 nm, and (h) the resulting mask from the “OR” logical operation of the 690 nm and 920 nm masks.

Fig. 5-5 shows segmentation examples of the best results among the three datasets for each of the classification approaches after estimating the corresponding optimal parameter, using the optimization expression f defined by Eq. (5.7). The blue and

red regions represent correctly classified pixels of MB and Hb, respectively, while the yellow regions represent misclassified pixels. As observed previously in Fig. 5-4, the changes in region size among the approaches are caused by the different LW-SLSC coherence masks that were computed for either single, pairs, or groups of wavelengths, depending on the requirements of each classification method. When qualitatively comparing the classified regions, the dual-wavelength atlas method showed the best classification performance, as the majority of each MB and Hb region were labelled correctly (i.e., no yellow regions are shown). Similar performance was observed for the spectral unmixing and spectral unmixing + NNMF, which were generated with an additive coefficient γ of 19.31 cm^{-1} and 9.10 cm^{-1} , respectively. Conversely, F-mode and k-means clustering could not properly detect signals from MB and Hb, respectively, showing a sensitivity and specificity of 0.76 and 0.79, respectively. A summary of the sensitivity, specificity, and accuracy obtained with the optimal parameter for each method is shown in Table 5-2.

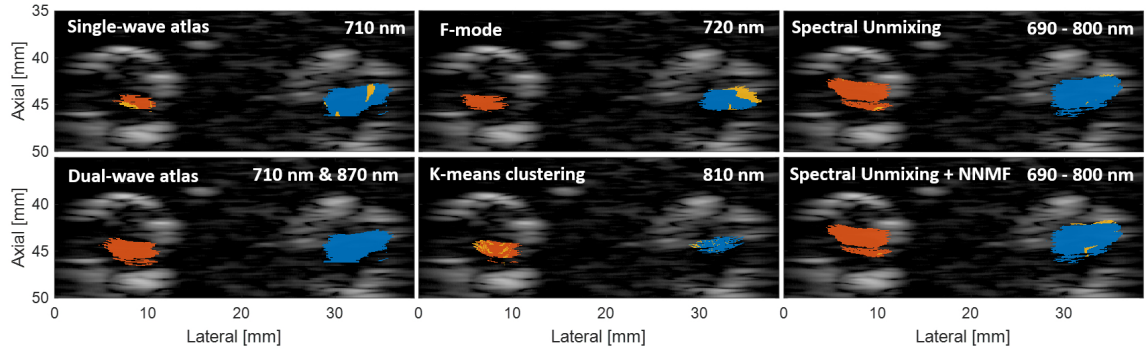


Figure 5-5. Example of segmented regions of MB and Hb using different classification approaches. The blue and red regions represent correctly classified pixels of MB and Hb, respectively, while the yellow regions represent misclassified pixels. Each image shows the frame of the dataset generated with the wavelength emission that achieved the highest accuracy.

5.3.2 Comparison of Sensitivity, Specificity, and Accuracy

Fig. 5-6 shows the combined results of sensitivity, specificity, and accuracy obtained from Datasets 1-3, using single-wavelength atlas, dual-wavelength atlas, spectral

Table 5-2. Best classification result achieved with each method. Bold font indicates the maximum value in each column

Method	Sensitivity	Specificity	Accuracy
Spectral unmixing	0.98	0.98	0.98
Spectral unmixing + NMF	0.95	0.99	0.97
F-mode imaging	0.76	0.99	0.84
k-means clustering	0.92	0.79	0.85
Single-wavelength atlas	0.93	0.82	0.91
Dual-wavelength atlas	1.00	1.00	1.00

unmixing, F-mode, and k-means clustering methods. Spectral unmixing and spectral unmixing + NMF were computed with $\gamma = 6.23 \text{ cm}^{-1}$ and $\gamma = 5.18 \text{ cm}^{-1}$, respectively. Defining an accuracy ≥ 0.80 as good classification, spectral unmixing and spectral unmixing + NMF showed a good mean accuracy of 0.85 and 0.87, respectively, among the three datasets. Similarly, dual-wavelength atlas method showed mean accuracy values greater than 0.85 for wavelength pairs of 690 nm and 810 nm through 840 nm and 870 nm, as shown in the green-colored middle region of the triangles showed in Fig. 5-6. In contrast, the maximum values of mean accuracy for the single-wavelength atlas method, F-mode imaging, and k-means clustering among the three datasets were 0.77, 0.74, and 0.72 for wavelengths of 890 nm, 750 nm, and 880 nm, respectively. These mean accuracy values were lower than the minimum accuracy required for good classification performance, suggesting that only the dual-wavelength atlas method and the spectral unmixing methods showed overall consistent classification performance.

As it is equally important to identify both MB and Hb regions, a high sensitivity and a low specificity pair, or vice-versa, corresponds in practice to a poor classification performance. Therefore, the totality of graphs shown in Fig. 5-6 must be analyzed from this perspective. For some accuracy regions that are shown in blue (i.e., adequate classification), the same regions are colored in red (i.e., poor classification) for either the corresponding specificity or sensitivity or colored in green (i.e., good classification).

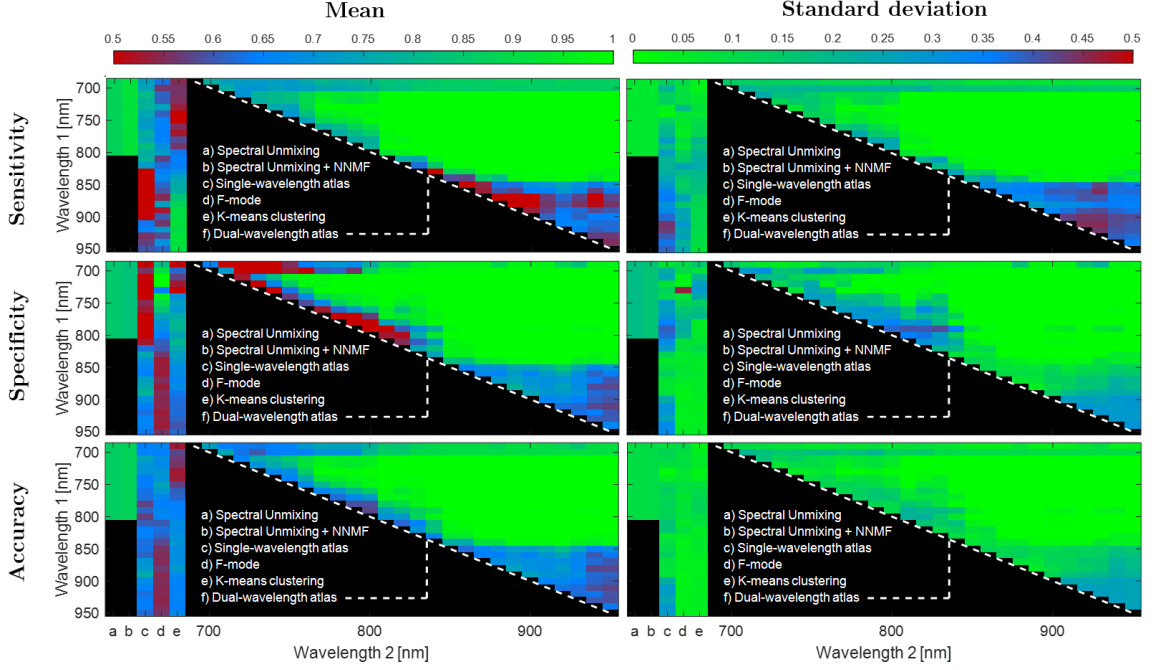


Figure 5-6. Overall classification results with dual-wavelength atlas, single-wavelength atlas, spectral unmixing methods, F-mode, and k-means clustering using Dataset 1, 2, and 3. Top, middle and bottom rows show the sensitivity, specificity and accuracy of classification, respectively. The left and right columns show the mean and standard deviation over 10 frames, respectively. For each image, the first 2 vertical stripes counting from the left represents the results for spectral unmixing and spectral unmixing + NNMF, respectively, which have a single value from 690 to 800 nm wavelengths. The next 3 stripes represent the results for single-wavelength atlas, F-mode, and k-means clustering, respectively, as a function of wavelength emission. Finally, the upper triangle represents the results of the dual-wavelength atlas for each pair of wavelength combination.

For example, the single-wavelength atlas method showed a mean \pm one standard deviation accuracy of 0.70 ± 0.06 over the wavelength range of 710-740 nm, while showing a sensitivity and specificity of 0.78 ± 0.08 and 0.40 ± 0.14 , respectively, over the same wavelength range. Similarly, the k-means clustering method showed a mean \pm one standard deviation sensitivity of 0.89 ± 0.11 over the wavelength range of 860-950 nm, while showing a specificity and accuracy of 0.63 ± 0.05 and 0.67 ± 0.04 , respectively, over the same wavelength range. These results further support the importance of evaluating sensitivity, specificity, and accuracy simultaneously, as described by Eq. (5.7), to determine the overall classification performance of each

method. The mean \pm one standard deviation for this combination of accuracy, sensitivity, and specificity (i.e., f in Eq. (5.7)), over the same wavelength ranges described above for the single-wavelength atlas and the k-means clustering methods were 0.65 ± 0.06 and 0.72 ± 0.04 , respectively.

Table 5-3 and Table 5-4 present summaries of quantitative metrics from the average among wavelengths and the average among the best 5 cases for each classification method, respectively. The quantitative results follow the same trend as those described for the qualitative results, where the dual-wavelength atlas method achieved the highest sensitivity, specificity, and accuracy among the other methods. Similarly, the method with the second highest average in the best-5-cases evaluation was the spectral unmixing + NMF.

Table 5-3. Mean \pm standard deviation of the sensitivity, specificity, and accuracy measured across the wavelengths investigated for each method. Bold font indicates the maximum value in each column.

Method	Sensitivity	Specificity	Accuracy
Spectral unmixing ^a	0.89 \pm 0.12	0.81 \pm 0.16	0.86 \pm 0.13
Spectral unmixing + NMF ^a	0.83 \pm 0.19	0.86 \pm 0.16	0.85 \pm 0.09
F-mode imaging	0.63 \pm 0.17	0.67 \pm 0.21	0.62 \pm 0.09
k-means clustering	0.70 \pm 0.21	0.67 \pm 0.15	0.64 \pm 0.08
Single-wavelength atlas	0.64 \pm 0.31	0.57 \pm 0.28	0.65 \pm 0.16
Dual-wavelength atlas	0.88 \pm 0.23	0.87 \pm 0.21	0.88 \pm 0.17

^a Means and standard deviations were measured across the range of γ values reported in Section 5.2.4.1

5.3.3 Spectra Examples & Multiple Possible Dual-Wavelength Combinations

Fig. 5-7(a) shows a representative example of spectra from the dual-wavelength atlas method and the equivalent stacked spectra from the single-wavelength atlas method. This display method was chosen to demonstrate the improvement in classification performance when using the dual-wavelength atlas method. For these examples, the testing spectra of 710 nm and 870 nm wavelengths were used, as this wavelength

Table 5-4. Average among best 5 cases for each method.^aBold font indicates the maximum value in each column.

Method	Sensitivity	Specificity	Accuracy
Spectral unmixing	0.91 ± 0.05	0.91 ± 0.03	0.91 ± 0.03
Spectral unmixing + NMF	0.94 ± 0.02	0.88 ± 0.09	0.91 ± 0.05
F-mode imaging	0.63 ± 0.07	0.94 ± 0.11	0.70 ± 0.08
k-means clustering	0.85 ± 0.14	0.66 ± 0.06	0.69 ± 0.05
Single-wavelength atlas	0.64 ± 0.29	0.65 ± 0.23	0.71 ± 0.12
Dual-wavelength atlas	1.00 ± 0.00	1.00 ± 0.00	1.00 ± 0.00

^a only one best case per wavelength, wavelength pair, or γ

pair was one of eighty nine to achieve a specificity and sensitivity of 1.00 when using the dual-wavelength atlas method. The mean and standard deviation of the spectra were calculated from the spectra of all segmented pixels of MB and Hb data acquired with 710 nm or 870 nm wavelength for each atlas method. Error bars show one standard deviation of the combined results from all kernels within selected ROIs, from 10 image acquisition frames, and from the 3 datasets. The overlapping spectra with the single-wavelength atlas method applied to either 710 nm or 870 nm wavelength acquisitions (top of Fig. 5-7(a)) resulted in no statistically significant differences between the amplitude of the spectra for MB and Hb ($p > 0.001$), while Hb and MB differentiation was achieved with statistical significance ($p < 0.001$) when using the dual-wavelength atlas method (bottom of Fig. 5-7(a)). This example illustrates that the enhanced differentiation achieved with the dual-wavelength atlas method can be attributed to the ability to differentiate the two spectra.

Fig. 5-7(b) shows a comparative evaluation of sensitivity and specificity between the atlas methods in an ROC-curve format. This display is included to support the observation that the dual-wavelength atlas method achieves high classification performance from a range of wavelengths combinations, whereas the other methods achieve their highest classification performance from just a few cases, based on the results shown in Fig. 5-6. For example, when a threshold region of 0.80 sensitivity

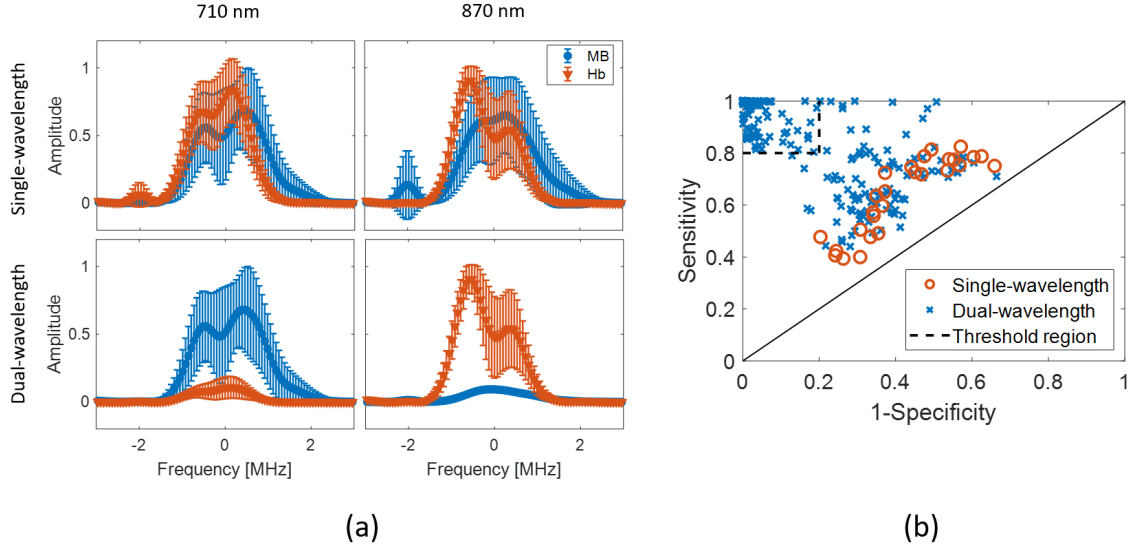


Figure 5-7. (a) Examples of stacked spectra of in-phase quadrature data from MB and Hb using (top) single-wavelength atlas method and (bottom) dual-wavelength atlas method. The spectra show combined results obtained with 710 nm and 870 nm laser wavelength. (b) Comparison of sensitivity and 1-specificity from single- and dual-wavelengths atlas method using a one frame per wavelength and wavelength pair, respectively. The threshold regions delimits cases with both sensitivity and specificity greater than 0.8, which represents a good classification performance.

and 0.80 specificity is defined as the criterion for adequate classification, Fig. 5-7(b) demonstrates that 241 wavelength pairs and 0 single wavelengths met this criterion for the dual- and single-wavelength atlas methods, respectively. Therefore, the dual-wavelength atlas method provides a flexible range of light emission wavelength pairs such that the ideal pair can be chosen to differentiate between the same chromophores across multiple imaging environments. This flexibility is necessary when an unwanted chromophore produces a considerable photoacoustic response at the originally selected wavelength pair.

5.3.4 Dataset Sensitivity

Fig. 5-8 shows the accuracy results of the spectral unmixing techniques when tested on Datasets 1-3 while varying the additive coefficient γ in Eq 5.3. The dashed line represents the optimal γ that achieved the highest average $f(\gamma)$ value among the

three datasets. When calculating the optimal γ_1 , γ_2 , and γ_3 for Datasets 1, 2, and 3, respectively, the absolute difference between the optimal γ and each γ_1 , γ_2 , and γ_3 in the conventional spectral unmixing method was 7.01 cm^{-1} , 21.87 cm^{-1} , and 2.70 cm^{-1} , respectively, resulting in a standard deviation of 12.35 cm^{-1} . In contrast, the difference between the optimal γ and the individual γ_1 , γ_2 , and γ_3 in spectral unmixing + NNMF resulted in a standard deviation of 1.37 cm^{-1} . This γ difference suggests that the optimal γ of spectral unmixing + NNMF is less sensitive to the testing data than that of conventional spectral unmixing. However, when evaluating the standard deviation of the classification accuracy at the optimal γ , spectral unmixing + NNMF produced standard deviations of 6.47%, 0.54%, and 0.34% for Datasets 1, 2, and 3, respectively, while conventional spectral unmixing produced standard deviations of 1.93%, 0.47%, and 0.48% for Datasets 1, 2, and 3, respectively. Thus, the spectral unmixing techniques did not demonstrate accuracy robustness across different datasets, and this detail must be considered in tandem with the γ differences.

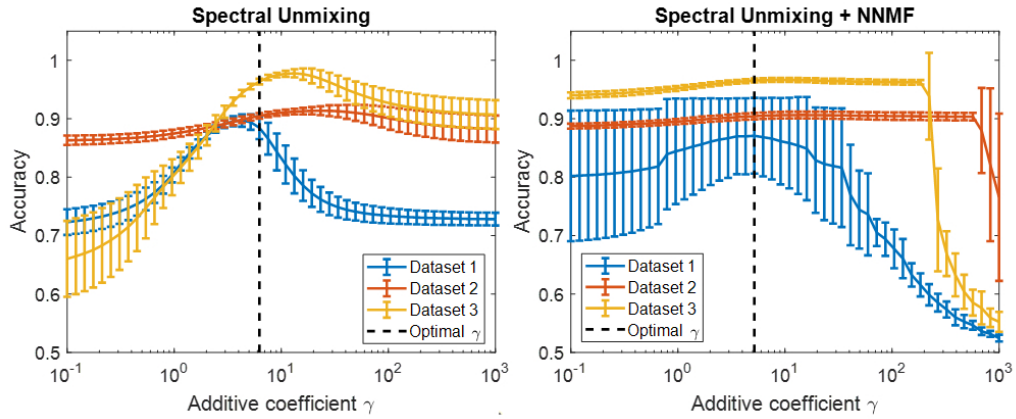


Figure 5-8. Classification accuracy of the spectral unmixing techniques for three testing datasets while varying the additive coefficient γ .

Fig. 5-9(a) shows a summary of the accuracy results obtained with the spectral unmixing, single- and- dual wavelength atlas, F-mode, and k-means clustering methods using the full range of wavelengths and additive coefficient γ . When comparing the distributions among Datasets 1-3, the maximum difference in median accuracy

measured for each dataset when applying spectral unmixing, spectral unmixing + NNMF, F-mode, k-means clustering, and the single-wavelength atlas methods was 15.8%, 21.2%, 6.7%, 4.3%, and 25.5%, respectively, while the dual wavelength atlas method showed a maximum difference in median accuracy of 1.4%. While these results display wide variations due to the inclusion of a wide range of wavelengths, wavelength pairs, or additive coefficient γ , only specific values can be selected in advance and later used in clinical practice.

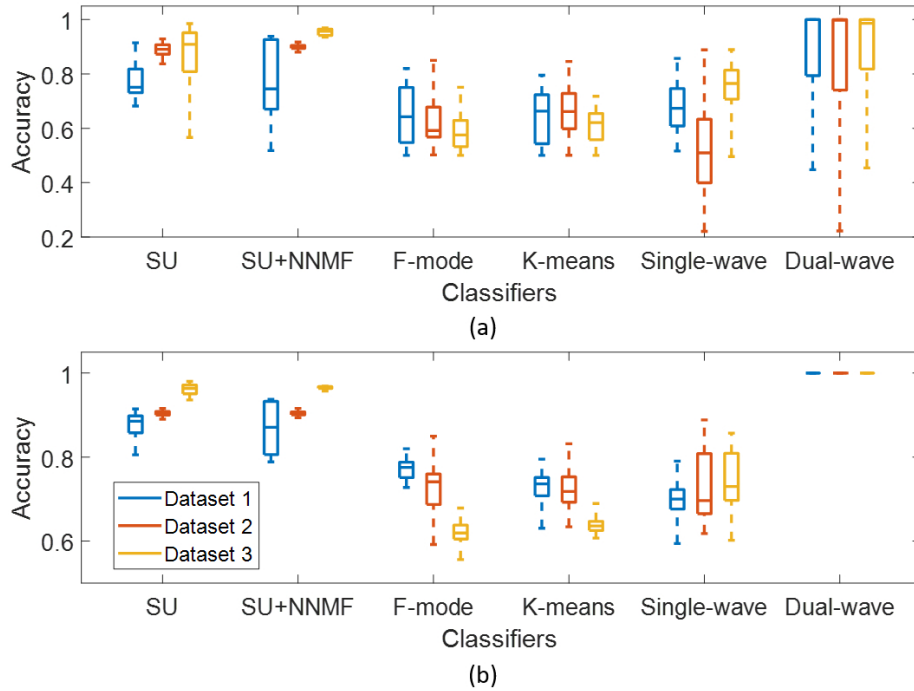


Figure 5-9. Classification accuracy of each method when tested on Datasets 1-3, evaluated with (a) the full range of wavelengths and additive coefficient γ (with each distribution obtained from 270-3510 samples, i.e., 10 acquired frames \times 27-351 wavelengths, wavelength pairs, or γ) and (b) the best 5 cases of wavelengths and γ among the datasets (with each distribution obtained from 50 samples, i.e., 10 frames \times 5 cases). SU = Spectral Unmixing, NNMF = Non-negative Matrix Factorization.

Therefore, Fig. 5-9(b) shows a subset of accuracy distributions obtained from the best 5 cases among the datasets, as defined in Section 5.2.6. The dual wavelength atlas method showed a maximum difference in median accuracy between any two datasets of 0%, which was significantly lower than that obtained from spectral unmix-

ing (7.8%), spectral unmixing + NMF (9.5%), F-mode (15.6%), k-means clustering (10.1%), and the single-wavelength atlas method (3.3%). In addition, when evaluating the dual-wavelength atlas method on Datasets 1-3, the 710-870 nm wavelength pair was present among the 5 pairs of wavelengths with the highest accuracy, with sensitivity, specificity, and accuracy of 1.00, 1.00, and 1.00, respectively. Therefore, the dual-wavelength atlas method implemented with this wavelength pair shows higher reproducibility of classification performance than spectral unmixing and other acoustic-based methods.

5.3.5 Sensitivity Against Fluence Changes

Fig. 5-10 shows the classification accuracy of each dataset acquired with varying fluence pairs. The best 5 cases of wavelengths and additive coefficient γ , as defined in Section 5.2.6. For each of the five existing methods, the maximum difference between the median accuracy values reported for any two fluence pairs (including the "Equal Fluence" Pair) was 3.3% for spectral unmixing, 3.8% for spectral unmixing + NMF, 18.4% for F-mode, 12.9% for k-means clustering, and 11.9% for the single-wavelength atlas method. For the dual wavelength atlas method, the maximum difference between the median accuracy values reported for any two fluence pairs was 0.1%, which is lower than the values reported for the five existing methods. These results demonstrate that the dual-wavelength atlas method is robust against changes in fluence levels when compared to acoustic-based methods that do not apply a normalization step such as F-mode.

5.3.6 Performance with Aberrating Media

Fig. 5-11 shows the classification accuracy from the dual-wavelength atlas method tested on the datasets obtained with added tissue layers. The five wavelength pairs are sorted by the median accuracy obtained in the absence of a layer (i.e., in descending order from left to right). When comparing the results obtained in the absence of a

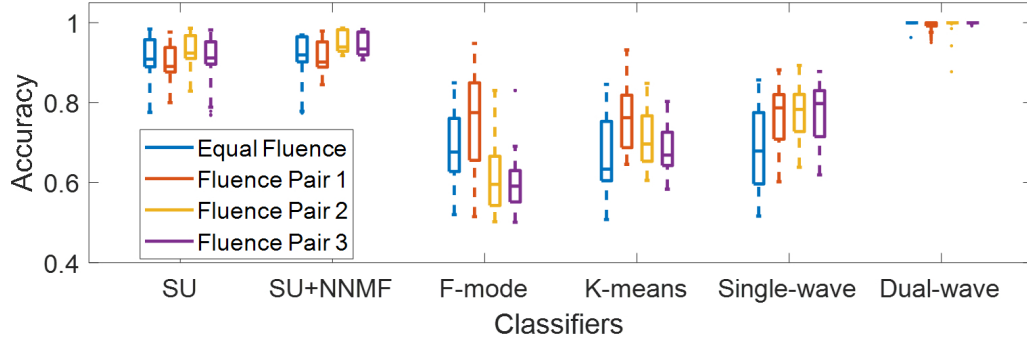


Figure 5-10. Classification accuracy of each method when tested with four fluence pairs, evaluated using the best 5 cases of wavelengths and additive coefficient γ among the datasets. Each distribution was obtained from 150 samples (10 frames \times 5 cases \times 3 datasets). SU = Spectral Unmixing, NNMF = Non-negative Matrix Factorization.

tissue layer, the 2-mm tissue layer resulted in no significant change to the median accuracy for the 780-870 nm and 780-950 nm wavelength pairs and decreased median accuracies of 3.0%, 11.9%, and 8.0% for wavelength pairs of 690-950 nm, 690-870 nm, and 690-780 nm, respectively. When comparing the results obtained in the absence of a tissue layer with the 5-mm tissue layer results, the 780-870 nm and 780-950 nm wavelength pair showed a decrease in median accuracy of 3.5% and 4.9%, respectively, which was lower than that obtained with the remaining wavelength pairs, yielding an average median accuracy decrease of 14.4%. Finally, when comparing the results obtained in the absence of a tissue layer with the 7-mm tissue layer results, the 780-870 nm wavelength pair showed a decrease in median accuracy of 7.1%, which was significantly lower than that obtained with the other wavelength pairs, yielding an average median accuracy decrease of 22.5%. Results demonstrate that the aberrating conditions generally reduce performance due to the presence of the fatty tissue, with a median classification accuracy of 92.9 % for a 7-mm-thick tissue layer when using a wavelength pair of 780-870 nm.

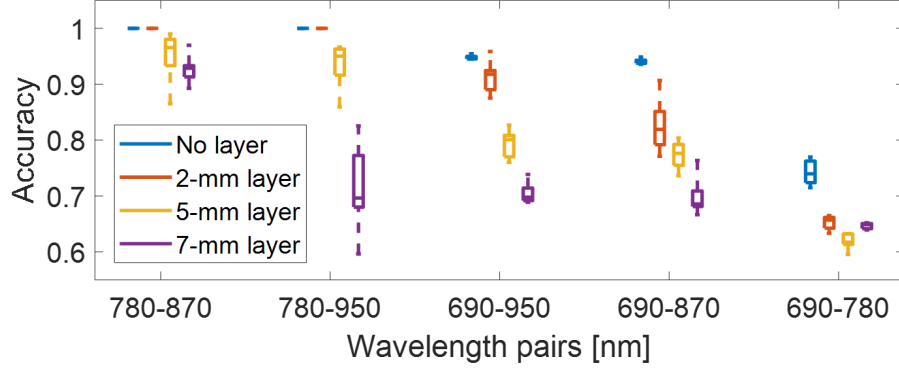


Figure 5-11. Classification accuracy of the dual-wavelength atlas method when varying the thickness of the aberrating tissue layers, evaluated with 5 different wavelength pairs. Each distribution was obtained from 10 samples (10 frames \times one wavelength pair)

5.4 Discussion

We demonstrated a novel method to accurately identify biological markers by analyzing the acoustic frequency response from either a single-wavelength emission (i.e., single-wavelength atlas method) or two consecutive wavelength emissions (i.e., dual-wavelength atlas method). Overall, the best classification accuracy obtained with the dual-wavelength atlas approach outperforms that obtained from previous methods with similar goals, including spectral unmixing [11, 13], F-mode imaging [18], and k-means clustering [17].

The dual-wavelength atlas method has three additional advantages over spectral unmixing techniques. First, the dual-wavelength atlas method does not require a significant number of wavelengths, which is often an impediment to both real-time capabilities and surgical implementation. With only two wavelength emissions, the overall acquisition time is significantly reduced as well as the memory bandwidth that is proportional to the number of acquired frames. Second, our method does not heavily depend on a hyperparameter to enhance its classification accuracy, contrary to both conventional and NNMF spectral unmixing techniques. In addition, as observed in Fig. 5-8(a), there was no single γ value that ensured the highest classification

accuracy for the three datasets using the conventional spectral unmixing technique, which suggests that testing on a fourth dataset would not necessarily have the optimal accuracy result when using the same γ . Third, the dual-wavelength atlas method shows consistent classification performance against different datasets, as observed in Fig. 5-8(b). Consequently, finding the same optimal wavelength pair for both datasets further supports the benefit of using only two wavelengths (i.e., 710 and 870 nm) for the identification of biological markers (i.e., MB and Hb) in future cases.

Normalization plays a key role in the single-wavelength atlas, dual-wavelength atlas, and k-means clustering methods because it prevents the use of amplitude as a distinguishing feature for classification. This is particularly important when characterizing structures located at different distances from the light source. By normalizing the spectrum from a single wave, both single-wavelength atlas and k-means clustering algorithms rely purely on the acoustic frequency content for tissue differentiation, which is often challenged by the limited frequency content obtained with a limited-bandwidth ultrasound transducer. In contrast, the dual-wavelength atlas method normalizes a pair of spectra, removing the amplitude dependency between two different regions but at the same time preserving the relative amplitude difference of two different light emission responses from the same region. In clinical practice, we envision dual excitation wavelengths illuminating the region of interest with a fast-switching laser source that quickly alternates between wavelengths, providing real-time labeling of photoacoustic-sensitive regions with comparable performance to that achieved with more conventional spectral unmixing techniques. The proposed method could be beneficial for a range of emerging photoacoustic imaging approaches oriented to surgeries and interventions [25, 26], such as hysterectomies [27–29], neurosurgeries [30–33], spinal fusion surgeries [34–36], as well as identification and distinction of metallic tool tips [28, 37], cardiac catheter tips [20], and needle tips [38] from other surrounding structures of interest.

Although the average accuracy values from the dual-wavelength atlas method shown in Table 5-3 are low (i.e., 0.88) in comparison to the best case of accuracy (i.e., 1.00), this occurs because we included the classification results from the 351 wavelength pairs combinations used in this study in the reported average. As observed in Fig. 5-6, several wavelength pairs yielded classification accuracy values <0.65 , which lowers the overall accuracy. A similar decrease was observed for the single-wavelength atlas, F-mode, and k-means clustering methods, as each method similarly used a range of wavelengths with most wavelengths producing poor classification results. However, in practice, only a reduced set of wavelength pairs would be used for the differentiation of MB and Hb with the dual-wavelength atlas method. Therefore, Table 5-4 represents a more realistic average from a reduced set of wavelength pairs for the dual-wavelength atlas method, and a reduced set of single wavelengths and hyper parameters for the other classification methods.

One limitation of the atlas approach is the availability of the sample material for generating a significant number of spectra in the training set. While most of the targeted materials for classification are either biological fluids or contrast agents, a non-fluid biological landmark (e.g., bone) would require a new setup to couple the tissue to the background PVCP without using additional photoacoustic-sensitive materials. In addition, the optical and acoustic properties of the biological materials contained in the PVCP chambers must be similar to the expected *in vivo* properties in order to maximize success. With consideration that the acoustic response from *in vivo* and *ex vivo* Hb may differ due to expected degradation of *ex vivo* blood, the datasets described throughout this chapter represented Hb in different states of degradation, and the dual-wavelength atlas method showed no significant change in the classification accuracy under these degradation conditions. We additionally demonstrated the robustness of the dual-wavelength atlas method against distortions of the acoustic response due to aberrating media. Future work will explore the impact

of additional confounding factors when characterizing biological tissues (e.g., decrease in blood oxygenation [39], deterioration of the lipid-rich myelin sheath of nerves [40]) on the classification performance of the dual-wavelength atlas method.

Additional future work includes improvements to the dual-wavelength atlas method for real-time identification of tissues, through the utilization of common parallelization and optimization strategies. The currently sequential comparison of measurements with atlas spectra can potentially be addressed with at least one of three possible strategies. First, graphical processing units (GPUs) may be employed for concurrent comparisons of a test spectrum with several training spectra. The feasibility of GPU-based NN classification has been widely studied and demonstrated in the literature [41–45]. Second, atlas factors that affect the computation time may be carefully adjusted (e.g., increase the coherence threshold of the LW-SLSC mask or reduce the number of acquired frames per wavelength emission) without compromising classification performance. Increasing the coherence threshold would produce smaller masks and thus, less pixels to evaluate for classification. Once a new coherence threshold is defined, the number of frames needed for classification can then be empirically determined by maximizing the combined sensitivity, specificity, and accuracy using Eq. (5.7). Third, rather than evaluating the photoacoustic spectra with an extensive look-up table (i.e., spectral atlas), the classification time can be reduced by implementing an artificial neural network (ANN) to learn and match features of the acoustic spectra (i.e., bypassing PCA feature extraction), which has been successfully implemented in previous studies [46, 47].

The proposed framework could be extended to multinomial classification (i.e., more than 2 tissues to classify), which is often necessary during *in vivo* interventions as photoacoustic signals originating from the surrounding tissue cannot be neglected. In contrast to binomial classification, multinomial classification would benefit from more robust feature extraction methods such as linear discriminant analysis (LDA) [48, 49]

or more robust classifiers such as sparse representation-based classifiers (SRC) [50, 51]. While the increase in the algorithm complexity can be addressed with the strategies discussed in the preceding paragraph, an alternative solution is to include a clustering criteria within the NN classification. Specifically, for trinomial classification where one of the regions would be labelled as a third component that does not exist in the atlas (e.g., background noise). Then, the acoustic spectra from this region can be identified when the error of the closest match surpasses a specific threshold, indicating the presence of a third component. Alternatively, NN-k or fuzzy C-means classification [52] may be employed to characterize the degree of belonging in regions where two materials are combined, with the potential benefit of assessing the percentage of a specific material within a region of interest.

5.5 Conclusions

We developed a novel acoustic-based photoacoustic classifier that relies on training sets to identify photoacoustic-sensitive materials. The proposed method is robust against changes in fluence levels and showed comparable sensitivity, specificity, and accuracy performance to those obtained with conventional and enhanced spectral unmixing methods. In clinical practice, we envision dual excitation wavelengths illuminating the region of interest with a fast-tuning laser source, providing real-time labeling of photoacoustic-sensitive regions with a GPU-based parallelized algorithm version or deep neural network architectures. Results from the presented experiments are promising for the identification of biological or bio-compatible markers (e.g., blood and contrast agents) during surgical interventions. By using the normalized photoacoustic response from two wavelength iterations, surgeons can localize structures of interest and surgical tools while avoiding other structures that are in close proximity to the targeted operating region.

5.6 Acknowledgments

This work was supported by NSF CAREER Award ECCS-1751522, NSF SCH Award IIS-2014088, NSF EEC-1852155, NIH Trailblazer Award R21-EB025621, and NIH R00-EB018994. The authors acknowledge the support of NVIDIA Corporation with the donation of the Titan Xp GPU used for this research.

5.7 Appendix: Parameter Optimization for Photoacoustic Spectral Analysis

To maximize the sensitivity, specificity, and accuracy of our approach (see Section 5.2.6 for metric definitions), the parameters for in-phase quadrature demodulation, PCA, and NN were first optimized through an iterative search. These parameters were the modulation frequency, filtered bandwidth, axial kernel size, number of principal components to use, and the k nearest neighbors used to determine the most common class in k-NN clustering. Each parameter was changed one at a time, and this search was repeated each time the parameter was changed. During each analysis, the optimal parameter found from the previous step was saved and used to find the new output until the optimal set of parameters were found. For the IQ-modulation, different combinations of bandwidth of 80-240% in intervals of 20% were tested with the modulation frequency which ranged from 2 MHz to 12 MHz in intervals of 2 MHz. Similarly, the axial kernel size was explored from 11 to 51 axial samples in increments of 2. For the PCA, the principal components were changed from 10 to 200 in steps of 10 and then from 1-10 in steps of 1. Finally, the NN classifier was analyzed by changing the classifier to 2-NN through 10-NN in increments of 1. The initial parameters were obtained from a previous publication in our group [23]. The optimization process was conducted on datasets obtained with laser wavelengths ranging from 690 nm to 950 nm in 10 nm increments.

Fig. 5-12 shows two known criteria to determine the optimal number of principal components used in the dual-wavelength atlas method. Each scatter point and error bar represents the mean and one standard deviation, respectively, of eigenvalues (left plot) and explained variance (right plot) from the 351 wavelength pairs (see Section 5.2.3) at a specific principal component. For the Kaiser rule [53], only the first principal component shows a distribution with values greater than 1.00, while the second principal component shows a mean eigenvalue less than 1.00. Similarly, the commonly accepted 80%-explained-variance threshold filter the first and second principal component when considering the mean value. However, when considering the standard deviation, the second principal component surpasses the variance threshold. Therefore, only the first principal component was used for the feature extraction in the dual-wavelength atlas method.

Fig. 5-13 shows the mean accuracy of classification results for the dual-wavelength atlas method before (left) and after (right) parameter optimization. The top right half of each image represents a triangle with each pixel displaying the average accuracy of classifying methylene blue and blood for a specific wavelength pair over 10 frames. The new parameter set consisted of a modulation frequency of 2 MHz, bandwidth of 140%, 30 axial samples, 1 principal component, and 1-NN. For each triangle, we define the “low-wavelength region” as wavelength pairs < 800 nm, the “high-wavelength region” as

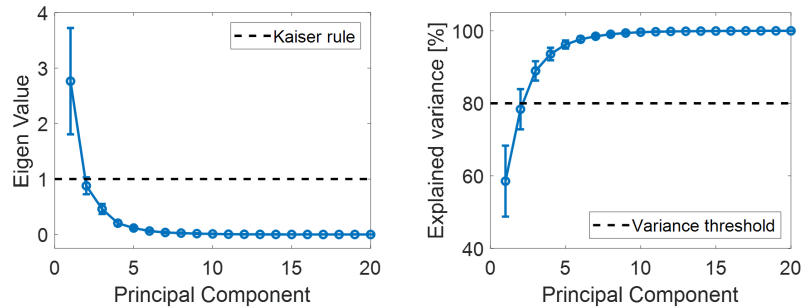


Figure 5-12. Criteria for determining the optimal number of principal components for the dual-wavelength atlas method using the (left) Kaiser rule [53] and (right) a 80% variance threshold.

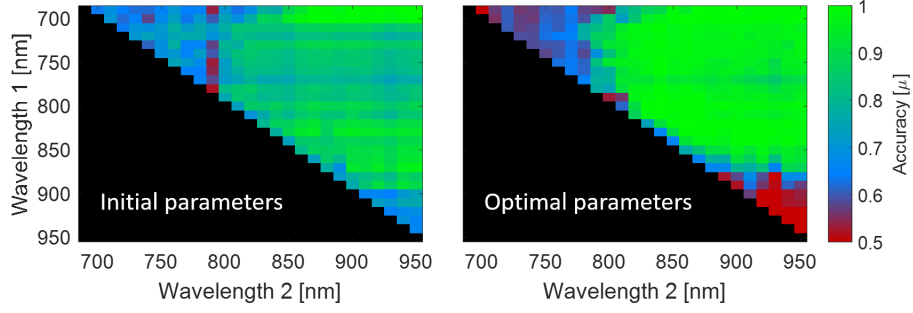


Figure 5-13. Mean accuracy classification results of the dual-wavelength atlas method per wavelength pair with a dataset of 10 frames per wavelength using the initial parameters of Gonzalez *et al.* [23] and the updated parameters.

wavelength pairs >850 nm, and the “mid-wavelength region” as wavelengths that do not belong to either the low- or high-wavelength regions. For wavelength pairs located in the mid-wavelength region, the mean accuracy increased from 85.45% to 95.67%. In contrast, for wavelength pairs that located in either the low- or high-wavelength region, the mean accuracy decreased from 74.67% to 67.40%. In clinical practice, we envision the use of a reduced set of wavelength pairs, choosing those that maximize the sensitivity, specificity and accuracy (i.e., mostly occurring in the mid-wavelength region) and otherwise omitting wavelength pairs that result in poor classification performance.

Fig. 5-14 shows a summary of sensitivity, specificity, and accuracy among the 351 wavelength pairs before and after parameter optimization. The mean \pm one standard deviation of sensitivity showed no significant change from $91.6 \pm 16.8\%$ to $90.9 \pm$

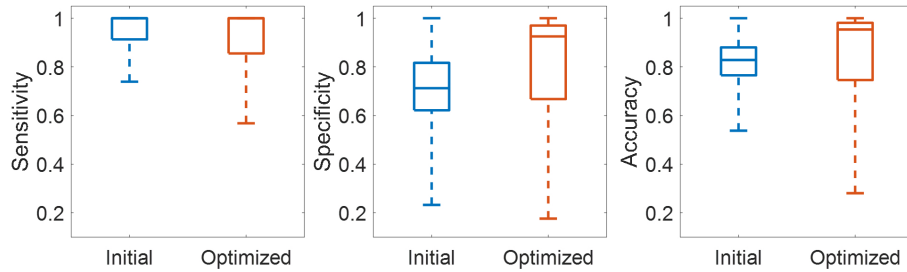


Figure 5-14. Summary of sensitivity, specificity, and accuracy results of the dual-wavelength atlas method before and after parameter optimization.

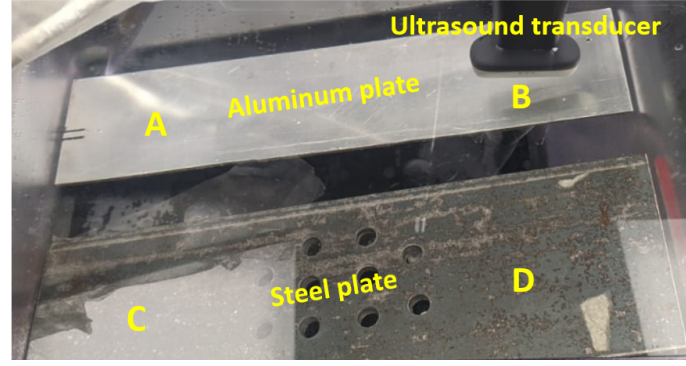


Figure 5-15. Setup for reference spectra acquisition. A and B represent the imaging depths of 5 and 9 cm for aluminum, respectively. C and D represent the imaging depths of 5 and 9 cm for steel, respectively.

14.8%. However, an increase in specificity was observed from $70.7 \pm 16.9\%$ to $81.7 \pm 20.9\%$, which in turn resulted in an overall increase of specificity from $81.5 \pm 10.4\%$ to $85.9 \pm 17.1\%$. Because blood was considered as negative samples for the specificity metric, the results suggest that the optimized version of the dual-wavelength atlas method can identify blood with more accuracy than with the initial parameter set used in Gonzalez *et al.* [23].

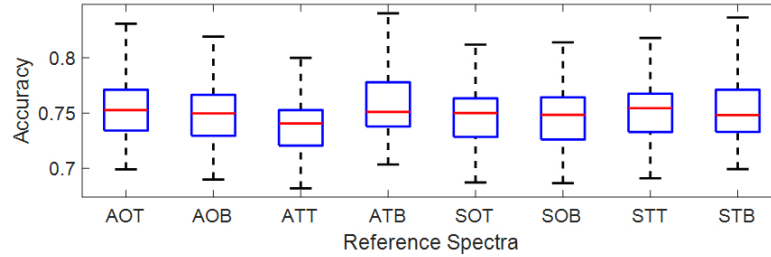


Figure 5-16. Mean classification accuracy of k-means clustering with different reference spectra. The box plots represent the group of frames evaluated with laser wavelength that achieved the overall best accuracy among reference spectra (i.e., 840 nm). The three letter codes on the abscissa represent the material of the reference (i.e., A = Aluminum or S = Steel), followed by the orientation of the material relative to the ultrasound transducer (i.e., O = Orthogonal or T = Tilted), followed by the imaging depth of 5 cm or 9 cm (i.e., T = Top or B = Bottom, respectively).

5.8 Appendix: Selection of Reference Spectra for K-means Clustering

Fig. 5-15 illustrates the ultrasound acquisition setup used to evaluate the performance variability of the method proposed by Cao *et al.* [17]. In particular, eight ultrasound reference spectra were acquired from two materials: (1) an aluminium plate and (2) a carbon-steel plate. These two materials contain relatively flat, reflective surfaces, which make them ideal for use as reference spectra [54]. These two materials also have acoustic properties that produce different pulse-echo responses [55, 56], which affects the normalization process applied to the acquired spectra and results in different classification accuracies.

Acquisitions were obtained after independently placing each material at axial depths of 5 cm or 9 cm from the L3-8 ultrasound transducer, tilted 45° or 0° relative to the elevation-lateral plane of the transducer. Each reference spectra was calculated by averaging the fast Fourier transform of scan lines across the lateral dimension. Then, a comparison of the accuracy results was conducted only for the subsets obtained from the optimal laser wavelength Θ , defined by Eq. (5.7) in the chapter. The reference spectra that produced the highest median classification accuracy was selected for comparison of the method by Cao *et al.* [17] with other methods reported throughout the chapter.

Fig. 5-16 shows the classification accuracy achieved after performing the k-means clustering step of the method of proposed by Cao *et al.* [17], obtained with a laser wavelength of 890 nm (which was the optimal parameter $\hat{\Theta}$ defined by Eq. (5.7) in the chapter) when using the reference spectra described above. The reference spectra reported for the k-means clustering method in Fig. 6 of the chapter was obtained from the tilted aluminum reference with an imaging depth of 9 cm (i.e., ATB in Fig. 5-16). This reference was chosen because it produced the greatest classification accuracy (i.e.,

84.0%).

References

- [1] E. A. Gonzalez, C. A. Graham, and M. A. Lediju Bell, “Acoustic frequency-based approach for identification of photoacoustic surgical biomarkers,” *Frontiers in Photonics*, vol. 2, 2021. DOI: [10.3389/fphoton.2021.716656](https://doi.org/10.3389/fphoton.2021.716656).
- [2] J. Glatz, N. C. Deliolanis, A. Buehler, D. Razansky, and V. Ntziachristos, “Blind source unmixing in multi-spectral optoacoustic tomography,” *Optics Express*, vol. 19, no. 4, pp. 3175–3184, 2011.
- [3] S. Tzoumas and V. Ntziachristos, “Spectral unmixing techniques for optoacoustic imaging of tissue pathophysiology,” *Philosophical Transactions of the Royal Society A: Mathematical, Physical and Engineering Sciences*, vol. 375, no. 2107, p. 20170262, 2017.
- [4] J. Gröhl, T. Kirchner, T. Adler, and L. Maier-Hein, “Estimation of blood oxygenation with learned spectral decoloring for quantitative photoacoustic imaging (LSD-qPAI),” *arXiv preprint arXiv:1902.05839*, 2019.
- [5] J. Gröhl, T. Kirchner, T. J. Adler, L. Hacker, N. Holzwarth, A. Hernández-Aguilera, M. A. Herrera, E. Santos, S. E. Bohndiek, and L. Maier-Hein, “Learned spectral decoloring enables photoacoustic oximetry,” *Scientific Reports*, vol. 11, no. 1, pp. 1–12, 2021.
- [6] R. Weissleder and V. Ntziachristos, “Shedding light onto live molecular targets,” *Nature Medicine*, vol. 9, no. 1, pp. 123–128, 2003.
- [7] J. Brunner, J. Yao, J. Laufer, and S. E. Bohndiek, “Photoacoustic imaging using genetically encoded reporters: A review,” *Journal of Biomedical Optics*, vol. 22, no. 7, p. 070901, 2017.
- [8] J. Weber, P. C. Beard, and S. E. Bohndiek, “Contrast agents for molecular photoacoustic imaging,” *Nature Methods*, vol. 13, no. 8, pp. 639–650, 2016.
- [9] U. Dahlstrand, R. Sheikh, A. Merdasa, R. Chakari, B. Persson, M. Cinthio, T. Erlöv, B. Gesslein, and M. Malmjö, “Photoacoustic imaging for three-dimensional visualization and delineation of basal cell carcinoma in patients,” *Photoacoustics*, vol. 18, p. 100187, 2020.
- [10] M. Arabul, M. Rutten, P. Bruneval, M. van Sambeek, F. van de Vosse, and R. Lopata, “Unmixing multi-spectral photoacoustic sources in human carotid plaques using non-negative independent component analysis,” *Photoacoustics*, vol. 15, p. 100140, 2019.
- [11] W. Xia, S. J. West, D. I. Nikitichev, S. Ourselin, P. C. Beard, and A. E. Desjardins, “Interventional multispectral photoacoustic imaging with a clinical linear array ultrasound probe for guiding nerve blocks,” in *Photons Plus Ultrasound: Imaging and Sensing 2016*, International Society for Optics and Photonics, vol. 9708, 2016, p. 97080C.
- [12] L. Ding, X. L. Deán-Ben, N. C. Burton, R. W. Sobol, V. Ntziachristos, and D. Razansky, “Constrained inversion and spectral unmixing in multispectral optoacoustic tomography,” *IEEE Transactions on Medical Imaging*, vol. 36, no. 8, pp. 1676–1685, 2017.
- [13] V. Grasso, J. Holthof, and J. Jose, “An automatic unmixing approach to detect tissue chromophores from multispectral photoacoustic imaging,” *Sensors*, vol. 20, no. 11, p. 3235, 2020.

- [14] R. E. Kumon, C. X. Deng, and X. Wang, "Frequency-domain analysis of photoacoustic imaging data from prostate adenocarcinoma tumors in a murine model," *Ultrasound in Medicine & Biology*, vol. 37, no. 5, pp. 834–839, 2011.
- [15] E. M. Strohm, E. S. Berndl, and M. C. Kolios, "Probing red blood cell morphology using high-frequency photoacoustics," *Biophysical Journal*, vol. 105, no. 1, pp. 59–67, 2013.
- [16] S. Wang, C. Tao, Y. Yang, X. Wang, and X. Liu, "Theoretical and experimental study of spectral characteristics of the photoacoustic signal from stochastically distributed particles," *IEEE Transactions on Ultrasonics, Ferroelectrics, and Frequency Control*, vol. 62, no. 7, pp. 1245–1255, 2015.
- [17] Y. Cao, A. Kole, L. Lan, P. Wang, J. Hui, M. Sturek, and J.-X. Cheng, "Spectral analysis assisted photoacoustic imaging for lipid composition differentiation," *Photoacoustics*, vol. 7, pp. 12–19, 2017.
- [18] M. J. Moore, E. Hysi, M. N. Fadhel, S. El-Rass, Y. Xiao, X.-Y. Wen, and M. C. Kolios, "Photoacoustic f-mode imaging for scale specific contrast in biological systems," *Communications Physics*, vol. 2, no. 1, pp. 1–10, 2019.
- [19] A. Wiacek, K. C. Wang, H. Wu, and M. A. L. Bell, "Dual-wavelength photoacoustic imaging for guidance of hysterectomy procedures," in *Advanced Biomedical and Clinical Diagnostic and Surgical Guidance Systems XVIII*, International Society for Optics and Photonics, vol. 11229, 2020, p. 112291D.
- [20] M. Graham, F. Assis, D. Allman, A. Wiacek, E. Gonzalez, M. Gubbi, J. Dong, H. Hou, S. Beck, J. Chrispin, and M. A. L. Bell, "In vivo demonstration of photoacoustic image guidance and robotic visual servoing for cardiac catheter-based interventions," *IEEE Transactions on Medical Imaging*, vol. 39, no. 4, pp. 1015–1029, 2020.
- [21] L. M. Hinkelman, T. D. Mast, L. A. Metlay, and R. C. Waag, "The effect of abdominal wall morphology on ultrasonic pulse distortion. Part I. Measurements," *The Journal of the Acoustical Society of America*, vol. 104, no. 6, pp. 3635–3649, 1998.
- [22] E. Gonzalez and M. A. L. Bell, "Segmenting bone structures in ultrasound images with Locally Weighted SLSC (LW-SLSC) beamforming," in *2018 IEEE International Ultrasonics Symposium (IUS)*, IEEE, 2018, pp. 1–9.
- [23] E. A. Gonzalez and M. A. L. Bell, "Acoustic frequency-based differentiation of photoacoustic signals from surgical biomarkers," in *2020 IEEE International Ultrasonics Symposium (IUS)*, IEEE, 2020, pp. 1–4.
- [24] A. Taruttis, A. Rosenthal, M. Kacprowicz, N. C. Burton, and V. Ntziachristos, "Multiscale multispectral optoacoustic tomography by a stationary wavelet transform prior to unmixing," *IEEE Transactions on Medical Imaging*, vol. 33, no. 5, pp. 1194–1202, 2014.
- [25] A. Wiacek and M. A. L. Bell, "Photoacoustic-guided surgery from head to toe," *Biomedical Optics Express*, vol. 12, no. 4, pp. 2079–2117, 2021.
- [26] M. A. Lediju Bell, "Photoacoustic imaging for surgical guidance: Principles, applications, and outlook," *Journal of Applied Physics*, vol. 128, no. 6, p. 060 904, 2020.

- [27] M. Allard, J. Shubert, and M. A. L. Bell, “Feasibility of photoacoustic guided hysterectomies with the da Vinci robot,” in *Medical Imaging 2018: Image-Guided Procedures, Robotic Interventions, and Modeling*, International Society for Optics and Photonics, vol. 10576, 2018, 105760A.
- [28] ———, “Feasibility of photoacoustic-guided teleoperated hysterectomies,” *Journal of Medical Imaging*, vol. 5, no. 2, p. 021 213, 2018.
- [29] A. Wiacek, K. C. Wang, and M. A. L. Bell, “Techniques to distinguish the ureter from the uterine artery in photoacoustic-guided hysterectomies,” in *Photons Plus Ultrasound: Imaging and Sensing 2019*, International Society for Optics and Photonics, vol. 10878, 2019, 108785K.
- [30] M. T. Graham, J. Huang, F. X. Creighton, and M. A. L. Bell, “Simulations and human cadaver head studies to identify optimal acoustic receiver locations for minimally invasive photoacoustic-guided neurosurgery,” *Photoacoustics*, vol. 19, p. 100 183, 2020.
- [31] M. A. L. Bell, A. K. Ostrowski, P. Kazanzides, and E. Boctor, “Feasibility of transcranial photoacoustic imaging for interventional guidance of endonasal surgeries,” in *Photons Plus Ultrasound: Imaging and Sensing 2014*, International Society for Optics and Photonics, vol. 8943, 2014, p. 894 307.
- [32] M. T. Graham, F. X. Creighton, and M. A. L. Bell, “Validation of eyelids as acoustic receiver locations for photoacoustic-guided neurosurgery,” in *Photons Plus Ultrasound: Imaging and Sensing 2021*, International Society for Optics and Photonics, vol. 11642, 2021, p. 1 164 228.
- [33] M. T. Graham, J. Y. Guo, and M. A. L. Bell, “Simultaneous visualization of nerves and blood vessels with multispectral photoacoustic imaging for intraoperative guidance of neurosurgeries,” in *Advanced Biomedical and Clinical Diagnostic and Surgical Guidance Systems XVII*, International Society for Optics and Photonics, vol. 10868, 2019, 108680R.
- [34] J. Shubert and M. A. L. Bell, “Photoacoustic imaging of a human vertebra: Implications for guiding spinal fusion surgeries,” *Physics in Medicine & Biology*, vol. 63, no. 14, p. 144 001, 2018.
- [35] E. A. Gonzalez, A. Jain, and M. A. L. Bell, “Combined ultrasound and photoacoustic image guidance of spinal pedicle cannulation demonstrated with intact ex vivo specimens,” *IEEE Transactions on Biomedical Engineering*, vol. 68, no. 8, pp. 2479–2489, 2020.
- [36] E. Gonzalez, A. Wiacek, and M. A. L. Bell, “Visualization of custom drill bit tips in a human vertebra for photoacoustic-guided spinal fusion surgeries,” in *Photons Plus Ultrasound: Imaging and Sensing 2019*, International Society for Optics and Photonics, vol. 10878, 2019, p. 108785M.
- [37] B. Eddins and M. A. L. Bell, “Design of a multifiber light delivery system for photoacoustic-guided surgery,” *Journal of Biomedical Optics*, vol. 22, no. 4, p. 041 011, 2017.
- [38] M. A. L. Bell and J. Shubert, “Photoacoustic-based visual servoing of a needle tip,” *Scientific Reports*, vol. 8, no. 1, p. 15 519, 2018.
- [39] M. Li, Y. Tang, and J. Yao, “Photoacoustic tomography of blood oxygenation: A mini review,” *Photoacoustics*, vol. 10, pp. 65–73, 2018.

- [40] J. Shen, C.-P. Zhou, X.-M. Zhong, R.-M. Guo, J. F. Griffith, L.-N. Cheng, X.-H. Duan, and B.-L. Liang, "MR neurography: T1 and T2 measurements in acute peripheral nerve traction injury in rabbits," *Radiology*, vol. 254, no. 3, pp. 729–738, 2010.
- [41] V. Garcia, E. Debreuve, F. Nielsen, and M. Barlaud, "K-nearest neighbor search: Fast GPU-based implementations and application to high-dimensional feature matching," in *2010 IEEE International Conference on Image Processing*, IEEE, 2010, pp. 3757–3760.
- [42] G. Florimbi, H. Fabelo, E. Torti, R. Lazcano, D. Madroñal, S. Ortega, R. Salvador, F. Leporati, G. Danese, A. Báez-Quevedo, G. Callico, E. Juarez, C. Sanz, and R. Sarmiento, "Accelerating the K-nearest neighbors filtering algorithm to optimize the real-time classification of human brain tumor in hyperspectral images," *Sensors*, vol. 18, no. 7, p. 2314, 2018.
- [43] L. Zhu, H. Jin, R. Zheng, and X. Feng, "Effective naive Bayes nearest neighbor based image classification on GPU," *The Journal of Supercomputing*, vol. 68, no. 2, pp. 820–848, 2014.
- [44] B. Aydin, "Parallel algorithms on nearest neighbor search," *Survey Paper, Georgia State University*, 2014.
- [45] R. Gil-Garcia, J. M. Badia-Contelles, and A. Pons-Porrata, "Parallel nearest neighbour algorithms for text categorization," in *European Conference on Parallel Processing*, Springer, 2007, pp. 328–337.
- [46] A. K. Jain and J. Mao, "A k-nearest neighbor artificial neural network classifier," in *IJCNN-91-Seattle International Joint Conference on Neural Networks*, IEEE, vol. 2, 1991, pp. 515–520.
- [47] L. Wang, X. Zhu, B. Yang, J. Guo, S. Liu, M. Li, J. Zhu, and A. Abraham, "Accelerating nearest neighbor partitioning neural network classifier based on CUDA," *Engineering Applications of Artificial Intelligence*, vol. 68, pp. 53–62, 2018.
- [48] P. N. Belhumeur, J. P. Hespanha, and D. J. Kriegman, "Eigenfaces vs. fisherfaces: Recognition using class specific linear projection," *IEEE Transactions on Pattern Analysis and Machine Intelligence*, vol. 19, no. 7, pp. 711–720, 1997.
- [49] K.-C. Kwak and W. Pedrycz, "Face recognition using a fuzzy fisherface classifier," *Pattern Recognition*, vol. 38, no. 10, pp. 1717–1732, 2005.
- [50] J. Wright, A. Y. Yang, A. Ganesh, S. S. Sastry, and Y. Ma, "Robust face recognition via sparse representation," *IEEE Transactions on Pattern Analysis and Machine Intelligence*, vol. 31, no. 2, pp. 210–227, 2008.
- [51] J. Yang, D. Chu, L. Zhang, Y. Xu, and J. Yang, "Sparse representation classifier steered discriminative projection with applications to face recognition," *IEEE Transactions on Neural Networks and Learning Systems*, vol. 24, no. 7, pp. 1023–1035, 2013.
- [52] K.-S. Chuang, H.-L. Tzeng, S. Chen, J. Wu, and T.-J. Chen, "Fuzzy c-means clustering with spatial information for image segmentation," *Computerized Medical Imaging and Graphics*, vol. 30, no. 1, pp. 9–15, 2006.
- [53] H. F. Kaiser, "The application of electronic computers to factor analysis," *Educational and Psychological Measurement*, vol. 20, no. 1, pp. 141–151, 1960.

- [54] R. E. Baddour, M. D. Sherar, J. Hunt, G. Czarnota, and M. C. Kolios, “High-frequency ultrasound scattering from microspheres and single cells,” *The Journal of the Acoustical Society of America*, vol. 117, no. 2, pp. 934–943, 2005.
- [55] N. De Morais and C. Brett, “Influence of power ultrasound on the corrosion of aluminium and high speed steel,” *Journal of Applied Electrochemistry*, vol. 32, no. 6, pp. 653–660, 2002.
- [56] N. Netshidavhini and B. M. Raymond, “Effects of various couplants on carbon steel and aluminium materials using ultrasonic testing,” in *18th World Conference on Nondestructive Testing*, 2012, pp. 16–20.

Chapter 6

Estimating Fractional Chromophore Contents during Surgical Interventions

The work presented in this chapter was published in the following manuscript:

E. A. Gonzalez and M. A. L. Bell, “Dual-wavelength photoacoustic atlas method to estimate fractional methylene blue and hemoglobin contents,” *Journal of Biomedical Optics*, vol. 27, no. 9, p. 096 002, 2022

6.1 Introduction

Exogenous chromophores [2, 3] play a critical role in photoacoustic drug delivery [4, 5], overcoming imaging challenges associated with visualizing low signal amplitudes, small vasculature targets, and deep structures that suffer from optical and acoustic attenuation. Over the past 20 years, exogenous chromophores have been administered to increase signal contrast with beneficial applications in angiogenesis for cancer monitoring [6, 7], enhanced photoacoustic angiography [8], lymph node tracers in breast cancer [9, 10], deep imaging [11], lymphatic drainage [12], and brain imaging [13]. Possible contrast agent chromophores include gold nanostructures [6, 14, 15], carbon nanotubes [16], fluorescent proteins [12, 17, 18], methylene blue (MB) [19, 20], and indocyanine green (ICG) [8, 21, 22] dyes.

Depending on the dose, exposure time, and number of target cells, adverse effects due to misuse of contrast agents include acute inflammation [23], apoptosis [23, 24], necrosis [15], cellular toxicity [25], allergies [26], reduction in cellular viability [27], nephropathy [28], hemolysis [29], and photodamage [30]. In addition, maximum absorption and clearance times (i.e., the time for the drug to completely leave the system) range from 5 minutes to 24 hours among the drug delivery approaches reported in the literature [21, 31–33], requiring different dose, delivery, and monitoring protocols.

Currently, most approaches to measuring the concentration levels of chromophores rely on the acquisition of photoacoustic responses from multiple laser wavelength emissions paired with spectral unmixing methods [34–41]. However, as real-time implementations are necessary for monitoring chromophores of short clearance time in applications like photoacoustic-guided surgery [42–45], traditional techniques are typically not feasible because of the lengthy acquisition times associated with transmitting multiple laser wavelengths to achieve a single estimate [46]. In addition, traditional spectral unmixing techniques do not typically consider differences in acoustic spectra, which has the potential to provide additional information for differentiation of exogenous and endogenous chromophores.

We previously proposed an acoustic frequency-based method to discriminate photoacoustic responses from different materials and overcome challenges with traditional spectral unmixing techniques [47]. By measuring the photoacoustic response from only two laser wavelengths, the initial version of our dual-wavelength atlas method achieved comparable sensitivity, specificity, and accuracy to traditional spectral unmixing methods [48, 49] and related classifiers [50, 51]. Based on the linear relationship between contrast agent concentration and photoacoustic amplitude [52–54], we hypothesize that our method can be extended to locally characterize the volumetric ratio between two photoacoustic-sensitive materials. Specifically, we focus on the exogenous chro-

mophore MB and the endogenous chromophore hemoglobin (Hb), motivated by the potential for photoacoustic-based catheter interventions performed with an optical fiber housed within a cardiac catheter inserted through a major vein [55]. MB would be administered through the catheter and eventually mix with Hb to enhance the visualization of target structures in vascular pathologies (e.g., atherosclerotic plaques [56], thrombi [57], tumor neovasculatures [58, 59], endothelia [60]), and the local concentration of MB vs. Hb would be monitored with our proposed method with either external [55] or intravascular [61] ultrasound sensor placement. This monitoring will enable real-time interventions to avoid adverse effects produced by the unnecessary accumulation of MB [62–65]. In addition, the MB used in the present study serves as a surrogate for other potential intravascular contrast agents that would similarly benefit from local concentration monitoring to prevent cell toxicity [25, 61].

The remainder of this paper is organized as follows. Section 6.2 details the phantom experimental setup, a novel dual-wavelength atlas method to estimate MB and Hb concentrations, and quantitative metrics for performance evaluation. Section 6.3 presents the quantitative evaluation of mixture estimation performance, as well as evaluation of linear and monotonic trends of estimated concentration versus ground-truth labels, including an assessment of appropriate region sizes to perform the proposed estimation. Section 6.4 discusses insights from these results, and Section 6.5 summarizes the clinical impact of the proposed methods.

6.2 Method

6.2.1 Experimental setup

A polyvinyl chloride-plastisol (PVCP) phantom was fabricated with hollow chambers, each with a diameter of 15 mm and a depth of 55 mm. To minimize the variability of ultrasound scattering among chambers due to different air bubble distributions, a single chamber was filled with either a 100 μ M aqueous solution of MB

from Fisher Scientific (Waltham, MA), blood (Hb), or a combination of MB and Hb. A 1-mm-diameter optical fiber was inserted in the filled chamber, and the fiber tip was positioned approximately 20 mm below the top surface. The optical fiber was connected to a Phocus Mobile laser (Opotek Inc., Carlsbad, CA, USA), transmitting laser light with wavelengths of 710 nm and 870 nm and with a laser energy of 3 mJ. The resulting photoacoustic signals were received by an Alpinion L3-8 linear array ultrasound probe (Alpinion Medical Systems, Seoul, South Korea) positioned on the lateral wall of the phantom, approximately 20 mm from the hollow chamber cross section. This experimental setup, which is shown in Fig. 6-1(a), has been described in previous publications [47, 66].

Two types of Hb samples were used in this study. First, 23 vials of fresh human Hb were obtained up to two days after blood draw and storage, mixed in a single container, and exposed to air for approximately 1 hour to minimize the variability of Hb oxygenation levels. Second, experimental whole porcine blood (Innovative Research, Novi, MI) was used on the fourth day of its reported 24-day lifetime.

A total of 11 concentration levels were prepared using different 2 mL mixtures of Hb and MB. These concentrations ranged from 0% to 100% in 10% increments of MB volume percentage. For example, for the 2 mL MB-Hb mixture, a concentration of 60% MB consisted of 1.2 mL of 100 μ M MB and 0.8 mL of Hb. Each concentration mixture was manually stirred with a syringe in a separate container. Unless otherwise stated, the % concentrations reported in this manuscript refer to the % MB concentration. Five trials were conducted for each concentration level by fixing the light-delivering optical fiber at 0°, with 20 photoacoustic frames (10 per wavelength) acquired per trial using a frame rate of 5 Hz. Note that two blocks of 64-channel aperture data were required to obtain an image created from 128 receive elements, which reduced the possible frame rate from 10 Hz (based on the 10 Hz laser pulse repetition frequency) to 5 Hz.

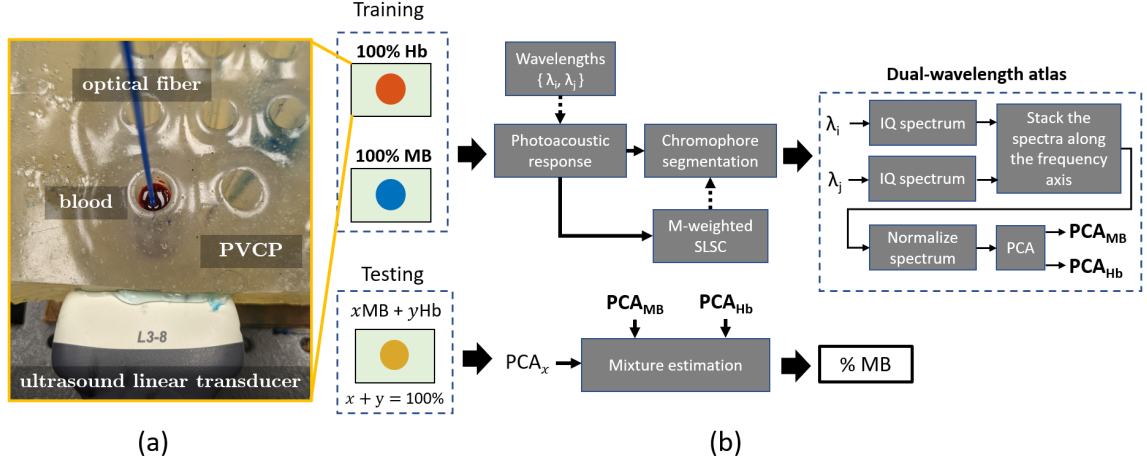


Figure 6-1. (a) Experimental setup and (b) framework of the dual-wavelength atlas method for mixture estimation of methylene blue (MB) and Hb (Hb)

6.2.2 Dual-wavelength atlas method for mixture estimation

The framework for mixture estimation is illustrated in Fig. 6-1(b), based on the dual-wavelength atlas method previously proposed for the identification of individual chromophores [47]. With this setup, frequency domain information is expected to be useful because the optical fiber is placed inside the PVC chamber, thus generating fluence maps that diminish radially from the tip of the optical fiber. This fluence distribution generates unequal acoustic frequency response, as volume regions of different sizes are being excited. Thus, the proposed algorithm is anticipated to leverage frequency domain information to differentiate photoacoustic responses from various concentrations of chromophores.

To implement the proposed approach, conventional delay-and-sum (DAS) beam-forming was first employed to create photoacoustic images for each wavelength emission, concentration, and trial. In contrast to preceding work [67], we used M-Weighted short-lag spatial coherence (SLSC)[68] with a cumulative lag $M = 20$ instead of conventional SLSC with $M = 5$ to generate the binary masks that segmented signals of interest and provided ground-truth labels. This specific M-Weighted SLSC cumulative lag value (i.e., $M = 20$) was chosen based on the comparison of SLSC[69] images with

M-weighted SLSC. First, a representative SLSC[69] photoacoustic image from the blood dataset was generated with $M = 5$. The same photoacoustic frame was then processed with M-weighted SLSC with M values ranging from 10 to 30. Binary masks generated with a -3 dB threshold were then created for each image, and the similarity was defined with the Dice coefficient [70]:

$$\text{Dice Coefficient} = \frac{2 \sum \text{AND}(\text{Mask}_{\text{SLSC}}, \text{Mask}_{\text{M-Weighted SLSC}})}{\sum \text{Mask}_{\text{SLSC}} + \sum \text{Mask}_{\text{M-Weighted SLSC}}} \times 100\%, \quad (6.1)$$

where AND is the logical "AND" operator between the binary masks. This process was then repeated for one trial of the human Hb dataset, containing 11 concentrations, 2 wavelengths, and 10 frames. The Dice coefficients calculated between SLSC and M-Weighted SLSC masks were then plotted as a function of M , resulting in $M = 20$ yielding the highest mean similarity to the SLSC masks with the least standard deviation.

The modification from SLSC in our preceding work [67] to M-Weighted SLSC in this work was implemented to increase the influence of lower lags over higher lags, thus creating less disjointed binary masks. A single binary mask was obtained per trial, resulting from the logical inclusive "OR" operation of 20 masks (obtained from 10 frames per two laser wavelengths).

As noted in Fig. 6-1(b) and in our previous work[67], for each image, only those pixels included in the coherence masks were used for feature extraction, training, and classification. In-phase and quadrature (IQ) demodulation was implemented with 2.75 MHz and 85% bandwidth, and the resulting analytic spectra from a sliding window of axial kernels was stacked along the frequency axis. For the last step of feature extraction, principal component analysis (PCA) was applied to the power of the stacked spectra in order to reduce the complexity of the feature space.

The training dataset consisted of a random trial of 0% MB (i.e., 100% Hb) and 100% MB, and the remaining trials and concentration levels were included in the

testing datasets. After the dual-wavelength atlas was constructed (i.e., PCA_{MB} and PCA_{Hb} in Fig. 6-1(b)), a mixture estimation algorithm was designed to obtain the concentration level of MB from a testing sample. First, $N = 1,000$ samples were randomly selected from the MB and Hb atlas. Then, assuming that mixtures are linear combinations of pure MB and Hb concentrations, a concentration distribution $C' \in \mathbb{R}^{N \times 1}$ was obtained using the following equation:

$$C'_x = \frac{1}{2} + \frac{\|\text{PCA}_x - \text{PCA}_{\text{Hb}}\|_1 - \|\text{PCA}_x - \text{PCA}_{\text{MB}}\|_1}{2\|\text{PCA}_{\text{Hb}} - \text{PCA}_{\text{MB}}\|_1}, \quad 0 \leq C' \leq 1 \quad (6.2)$$

where PCA_x is the projected spectra of $x\%$ testing concentration, $\|\cdot\|_1$ is the Manhattan norm, and each PCA matrix is of size $\mathbb{R}^{N \times p}$ with p principal components. A histogram filter was then applied to the C' vector, where the bin with the highest number of individuals out of 10 bins was extracted. The mean value C'' was computed from the reduced C' vector, and the process was repeated for each valid pixel and frame of the trial. Finally, a median filter was applied to the concentration maps with a kernel of $0.64 \times 0.70 \text{ mm} \times 30$ in the axial, lateral, and frame dimensions, respectively. The 0.64 mm axial kernel length was selected to reside within the frequency response of received photoacoustic signals, which ranged 2.00 MHz to 2.75 MHz, corresponding to wavelengths ranging 0.77 mm to 0.56 mm, respectively. As the lateral and axial resolution of an image differs, the lateral kernel width (i.e., 0.70 mm) was chosen to be the closest possible match to the axial kernel length. The frame dimension of the kernel reduced the concentration tensor from $C'' \in \mathbb{R}^{N_i \times N_j \times N_f}$ to $C \in \mathbb{R}^{N_i \times N_j}$, where N_i and N_j are the number of rows and columns, respectively, of the reconstructed photoacoustic image.

Because Eq (6.2) is applied on frequency data, the three most influential parameters of the dual-wavelength atlas method for the estimation of C are the axial kernel size, threshold of spectral log compression, and number of principal components. An

increase in axial kernel size improves the accuracy of the estimation of spectral amplitudes in the Fourier space. The threshold of spectral log compression adds a tolerance to the discrimination between spectral peaks, which affects the variance that is computed in the PCA. The number of principal components controls the amount of information that is reduced to the feature space.

To provide complementary information regarding the location of photoacoustic targets in the imaging plane, the displayed concentration maps were overlaid with an ultrasound image of the plastisol chamber processed with locally-weighted SLSC (LW-SLSC) [71], using a regularization factor $\alpha = 1$ and a $1.25 \text{ mm} \times 1.2 \text{ mm}$ kernel. The LW-SLSC parameters were obtained from our previous optimization study [67]. A factor of $\alpha=1$ corresponded to an equal weight between cost and penalty function for calculating the optimal coefficients in LW-SLSC. An axial kernel size of 1.25 corresponded to approximately 4.5λ where λ is the wavelength associated with the center frequency of the L3-8 ultrasound probe.

6.2.3 Quantitative metrics

To evaluate the overall accuracy of the dual-wavelength atlas method for mixture estimation, the estimated concentration levels C were first ordered as a function of the ground-truth labels k . The function $f_1 : C(k)$ was then compared to $f_2 : C = k$, representing a 1:1 relationship between estimated and true concentrations. Finally, the coefficient of determination R^2 was used to quantify the performance of the dual-wavelength atlas method:

$$R^2 = 1 - \frac{\sum_k \sum_i C_{ki} - k}{\sum_k \sum_i C_{ki} - \bar{C}} \quad (6.3)$$

where C_{ki} is the estimated concentration of measurement i for a ground-truth concentration k and \bar{C} is the mean estimated concentration. In addition, the R^2 metric was used to assess the linearity of the photoacoustic spectra obtained from mixtures of

MB and Hb by implementing linear regression of spectral amplitudes as a function of the ground-truth concentrations.

Similarly, monotonicity was evaluated in two cases: (1) between photoacoustic spectral amplitudes of a specific frequency and ground-truth concentrations and (2) between estimated and ground-truth concentrations. The monotonic trend of these data pairs were quantified with the Spearman's rank correlation coefficient ρ , described in the following equation [72]:

$$\rho = \frac{\text{cov}(R(X), R(Y))}{\sigma_{R(X)}\sigma_{R(Y)}} \quad (6.4)$$

where $R(X)$ and $R(Y)$ are the rank variables of the measurements X and Y, respectively, X is either the spectral amplitudes or estimated concentrations, Y is the ground-truth concentration, cov represents covariance, and σ is the standard deviation of the rank variables. Spearman's ρ of values 1.0 and -1.0 represent perfect monotonic trends between measurements X and Y that are increasing and decreasing, respectively. Note that the Spearman's ρ measures the level of monotonicity, rather than determining whether or not an evaluated function is monotonic. In this study, we characterize $|\rho| \geq 0.8$ as a strong monotonic trend.

The mean absolute error (MAE) was used to assess the accuracy of the generated concentration maps:

$$\text{MAE}_k = \frac{\sum_{i=1}^{N_k} |C_{ki} - k|}{N_k} \quad (6.5)$$

where C_{ki} is the estimated concentration of pixel i for a ground-truth concentration k , and N_k is the total number of pixels of the concentration map k .

Finally, processing times were computed for the each stage of the dual-wavelength atlas method applied on the human Hb dataset. These stages were: (1) generation of coherence masks, (2) generation of acoustic spectra and spectra stacking, (3) PCA, and (4) estimation of MB concentrations, where the last stage included projection to

the feature space using the principal component coefficient obtained from the atlas. These processing times were evaluated individually when training our method (i.e., constructing the atlas) and testing our method on a single frame (i.e., estimating a concentration map). The processing times for Stages (3) and (4) were only calculated for training and testing, respectively. For training, robustness in the estimation of computation times was achieved by averaging the processing times from 5 different trials of 0% concentration. Similarly, robustness in the estimation of computation times for testing was achieved by averaging the processing times from every frame of the testing dataset detailed in Section 6.2.2. Computation times were measured using the MATLAB (Natick, MA) environment executed on an Intel Core i5-6600K processor with 32 GB RAM and a TITAN Xp graphical processing unit (GPU). To enhance the computation speed of Stage (1) for all results reported in this manuscript, M-weighted SLSC was implemented on the GPU described above, following the architecture of preceding work [69]. In addition, this GPU-M-Weighted SLSC approach and the previously-reported GPU-SLSC approach[69] were both implemented to obtain results for Equation 6.1 in Section 6.2.2.

6.3 Results

6.3.1 Concentration Estimations from MB and Human Hb

Fig. 6-2 shows the results from the photoacoustic spectra obtained with mixtures of MB and human Hb. Stacked photoacoustic spectra are shown in Fig. 6-2(a) with the y axis denoting mixture concentration and the x axis denoting acoustic frequency for optical wavelengths 710 nm (left) and 870 nm (right). Each concentration block separated by the dashed white lines in Fig. 6-2(a) shows 20,000 spectra samples that were randomly selected from the total number of training trials, frames, and kernels. Although a subtle frequency shift is observed in the spectra obtained with the 710 nm wavelength when increasing the MB concentration level, the spectral shift across the

mixture for the 710-nm response was not strongly monotonic ($\rho = -0.63$). Similarly, no apparent spectral shift was observed for the 870-nm response ($\rho = -0.27$). One possible cause of the frequency shift in the spectra obtained with the 710 nm wavelength is the photoacoustic interaction with residual particles of MB in the PVCP chamber. These particles were unable to be removed as they stained the chamber walls and they likely added frequency components to the overall spectral response of different chromophore concentrations.

Fig. 6-2(b) displays the linearity and monotonicity evaluation results as a function of the acoustic frequency for multiple image dynamic ranges. The y axes denote the ρ (left) and R^2 (right) for and linearity and monotonicity evaluations, respectively. The x axis of each plot is divided into acoustic frequencies for optical wavelengths of 710

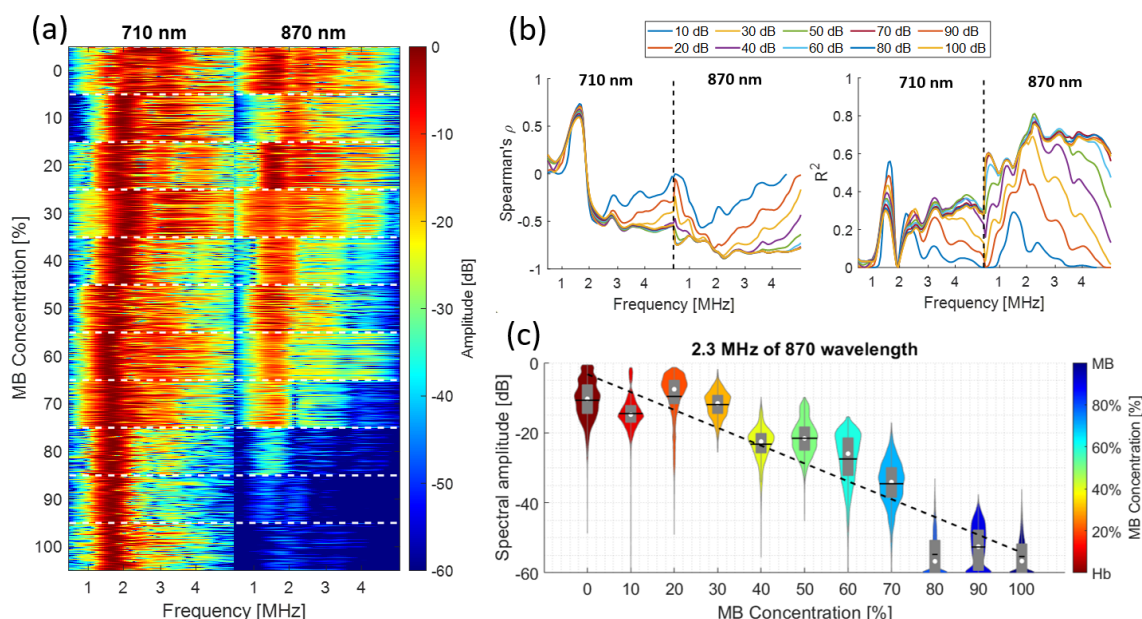


Figure 6-2. Evaluation of monotonicity and linearity of photoacoustic spectra obtained from mixtures of MB and Hb. (a) Stacked photoacoustic spectra of several mixture concentration (y axis) when using 710 nm and 870 nm laser wavelength (x axis). Each spectrum is normalized and log compressed to a 60 dB dynamic range. (b) Spearman's ρ coefficient and R^2 values of linear regression of concentration levels vs. acoustic frequency while varying the log compression dynamic range of the acoustic spectra. (c) Example of an acoustic frequency whose spectral amplitude of concentration levels follow a monotonic trend ($\rho = -0.88$) and a linear trend ($R^2 = 0.76$).

nm (left) and 870 nm (right). In the acoustic frequency range 0.5-5 MHz for 870 nm wavelength, as the dynamic range decreases from 40 dB to 10 dB, the mean \pm one standard deviation of improvements in Spearman's ρ and R^2 were -0.47 ± 0.15 and 0.45 ± 0.14 , respectively. For dynamic ranges greater than 40 dB, the results primarily overlap, and there is less improvement. This overlap likely occurs because the log compression reaches the resolution limit of the acquired photoacoustic amplitudes. However, for 710 nm wavelength, only the acoustic frequency range from 2.4-5 MHz shows ρ and R^2 changes when varying the log compression from 10 to 40 dB. In the acoustic frequency range 0.5-2.4 MHz, results primarily overlap regardless of the chosen dynamic range. This overlap likely occurs because of the strong spectral peak observed from 1.5 MHz to 2.5 MHz for nearly every MB concentration in Fig. 6-2(a) (i.e., the spectral shift pattern described in the preceding paragraph). This strong spectral peak is robust against log compression, which generates minimal changes to the Spearman's ρ and variation of to the R^2 .

Focusing on the R^2 results, multiple strong linear trends were observed when results were obtained with 870 nm laser wavelength, yielding a mean \pm one standard deviation R^2 of 0.74 ± 0.14 for frequencies ranging from 0.5 to 5 MHz and thresholds from 10 to 100 dB. In contrast, no strong linearity was observed for the 710-nm region, yielding an $R^2 = 0.32 \pm 0.21$ for the same range of frequencies and thresholds as the 870-nm region. The strong spectral peak observed in Fig. 6-2 at 710 nm wavelength yielded a maximum R^2 of 0.55 with a dynamic range of 10 dB, while the maximum peak observed in 870 nm was 0.81 with a dynamic range of 50 dB. These results suggest that Hb has a stronger influence on the linear relationship of acoustic frequency vs. concentration compared to MB.

Fig. 6-2(c) shows the linear fit for the acoustic frequency of 2.3 MHz and the dynamic range of 60 dB (i.e., parameters that produced the maximum R^2 in Fig. 6-2(b)). The y axis denotes the log-compressed spectral amplitudes, and the x axis

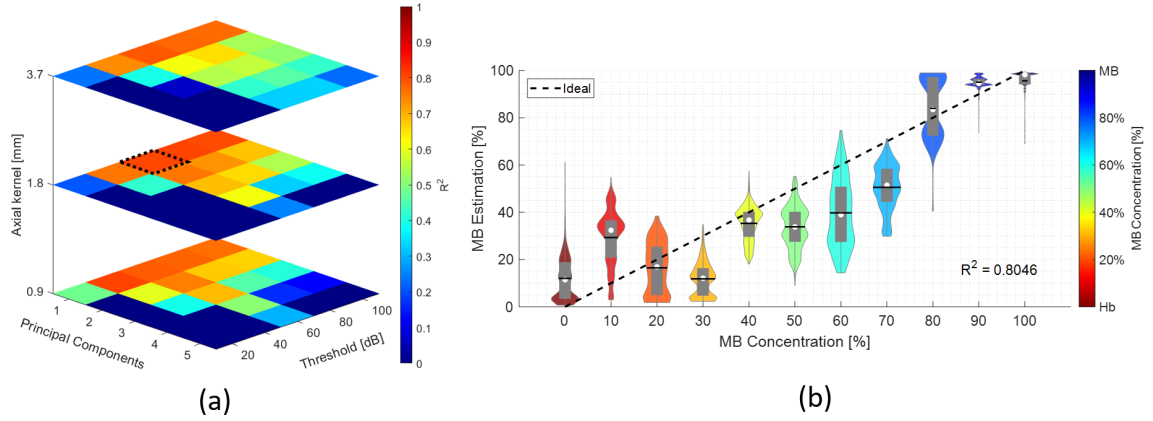


Figure 6-3. Performance optimization of the dual-wavelength atlas algorithm using the human Hb dataset. (a) R^2 values as a function of axial kernel size (z axis), threshold for spectra log compression (x axis), and number of principal components used (y axis). (b) Examples of mixture estimations (y axis) vs ground truth concentrations (x axis) when using the parameter set that yielded the highest R^2 value (i.e., 0.80), represented by dotted square in (a)

denotes the ground-truth concentrations. For each violin plot, the shape, horizontal line, white circle, and gray box represent the kernel density estimate of the data points, mean, median, and interquartile range, respectively. $R^2=0.78$, suggesting a strong linearity and monotonicity between the spectral amplitudes of photoacoustic signals and ground-truth concentrations. The Spearman's ρ was 0.89, which indicates that there is a high level of monotonicity.

Fig. 6-3 shows the optimization of the dual-wavelength atlas method using the human Hb dataset by maximizing the R^2 fit of a 1:1 slope of estimated vs. ground-true concentrations. The variation of R^2 values as a function the three most influential parameter of the dual-wavelength atlas method is shown in Fig. 6-3(a). The z axis denotes the axial kernel size, and the orthogonal axes denotes the number of principal components used and threshold for spectra log compression, respectively. Although increasing the axial kernel size improved the accuracy of the spectral amplitude generated with fast Fourier transforms, no clear improvement was observed when measuring the overall R^2 values. Similarly, parameter sets using two principal

components yielded $R^2 \geq 0.7$, suggesting a good estimation performance when using more than one principal component. However, no improvement was observed for $PC \geq 3$. Finally, increasing the threshold from 20 dB to 60 dB improved the R^2 values when other parameters remained fixed, and no additional improvement was observed for dynamic range thresholds ≥ 60 dB.

Fig. 6-3(b) shows an example of concentration estimation vs. ground-truth concentration when using the optimal set of parameters that yielded the greatest R^2 value, denoted by the dashed black box in Fig. 6-3(a). For this optimized estimation result, the R^2 value and Spearman's ρ was 0.80 and 0.89, respectively, indicating a high degree of linearity and monotonicity, respectively.

6.3.2 Concentration Estimations from MB and Porcine Hb

Fig. 6-4 shows the estimated concentrations when using porcine Hb. The sensitivity of estimated R^2 values while varying two parameters of the dual-wavelength atlas method is shown in Fig. 6-4(a) with the y-axis denoting the threshold for spectra log compression and the x-axis denoting the number of principal components used. These R^2 values were computed by fixing the axial kernel size to 1.8 mm (i.e., optimal

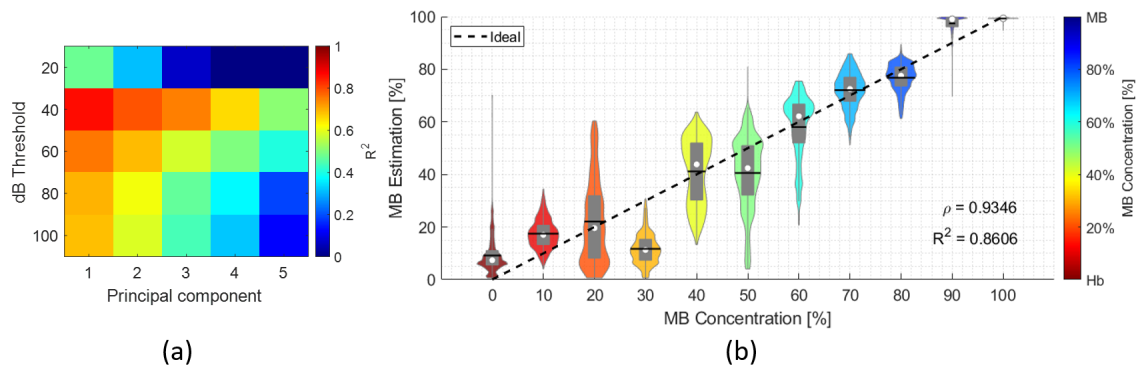


Figure 6-4. Estimated concentrations from porcine Hb. (a) R^2 value of a 1:1 linear fit between estimated and true concentration levels while varying the threshold for spectra log compression (y axis) and number of principal components used (x axis). (b) Mixture estimation (y axis) vs ground truth concentration (x axis) when using a 40 dB threshold and 1 principal component.

parameter obtained in Fig. 6-3(a)). Overall, the effect of varying the number of principal components and the dB threshold implemented prior to the estimating R^2 values showed similar trends to those observed in Fig. 6-3(a) (i.e., decreasing estimation performance with increasing the number of principal components). However, the optimal set of parameters included a threshold of 40 dB instead of the 60 dB threshold obtained in the experiment using human Hb (i.e., Fig. 6-3(a)), with $R^2=0.86$ and $\rho=0.93$.

Fig. 6-4(b) shows detailed estimation results when using the optimal set of parameters from Fig. 6-4(a). The overall performance of the dual-wavelength atlas method when using the porcine Hb was measured by computing the MAE between the vector constructed with the mean of each violin plot and the ground-truth labels, yielding a value of 6.53%. For comparison, the MAE obtained from the optimal parameter set using the human Hb (i.e., Fig. 6-3(b)) was 10.49%. Thus, the dual-wavelength atlas method generated more accurate estimates of MB concentration when using porcine Hb instead of human Hb, which can be attributed to the uniformity in chemical composition and oxygenation levels of the porcine Hb samples.

Fig. 6-5 shows example DAS photoacoustic images, coherence masks, and an estimated concentration map for a ground-truth concentration of 60% of a single trial. These DAS images were normalized to the maximum amplitude value obtained from both 710-nm and 870-nm laser wavelength responses and displayed with 35 dB dynamic range to offer a direct comparison across wavelengths. The contours within each image represent the -3dB boundary of the coherence mask with an area of 5.32 mm². Note that these masks include the low-amplitude regions of the photoacoustic images which appear as if minimal signal is present, which highlights the benefit of the coherence mask that is used to determine the presence of coherent signals, regardless of amplitude. The MAE between the concentration map and the ground truth is 9.68%.

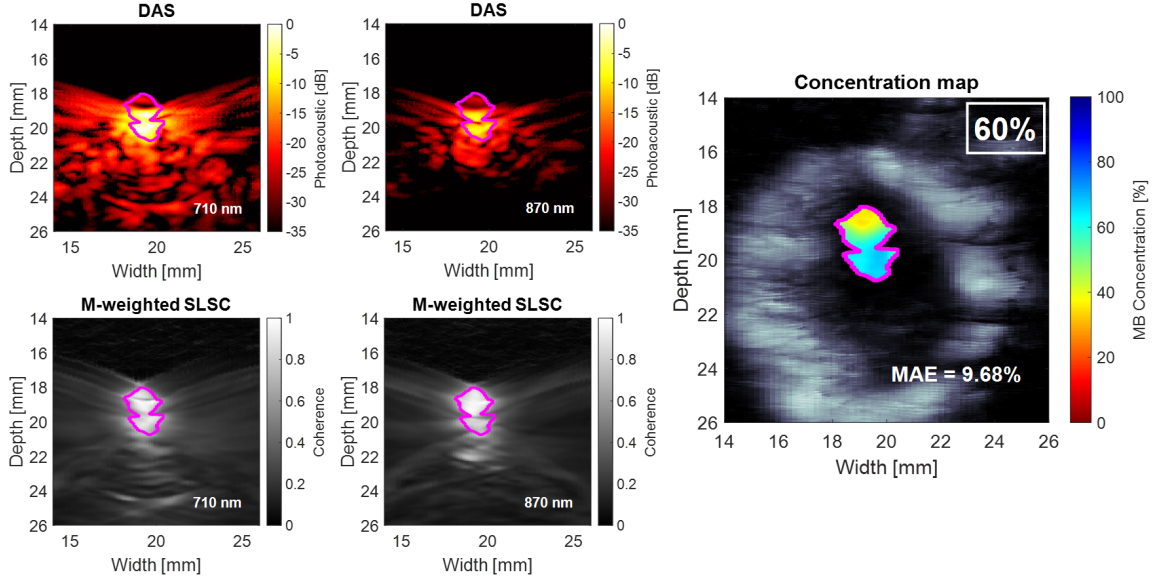


Figure 6-5. Example of photoacoustic DAS images, coherence masks used for segmentation, and estimated concentration map for a ground-truth concentration of 60% (i.e., 60% MB and 40% experimental porcine Hb). The purple contours represent the masks obtained by thresholding the coherence images at -3 dB and merging the results from 710 nm and 870 nm.

Table 6-1 reports the average processing times for each stage of the dual-wavelength atlas method using the porcine Hb dataset. Without considering acquisition times and transferring times of raw photoacoustic data, the construction of the dual-wavelength atlas was completed in less than 6 minutes, while the mean \pm one standard deviation processing time of a single concentration map was 9.2 ± 0.5 seconds. This <10 minutes processing time is relatively fast in comparison to the total procedure times of cardiovascular interventions (e.g., the average procedure time of perfusion coronary interventions is 76 ± 31 min [73]), and it can be performed prior to the initiation of the procedure .

Fig. 6-6 shows examples of concentration maps obtained from one trial per ground-truth concentration results. The 30% concentration map produced the greatest MAE of 14.80%, whereas the 100% concentration maps produced the lowest MAE of 0.72%. These deviations agree with the overall errors shown in Fig. 6-4(b), where 30% and 100% ground-truth concentrations reported MAEs of 18.29% and 0.75%, respectively.

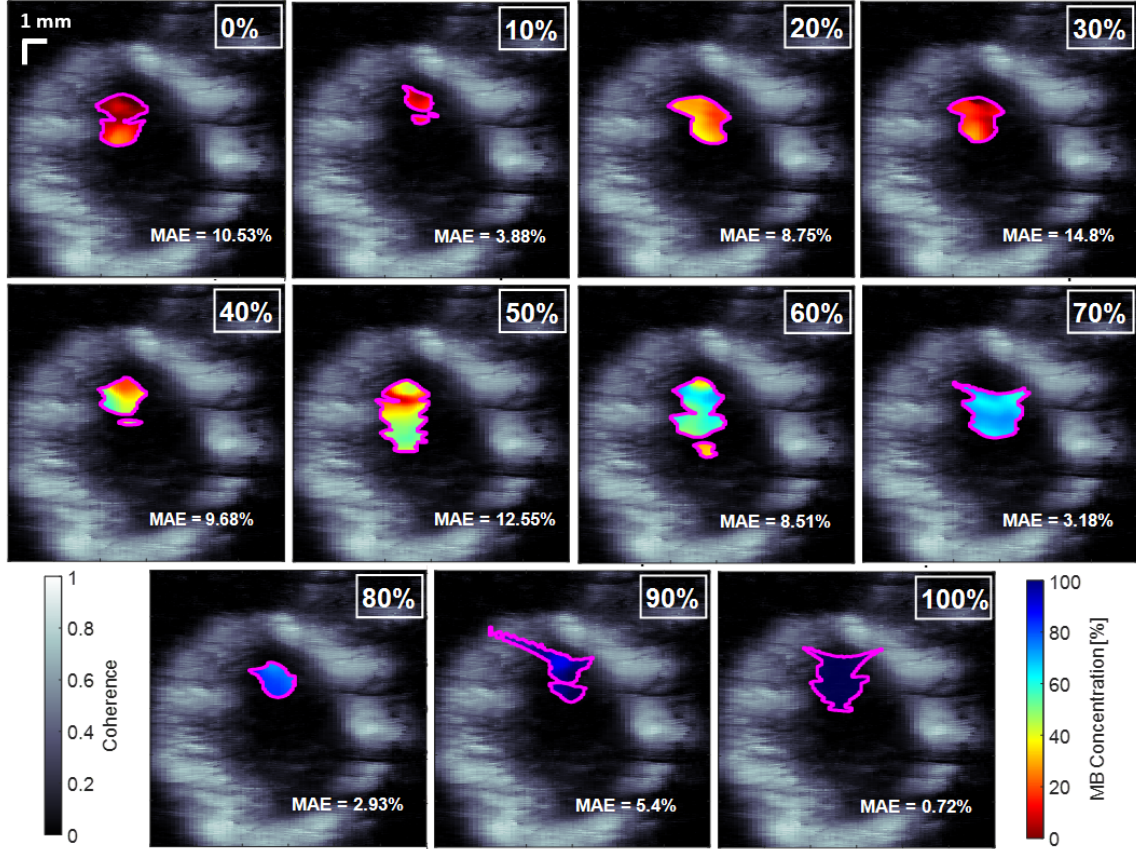


Figure 6-6. Examples of concentration maps of MB and porcine Hb generated by the dual-wavelength atlas method in a phantom experiment. The concentration maps (colored) are overlaid on ultrasound images generated with LW-SLSC.

Overall, the dual-wavelength atlas method achieved greater accuracy when estimating concentration levels that primarily include MB.

Our initial dual-wavelength atlas method used LW-SLSC beamforming to extract meaningful photoacoustic data [47]. The method herein uses M-Weighted SLSC beamforming, rather than LW-SLSC beamforming, in order to reduce the extensive processing times required to generate coherence masks for a total of 2,200 frames (i.e., 11 concentrations \times 2 wavelengths \times 10 frames \times 5 trials \times 2 datasets) of photoacoustic data. However, considering that only a single ultrasound image is needed to show the structural detail surrounding the concentration maps in Figs. 6-5 and 6-6, LW-SLSC was employed to beamform the background ultrasound image and

Table 6-1. Processing times (in seconds) for each training and testing stage of the dual-wavelength atlas method

Stage	Training	Testing (one frame)
Generate coherence masks	135.5 ± 0.4 s	2.3 ± 0.1 s
Convert to frequency domain	180.9 ± 23.6 s	6.4 ± 0.8 s
Apply PCA	2.6 ± 0.1 s	-
Estimate concentrations	-	0.6 ± 0.2 s
Total	319.2 ± 23.7 s	9.2 ± 0.5 s

improve the contrast, edges, and interpretation of the structural details surrounding the photoacoustic signals.

6.3.3 Effect of mask size on concentration estimation performance

To illustrate the impact of mask size on estimation performance, coherence masks were generated from M-weighted SLSC images with coherence thresholds ranging from 0.3 to 0.9 in increments of 0.02. These masks were used to segment photoacoustic signals from the human blood dataset and generated concentration maps of different sizes. Then, for each coherence threshold, the mean absolute error was calculated for the entire 10 frames per 11 concentration levels.

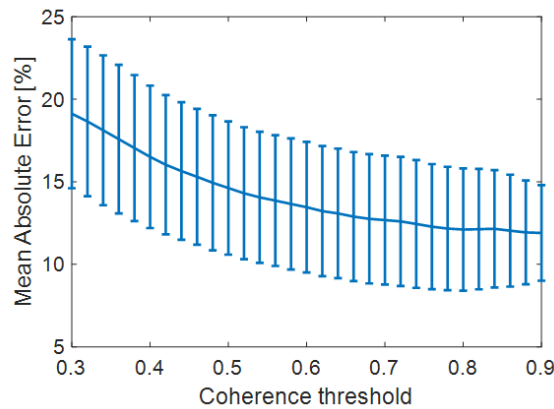


Figure 6-7. Mean absolute error of the estimated chromophore concentration obtained with the dual-wavelength atlas method as a function of M-weighted SLSC coherence thresholds.

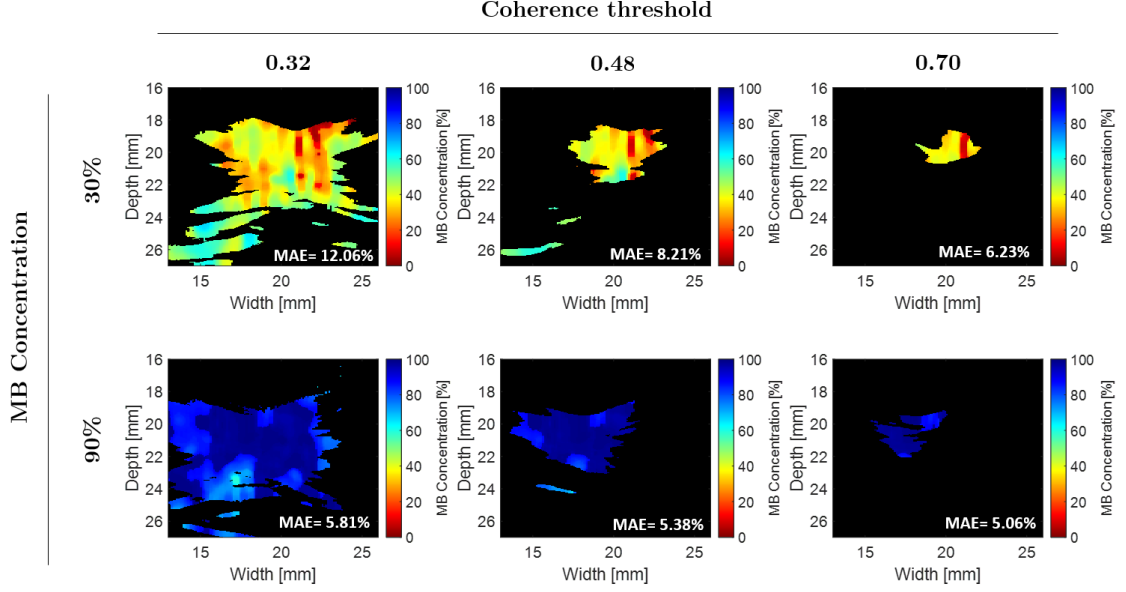


Figure 6-8. Example concentration maps generated with different coherence threshold values.

Fig. 6-7 shows the performance of the dual-wavelength atlas method when using segmented masks generated with varying coherence thresholds. Overall, the mean absolute error decreases when using higher coherence thresholds to generate the segmentation masks. Therefore, we selected a coherence threshold of 0.7 to generate all coherence masks in the experiment results of manuscript.

Fig. 6-8 shows examples of concentration maps with a mixture of 30% MB (top) and 90% MB (bottom) when using coherence thresholds of 0.32, 0.48, and 0.70 (from left to right, respectively). The measured MAE are reported in the lower right corner of each image. For the 30% MB mixture, when increasing the coherence threshold from 0.32 to 0.70, a MAE decrease from 12.06% to 6.23% (i.e., 5.83% decrease) is observed. The reduced error is attributed to absence of inaccurate estimates near the bottom of the 0.70 concentration map. In contrast, for the 90% MB mixture, when increasing the coherence threshold from 0.32 to 0.70, a MAE decrease of from 5.81% to 5.06% (i.e., 0.75% decrease) is observed, which can be attributed to a more uniform distribution of the mixture across the chamber. Overall, decreasing the mask size of

the region of interest with more appropriate thresholding increases the performance of the dual-wavelength atlas method, as observed in Figs. 6-7 and 6-8.

6.4 Discussion

We developed a novel photoacoustic-based, dual-wavelength atlas method that accurately estimates and generates concentration maps of a mixture of endogenous and exogenous chromophores (i.e., MB and Hb, respectively). The method builds on our previous dual-wavelength approach [47] and measures the photoacoustic spectra obtained from two laser wavelength emissions as a linear combination of the chromophore spectra stored in an atlas. Linearity and monotonicity were confirmed with analyses of acoustic spectra and estimated concentrations as the ground-truth concentration increased, as shown in Figs. 6-3 and 6-4, respectively.

Method optimization (see Fig. 6-3(a)) resulted in requiring only the first principal component for feature reduction, which agrees with previous optimization results of the dual-wavelength atlas method [47, 67]. However, the number principal component as well as the axial kernel size required for accurate estimation may increase with noise and diverse photoacoustic responses obtained from different factors, such as fiber tip geometries [74–76], vessel size [77–79], absorber size [80–82], *ex vivo* [83], and *in vivo* [84, 85] data. Future studies will investigate the effect of these factors in the optimization process of our method.

There are three main factors that contribute to the variability of the estimated concentration maps shown in Fig. 6-6. First, the energy fluctuations provided by the laser system translated into unequal fluence among frames (e.g., the mean \pm one standard deviation of the laser energy at the fiber tip was 3.13 ± 0.4 mJ for the human Hb experiment). Second, decreasing the coherence threshold chosen to segment meaningful photoacoustic signals when generating M-weighted SLSC masks decreased the estimation performance of the dual-wavelength atlas method, as show in Figs. 6-7

and 6-8. Third, while precautions were taken to minimize differences in oxygen saturation among Hb samples, such variations were not negligible. Energy fluctuations among consecutive frames and difference in oxygen-saturation levels can be reduced when using fast-tuning lasers and fresh Hb from a single patient, respectively, in more realistic clinical scenarios.

When extending our approach to other ultrasound systems, implementation with a different transducer bandwidth would require an additional IQ calibration step to maximize chromophore concentration estimation performance. Typically, the IQ compression of radiofrequency signals is conducted using a modulation frequency equal to the central frequency of the ultrasound transducer. However, as observed in the stacked spectra shown in Fig. 6-2, most of the frequency content resides within 1 to 4 MHz, while the corresponding transducer center frequency is 5.5 MHz. Therefore, the modulation frequency and bandwidth parameter of the IQ modulation step should be adjusted [67] to segment meaningful spectra from the total bandwidth of the transducer and thus enhance the estimation performance of the proposed algorithm.

In vivo deployment of the dual-wavelength atlas method for mixture estimation requires two considerations. First, given that constructing a photoacoustic atlas is relatively fast (i.e., <10 minutes), extracting presurgical Hb samples from a single patient would be beneficial to minimize the estimation variability due to Hb samples from different patients at different draw times in the training set. Second, smaller vasculature are expected to yield different spectral responses because the frequency components are dependent on the volume of the chamber that is irradiated [79, 86]. For reference, the diameter of the PVCP chamber simulated the average size of the inferior vena cava (i.e., 0.46 to 2.26 cm in diameter [87]). Therefore, vessel-specific parameter optimization is a possible future direction that can be explored with various chamber diameters.

6.5 Conclusion

The work contained herein is the first to present an acoustic-based photoacoustic estimator that relies on training sets to estimate concentration levels from mixtures of photoacoustic-sensitive materials. The proposed method consisted of measuring the acoustic spectra obtained from two laser wavelength emissions as a linear combination of the chromophore spectra stored in an atlas. This linear combination assumption was confirmed with phantom experiments. In clinical practice, we envision dual excitation wavelengths illuminating the region of interest with a fast-tuning laser source, providing real-time labeling of photoacoustic-sensitive regions with a parallelized version of the algorithm. The results from the presented experiments are promising for real-time monitoring of the concentration of contrast agents in the operating room.

6.6 Acknowledgments

This work was supported by NSF CAREER Award ECCS-1751522, NSF SCH Award No. NSF IIS-2014088, and NIH R00-EB018994. The authors acknowledge the support of NVIDIA Corporation with the donation of the Titan Xp GPU used for this research.

References

- [1] E. A. Gonzalez and M. A. L. Bell, “Dual-wavelength photoacoustic atlas method to estimate fractional methylene blue and hemoglobin contents,” *Journal of Biomedical Optics*, vol. 27, no. 9, p. 096 002, 2022.
- [2] H. Xu, Q. Li, L. Wang, Y. He, J. Shi, B. Tang, and C. Fan, “Nanoscale optical probes for cellular imaging,” *Chemical Society Reviews*, vol. 43, no. 8, pp. 2650–2661, 2014.
- [3] D. Wu, L. Huang, M. S. Jiang, and H. Jiang, “Contrast agents for photoacoustic and thermoacoustic imaging: A review,” *International Journal of Molecular Sciences*, vol. 15, no. 12, pp. 23 616–23 639, 2014.
- [4] C. Moore and J. V. Jokerst, “Strategies for image-guided therapy, surgery, and drug delivery using photoacoustic imaging,” *Theranostics*, vol. 9, no. 6, p. 1550, 2019.
- [5] J. Xia, C. Kim, and J. F. Lovell, “Opportunities for photoacoustic-guided drug delivery,” *Current Drug Targets*, vol. 16, no. 6, pp. 571–581, 2015.
- [6] L. Nie, S. Wang, X. Wang, P. Rong, Y. Ma, G. Liu, P. Huang, G. Lu, and X. Chen, “In vivo volumetric photoacoustic molecular angiography and therapeutic monitoring with targeted plasmonic nanostars,” *Small*, vol. 10, no. 8, pp. 1585–1593, 2014.
- [7] S. Mallidi, G. P. Luke, and S. Emelianov, “Photoacoustic imaging in cancer detection, diagnosis, and treatment guidance,” *Trends in Biotechnology*, vol. 29, no. 5, pp. 213–221, 2011.
- [8] X. Wang, G. Ku, M. A. Wegiel, D. J. Bornhop, G. Stoica, and L. V. Wang, “Noninvasive photoacoustic angiography of animal brains in vivo with near-infrared light and an optical contrast agent,” *Optics Letters*, vol. 29, no. 7, pp. 730–732, 2004.
- [9] C. Kim, T. N. Erpelding, L. Jankovic, M. D. Pashley, and L. V. Wang, “Deeply penetrating in vivo photoacoustic imaging using a clinical ultrasound array system,” *Biomedical Optics Express*, vol. 1, no. 1, pp. 278–284, 2010.
- [10] C. Kim, T. N. Erpelding, L. Jankovic, and L. V. Wang, “Performance benchmarks of an array-based hand-held photoacoustic probe adapted from a clinical ultrasound system for non-invasive sentinel lymph node imaging,” *Philosophical Transactions of the Royal Society A: Mathematical, Physical and Engineering Sciences*, vol. 369, no. 1955, pp. 4644–4650, 2011.
- [11] G. Ku and L. V. Wang, “Deeply penetrating photoacoustic tomography in biological tissues enhanced with an optical contrast agent,” *Optics Letters*, vol. 30, no. 5, pp. 507–509, 2005.
- [12] K. Cardinell, N. Gupta, B. D. Koivisto, J. C. Kumaradas, X. Zhou, H. Irving, P. Luciani, and Y. H. Yücel, “A novel photoacoustic-fluorescent contrast agent for quantitative imaging of lymphatic drainage,” *Photoacoustics*, vol. 21, p. 100 239, 2021.
- [13] D. Wang, Y. Wu, and J. Xia, “Review on photoacoustic imaging of the brain using nanoprobes,” *Neurophotonics*, vol. 3, no. 1, p. 010 901, 2016.
- [14] D. Pan, M. Pramanik, A. Senpan, J. S. Allen, H. Zhang, S. A. Wickline, L. V. Wang, and G. M. Lanza, “Molecular photoacoustic imaging of angiogenesis with integrin-targeted gold nanobeacons,” *The FASEB Journal*, vol. 25, no. 3, pp. 875–882, 2011.

- [15] Y.-J. Gu, J. Cheng, C.-C. Lin, Y. W. Lam, S. H. Cheng, and W.-T. Wong, "Nuclear penetration of surface functionalized gold nanoparticles," *Toxicology and Applied Pharmacology*, vol. 237, no. 2, pp. 196–204, 2009.
- [16] J. Koo, M. Jeon, Y. Oh, H. W. Kang, J. Kim, C. Kim, and J. Oh, "In vivo non-ionizing photoacoustic mapping of sentinel lymph nodes and bladders with ICG-enhanced carbon nanotubes," *Physics in Medicine & Biology*, vol. 57, no. 23, p. 7853, 2012.
- [17] G. S. Filonov, A. Krumholz, J. Xia, J. Yao, L. V. Wang, and V. V. Verkhusha, "Deep-tissue photoacoustic tomography of a genetically encoded near-infrared fluorescent probe," *Angewandte Chemie*, vol. 124, no. 6, pp. 1477–1480, 2012.
- [18] D. Razansky, M. Distel, C. Vinegoni, R. Ma, N. Perrimon, R. W. Köster, and V. Ntziachristos, "Multispectral opto-acoustic tomography of deep-seated fluorescent proteins in vivo," *Nature Photonics*, vol. 3, no. 7, pp. 412–417, 2009.
- [19] M. Jeon, W. Song, E. Huynh, J. Kim, J. Kim, B. L. Helfield, B. Y. Leung, D. E. Geortz, G. Zheng, J. Oh, J. F. Lovell, and C. Kim, "Methylene blue microbubbles as a model dual-modality contrast agent for ultrasound and activatable photoacoustic imaging," *Journal of Biomedical Optics*, vol. 19, no. 1, p. 016 005, 2014.
- [20] K. H. Song, E. W. Stein, J. A. Margenthaler, and L. V. Wang, "Noninvasive photoacoustic identification of sentinel lymph nodes containing methylene blue in vivo in a rat model," *Journal of Biomedical Optics*, vol. 13, no. 5, p. 054 033, 2008.
- [21] J. R. Rajian, M. L. Fabiilli, J. B. Fowlkes, P. L. Carson, and X. Wang, "Drug delivery monitoring by photoacoustic tomography with an icg encapsulated double emulsion," *Optics Express*, vol. 19, no. 15, pp. 14 335–14 347, 2011.
- [22] J. P. Thawani, A. Amirshaghagh, L. Yan, J. M. Stein, J. Liu, and A. Tsourkas, "Photoacoustic-guided surgery with indocyanine green-coated superparamagnetic iron oxide nanoparticle clusters," *Small*, vol. 13, no. 37, p. 1 701 300, 2017.
- [23] W.-S. Cho, M. Cho, J. Jeong, M. Choi, H.-Y. Cho, B. S. Han, S. H. Kim, H. O. Kim, Y. T. Lim, B. H. Chung, and J. Jeong, "Acute toxicity and pharmacokinetics of 13 nm-sized peg-coated gold nanoparticles," *Toxicology and Applied pharmacology*, vol. 236, no. 1, pp. 16–24, 2009.
- [24] M. Tsoi, H. Kuhn, W. Brandau, H. Esche, and G. Schmid, "Cellular uptake and toxicity of Au55 clusters," *Small*, vol. 1, no. 8-9, pp. 841–844, 2005.
- [25] A. M. Alkilany and C. J. Murphy, "Toxicity and cellular uptake of gold nanoparticles: What we have learned so far?" *Journal of Nanoparticle Research*, vol. 12, no. 7, pp. 2313–2333, 2010.
- [26] M. Hope-Ross, L. A. Yannuzzi, E. S. Gragoudas, D. R. Guyer, J. S. Slakter, J. A. Sorenson, S. Krupsky, D. A. Orlock, and C. A. Puliafito, "Adverse reactions due to indocyanine green," *Ophthalmology*, vol. 101, no. 3, pp. 529–533, 1994.
- [27] N. Salahuddin, A. Akelah, M. Elnagar, and M. A. Abdelwahab, "Antibacterial and cytotoxicity of methylene blue loaded-cellulose nanocarrier on breast cancer cell line," *Carbohydrate Polymer Technologies and Applications*, vol. 2, p. 100 138, 2021.
- [28] T. H. Au, A. Bruckner, S. M. Mohiuddin, and D. E. Hilleman, "The prevention of contrast-induced nephropathy," *Annals of Pharmacotherapy*, vol. 48, no. 10, pp. 1332–1342, 2014.

- [29] C. Kim, K. H. Song, F. Gao, and L. V. Wang, “Sentinel lymph nodes and lymphatic vessels: Noninvasive dual-modality in vivo mapping by using indocyanine green in rats—volumetric spectroscopic photoacoustic imaging and planar fluorescence imaging,” *Radiology*, vol. 255, no. 2, pp. 442–450, 2010.
- [30] J. J. Nogueira, M. Meixner, M. Bittermann, and L. González, “Impact of lipid environment on photodamage activation of methylene blue,” *ChemPhotoChem*, vol. 1, no. 5, pp. 178–182, 2017.
- [31] V. P. Zharov, E. I. Galanzha, E. V. Shashkov, N. G. Khlebtsov, and V. V. Tuchin, “In vivo photoacoustic flow cytometry for monitoring of circulating single cancer cells and contrast agents,” *Optics Letters*, vol. 31, no. 24, pp. 3623–3625, 2006.
- [32] L. Nie, M. Chen, X. Sun, P. Rong, N. Zheng, and X. Chen, “Palladium nanosheets as highly stable and effective contrast agents for in vivo photoacoustic molecular imaging,” *Nanoscale*, vol. 6, no. 3, pp. 1271–1276, 2014.
- [33] D. Pan, B. Kim, L. V. Wang, and G. M. Lanza, “A brief account of nanoparticle contrast agents for photoacoustic imaging,” *Wiley Interdisciplinary Reviews: Nanomedicine and Nanobiotechnology*, vol. 5, no. 6, pp. 517–543, 2013.
- [34] S. Tzoumas and V. Ntziachristos, “Spectral unmixing techniques for optoacoustic imaging of tissue pathophysiology,” *Philosophical Transactions of the Royal Society A: Mathematical, Physical and Engineering Sciences*, vol. 375, no. 2107, p. 20170262, 2017.
- [35] J. Gröhl, T. Kirchner, T. Adler, and L. Maier-Hein, “Estimation of blood oxygenation with learned spectral decoloring for quantitative photoacoustic imaging (LSD-qPAI),” *arXiv preprint arXiv:1902.05839*, 2019.
- [36] J. Gröhl, T. Kirchner, T. J. Adler, L. Hacker, N. Holzwarth, A. Hernández-Aguilera, M. A. Herrera, E. Santos, S. E. Bohndiek, and L. Maier-Hein, “Learned spectral decoloring enables photoacoustic oximetry,” *Scientific Reports*, vol. 11, no. 1, pp. 1–12, 2021.
- [37] U. Dahlstrand, R. Sheikh, A. Merdasa, R. Chakari, B. Persson, M. Cinthio, T. Erlöv, B. Gesslein, and M. Malmjö, “Photoacoustic imaging for three-dimensional visualization and delineation of basal cell carcinoma in patients,” *Photoacoustics*, vol. 18, p. 100187, 2020.
- [38] M. Arabul, M. Rutten, P. Bruneval, M. van Sambeek, F. van de Vosse, and R. Lopata, “Unmixing multi-spectral photoacoustic sources in human carotid plaques using non-negative independent component analysis,” *Photoacoustics*, vol. 15, p. 100140, 2019.
- [39] J. Weber, P. C. Beard, and S. E. Bohndiek, “Contrast agents for molecular photoacoustic imaging,” *Nature Methods*, vol. 13, no. 8, pp. 639–650, 2016.
- [40] R. Weissleder and V. Ntziachristos, “Shedding light onto live molecular targets,” *Nature Medicine*, vol. 9, no. 1, pp. 123–128, 2003.
- [41] J. Brunner, J. Yao, J. Laufer, and S. E. Bohndiek, “Photoacoustic imaging using genetically encoded reporters: A review,” *Journal of Biomedical Optics*, vol. 22, no. 7, p. 070901, 2017.
- [42] M. A. Lediju Bell, “Photoacoustic imaging for surgical guidance: Principles, applications, and outlook,” *Journal of Applied Physics*, vol. 128, no. 6, p. 060904, 2020.

- [43] A. Wiacek, K. C. Wang, H. Wu, and M. A. L. Bell, "Dual-wavelength photoacoustic imaging for guidance of hysterectomy procedures," in *Advanced Biomedical and Clinical Diagnostic and Surgical Guidance Systems XVIII*, International Society for Optics and Photonics, vol. 11229, 2020, p. 112291D.
- [44] A. Wiacek and M. A. L. Bell, "Photoacoustic-guided surgery from head to toe," *Biomedical Optics Express*, vol. 12, no. 4, pp. 2079–2117, 2021.
- [45] E. M. Donnelly, K. P. Kubelick, D. S. Dumani, and S. Y. Emelianov, "Photoacoustic image-guided delivery of plasmonic-nanoparticle-labeled mesenchymal stem cells to the spinal cord," *Nano Letters*, vol. 18, no. 10, pp. 6625–6632, 2018.
- [46] J. Glatz, N. C. Deliolanis, A. Buehler, D. Razansky, and V. Ntziachristos, "Blind source unmixing in multi-spectral optoacoustic tomography," *Optics Express*, vol. 19, no. 4, pp. 3175–3184, 2011.
- [47] E. A. Gonzalez, C. A. Graham, and M. A. Lediju Bell, "Acoustic frequency-based approach for identification of photoacoustic surgical biomarkers," *Frontiers in Photonics*, vol. 2, 2021. DOI: [10.3389/fphot.2021.716656](https://doi.org/10.3389/fphot.2021.716656).
- [48] V. Grasso, J. Holthof, and J. Jose, "An automatic unmixing approach to detect tissue chromophores from multispectral photoacoustic imaging," *Sensors*, vol. 20, no. 11, p. 3235, 2020.
- [49] W. Xia, S. J. West, D. I. Nikitichev, S. Ourselin, P. C. Beard, and A. E. Desjardins, "Interventional multispectral photoacoustic imaging with a clinical linear array ultrasound probe for guiding nerve blocks," in *Photons Plus Ultrasound: Imaging and Sensing 2016*, International Society for Optics and Photonics, vol. 9708, 2016, p. 97080C.
- [50] Y. Cao, A. Kole, L. Lan, P. Wang, J. Hui, M. Sturek, and J.-X. Cheng, "Spectral analysis assisted photoacoustic imaging for lipid composition differentiation," *Photoacoustics*, vol. 7, pp. 12–19, 2017.
- [51] M. J. Moore, E. Hysi, M. N. Fadhel, S. El-Rass, Y. Xiao, X.-Y. Wen, and M. C. Kolios, "Photoacoustic F-mode imaging for scale specific contrast in biological systems," *Communications Physics*, vol. 2, no. 1, pp. 1–10, 2019.
- [52] A. S. Jeevarathinam, N. Pai, K. Huang, A. Hariri, J. Wang, Y. Bai, L. Wang, T. Hancock, S. Keys, W. Penny, and J. V. Jokerst, "A cellulose-based photoacoustic sensor to measure heparin concentration and activity in human blood samples," *Biosensors and Bioelectronics*, vol. 126, pp. 831–837, 2019.
- [53] K. J. Cash, C. Li, J. Xia, L. V. Wang, and H. A. Clark, "Optical drug monitoring: Photoacoustic imaging of nanosensors to monitor therapeutic lithium in vivo," *ACS Nano*, vol. 9, no. 2, pp. 1692–1698, 2015.
- [54] I.-T. Ho, J. L. Sessler, S. S. Gambhir, and J. V. Jokerst, "Parts per billion detection of uranium with a porphyrinoid-containing nanoparticle and in vivo photoacoustic imaging," *Analyst*, vol. 140, no. 11, pp. 3731–3737, 2015.
- [55] M. Graham, F. Assis, D. Allman, A. Wiacek, E. Gonzalez, M. Gubbi, J. Dong, H. Hou, S. Beck, J. Chrispin, and M. A. L. Bell, "In vivo demonstration of photoacoustic image guidance and robotic visual servoing for cardiac catheter-based interventions," *IEEE Transactions on Medical Imaging*, vol. 39, no. 4, pp. 1015–1029, 2020.

- [56] N. Q. Bui, K. K. Hlaing, V. P. Nguyen, T. H. Nguyen, Y.-O. Oh, X. F. Fan, Y. W. Lee, S. Y. Nam, H. W. Kang, and J. Oh, "Intravascular ultrasonic-photoacoustic (ivup) endoscope with 2.2-mm diameter catheter for medical imaging," *Computerized Medical Imaging and Graphics*, vol. 45, pp. 57–62, 2015.
- [57] S. Raut and P. Gaffney, "Evaluation of the fibrin binding profile of two anti-fibrin monoclonal antibodies," *Thrombosis and Haemostasis*, vol. 76, no. 07, pp. 056–064, 1996.
- [58] A. De La Zerda, C. Zavaleta, S. Keren, S. Vaithilingam, S. Bodapati, Z. Liu, J. Levi, B. R. Smith, T.-J. Ma, O. Oralkan, Z. Cheng, X. Chen, H. Dai, B. T. Khuri-Yakub, and S. S. Gambhir, "Carbon nanotubes as photoacoustic molecular imaging agents in living mice," *Nature Nanotechnology*, vol. 3, no. 9, pp. 557–562, 2008.
- [59] A. d. l. Zerda, Z. Liu, S. Bodapati, R. Teed, S. Vaithilingam, B. T. Khuri-Yakub, X. Chen, H. Dai, and S. S. Gambhir, "Ultrahigh sensitivity carbon nanotube agents for photoacoustic molecular imaging in living mice," *Nano Letters*, vol. 10, no. 6, pp. 2168–2172, 2010.
- [60] D. A. Cheresh, "Integrins in thrombosis, wound healing and cancer," *Biochemical Society Transactions*, vol. 19, no. 4, pp. 835–838, 1991.
- [61] T. Sowers and S. Emelianov, "Exogenous imaging contrast and therapeutic agents for intravascular photoacoustic imaging and image-guided therapy," *Physics in Medicine & Biology*, vol. 63, no. 22, 22TR01, 2018.
- [62] S. J. Wagner, A. Skripchenko, D. Robinette, J. W. Foley, and L. Cincotta, "Factors affecting virus photoinactivation by a series of phenothiazine dyes," *Photochemistry and Photobiology*, vol. 67, no. 3, pp. 343–349, 1998.
- [63] I. Jack Clifton and J. B. Leikin, "Methylene blue," *American Journal of Therapeutics*, vol. 10, no. 4, pp. 289–291, 2003.
- [64] P. R. Ginimuge and S. Jyothi, "Methylene blue: Revisited," *Journal of Anaesthesiology, Clinical Pharmacology*, vol. 26, no. 4, p. 517, 2010.
- [65] K. Buchholz, R. H. Schirmer, J. K. Eubel, M. B. Akoachere, T. Dandekar, K. Becker, and S. Gromer, "Interactions of methylene blue with human disulfide reductases and their orthologues from plasmodium falciparum," *Antimicrobial Agents and Chemotherapy*, vol. 52, no. 1, pp. 183–191, 2008.
- [66] E. A. Gonzalez and M. A. L. Bell, "Acoustic frequency-based differentiation of photoacoustic signals from surgical biomarkers," in *2020 IEEE International Ultrasonics Symposium (IUS)*, IEEE, 2020, pp. 1–4.
- [67] E. A. Gonzalez, C. A. Graham, and M. A. L. Bell, "Optimization of a dual wavelength atlas technique to differentiate methylene blue from hemoglobin in photoacoustic signals," in *Proc. of SPIE Vol.*, vol. 11960, 2022, 119600A–1.
- [68] A. A. Nair, T. D. Tran, and M. A. L. Bell, "Robust short-lag spatial coherence imaging," *IEEE Transactions on Ultrasonics, Ferroelectrics, and Frequency Control*, vol. 65, no. 3, pp. 366–377, 2017.
- [69] E. A. Gonzalez and M. A. L. Bell, "GPU implementation of photoacoustic short-lag spatial coherence imaging for improved image-guided interventions," *Journal of Biomedical Optics*, vol. 25, no. 7, pp. 1–19, 2020.

- [70] B. Guindon and Y. Zhang, "Application of the dice coefficient to accuracy assessment of object-based image classification," *Canadian Journal of Remote Sensing*, vol. 43, no. 1, pp. 48–61, 2017.
- [71] E. A. Gonzalez, A. Jain, and M. A. L. Bell, "Combined ultrasound and photoacoustic image guidance of spinal pedicle cannulation demonstrated with intact ex vivo specimens," *IEEE Transactions on Biomedical Engineering*, vol. 68, no. 8, pp. 2479–2489, 2020.
- [72] P. Sprent, *Applied nonparametric statistical methods*. Springer Science & Business Media, 2012.
- [73] I. Schiks, L. Schoonhoven, F. Verheugt, W. Aengevaeren, and T. Van Achterberg, "Performance evaluation of arterial femoral sheath removal by registered nurses after pci," *European Journal of Cardiovascular Nursing*, vol. 6, no. 3, pp. 172–177, 2007.
- [74] E. Gonzalez, A. Wiacek, and M. A. L. Bell, "Visualization of custom drill bit tips in a human vertebra for photoacoustic-guided spinal fusion surgeries," in *Photons Plus Ultrasound: Imaging and Sensing 2019*, International Society for Optics and Photonics, vol. 10878, 2019, p. 108785M.
- [75] B. Eddins and M. A. L. Bell, "Design of a multifiber light delivery system for photoacoustic-guided surgery," *Journal of Biomedical Optics*, vol. 22, no. 4, p. 041 011, 2017.
- [76] J. Shubert and M. A. L. Bell, "A novel drill design for photoacoustic guided surgeries," in *Photons Plus Ultrasound: Imaging and Sensing 2018*, International Society for Optics and Photonics, vol. 10494, 2018, 104940J.
- [77] M. Zhang, Y. Chen, W. Xie, S. Wu, J. Liao, and Q. Cheng, "Photoacoustic power azimuth spectrum for microvascular evaluation," *Photoacoustics*, vol. 22, p. 100 260, 2021.
- [78] Y. Jiang, T. Harrison, J. C. Ranasinghesagara, and R. J. Zemp, "Photoacoustic and high-frequency power doppler ultrasound biomicroscopy: A comparative study," *Journal of Biomedical Optics*, vol. 15, no. 5, p. 056 008, 2010.
- [79] R. G. Kolkman, P. J. Brands, W. Steenbergen, and T. G. van Leeuwen, "Real-time in vivo photoacoustic and ultrasound imaging," *Journal of Biomedical Optics*, vol. 13, no. 5, p. 050 510, 2008.
- [80] E. Hysi, M. N. Fadhel, M. J. Moore, J. Zalev, E. M. Strohm, and M. C. Kolios, "Insights into photoacoustic speckle and applications in tumor characterization," *Photoacoustics*, vol. 14, pp. 37–48, 2019.
- [81] J. K. Gamelin, A. Aquirre, A. Maurudis, F. Huang, D. Castillo, L. V. Wang, and Q. Zhu, "Curved array photoacoustic tomographic system for small animal imaging," *Journal of Biomedical Optics*, vol. 13, no. 2, p. 024 007, 2008.
- [82] E. M. Strohm and M. C. Kolios, "Classification of blood cells and tumor cells using label-free ultrasound and photoacoustics," *Cytometry Part A*, vol. 87, no. 8, pp. 741–749, 2015.
- [83] V. Daeichin, M. Wu, N. De Jong, A. F. van der Steen, and G. van Soest, "Frequency analysis of the photoacoustic signal generated by coronary atherosclerotic plaque," *Ultrasound in Medicine & Biology*, vol. 42, no. 8, pp. 2017–2025, 2016.

- [84] R. E. Kumon, C. X. Deng, and X. Wang, “Frequency-domain analysis of photoacoustic imaging data from prostate adenocarcinoma tumors in a murine model,” *Ultrasound in Medicine & Biology*, vol. 37, no. 5, pp. 834–839, 2011.
- [85] T. Feng, Y. Zhu, C. Liu, S. Du, D. Ta, Q. Cheng, and J. Yuan, “Ultrasound-guided detection and segmentation of photoacoustic signals from bone tissue in vivo,” *Applied Sciences*, vol. 11, no. 1, p. 19, 2020.
- [86] G. Diebold, T. Sun, and M. Khan, “Photoacoustic monopole radiation in one, two, and three dimensions,” *Physical Review Letters*, vol. 67, no. 24, p. 3384, 1991.
- [87] S. Patil, S. Jadhav, N. Shetty, J. Kharge, B. Puttegowda, R. Ramalingam, and M. N. Cholenahally, “Assessment of inferior vena cava diameter by echocardiography in normal indian population: A prospective observational study,” *Indian Heart Journal*, vol. 68, S26–S30, 2016.

Chapter 7

Conclusions and Future Directions

7.1 Summary

In this dissertation, we addressed primary challenges with implementing a combined ultrasound- and photoacoustic-based surgical guidance system aimed at clinical scenarios inside and surrounding the spine. A summary of the timeline of published journal articles and conference proceedings, color-coded by four subfields, is shown in Fig. 7-1. First, for preoperative registration, we introduced the coherence-based LW-SLSC beamformer to segment key landmarks associated with bone and surgical tool tips. Once we located anatomical regions of interest, we differentiated bone content with a novel contour analysis of photoacoustic signals in order to avoid accidental bone breaches. To enhance the feasibility of our algorithms for real-time implementations, we developed a GPU-SLSC beamformer that is suitable for photoacoustic-based visual servoing tasks and miniaturization of laser sources for photoacoustic imaging. Finally, we used this real-time beamformer to localize catheter tips during cardiac interventions, and developed a photoacoustic-based dual-wavelength atlas method for the identification and estimation of mixture concentration from exogenous and endogenous chromophores, which is beneficial to monitor and avoid the adverse effects associated with incorrect contrast agent doses. These four contributions are beneficial

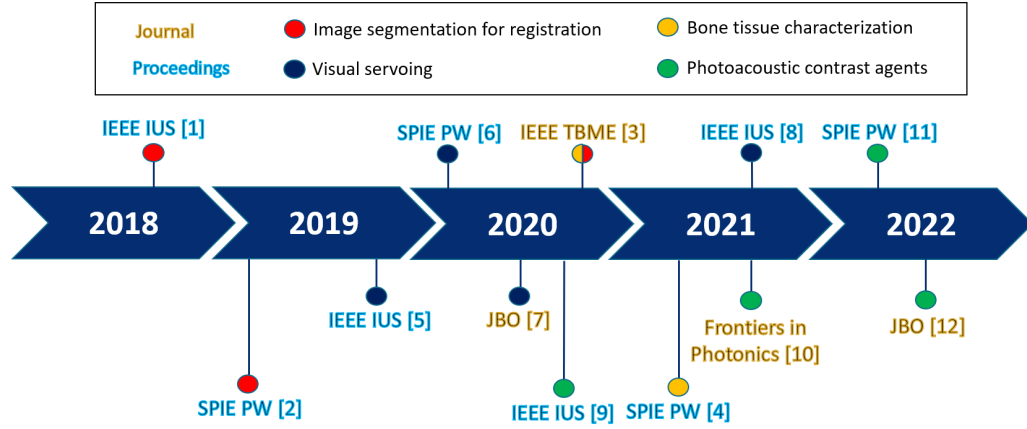


Figure 7-1. Timeline of publications towards the implementation of an ultrasound- and photoacoustic-based surgical guidance system. The publications are grouped by novel solutions to the primary challenges tackled in this thesis: (1) image segmentation for registration [1–3], (2) bone tissue characterization [3, 4], (3) visual servoing [5–8], and (4) photoacoustic contrast agents [9–12]

for the transition of photoacoustic-based surgical guidance towards more challenging clinical scenarios with real-time, reliable, and portable capabilities to characterize biomarkers in the operating room.

The utility of coherence beamforming techniques were demonstrated for each of the four contributions described above. Specifically, SLSC, LW-SLSC, and/or GPU-SLSC played four unique roles throughout this dissertation: (1) enhancement of ultrasound bone boundaries for accurate registration, (2) photoacoustic localization of surgical tool tips, (3) enhancement of photoacoustic image signal-to-noise ratios acquired with low laser energies, and (4) identification followed by segmentation of regions of interest for photoacoustic spectroscopy. Therefore, coherence-based beamforming is fundamental to successful implementation of the combined ultrasound and photoacoustic surgical guidance system described herein.

7.2 Future Directions

7.2.1 Real-Time Coherence-Based Bone Segmentation

LW-SLSC has demonstrated promise to segment bone structures, enabling 2D ultrasound-to-CT registration during surgical interventions located in the spine. In order to deploy this technique in intraoperative imaging protocols, real-time computations of segmented bone structures are required. There are two possible paths for accomplishing computational speed-up. First, given that LW-SLSC operates on independent kernels \hat{R}_i as described in Chapter 2 (Section 2.2.1.2), real-time imaging can be achieved by concurrent execution of each \hat{R}_i in a separate thread inside a GPU. The feasibility of this approach has already been demonstrated in Chapter 4 with the development of the GPU version of photoacoustic SLSC. Similarly, a parallelized version of LW-SLSC can be optimized with the use of *ad hoc* libraries designed for matrix multiplication [13] as well as with the use of efficient approaches for dense/sparse matrix operations [14, 15].

The second possible pathway for computational speed-up incorporates neural networks, which have demonstrated potential to bypass the computational complexity of advanced beamforming techniques [16–18]. We previously developed a deep neural network architecture (i.e., CohereNet) to estimate spatial coherence functions [19], which are foundational to LW-SLSC imaging. This deep learning approach achieved real-time computational processing times and can potentially be adapted to include the additional regularization steps needed for LW-SLSC imaging.

7.2.2 Complementary Bone Characterization

In this dissertation, the discrimination of cortical from cancellous bone was achieved by assessing the spatial morphology of the received photoacoustic responses. However, there are other mechanical properties with similar promise to characterize bone using photoacoustic-based techniques, such as temperature-induced amplitude changes [20,

21], guided waves [22, 23], spectral parameters [24–26], and multiple-wavelength behaviour of received photoacoustic signals [27–29]. Therefore, we hypothesize that the inclusion of these mechanical properties for a more robust bone characterization will provide the surgeon with complementary insight to avoid cortical walls when drilling through the pedicle during spinal fusion surgeries.

7.2.3 Visual Servoing with Pulsed Laser Diodes

Because we demonstrated that successful visual servoing tasks can be achieved with low laser energies, we can use smaller devices for our light delivery system. Good candidates for miniaturized laser sources are pulsed laser diodes, which are reliable, less-expensive, hand-held, and light-weight (about 200 g) alternatives in comparison to the standard Q-switched Nd:YAG/OPO (Optical Parametric Oscillator) lasers used in many photoacoustic imaging applications [30–32]. Hence, the next step for the translation of a portable ultrasound- and photoacoustic-based image guided system consists of exploring the performance of visual servoing tasks using GPU-SLSC photoacoustic images obtained from pulsed laser diodes. The miniaturization of our system will enable surgical guidance in compact rooms with reduced procurement costs, which are critical requirements for implementing image-guidance at medical facilities with low-resource infrastructures.

7.2.4 *In Vivo* Estimation of Mixture Concentrations

In order to transition the dual-wavelength atlas method to determine epidural spreading during spinal injections we need to address three additional tasks. First, as discussed in Chapter 6 (Section 6.4), a vessel-specific parameter optimization is required when administering contrast agents in soft tissue with smaller vasculature compared to cardiac catheter interventions. Second, the atlas should be trained with the chromophore (i.e., lipid) corresponding to the tissue that would most likely interact with the epidural (i.e., nerve). Third, as the method relies on the acquisition of two

laser wavelengths, upgrading the Q-switched Nd:YAG/OPO laser sources to stimulated Raman scattering laser sources [33, 34] could be an interesting option to ensure the feasibility of real-time mixture estimation during catheter interventions.

7.3 Outlook

This dissertation introduces four novel contributions that are beneficial for the transition of a combined ultrasound- and photoacoustic-based image-guidance system towards challenging scenarios of surgical navigation. Focusing on bone structures inside and surrounding the spine, the newly combined systems and techniques demonstrated herein feature robust, accurate, and real-time capabilities to register to preoperative images, localize surgical tool tips, and characterize biomarkers. These contributions strengthen the range of possibilities for spinous and transthoracic ultrasound and photoacoustic navigation, broaden the scope of this field, and shorten the road to clinical implementation in the operating room.

References

- [1] E. Gonzalez and M. A. L. Bell, “Segmenting bone structures in ultrasound images with locally weighted SLSC (LW-SLSC) beamforming,” in *2018 IEEE International Ultrasonics Symposium (IUS)*, IEEE, 2018, pp. 1–9.
- [2] E. Gonzalez, A. Wiacek, and M. A. L. Bell, “Visualization of custom drill bit tips in a human vertebra for photoacoustic-guided spinal fusion surgeries,” in *Photons Plus Ultrasound: Imaging and Sensing 2019*, SPIE, vol. 10878, 2019, pp. 489–495.
- [3] E. A. Gonzalez, A. Jain, and M. A. L. Bell, “Combined ultrasound and photoacoustic image guidance of spinal pedicle cannulation demonstrated with intact ex vivo specimens,” *IEEE Transactions on Biomedical Engineering*, vol. 68, no. 8, pp. 2479–2489, 2020.
- [4] E. Gonzalez, A. Jain, and M. A. L. Bell, “Photoacoustic differentiation of cortical from cancellous bone in the lumbar vertebrae of an intact human cadaver to prevent bone breaches during spinal fusion surgeries,” in *Photons Plus Ultrasound: Imaging and Sensing 2021*, International Society for Optics and Photonics, vol. 11642, 2021, p. 1 164 210.
- [5] E. Gonzalez, M. R. Gubbi, and M. A. L. Bell, “GPU implementation of coherence-based photoacoustic beamforming for autonomous visual servoing,” in *2019 IEEE International Ultrasonics Symposium (IUS)*, IEEE, 2019, pp. 24–27.
- [6] E. Gonzalez and M. A. L. Bell, “A GPU approach to real-time coherence-based photoacoustic imaging and its application to photoacoustic visual servoing,” in *Photons Plus Ultrasound: Imaging and Sensing 2020*, International Society for Optics and Photonics, vol. 11240, 2020, p. 1 124 054.
- [7] E. A. Gonzalez and M. A. L. Bell, “GPU implementation of photoacoustic short-lag spatial coherence imaging for improved image-guided interventions,” *Journal of Biomedical Optics*, vol. 25, no. 7, p. 077 002, 2020.
- [8] E. A. Gonzalez, F. Assis, J. Chrispin, and M. A. L. Bell, “A beamformer-independent method to predict photoacoustic visual servoing system failure from a single image frame,” in *2021 IEEE International Ultrasonics Symposium (IUS)*, IEEE, 2021, pp. 1–4.
- [9] E. A. Gonzalez and M. A. L. Bell, “Acoustic frequency-based differentiation of photoacoustic signals from surgical biomarkers,” in *2020 IEEE International Ultrasonics Symposium (IUS)*, IEEE, 2020, pp. 1–4.
- [10] E. A. Gonzalez, C. A. Graham, and M. A. Lediju Bell, “Acoustic frequency-based approach for identification of photoacoustic surgical biomarkers,” *Frontiers in Photonics*, vol. 2, 2021.
- [11] E. A. Gonzalez, C. A. Graham, and M. A. L. Bell, “Optimization of a dual wavelength atlas technique to differentiate methylene blue from hemoglobin in photoacoustic signals,” in *Photons Plus Ultrasound: Imaging and Sensing 2022*, SPIE, vol. 11960, 2022, pp. 51–58.
- [12] E. A. Gonzalez and M. A. L. Bell, “Dual-wavelength photoacoustic atlas method to estimate fractional methylene blue and hemoglobin contents,” *Journal of Biomedical Optics*, vol. 27, no. 9, p. 096 002, 2022.

- [13] A. Kerr, D. Merrill, J. Demouth, and J. Tran, “Cutlass: Fast linear algebra in CUDA C++,” *NVIDIA Developer Blog*, 2017.
- [14] X. Liu, Y. Liu, H. Yang, M. Dun, B. Yin, Z. Luan, and D. Qian, “Accelerating approximate matrix multiplication for near-sparse matrices on GPUs,” *The Journal of Supercomputing*, pp. 1–28, 2022.
- [15] J. Fernández, J. Perez-Cerrolaza, I. Agirre, A. J. Calderon, J. Abella, and F. J. Cazorla, “On the safe deployment of matrix multiplication in massively parallel safety-related systems,” *Applied Sciences*, vol. 12, no. 8, p. 3779, 2022.
- [16] R. Zhuang and J. Chen, “Deep learning based minimum variance beamforming for ultrasound imaging,” in *Smart Ultrasound Imaging and Perinatal, Preterm and Paediatric Image Analysis*, Springer, 2019, pp. 83–91.
- [17] A. C. Luchies and B. C. Byram, “Deep neural networks for ultrasound beamforming,” *IEEE Transactions on Medical Imaging*, vol. 37, no. 9, pp. 2010–2021, 2018.
- [18] B. Luijten, R. Cohen, F. J. de Bruijn, H. A. Schmeitz, M. Mischi, Y. C. Eldar, and R. J. van Sloun, “Deep learning for fast adaptive beamforming,” in *ICASSP 2019-2019 IEEE International Conference on Acoustics, Speech and Signal Processing (ICASSP)*, IEEE, 2019, pp. 1333–1337.
- [19] A. Wiacek, E. González, and M. A. L. Bell, “Coherenet: A deep learning architecture for ultrasound spatial correlation estimation and coherence-based beamforming,” *IEEE Transactions on Ultrasonics, Ferroelectrics, and Frequency Control*, vol. 67, no. 12, pp. 2574–2583, 2020.
- [20] T. Feng, K. M. Kozloff, C. Tian, J. E. Perosky, Y.-S. Hsiao, S. Du, J. Yuan, C. X. Deng, and X. Wang, “Bone assessment via thermal photo-acoustic measurements,” *Optics Letters*, vol. 40, no. 8, pp. 1721–1724, 2015.
- [21] A. K. Thella, J. Rizkalla, N. Rath, M. Kakani, A. Helmy, P. Salama, and M. E. Rizkalla, “Dynamic thermal/acoustic response for human bone materials at different energy levels: A diagnosis approach,” *Journal of Orthopaedics*, vol. 14, no. 1, pp. 85–90, 2017.
- [22] P. Moilanen, Z. Zhao, P. Karppinen, T. Karppinen, V. Kilappa, J. Pirhonen, R. Myllylä, E. Hægström, and J. Timonen, “Photo-acoustic excitation and optical detection of fundamental flexural guided wave in coated bone phantoms,” *Ultrasound in Medicine & Biology*, vol. 40, no. 3, pp. 521–531, 2014.
- [23] I. Steinberg, L. Shiloh, I. Gannot, and A. Eyal, “First-in-human study of bone pathologies using low-cost and compact dual-wavelength photoacoustic system,” *IEEE Journal of Selected Topics in Quantum Electronics*, vol. 25, no. 1, pp. 1–8, 2018.
- [24] B. Lashkari, L. Yang, and A. Mandelis, “The application of backscattered ultrasound and photoacoustic signals for assessment of bone collagen and mineral contents,” *Quantitative Imaging in Medicine and Surgery*, vol. 5, no. 1, p. 46, 2015.
- [25] W. Xie, T. Feng, M. Zhang, J. Li, D. Ta, L. Cheng, and Q. Cheng, “Wavelet transform-based photoacoustic time-frequency spectral analysis for bone assessment,” *Photoacoustics*, vol. 22, p. 100 259, 2021.
- [26] L. Yang, B. Lashkari, J. W. Tan, and A. Mandelis, “Photoacoustic and ultrasound imaging of cancellous bone tissue,” *Journal of Biomedical Optics*, vol. 20, no. 7, p. 076 016, 2015.

- [27] T. Feng, Y. Zhu, K. M. Kozloff, B. Khoury, Y. Xie, X. Wang, M. Cao, J. Yuan, D. Ta, and Q. Cheng, "Bone chemical composition assessment with multi-wavelength photoacoustic analysis," *Applied Sciences*, vol. 10, no. 22, p. 8214, 2020.
- [28] T. Feng, Y. Xie, W. Xie, D. Ta, and Q. Cheng, "Bone chemical composition analysis using photoacoustic technique," *Frontiers in Physics*, vol. 8, p. 594, 2020.
- [29] T. Feng, Y. Ge, Y. Xie, W. Xie, C. Liu, L. Li, D. Ta, Q. Jiang, and Q. Cheng, "Detection of collagen by multi-wavelength photoacoustic analysis as a biomarker for bone health assessment," *Photoacoustics*, vol. 24, p. 100 296, 2021.
- [30] P. K. Upputuri and M. Pramanik, "Fast photoacoustic imaging systems using pulsed laser diodes: A review," *Biomedical Engineering Letters*, vol. 8, no. 2, pp. 167–181, 2018.
- [31] A. Hariri, A. Fatima, N. Mohammadian, S. Mahmoodkalayeh, M. A. Ansari, N. Bely, and M. R. Avanaki, "Development of low-cost photoacoustic imaging systems using very low-energy pulsed laser diodes," *Journal of Biomedical Optics*, vol. 22, no. 7, p. 075 001, 2017.
- [32] M. A. L. Bell, X. Guo, H. J. Kang, and E. Boctor, "Improved contrast in laser-diode-based photoacoustic images with short-lag spatial coherence beamforming," in *2014 IEEE International Ultrasonics Symposium*, IEEE, 2014, pp. 37–40.
- [33] J. Chen, Y. Zhang, L. He, Y. Liang, and L. Wang, "Wide-field polygon-scanning photoacoustic microscopy of oxygen saturation at 1-mhz a-line rate," *Photoacoustics*, vol. 20, p. 100 195, 2020.
- [34] S. M. Park, S.-W. Cho, B.-M. Kim, T. G. Lee, C.-S. Kim, and S.-W. Lee, "Quickly alternating green and red laser source for real-time multispectral photoacoustic microscopy," *Photoacoustics*, vol. 20, p. 100 204, 2020.

Biographical sketch

Eduardo A. Gonzalez was born Lima, Peru, in 1989. He is a graduate student of biomedical engineering at Johns Hopkins University. He received his BS degree in electronic engineering from the Pontificia Universidad Catolica del Peru (PUCP) in 2013 and his master's degree in mechatronics engineering from PUCP and the Technische Universtaet Ilmenau (TUI), Germany, in 2016. He is a recipient of the 2017 Fulbright Fellowship. His research interests include translational research, real-time ultrasound imaging, advanced beamforming, quantitative ultrasound, elastography, and photoacoustic imaging aimed for surgical interventions.

EDUARDO A. GONZALEZ

RESEARCH FOCUS

Medical imaging; Algorithm optimization; Ultrasound imaging; Photoacoustic imaging; Beam-forming; Elasticity imaging; Parallel processing; Image and signal processing; Quantitative ultrasound imaging; GPU applications, Machine Learning, Deep Learning;

EDUCATION

Johns Hopkins University (JHU), USA *August 2017 - present*
Ph.D. Candidate in Biomedical Engineering

Technische Universitaet Ilmenau (TUI), Germany *July 2016*
M.Sc. in Mechatronic Engineering
Thesis: “Real-time quantitative sonoelastography in an ultrasound research system”
Advisor: Pu Li, Ph.D.

Pontificia Universidad Catolica del Peru (PUCP), Peru *July 2016*
M.Sc. in Mechatronic Engineering, ranked 3 out of 51
Advisor: Benjamin Castaneda, Ph.D.

Pontificia Universidad Catolica del Peru (PUCP), Peru *December 2012*
B.Sc. Electronic (Electrical) Engineering, ranked 2 out of 48.
Engineering License with outstanding mention, January 2013
Thesis: “3D Reconstruction: Implementation of a translation tracking system on a ultrasonic transducer”, advisor: Roberto Lavarello, Ph.D.

PROFESSIONAL MEMBERSHIP

IEEE Ultrasonics Ferroelectrics and Frequency Control Society (UFFC)
IEEE Engineering in Medicine and Biology Society (EMB)
International Society for Optics and Photonics (SPIE)
IEEE Biomedical Engineering Society (BMES)

SCHOLARSHIPS AND AWARDS

IEEE International Travel Award for the International Ultrasonics Symposium *2019*
Fulbright Foreign Student Program *2017*
Deutscher Akademischer Austausch Dienst (DAAD) *2015*
CONCYTEC-Perú grant for the Master program in Mechatronic Engineering *2014*
Marco Polo-PUCP Grant for internship of graduate students *2014*

PUBLICATIONS

Book Chapter

1. **E. A. González**, F. L. Casado, and B. Castaneda, “Clinical applications of elastographic methods to improve prostate cancer evaluation,” in *Tissue Elasticity Imaging*, Elsevier, 2020, pp. 47–66

Peer Reviewed Journal Articles

1. **E. A. González**, and M. A. L. Bell, “Photoacoustic imaging and characterization of bone in medicine: Overview, applications, and outlook,” *To be published on 2023*
2. **E. A. González**, and M. A. L. Bell, “Dual-wavelength photoacoustic atlas method to estimate fractional methylene blue and hemoglobin contents,” *Journal of Biomedical Optics*, vol. 27, no. 9, p. 096 002, 2022
3. M. R. Gubbi, **E. A. González**, and M. A. L. Bell, “Theoretical framework to predict generalized contrast-to-noise ratios of photoacoustic images with applications to computer vision,” *IEEE Transactions on Ultrasonics, Ferroelectrics, and Frequency Control*, 2022
4. **E. A. González**, C. A. Graham, and M. A. L. Bell, “Acoustic frequency-based approach for identification of photoacoustic surgical biomarkers,” *Frontiers in Photonics*, vol. 2, 2021
5. **E. A. González**, A. Jain, and M. A. L. Bell, “Combined ultrasound and photoacoustic image guidance of spinal pedicle cannulation demonstrated with intact ex vivo specimens,” *IEEE Transactions on Biomedical Engineering*, 2020
6. **E. A. González**, and M. A. L. Bell, “GPU implementation of photoacoustic short-lag spatial coherence imaging for improved image-guided interventions,” *Journal of Biomedical Optics*, vol. 25, no. 7, p. 077 002, 2020
7. A. Wiacek, **E. A. González**, and M. A. L. Bell, “Coherenet: A deep learning architecture for ultrasound spatial correlation estimation and coherence-based beamforming,” *IEEE Transactions on Ultrasonics, Ferroelectrics, and Frequency Control*, 2020
8. M. Graham, F. Assis, D. Allman, A. Wiacek, **E. A. González**, M. Gubbi, J. Dong, H. Hou, S. Beck, J. Chrispin, and M. A. L. Bell, “In vivo demonstration of photoacoustic image guidance and robotic visual servoing for cardiac catheter-based interventions,” *IEEE Transactions on Medical Imaging*, 2020
9. K. M. Kempinski, A. Wiacek, M. Graham, **E. A. González**, B. Goodson, D. Allman, J. Palmer, H. Hou, S. Beck, J. He, and M. A. L. Bell, “In vivo photoacoustic imaging of major blood vessels in the pancreas and liver during surgery,” *Journal of Biomedical Optics*, vol. 24, no. 12, p. 121 905, 2019
10. **E. A. González**, S. E. Romero, and B. Castaneda, “Real-time crawling wave sonoelastography for human muscle characterization: Initial results,” *IEEE Transactions on Ultrasonics, Ferroelectrics, and Frequency Control*, vol. 66, no. 3, pp. 563–571, 2018
11. A. Saavedra, J. Guerrero, J. Pinto, **E. A. González**, and B. Castañeda, “Aspectos físicos de las técnicas elastográficas basadas en ultrasonido,” *Καρκίνος*, p. 34, 2014

Conference Proceedings and Associated Presentations

1. J. Zhang, A. Wiacek, **E. A. González**, Z. Feng, K. Ding, and M. A. L. Bell, “A Flexible Array Transducer for Photoacoustic-Guided Surgery,” in *2022 IEEE International Ultrasonics Symposium (IUS)*, IEEE, 2022, pp. 1–4
2. **E. A. González**, C. A. Graham, and M. A. L. Bell, “Optimization of a dual wavelength atlas technique to differentiate methylene blue from hemoglobin in photoacoustic signals,” in *Photons Plus Ultrasound: Imaging and Sensing 2022*, SPIE, vol. 11960, 2022, pp. 51–58
3. **E. A. González**, F. Assis, C. J., and M. A. L. Bell, “A beamformer-independent method to predict photoacoustic visual servoing system failure from a single image frame,” in *2021 IEEE International Ultrasonics Symposium (IUS)*, IEEE, 2021, pp. 1–4

4. **E. A. González**, A. Jain, and M. A. L. Bell, "Photoacoustic differentiation of cortical from cancellous bone in the lumbar vertebrae of an intact human cadaver to prevent bone breaches during spinal fusion surgeries," in *Photons Plus Ultrasound: Imaging and Sensing 2021*, International Society for Optics and Photonics, vol. 11642, 2021, p. 1 164 210
5. **E. A. González**, and M. A. L. Bell, "Acoustic frequency-based differentiation of photoacoustic signals from surgical biomarkers," in *2020 IEEE International Ultrasonics Symposium (IUS)*, IEEE, 2020, pp. 1–4
6. **E. A. González**, and M. A. L. Bell, "A GPU approach to real-time coherence-based photoacoustic imaging and its application to photoacoustic visual servoing," in *Photons Plus Ultrasound: Imaging and Sensing 2020*, International Society for Optics and Photonics, vol. 11240, 2020, p. 1 124 054
7. **E. A. González**, M. R. Gubbi, and M. A. L. Bell, "GPU implementation of coherence-based photoacoustic beamforming for autonomous visual servoing," in *2019 IEEE International Ultrasonics Symposium (IUS)*, IEEE, 2019, pp. 24–27
8. K. M. Kempinski, A. Wiacek, J. Palmer, M. Graham, **E. A. González**, B. Goodson, D. Allman, H. Hou, S. Beck, J. He, and M. A. L. Bell, "In vivo demonstration of photoacoustic-guided liver surgery," in *Photons Plus Ultrasound: Imaging and Sensing 2019*, International Society for Optics and Photonics, vol. 10878, 2019, 108782T
9. **E. A. González**, A. Wiacek, and M. A. L. Bell, "Visualization of custom drill bit tips in a human vertebra for photoacoustic-guided spinal fusion surgeries," in *Photons Plus Ultrasound: Imaging and Sensing 2019*, International Society for Optics and Photonics, vol. 10878, 2019, p. 108785M
10. **E. A. González**, and M. A. L. Bell, "Segmenting bone structures in ultrasound images with Locally Weighted SLSC (LW-SLSC) beamforming," in *2018 IEEE International Ultrasonics Symposium (IUS)*, IEEE, 2018, pp. 1–9
11. O. Zenteno, **E. A. González**, S. Treuillet, B. M. Valencia, B. Castaneda, A. Llanos-Cuentas, and Y. Lucas, "Volumetric monitoring of cutaneous leishmaniasis ulcers: Can camera be as accurate as laser scanner?" *Computer Methods in Biomechanics and Biomedical Engineering: Imaging & Visualization*, pp. 1–9, 2018
12. G. Valenzuela, R. Laimes, I. Chavez, C. Salazar, **E. A. González**, I. Tirado, J. Pinto, J. Guerrero, and R. J. Lavarello, "In vivo diagnosis of metastasis in cervical lymph nodes using backscatter coefficients," in *2018 IEEE International Ultrasonics Symposium (IUS)*, IEEE, 2018, pp. 1–4
13. O. Zenteno, **E. A. González**, S. Treuillet, B. Castañeda, B. Valencia, A. Llanos, and Y. Lucas, "Volume estimation of skin ulcers: Can cameras be as accurate as laser scanners?" In *European Congress on Computational Methods in Applied Sciences and Engineering*, Springer, 2017, pp. 735–744
14. S. E. Romero, **E. A. González**, R. Lavarello, and B. Castañeda, "A comparative study between parallel and normal excitation for crawling wave sonoelastography," in *12th International Symposium on Medical Information Processing and Analysis*, International Society for Optics and Photonics, vol. 10160, 2017, 101601G
15. **E. A. González**, P. Li, J. Ormachea, K. Parker, R. Lavarello, and B. Castañeda, "Regularized wavelength average velocity estimator for quantitative ultrasound elastography," in *2016 IEEE International Ultrasonics Symposium (IUS)*, IEEE, 2016, pp. 1–4
16. **E. A. González**, J. Ormachea, K. J. Parker, and B. Castaneda, "Wavelength average

- velocity estimator for ultrasound elastography,” in *2016 IEEE 13th International Symposium on Biomedical Imaging (ISBI)*, IEEE, 2016, pp. 1017–1020
17. **E. A. González**, N. Sheth, B. Castañeda, J. Dahl, and R. Lavarello, “Accuracy of backscatter coefficient estimation in aberrating media using different phase aberration correction strategies-a simulation study,” in *Ultrasonics Symposium (IUS), 2014 IEEE International*, IEEE, 2014, pp. 2438–2441